QUALITY BY DESIGN

Improving Pre-Stressed Reinforcement for Concrete Railroad Ties via Geometrical Dimensioning and Tolerancing

by

MARK DAVIS HAYNES

B.S., Industrial Engineering, Kansas State University, 2011

AN ABSTRACT OF A DISSERTATION

submitted in partial fulfillment of the requirements for the degree

DOCTORATE OF INDUSTRIAL ENGINEERING

Department of Industrial Engineering
College of Engineering

KANSAS STATE UNIVERSITY
Manhattan, Kansas

2015

Abstract

Quality is a result of product design and production control. Product design must maximize the ability to function across variations in production and environment. Production control must monitor and maintain the key design characteristics necessary for the intended function. Failure to do so results in premature part failure and increased costs. This has occurred in the production of modern cross ties. By designing quality into the product and production process, performance is maximized.

This research presents a methodology for incorporating quality into the product design and production process. For product design, a relationship between product performance and design parameters is established by modeling techniques. These models provide a means to redesign the product to maximize performance and to understand the sensitivity of the design to fluctuation in production and environment. These models also establish the key design parameters that are critical for sustaining quality. For production, a method of monitoring the key design parameters is presented that provides an affordable means of automated inspection. Automated inspection removes operator error from the inspection process and allows for greater sampling rates to be achieved. The methodology presented allows for a potential of 100% inspection to be achieved with minimal impact to production costs.

The research is applied to the analysis and quality control of pre-stressing steel reinforcement for concrete cross-ties. This application provides an opportunity to test and verify the research findings on a real world problem.

Novel automated 3D spatial analysis algorithms are presented. This research furthers the state of the art of performing Geometrical Dimensioning and Tolerancing (GD&T). A cost effective method of non-contact surface profiling was developed with high resolution and high density surface profiles. The combined research findings present a methodology of achieving quality by design.

QUALITY BY DESIGN

Improving Pre-Stressed Reinforcement for Concrete Railroad Ties via Geometrical Dimensioning and Tolerancing

by

MARK DAVIS HAYNES

B.S., Industrial Engineering, Kansas State University, 2011

A DISSERTATION

submitted in partial fulfillment of the requirements for the degree

DOCTORATE OF INDUSTRIAL ENGINEERING

Department of Industrial Engineering
College of Engineering

KANSAS STATE UNIVERSITY
Manhattan, Kansas

2015

Approved by:

Major Professor
Chih-Hang John Wu

Copyright

Abstract

Quality is a result of product design and production control. Product design must maximize the ability to function across variations in production and environment. Production control must monitor and maintain the key design characteristics necessary for the intended function. Failure to do so results in premature part failure and increased costs. This has occurred in the production of modern cross ties. By designing quality into the product and production process, performance is maximized.

This research presents a methodology for incorporating quality into the product design and production process. For product design, a relationship between product performance and design parameters is established by modeling techniques. These models provide a means to redesign the product to maximize performance and to understand the sensitivity of the design to fluctuation in production and environment. These models also establish the key design parameters that are critical for sustaining quality. For production, a method of monitoring the key design parameters is presented that provides an affordable means of automated inspection. Automated inspection removes operator error from the inspection process and allows for greater sampling rates to be achieved. The methodology presented allows for a potential of 100% inspection to be achieved with minimal impact to production costs.

The research is applied to the analysis and quality control of pre-stressing steel reinforcement for concrete cross-ties. This application provides an opportunity to test and verify the research findings on a real world problem.

Novel automated 3D spatial analysis algorithms are presented. This research furthers the state of the art of performing Geometrical Dimensioning and Tolerancing (GD&T). A cost effective method of non-contact surface profiling was developed with high resolution and high density surface profiles. The combined research findings present a methodology of achieving quality by design.

Contents

Figures

Tables

Acknowledgements

The author would like to thank the Federal Railroad Administration (FRA) for providing funding that made this research possible. Additionally, LB Foster/CXT Concrete Ties has donated extensive resources, including all of the reinforcements, to make the project a success. I would also like to thank Drs. Hailing Yu and David Jeong at the John A. Volpe National Transportation Systems Center for their valuable suggestions and parallel analysis work. In addition, the Precast/Pre-stressed Concrete Institute (PCI) for establishing an industry advisory panel to the project, the Kansas State University's University Transportation Center (K-State UTC) for graduate student tuition support. Finally, special thanks to my committee members for their guidance and support throughout the project.

Dedication

For the educators within my life who made this possible.

Preface

Through this research Kansas State University has developed a means of improving the design and quality of pre-stressing steel reinforcement wires used in concrete ties. A non-contact indent profiling system has been developed that can provide full geometrical definition of the pre-stressing reinforcement wire. The system has been utilized to understand and create models relating the indent geometries of the reinforcement wire to the performance of the concrete cross tie.

It is recommended that these research findings be used to develop optimized reinforcement wire geometry and to provide sustaining reinforcement wire quality control. Modifications should be made to ASTM-A881 within accordance to these findings so that the production and testing requirements of the pre-stressing steel reinforcement wire may be improved.

The application of this research is to resolve ongoing issues with premature failure of pre-stressed concrete cross ties. Within this study 13 commercially available and 12 custom-made reinforcement wires have been studied. A new non-contact indent profiling system has been developed to collect detailed surface profiles of the pre-stressing steel. New geometrical feature measurements and processing algorithms have been developed to provide detailed measurement of pre-stressing steel within accordance to the dimensioning and tolerancing guidelines of ASME Y14.5-2009. These geometrical features have been found to have a significant relationship with the transfer length and fracture propensity of concrete cross ties. Models have been created that provide the ability to predict the transfer length of concrete cross ties given the results of the non-contact indent profiling system. This system provides a means of improving the design quality of reinforcement steel and a means of sustaining quality control throughout the production lifecycle.

Chapter 1 — Introduction

This research provides a detailed analysis into the influence of pre-stressing steel reinforcement surface profile on the quality and reliability of pre-stressed concrete railroad ties. This research addresses ongoing problems with the design and quality control of modern pre-stressed concrete railroad ties. The research identifies critical aspects of the geometrical design of pre-stressing reinforcement wire that directly relate to pre-stressed concrete railroad ties. Novel geometrical features have been established that have a strong correlation to the transfer length of pre-stressed concrete members. A method of measuring and performing quality control on the geometrical design is presented. The method relies on principles of datuming and measurement as defined by ASME Y14.5-2009 standard for Dimensioning and Tolerancing [1,2].

The indent geometry on the surface of pre-stressing steel reinforcement wire has been found to have a direct relationship with the splitting potential of the reinforcement wire and the transfer length of concrete members using the wire [4,8].

Within this study 13 commercially available reinforcement wires have been measured and tested to determine how their design will influence the quality of concrete railroad ties. In addition 12 custom new reinforcement wire geometries were made. The analysis of commercially available reinforcement wires provides an understanding of the current variation of wire types available in the industry. The custom geometries provide controlled variation of the geometrical features to identify which geometrical features and their ranges are significant for pre-stressed concrete railroad tie quality.

A novel 3D surface profilometry system has been developed that provides detailed surface profile information of pre-stressing steel with a resolution of one micron. Such a detailed surface profiling of concrete reinforcement steel has never been done before. This profilometry system provides both a means of engineering improved reinforcement wire designs and implementing more complete reinforcement wire quality control. Scanning systems developed with data processing rates and overall design characteristics suited for practical industrial application [6].

Novel 3D spatial analysis and geometrical feature measurement algorithms have been developed to provide automated and semi-automated analysis of high resolution surface profiles. The geometrical feature measurement algorithms have been proven within this study to perform better than the current ASTM-A881 profile requirements and predicting the performance of pre-stressed concrete members made with the reinforcement steel. The algorithms adhere to the principles of datuming and measurement defined by ASME Y14.5-2009. Dimensional requirements defined with stable, functional, and usable datums provide a more robust means of measurement across different testing systems and different measurement operators [2,3,5,7].

Novel theoretical and statistical models have been developed that predict the transfer length given reinforcement wire geometry. Models have been developed with a coefficient of determination in excess of 95% and strong statistical significance. Empirical models are based upon testing of 4 wire concrete prisms with known transfer lengths [4]. Theoretical models rely on fundamental principles of friction coefficients and adhesive shear properties of concrete. Models have been developed combining reinforcement wire geometry and release strength of the concrete member to create an all-inclusive model to predict transfer length given the conditions of the concrete member [8].

With the findings from this research new pre-stressing indent profiles may be designed that improve the life expectancy and load capacity of concrete railroad ties. The systems developed from this research can be implemented in production to provide sustaining quality control at a standard currently not possible with the current industry practices defined by ASTM-A881 [4,8].

1.1 Background

This section documents the background information needed to understand the deficiencies in the current ASTM A881 standard and fundamental principles of geometrical measurement and dimensioning that are necessary for adequate quality control of pre-stressing steel reinforcement wire indent profiles.

1.1.1 Problem Statement

Premature failure of pre-stressed concrete railroad ties in the field are a costly occurrence with modern tie design. Concrete railroad ties are intended to have higher load capacities and life spans with less maintenance than common wooden cross ties. Due to unpredictable behavior, concrete ties currently are not meeting their designed life and load expectancies. This results in expensive maintenance costs and additional track downtime.

A key predictor of the performance of a pre-stressed concrete cross tie is the transfer length. The transfer length is defined as the distance required to transfer the pre-stressing forces of the reinforcement into the concrete member. Assuring that the transfer length is less than the position of the rail seat is necessary to establish the full pre-stressing force prior to the load point of the concrete tie.

The indent geometries embedded into the surface of the pre-stressing steel reinforcement wire are a key predictor to the concrete members transfer length and the overall performance of the concrete tie. This research investigates the influence of these geometrical features and methods of sustaining geometrical quality control.

1.1.2 ASTM A881-2010 Standard

The current standard for pre-stressing steel reinforcement wire design is ASTM A881-2010. This document specifies the requirements for the material, mechanical properties, requirements for indentations, packaging and other general requirements of the reinforcement wire. In respects to the indent geometry requirements for the indent edge wall angle (A), indent depth (a), indent length (L), and pitch/period (P). The dimensions are illustrated in the figure below.

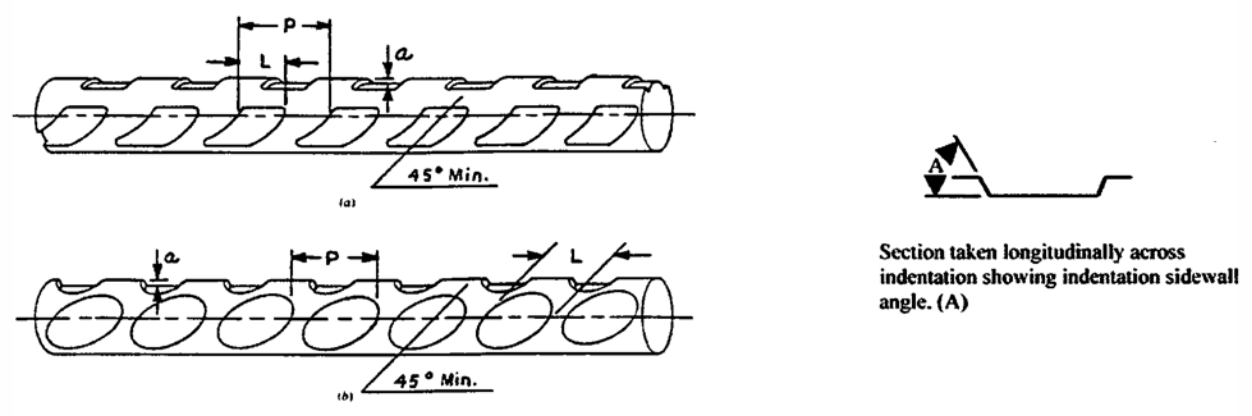

Figure 1. ASTM A881 Geometrical Feature Requirements[12]

It is also stated that the indent will be orientated at an angle of at least 45°. The table below shows acceptable values for two wire types within the standard. The 5.32mm (.2094in) diameter wire is considered within the scope of this research project.

Table 1. ASTM A881 Wire Dimensions[12]

Wire Type	Diameter		Depth, *a*		Length, *L*		Pitch, *P*	
	in.	[mm]	in.	[mm]	in.	[mm]	in.	[mm]
1	0.198	[5.03]	0.005	[0.13]	0.138	[3.5]	0.217	[5.5]
2	0.2094	[5.32]	0.0045	[0.115]	0.138	[3.5]	0.215	[5.46]

The standard does not provide a detailed requirement as to how the indents shall be measured. This is left to be decided amongst the purchaser and supplier. The current standard does not state which geometrical features of the wire contribute greatest to the wires performance. In order determine ideal design parameters for a reinforcement wire, it is necessary to first establish the amount of influence each parameter has on the performance of the wire. Next, this must be followed with a detailed measurement protocol to make determining the produced geometry controlled and repeatable. Current methods of using depth micrometers and probes do not analyze the full non-uniform surface profile of the indents. Geometrical features such as the indent edge wall angle are not constant and are varying throughout the indent feature, and con not be fully defined with these limited measurement techniques.

1.1.3 Geometrical Dimensioning and Tolerancing (GD&T)

The current standard for stating and interpreting geometrical dimensions and tolerances is ASME Y14.5m-1994. The standard presents four fundamental types of controls which are location, size, orientation, and form. These controls can be specified using a variety of geometrical characteristics which include the following:

- Straightness
- Flatness
- Circularity
- Cylindricity
- Angularity
- Profile
- Position
- Runout
- Symmetry

These are the primary geometric characteristics and most part geometries can be defined from the above mentioned list. Other geometrical characteristics exist for additional part definition. Location and orientation of parts are to always be made with respects to a datum reference frame. Controls of Size are not required to be with respects to datums and controls of form should never be made with respects to datums.

Datum Reference Frames

As per ASTM Y14.5-2009, in order to define a consistant measurement process that is unambiguous for interpretation it is necessary to define the datum reference frame. The datum reference frame (DRF) provides theoretical points, axes, lines, or planes as to which measurements can be made from. By defining measurements from datums, the orientation and position of the part during the measurement process is unambiguous [10].

As the indent geometry of pre-stressing steel is irregular, variation in measurement procedures can create widely different results. A basic illustration of the concept is shown below in the

measurement of a rectangular block. Depending upon the method used to locate the rectangular part, multiple length measurements can be determined. The location of the part as shown on the left creates a long length measurement. The location of the part as shown on the right creates a shorter length measurement. By defining an order of precedence in locating the part a repeatable measurement requirement can be communicated. The part shown below should be located to datum *A* then *B* every time so that the measurement is repeatable amongst different individuals and with different measurement equipment.

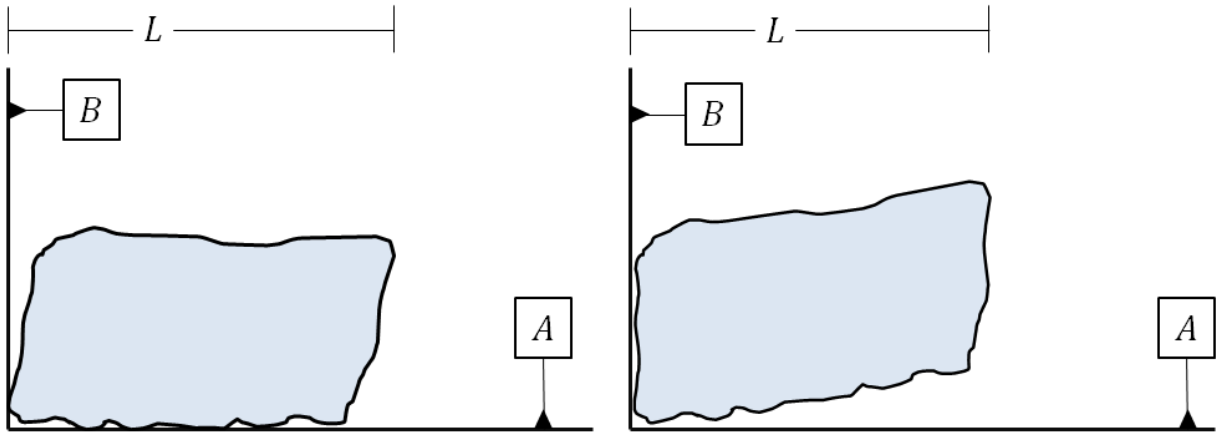

Figure 2. Necessity of Datums for Stable and Repeatable Measurement

This need for datum reference frames is also seen for the pre-stressing steel reinforcement wire indent geometry. Below is an illustration of a typical chevron style indent geometry. These indent shapes are the most common variety considered within this study.

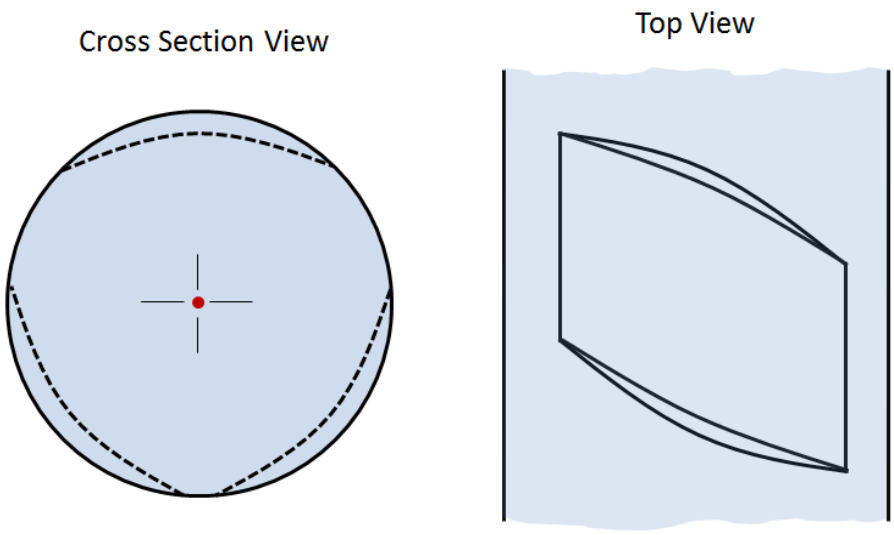

Figure 3. Illustration of Typical Chevron Style Reinfocement Wire

Typically the indent depth is measured at the deepest portion of the indent with the wire fixated to a table and rolled to the position of maximum depth. The figure below shows a typical cross section of a chevron style reinforcement wire. As the maximum depth is constant over a large portion of the indented region, the depth measurement may be taken by the user at an angle that is not orthogonal to the surface of the wire.

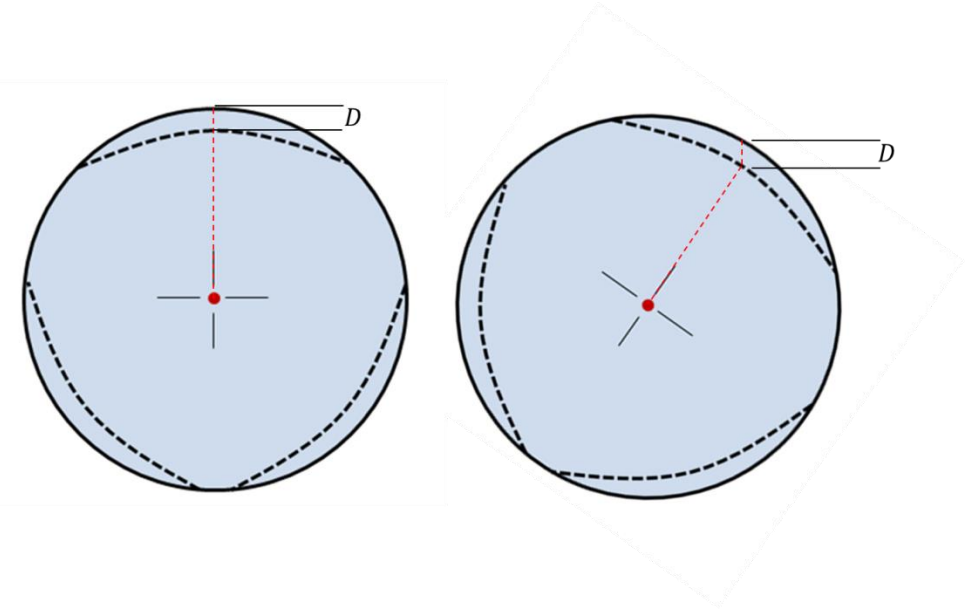

Figure 4. Example Issue of a Measurement without Datum Definition

By defining a datum axis A and then declaring that the depth measurement is to be made with respect to datum A the measurement may be taken consistently regardless of rotation of the part.

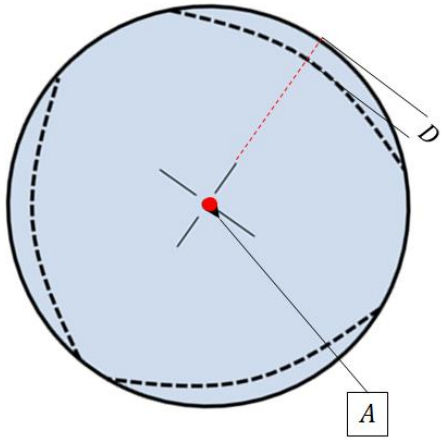

Figure 5. Benefits of a Datum Based Measurement

The use of datum's provides a repeatable measurement requirement, that is independent of the measurement device. This allows for specifications to be made that will be repeatable among different end users and operating equipment.

1.1.4 Minimal Zone Measurements

Minimal zone measurements provide a means to fit a perfect geometric form to a non-perfect collection of measured data points. For Geometric Dimensioning & Tolerancing (GD&T) applications the most common types of geometric forms fitted are points, axes, and planes.

Spatial Translation and Rotation

In order to calculate the minimal zone for any application, it is necessary first to have an understanding as to how to translate and rotate points within a Cartesian coordinate system. A tolerance zone unrestrained to a datum reference frame has six degrees of freedom. Three degrees are for translation and three degrees are for rotation in a 3-Dimensional space. In order to calculate the tolerance zone for a data set, the point cloud must be aligned in translation and rotation to the surface profile. These translations and rotations are $(T_x, T_y T_z, \theta_x, \theta_y, \theta_z)$, for six degrees of freedom in Cartesian space.

Given an initial point cloud, C', with each row of the matrix representing a data point. The data points defined by position $(x_i', y_i', z_i'): i \in [1, N]$.

$$C' = \begin{bmatrix} x_1' & y_1' & z_1' \\ x_2' & y_2' & z_2' \\ x_3' & y_3' & z_3' \\ \vdots & \vdots & \vdots \\ x_N' & y_N' & z_N' \end{bmatrix}$$

The matrix C' can be translated by adding with matrix T, where T is an N by 3 matrix.

$$T = \begin{bmatrix} T_x & T_y & T_z \\ T_x & T_y & T_z \\ \vdots & \vdots & \vdots \\ T_x & T_y & T_z \end{bmatrix}$$

The rotation can be defined by the three rotation matrices R_x,R_y, and R_z. Multiplying the matrices together gives a resultant rotation matrix, R.

$$R_x = \begin{bmatrix} 1 & 0 & 0 \\ 0 & \cos(\theta_x) & -\sin(\theta_x) \\ 0 & \sin(\theta_x) & \cos(\theta_x) \end{bmatrix} \quad R_y = \begin{bmatrix} \cos(\theta_y) & 0 & \sin(\theta_y) \\ 0 & 1 & 0 \\ -\sin(\theta_y) & 0 & \cos(\theta_y) \end{bmatrix} \quad R_z = \begin{bmatrix} \cos(\theta_z) & -\sin(\theta_z) & 0 \\ \sin(\theta_z) & \cos(\theta_z) & 0 \\ 0 & 0 & 1 \end{bmatrix}$$

$$R = R_x R_y R_z$$

This form of matrix rotation is known as gimbal rotation. An alternative solution would be to use quaternion rotation matrices, with two variables defining the axis direction and one variable defining the amount of rotation about the axis.

The repositioned point cloud is defined by matrix $C: C = (C' + T)R$.

$$C = \begin{bmatrix} x_1 & y_1 & z_1 \\ x_2 & y_2 & z_2 \\ x_3 & y_3 & z_3 \\ \vdots & \vdots & \vdots \\ x_N & y_N & z_N \end{bmatrix} = (C' + T)R$$

Linear Zone (Straightness)

The linear zone is used to determine a representative line of the data set. The linear zone is a 1 dimensional search problem. The linear zone which is used to determine the straightness of the set of points is found by determining the angle of orientation θ that minimizes the distance between two parallel lines. The first line is at a position greater than all points, the second line is at a position less than all points. [37]

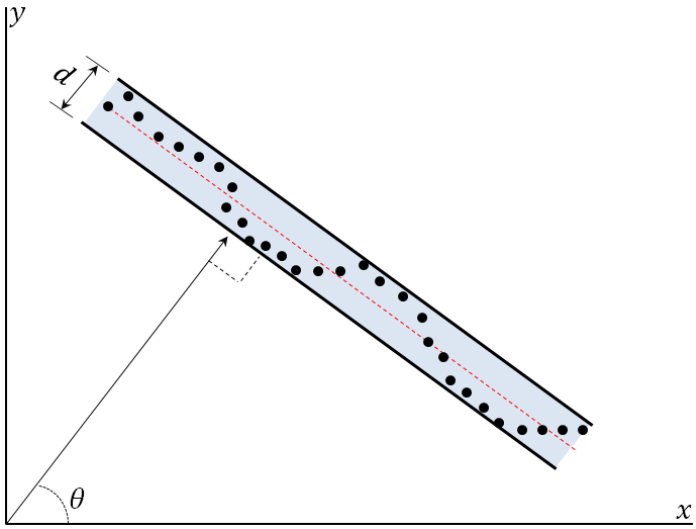

Figure 6. Linear Zone

A simple model of the problem can be made by rotating the data points at angle θ until a local minimum is found. Minimizing the distance,d, which is the distance between two parallel lines, $l_1$and l_2. Where $l_2$is greater than all data points and $l_1$is less than all data points.

$$Minimize\ d = l_2 - l_1$$
$$Subject\ to\ \forall_{i=0}^{N} x_i \sin(\theta) + y_i \cos(\theta) \geq l_1$$
$$\forall_{i=0}^{N} x_i \sin(\theta) + y_i \cos(\theta) \leq l_2$$

Planar Zone (Flatness)

Similar to straightness, flatness is applied to 3-dimensional surfaces. The minimal planar zone is a two dimensional search problem. The linear zone is used to determine the flatness of the set of points. This is found by determining the two angles of orientation, θ_1 and θ_2 that minimizes the distance between the two parallel planes, p_1 and p_2. The first plane is constrained to a position greater than all data points. The second plane is at a position less than all data points. [37]

$$Minimize\ d = p_2 - p_1$$
$$Subject\ to\ \forall_{i=0}^{N}\ \ y_i \sin(\theta_2) + [-x_i \sin(\theta_1) + z_i \cos(\theta_1)]\cos(\theta_2) \geq p_1$$
$$\forall_{i=0}^{N}\ \ y_i \sin(\theta_2) + [-x_i \sin(\theta_1) + z_i \cos(\theta_1)]\cos(\theta_2) \leq p_2$$

Circular Zone (Circularity)

The figure below shows how the circular zone is calculated. The blue shaded region represents all the data points bounded by two concentric circles. The first circle circumscribes all data points. The second circle inscribes all data points. The center point of these two concentric circles is used as the datum reference point for the circle. The radius of the circle is the mid radius between r_1 and r_2 $\left((r_2 - r_1)/2\right)$. [37]

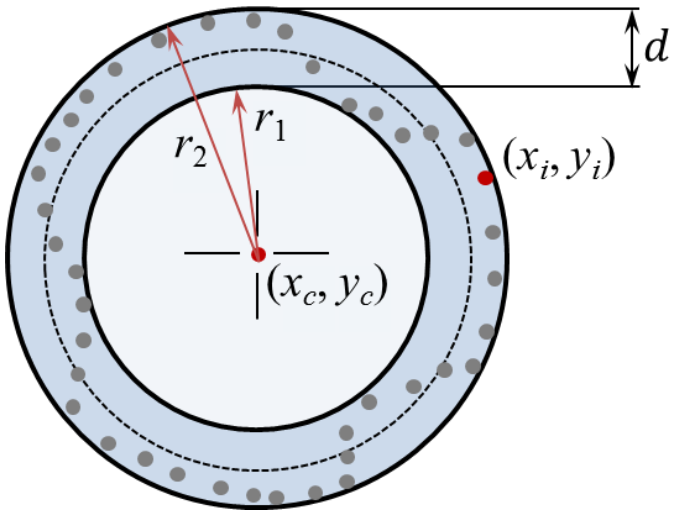

Figure 7. Circular Zone

$$Minimize\ d = r_2 - r_1$$
$$Subject\ to\ \forall_{i=0}^{N}(x_i - x_c)^2 + (y_i - y_c)^2 \geq r_1^2$$
$$\forall_{i=0}^{N}\,(x_i - x_c)^2 + (y_i - y_c)^2 \leq r_2^2$$

Above is the required optimization. With $(x_i, y_i): i \in [0, N]$ and (x_c, y_c) represents the center datum point. r_1 is the radius of the circle less than all data points and $r_2$is the radius of the circle greater than all data points and the objective is their minimal difference [24].

Cylindrical Zone (Cylindricity)

Shown in Figure 8, where d_i is the radial distance of the data point from the theoretical line determined by the two points p_α and p_β. The objective function is subject to the radius Z_1being greater than radius of all data points from the center axis and the radius Z_2 being less than radius of all data points from the center axis. In order to minimize the objective function the concentric cylinders can be translated and rotated in an iterative manner to obtain the local minimum. [37]

In order to solve this problem the position of the points $p_\alpha$and p_β are iteratively changed by the Nelder-Mead method until convergence is reached. If we assume the two points are fixed to z-planes that are a constant distance apart then we only have four parameters that can be varied by the Nelder-Mead $(p_{\alpha x}, p_{\alpha y}, p_{\beta x}, p_{\beta y})$. This presents a four dimensional non-linear search problem. The alternative method to define this model is with a single data points x and y values and then two angular values to represent pitch and yaw of the line.

Once this Nelder-Mead algorithm is completed, the result is the position of the center axis that adheres to the ANSI Y14.5 requirements for dimensioning and tolerancing. This reference axis will be used in determining the radial values of all data points from the center of the wire. This will provide a means of determining depth of the indented regions on the wire surface [24].

$$\min\{Z_1 - Z_2\}$$
$$s.t. Z_1 \geq d_i \forall_{i=1}^{I}$$
$$Z_2 \leq d_i \forall_{i=1}^{I}$$
$$d_i = \frac{|(p_i - p_\alpha) \times (p_i - p_\beta)|}{|(p_\beta - p_\alpha)|}$$

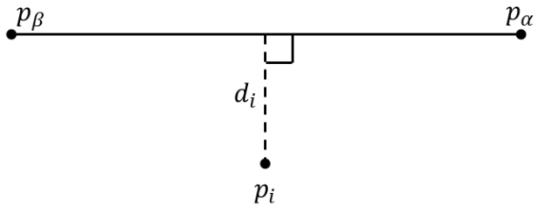

Figure 8. Point to Line Distance

Profile Zone (Surface Profile)

All surfaces whether freeform, planar, or cylindrical can be constrained by a Surface Profile Tolerance as defined by the ASME Y14.5-2009. For a general surface consider $f_{nom}(x, y, z) = D_{nom}$, where D_{nom} is the minimum distance from point (x, y, z) to the given nominal surface profile. Positive values of D_{nom} represents data points above the nominal surface, negative values of D_{nom} represent data points below the nominal surface. The minimum zone can be defined as follows:

$$\min\{Z_1 - Z_2\}$$
$$s.t. Z_1 \geq D_{nom,i} \forall_{i=1}^{N}$$
$$Z_2 \leq D_{nom,i} \forall_{i=1}^{N}$$
$$D_{nom,i} = f_{nom}(x_i, y_i, z_i)$$

In some cases it may be difficult to define a surface profile by a function. An alternative solution is to define the surface profile as a set of nominal points, $(x_{nom}, y_{nom}, z_{nom})$, with direction vectors that represent the normal vector to the surface, (a, b, c) at location $(x_{nom}, y_{nom}, z_{nom})$. The normal vector must be pointing away from the surface of the part. An approximation may be made by calculating the signed distance of the actual point from the nominal point along the nominal points normal vector. This distance is defined as G.

$$G = \frac{a(x_{nom} - x) + b(y_{nom} - y) + c(z_{nom} - z)}{\sqrt{a^2 + b^2 + c^2}}$$

For every data point there must be a nominal point and nominal vector pointing normal to the surface. So for all data points $(x_i, y_i, z_i): i \in [1, N]$, there is a corresponding nominal position $(x_{nom,i}, y_{nom,i}, z_{nom,i})$ and nominal direction vector $(a_i, b_i c_i)$ that points away from the surface. The profile zone can be defined as follows:

$$\begin{aligned} &\min\{Z_1 - Z_2\} \\ &s.t. Z_1 \geq G_i \ \forall_{i=1}^{N} \\ &Z_2 \leq G_i \ \forall_{i=1}^{N} \\ &G_i = \frac{\left|a\left(x_{nom,i} - x_i\right) + b\left(y_{nom,i} - y_i\right) + c\left(z_{nom,i} - z_i\right)\right|}{\sqrt{a_i^2 + b_i^2 + c_i^2}} \end{aligned}$$

Ellipsoidal Zone (Orientation)

Expanding upon the concept of circular zone is the ellipsoidal zone. As the name describes, the ellipsoidal zone is determined by finding the position and orientation of two concentric ellipses that are of the minimum distance apart. Figure 9 illustrates how the ellipsoidal zone is determined. The thin dotted line shows the fitted ellipse with major axis a and minor axis b. All data points are at most within distance d of the ellipse. The ellipsoidal zone is of size $2d$.

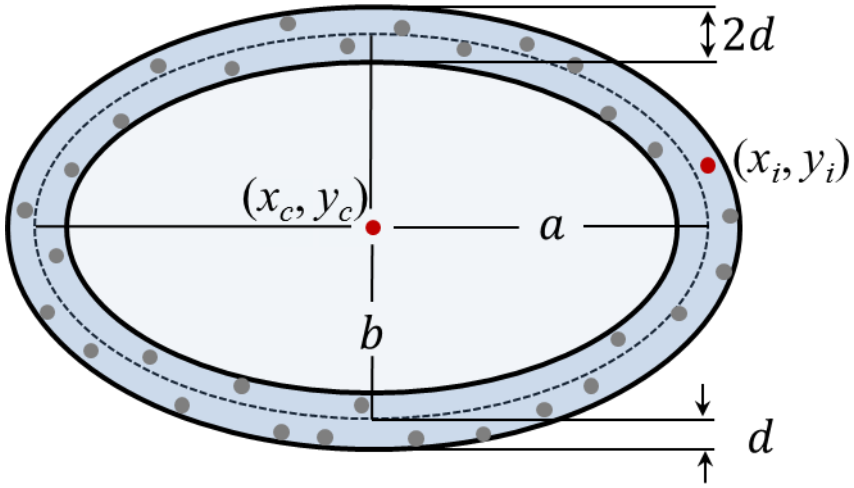

Figure 9. Ellipsoidal Zone

The distance from a given point to a point on an ellipse can be expressed by the equation below. In order to determine the minimum distance from the ellipse to the point a root finding must be used to iterate through values of θ such that d is minimized.

$$minimize\ d = \sqrt{(x - a\cos(\theta))^2 + (y - b\sin(\theta))^2}$$

To find the ellipsoidal zone the data points P_i with a position (x_i, y_i) set by the translation and rotation such that $P_i = (P_i' + T)R$. With decision variables a, b, T_x, T_y, and $R_z$the points can be translated and rotated such that the ellipsoidal zone is minimized. For each iteration a root finding method must be used to determine θ_i the parametric parameter of the ellipse for data point i.

$$Minimize\ 2d$$

$$Subject\ to\ \forall_{i=0}^{N}\sqrt{(x_i - a\cos(\theta_i))^2 + (y_i - b\sin(\theta_i))^2} \leq d$$

1.1.5 Non-Uniform and Complex Geometry Analysis

The typical commercially available indents available in the industry have a non-uniform geometry. The shape of a single indent profile is complex and widely varying from one manufacturer to the next. Gradual transitions from indent edge walls to the indent basin make determination of transition points difficult. Additionally, the indent edge is almost always

varying in angle and length across the indent region. As the indent geometries are only 100-200 microns in depth and the surface of the steel has a roughness ranging on the order of 10-15 microns, indent profiles are inherently difficult to measure and difficult to fully define the geometry and its requirements.

Figure 10 shows the indents isolated from a scanned reinforcement wire sample. The indents are colored with respects to the radial value of the surface profile. Areas with a low radius value from the center axis of the wire are shown in blue. Areas with a high radius value from the center axis of the wire are shown in red/magenta. As can been seen in the image the shape of the actual indent has complex curves and the indent depth is non-consistent throughout the indent profile.

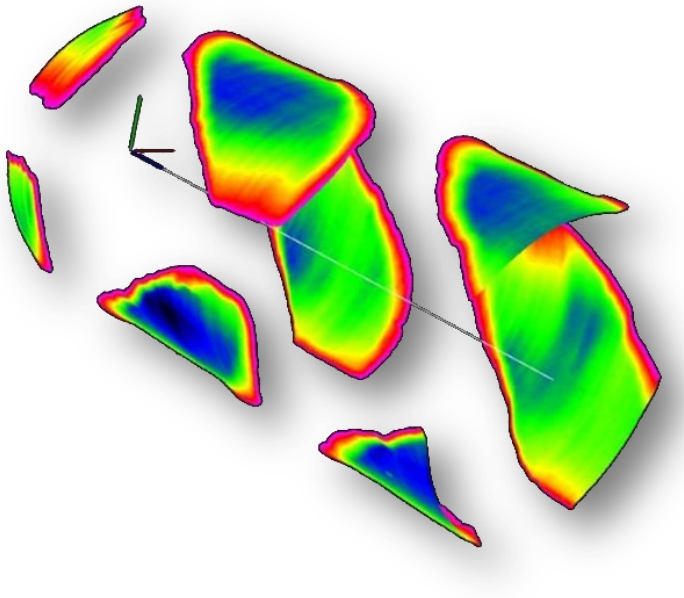

Figure 10. Isolated Indent Geometries from a Scanned Reinforcement Wire

Ideally the indent would be sectionalized so that each section defines a different aspect of the wire and each section has design requirements and tolerances that should be maintained. However, as seen in Figure 10 the transition from each section is not easy to define. Further difficulties arise when comparing wires from different manufactures as each manufacture has

their own unique surface profile. The indent edge wall is constantly varying over its section as is the indent basin; this prevents defining the geometry as simply a planar indent edge wall at a set orientation angle and an indent basin of depth. This is how currently the ASTM-A881 standard defines the geometry. However, there exist many wires that have large maximum depths with relatively low overall indent depth. There are also indents with steep edge wall angles at the position of maximum depth and at the indent extremities have very shallow edge wall angles.

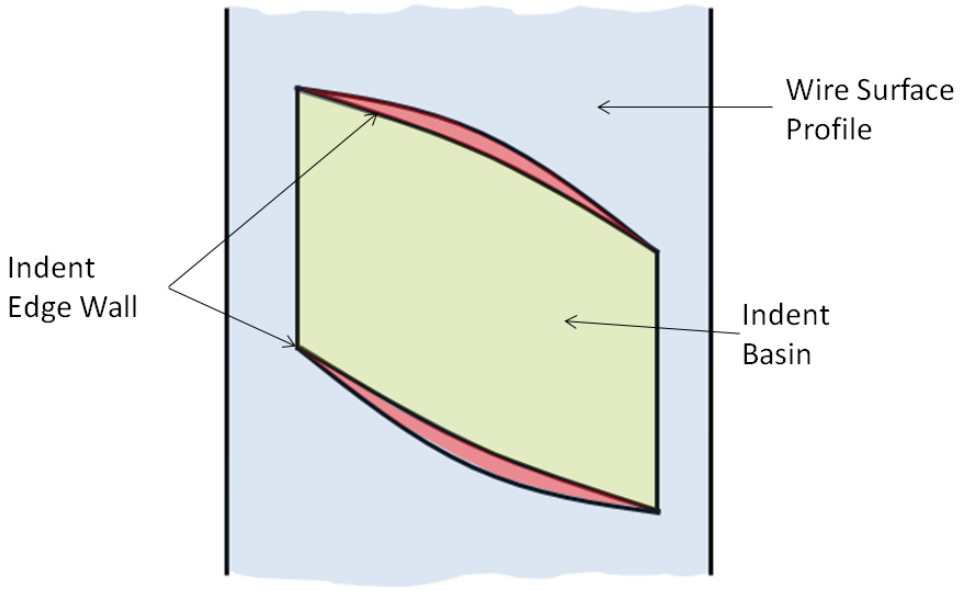

Figure 11. Sections of a Chevron Reinforcement Wire

The microscope image in Figure 12 is of wire sample WD. Wire sample WD very clearly has a varying indent edge wall angle when measuring the edge wall angle down the axis of the reinforcement wire. The indent edge wall angle at the location of maximum indent depth does not best represent the overall profile of this indent edge wall.

Figure 12. Wire WD, Non Constant Axial Edge Wall Angle

Figure 13 shows a 2D profile of an indent for wire type WF at its maximum depth. The graph's vertical axis has been scaled to show the detail of surface variation of the indent. The indent basin gradually blends with the indent edge wall at the bottom left of the graph. At the top right side of the graph the indent edge wall gradually blends with the wire surface profile. This makes determination of the boundary condition that defines the indent edge wall and basin difficult.

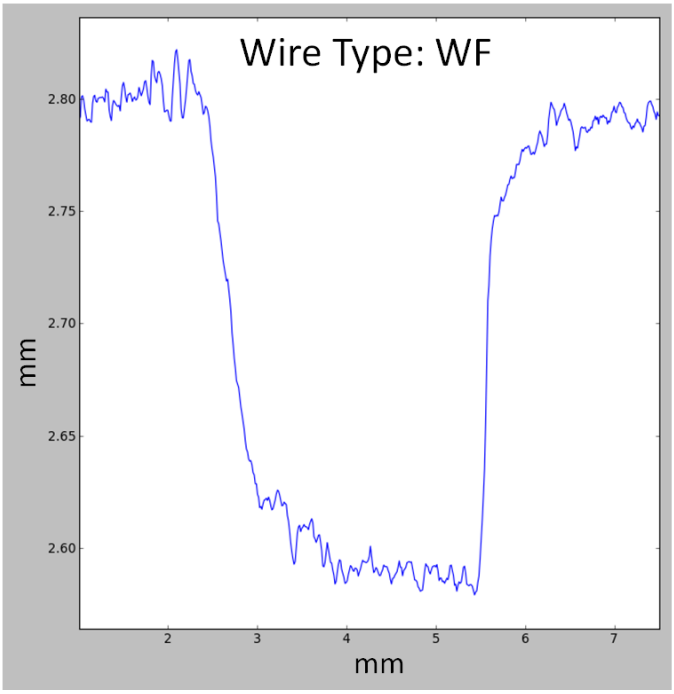

Figure 13. Unclear Indent Basin and Edge Wall

The complex profile of the indent geometry makes simple definitions – such as indent measured at maximum depth and indent edge wall measured at location of maximum depth – unreliable at fully defining the profile of the indent. This necessitates a method of analyzing the indent that performs a full form measurement.

1.1.6 Data Acquisition

Current industry practices of ASTM-A881 use a depth indicator to measure the maximum indent depth relative to the wire outer surface profile. The use of a linear displacement device along with the depth indicator allows the operator to measure the indent edge wall angle. In order to perform an analysis of the entire surface profile a new measurement and data collection method is needed.

Commercially available 3D scanners either do not have a working accuracy and resolution suited for the small indent profiles or they come at costs that are prohibitive for their use within this research and for use as an applicable quality control device for production. As such, four new 3D scanning prototypes were developed to measure the full profile of the reinforcement wire.

The prototype systems allowed for sampling and analysis of the currently available reinforcement steel, the prototypes also present a practical solution for industrial quality control applications.

1.1.7 Modeling Performance

Models were developed to determine which geometrical features have a significant relationship to the performance of the pre-stressing steel reinforcement wire. Both theoretical and statistical models were used in order to determine what relationship the reinforcement wire geometry has with the performance of the concrete member. The models provide several benefits. First, they identify which geometrical features are critical to the performance of the reinforcement wire. Second, they identify which geometrical features can and cannot be combined to create a representation of the reinforcement wire performance. Third, they provide a means of improving the reinforcement wire geometry to minimize transfer length while minimizing the fracture propensity induced by the wire. Finally, they provide a means of implementing quality control of the overall concrete tie based upon information about the detailed indent geometry.

The transfer length of concrete prisms and actual concrete cross ties were used within this study. The transfer lengths were calculated by a combination of whittemore gauges and a non-contact optical strain gage [15]. The optical strain gage was developed for determining transfer length in concrete ties [41, 36]. Extensive testing of the optical strain gage was done to confirm its ability to determine transfer length [34, 27, 9]. Currently work is being done to develop a non-contact transfer length measurement system for commercial use [14]. Transfer length of a concrete member is dependent upon many factors [60]. The concrete-aggregate mix, water ratio, release strength, and other factors all contribute variation to the transfer length. This research isolates the impact that the indent geometry has on transfer length.

Transfer lengths were determined with the use of the Zhao-Lee method [13]. This method was tested and verified against the 95% Average Maximum Strain (AMS) method [9]. The generalized Zhao-Lee method is in unbiased method of measuring transfer length that is capable of accommodating for concrete member with irregular geometries [35].

1.1.8 Research Map

Figure 14 shows the relationship of this research project and previous fields of study. As this is an interdisciplinary research project, prior research comes from a very broad background of engineering disciplines. The research map highlights four independent fields of research. These are Non-Linear Search, GD&T & Measurements, Spatial Feature Recognition, and Reinforcement Indent Design. This research project has contributed to each of these fields individually and is dependent upon them.

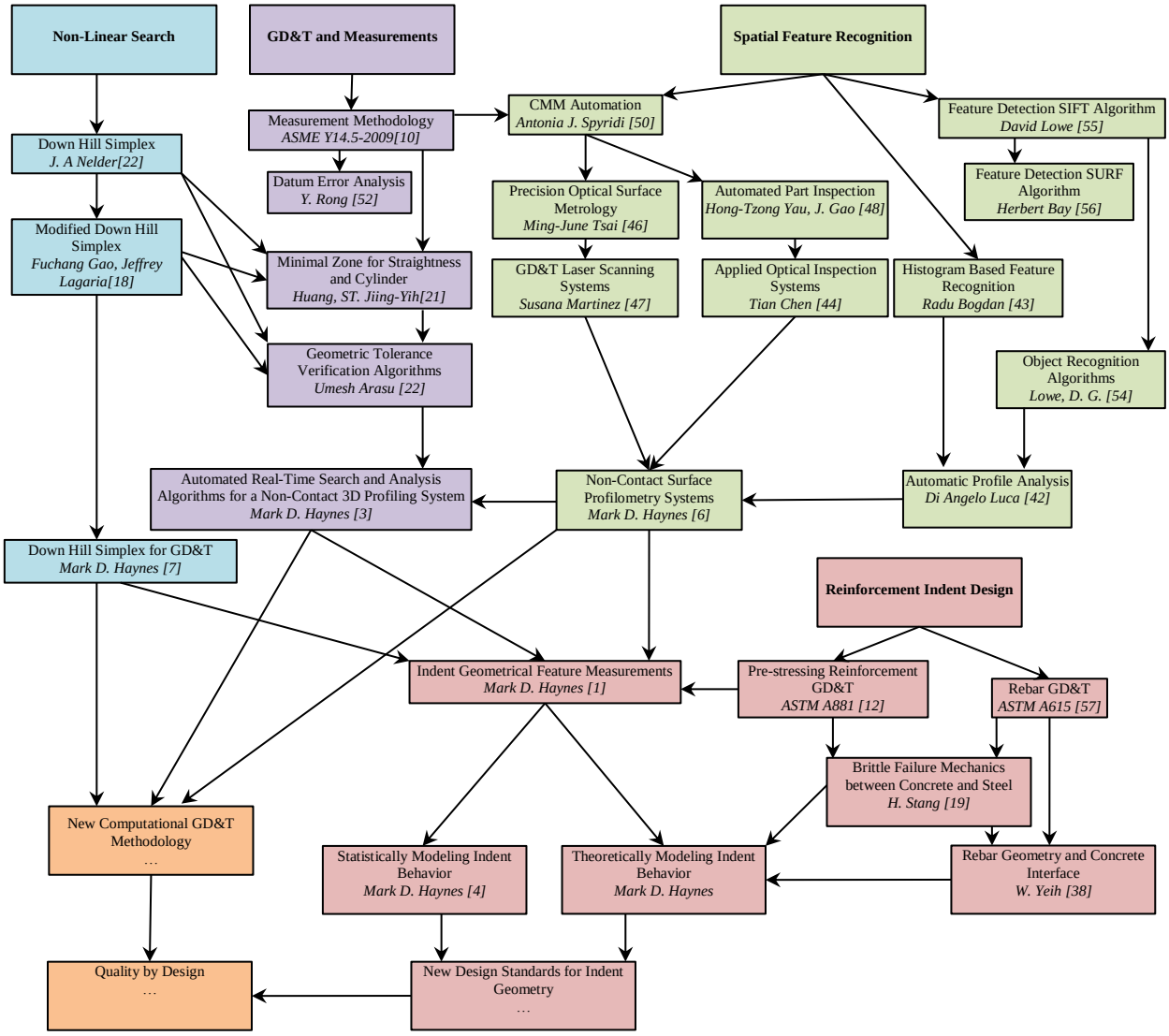

Figure 14. Research Map

1.2 Motivation

The list below provides a few key motivations for this research:

1. Can we create a new method of performing non-contact surface profiling that offers accurate surface measurements, high-speed and spatially dense data acquisition, with feasible system costs?
2. Can we create new algorithms that are suited for the unconventional data types of part surface profiles? Can we achieve the automated feature recognition needed for GD&T? What algorithms and programming methodologies will allow for efficient and effective data processing?
3. With millions of data points per surface profile, what new and more general measurements can be performed that were not previously possible, can these new measurements adhere to the guidelines and protocol of ASME Y14.5-2009?

1.3 Objectives and Scope

The focus of this research is to develop autonomous quality control systems that serve to improve the geometrical dimensioning and tolerancing of pre-stressed steel reinforcement wire. This research intends to achieve the following goals:

1. Research new geometrical feature measurements and algorithms that provide valuable definition of the quality of the reinforcement wire.
2. Research algorithms for geometrical feature recognition and extraction to provide an automated and repeatable method of measurement
3. Research non-linear search algorithms to improve the minimal zone measurement results and computation times for GD&T minimal zone problem sets.
4. Research new hardware and electronics to provide a cost effective and accurate method for profiling indent geometries.
5. Establish statistical models that predict the transfer length given the geometrical features of the pre-stressing steel reinforcement wire.
6. Establish theoretical models that predict the transfer length given the geometrical features of the pre-stressing steel reinforcement wire.
7. Validate the research findings through controlled experimentation

This research addresses two fundamental questions. First, what features of the pre-stressing reinforcement steel contribute to the quality of concrete members? Second, what parameters should those features have and how can they be measured to provide an improved pre-stressed concrete railroad tie and a means of controlling the quality throughout the production lifecycle.

1.4 Contribution

The list below presents key contributions this research provides to the technical community:

1. Improved definition of the design and inspection process of reinforcement wire are proposed for inclusion into ASTM A881
2. Geometrical features (Volumetric Void and Surface Area) found critical for part performance are proposed for inclusion into the GD&T standard ASME Y14.5
3. Discovered the Nelder-Mead simplex as the best solution for GD&T non-linear search class of problems
4. Modification of the Nelder-Mead simplex is presented with a superior performance for GD&T non-linear search
5. GPU parallel computing technique is presented for GD&T non-linear search and provides a significant speed improvement as compared to a serial implementation
6. Filtering and correction algorithms were created for 3D spatial analysis to correct for erroneous values in non-contact scan data
7. Robust algorithmic machine calibration and datum alignment methodology created to replace mechanical machine calibration
8. Segmentation algorithms to isolate geometrical features in a point cloud for individualized analysis
9. Automated measurement algorithms for critical geometrical features to provide a measurements without human bias
10. Algorithms for manipulating large scale point clouds within time constraints needed for industrial application
11. 3D visualization tool created for large scale point cloud metrology
12. Method of achieving high-speed non-contact profiling at an affordable cost
13. Solutions for high speed sensory and motion control synchronization

14. Method for verifying the quality of reinforcement steel
15. Research review of the current commercially available wires
16. Discovery of conditions likely to result in concrete fracture
17. Discovery of indent basin angle and its potential influence on fracture propensity
18. Discovery of edge wall angle influence on fracture propensity
19. Methodology for controlled fabrication and testing of isolated indent features (indent machining)
20. Discovery of relationship of indent features and tie quality(TL)
21. Multivariate regression models that can predict TL from wire geometry
22. Development of a Bond Index Number (BIN)
23. First theoretical understanding of the wire to concrete interface to include detail indent and wire geometry

1.5 Overall Approach

This research project relies on new developments in many independent fields of engineering for success. As such, great focus was made to provide early proof of concepts in each area of research. Early validations were performed to verify the ability to meet research requirements. Several iterations of developing proof of concepts, expanding, and implementing were used to complete the research. In total four uniquely different 3D systems were developed throughout the research. Each design improved upon its successor and allowed for new findings to be achieved.

1.6 Organization of the Report

This report is broken into nine major chapters. Each chapter is an independent research category that was pursued throughout the project. The chapters are organized as follows:

2. Geometrical Feature Measurements

Geometrical features used to fully define the indent geometries in pre-stressing steel reinforcement wire

3. Non-Linear Search in GD&T

Algorithms used to solve the non-linear problems as defined in chapter two.

4. Indent Profiling System Software and Algorithms

Algorithms used to filter erroneous data points, calibrate hardware, identify indent regions, and perform measurements.

5. Indent Profiling System Hardware and Electronics

Research and development of four 3D scanning systems specialized for pre-stressing reinforcement steel.

6. Wire Analysis and Measurements

Measurement results found using the findings of chapters two, three, and four

7. Statistical Modeling

Multivariate regressions developed to predict transfer length of concrete prisms given the indent geometrical feature measurements from chapter five as input parameters. Also contains individual correlations with the wire geometrical features and transfer length.

8. Theoretical Modeling

Theoretical models were developed that rely on coefficient of friction and adhesive shear forces to predict the transfer length and pull out force of a reinforcement wire

9. Validations

Validations to the measurement system presented in the previous chapters

10. Conclusion

Discussion of the major findings that have been discovered within this research

Chapter 2 — Geometrical Feature Measurements

This chapter documents the geometrical features measured of indent profiles on the surface of 5.32 mm diameter pre-stressing steel reinforcement wire. Throughout this research over 18 different geometrical feature measurements were studied that define the indent surface profile. Novel geometrical feature measurements were used that define the indent's volumetric void and indent surface area.

2.1 Introduction

The purpose of this research was to investigate a new standard of measurement methods for pre-stressing steel reinforcement wire used in concrete railroad ties. Currently the standards for pre-stressing steel reinforcement wire measurement require only limited measurements to be performed that do not fully define the indent geometry. In previous research a variety of un-tensioned and tensioned pullout experiments were performed [12,13]. Models were generated that fit this experimental data to the reinforcement wire [10]. Through this previous research new geometrical features were found that provide stronger correlation to transfer length and pull out tests than previously required geometrical features. These new measurement protocols utilize parameters that better predict the transfer length and the pull out force of reinforcement wire [10]. Which if utilized, can improve reinforcement wire quality control and design specifications. The wires considered in this study are a 5.32mm diameter chevron type reinforcement that is currently available within the industry. The indent depths within this study range from 100 to 200 microns. The indents are at an approximate 45 degree angle and are about 3-5 mm wide and 4-8mm long.

Developed within this research is a new means of identifying and extracting geometrical feature statistics from a non-contact precision-measurement 3D profilometer. Autonomous algorithms have been developed to search through large-scale Cartesian point clouds to identify and extract geometrical features. These algorithms are developed with the intent of providing real-time production quality control of cold-rolled steel wires. The geometry of the wire is critical in the performance of the overall concrete structure.

For this research a custom 3D non-contact profilometry system has been developed that utilizes laser displacement sensors for micron resolution surface profiling. Optimizations in the control and sensory system allow for data points to be collected at up to an approximate 400,000 points per second. In order to achieve geometrical feature extraction and tolerancing with this large volume of data, the algorithms employed are optimized for parsing large data quantities. The methods used provide a unique means of maintaining high resolution data of the surface profiles while keeping algorithm running times within practical bounds for industrial application.

By a combination of regional sampling, iterative search, spatial filtering, frequency filtering, spatial clustering, and template matching; a robust feature identification method has been developed. These algorithms provide an autonomous means of verifying tolerances in geometrical features. The key method of identifying the features is through a combination of downhill simplex and geometrical feature templates. By performing downhill simplex through several procedural programming layers of different search and filtering techniques, very specific geometrical features can be identified within the point cloud and analyzed for proper tolerancing. Being able to perform this quality control in real time provides significant opportunities in cost savings in both equipment protection and waste minimization.

In order to handle real-time data analysis a significant portion of the computational search algorithm is handled by the graphical processor unit (GPU). By parallel processing search iterations and effectively spreading the sampling of data, algorithm run times are greatly reduced.

Along with the efforts to minimize search algorithm run times, efforts have been taken to reduce the computational load of the templates that are used in identifying geometrical features. In order to create a light weight template for geometrical features, the templates are made in a branching procedural scheme. Each geometrical feature in consideration is broken down into several geometrical attributes. The shorter runtime geometrical attributes such as frequency variations are used first most to identify potential geometrical features. Once a potential geometrical feature is established, several different geometrical attributes are tested to see if there exists a match between the template and the considered region.

These efforts to improve feature recognition in 3D Cartesian point clouds have broader impacts in computational surface analysis and metrology than just the applied research of cold-rolled steel wires. By developing a light weight and accurate means to autonomously recognize features in 3 dimensional space, many opportunities are made available in computer visioning systems and automated surface metrology analysis without having to limit data density.

2.2 Background

Contemporary concrete railroad ties reinforced with pre-stressing steel reinforcement wires have experienced sporadic premature failures much shorter than their designed life span. There are two primary design influences of the reinforcement wire that can be directly related to the cross ties life span. The first is the transfer length of the reinforcement wire. Larger indent depths produce shorter transfer lengths. Transfer lengths that are too long will not have the full pre stressing forces at the rail seat, while transfer lengths that are too short can produce excessive stress at the end of the tie and produce fracture. The second is the indent edge wall angle; a shallower indent edge wall produces greater radial forces into the concrete rail road tie. Some radial force may produce compressive loading around the wire prevent concrete shear, however, if the radial forces are too large the wire may induce fracture propagation.

Figure 15 shows the type of reinforcement wires that these measurement protocols can be applied on. These wires have 3 rows of chevron type indentations that vary in depth, length, width, and edge slope as well as variations in their overall general shape. Some of these chevron style reinforcements have crisp surface profiles others have rounded shapes. In addition to the unique geometries, each wire has its own surface finish that may influence how well it bonds with the surrounding concrete.

Figure 15. Reinforcement Wire Samples in Study

Pre-stressed steel reinforcement wires are commonly used in many structural concrete members. This research on automated extraction algorithms is focused on providing quality control for pre-stressing steel reinforcement wires used in concrete railroad ties. During this research and development, a total of 11 different reinforcement wires available in the market were studied as well as 1 additional reinforcement wire with no indent pattern to serve as a baseline in experimentation. The 11 wires available in the market all have uniquely different surface profiles. It has been found through experiments with the developed 3D non-contact profilometry system and its software that these varying geometries of wire result in a wide distribution of performances. Furthermore, the profilometry system has identified which geometrical features have statistically significant correlations to the performance of concrete members. By knowing the statistically significant geometrical features of the reinforcement wire, various methods of quality control can be implemented with the profilometry system to autonomously verify the key features of the steel are within tolerance during production. In addition the system offers a means of predicting the performance of untested geometries of reinforcement wires through surface profile and metrology analysis. Figure 16 shows an example of railroad ties in the field that have failed. In the bottom left of the image, railroad ties show large end fractures.

Figure 16. Failed Pre-stressed Concrete Railroad Ties

It is understood that the internal forces generated from the pre-stressing steel wires are critical for strength and longevity of the concrete tie. The distance required for the pre-stressing forces of the steel reinforcement to transfer to a maximum load in the concrete is known as the Transfer Length. Figure 17 illustrates transfer length for a pre-stressed concrete railroad tie. Transfer Lengths that exceed the position of the rail seat makes the railroad tie prone to failure as the tie is not at its full horizontal compression forces where it experiences its vertical loading. By developing a profilometer to identify and provide quality control of what is an ideal geometry of a pre-stressing steel reinforcement wire which provides a proper transfer length; concrete railroad tie failures can be reduced. For these reasons the transfer length is chosen as the output metric for the developed profilometry system.

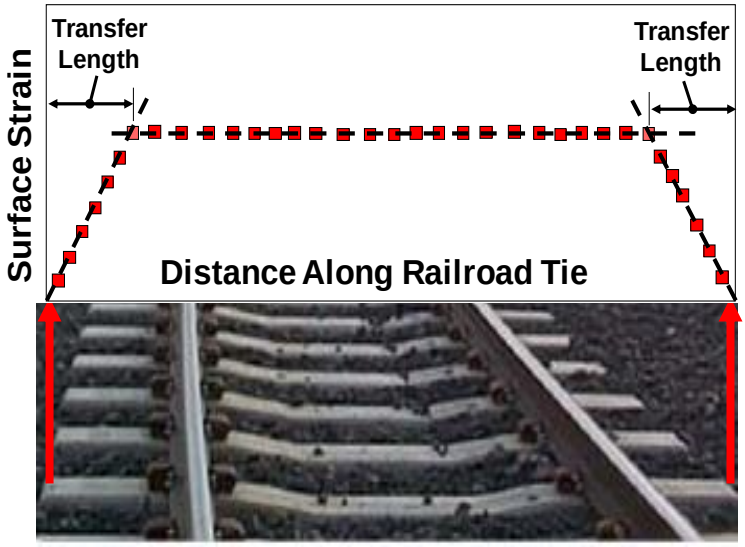

Figure 17. Definition of Transfer Length

Figure 18 below shows the chevron style reinforcements considered in this study. The indent patterns on the surface of these wires are cold rolled with three independent wheels to press indents into the surface. Overtime during the production of this wire, the indent dies on the wheel wear out. Being able to identify when these dies have worn passed their tolerances is critical for producing quality reinforcement steel.

Figure 18. Pre-stressing Steel Reinforcement Wires

The custom developed non-contact 3D profilometry system was developed to collect surface data of the reinforcement wire. The system was configured to take 1 million surface measurements per one centimeter length of reinforcement wire. The information is stored initially in a cylindrical coordinate format (r, θ, h). The radius, r, is the radius of the reinforcement surface from the center axis. This measurement is determined by the non-contact sensor used in the 3D profilometry system. The angular position and height – θ and h respectively – are determined by the position of the motion control stages used by the profilometry system. These measurement values are inferred by the position of the motion control stages.

Figure 19 shows the microscope images of all 12 reinforcement wires on the left hand side and the 3D models generated from the collected surface data on the right for a one centimeter length. For each reinforcement wire, the indent patterns are clearly visible within the 3D models. The system effectively acquires the information needed to determine the dimensions of the indent geometries on the surface of the wire. These 3D models were rendered in a .stl triangular facet format using the open source software MeshLab. The majority of the reinforcement types below are chevron style with small periodic indentations on the surface. Other reinforcement types include spiral reinforcement wires, and dot indent reinforcements. The reinforcement wire shown in the top left is smooth with no indentations and is used as a baseline in this analysis.

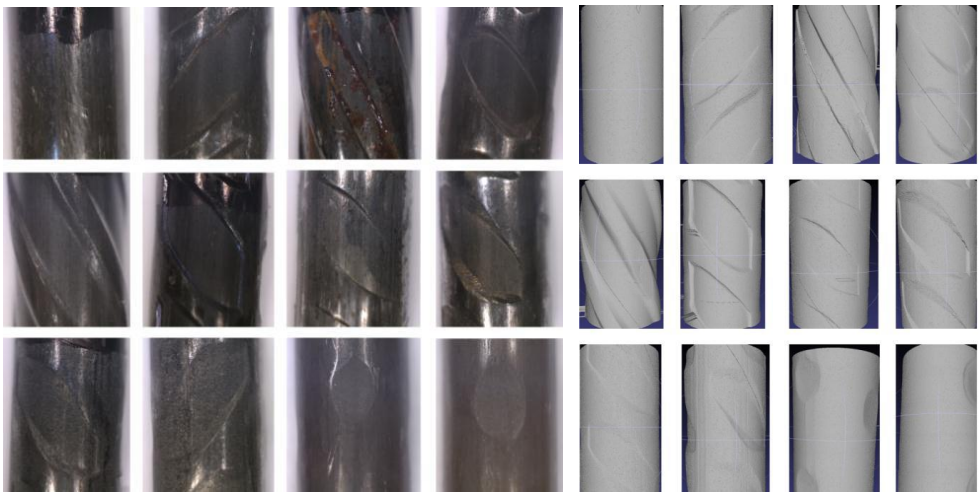

Figure 19. Collected Data of 12 Reinforcement Wires

The previous information provides a need for collected reinforcement wire surface profiles and measurements as well as a means to acquire these measurements. In order to autonomously acquire geometrical feature information from this collected data. Algorithms need to be defined to detect and extract the geometrical feature information.

2.3 Algorithm Design

As the majority of the reinforcement wires used in this study are chevron style. The algorithms developed will focus on identifying and extracting geometrical feature information from these reinforcement wire types. For these indent patterns there are several geometrical features that need to be identified and measured. Table 2 below shows the geometrical features that are the objective metrics from the designed algorithms. Some of the metrics shown can be calculated easily with little algorithmic complexity, these metrics are useful as they be computed quickly for real-time applications. Other metrics provide much more detailed information on the dimensioning and tolerancing of the reinforcement wire in consideration.

Table 2. Geometrical Features List for Algorithmic Extraction

	Name	Abbreviation	Definition
1	**Average Radial Value**	AvgVal	Average value collected from noncontact sensor (mm)
2	**Indent Depth**	Depth	Depth of the indented region (mm)
3	**Indent Projected Surface Area**	PSA	Projected surface area of the indent (mm^2)
4	**Indent Volumetric Void**	VV	Volumetric space of the indented region (mm^3)
5	**Indent Projected Surface Area per cm**	PSAcm	Projected surface area of the indent per cm length of reinforcement (mm^2)
6	**Indent Volumetric Void per cm**	VVcm	Volumetric space of the indented region per cm length of reinforcement (mm^3)
7	**Indent Orientation**	Ori	Orientation of the indented region (Deg./Rad.)
8	**Indent Length**	EL	Length of the ellipsoidal region from fitted ellipse of indent (mm)
9	**Indent Width**	EW	Width of the ellipsoidal region from fitted ellipse of indent (mm)
10	**Indent Axial Length**	axialdist	Indent length as measured across the axis of the reinforcement wire (mm)
11	**Indent Radial Width**	RotatDist	Indent width as measured across the axis of the reinforcement wire (mm)
12	**Indent Surface Area**	TFSA	Indent surface area as measured by the sum of the triangular facets (mm^2)
13	**First Laplacian**	Lap1	Average value of the first order laplacian filter (mm)
14	**Second Laplacian**	Lap2	Average value of the second order laplacian filter (mm)
15	**Indent Edge Projected Surface Area**	EdgePSA	Indent edge projected surface area (mm^2)
16	**Indent Edge Triangular Facet Surface Area**	EdgeTFSA	Indent edge surface area as measured by the sum of the triangular facets (mm^2)
17	**Indent Edge Average Slope**	EdgePSAtfsa	Indent edge slope determined by dividing EdgePSA by EdgeTFSA (unitless)
18	**Indent Edge Slope**	EdgeSlope	Slope of the indented edge (Deg./Rad.)

In order to achieve successful geometrical feature recognition with this wide assortment of metrics, a search algorithm that can be applied ubiquitously is preferred. This allows for the same algorithm to be applied to all metrics which reduces design complexity. The algorithm chosen for this was an iterative non-linear search algorithm. Non-linear search algorithms provide the greatest flexibility for application methodology; however, the iterative nature raises concerns for computational time in real-time applications.

2.4 Measurement Methodology

For these reinforcement wires, seven new measurement methods are presented for the following measurements:

1. Indent Depth
2. Indent Length
3. Indent Width
4. Indent Volume
5. Indent Surface Area
6. Indent Edge Slope
7. Indent Edge Surface Area

2.5 Datum Axis

The first step in being able to measure these indents is determining a reference frame or datum. The ideal datum for these reinforcement wires is determining the center axis of the wire. Figure 20 shows a simple sketch of the reinforcement wires surface. Through the use of a CMM or other surface profiling system, data points can be collected all along the cylindrical surface of the wire. For all the following figures gray and green points represent the data points that were acquired from the surface profiling process.

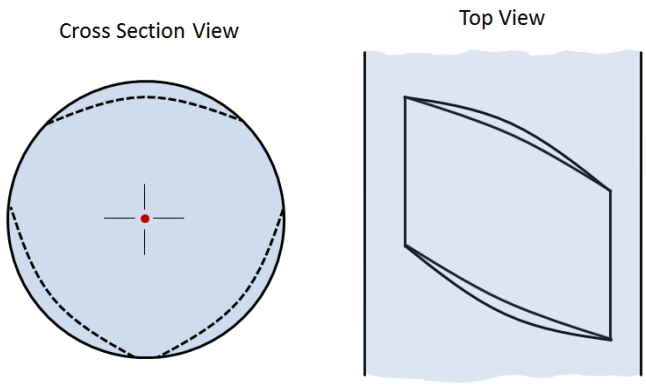

Figure 20: Pre-stressing Reinforcement Wire Typical Profile

The datum axis is obtained with a minimal cylindrical zone method [1,2,3]. This is done by bounding the surface profile by two concentric cylinders. The first cylinder circumscribes all data points. The second cylinder inscribes all data points. The center axis of these two cylinders can be used as the datum of the acquired surface profile and this datum adheres to the guidelines within ASME Y14.5-2009 [1].

Figure 21 below shows a simple 2D example of how the datum is determined. The blue shaded region represents all the data points bounded between two concentric circles.

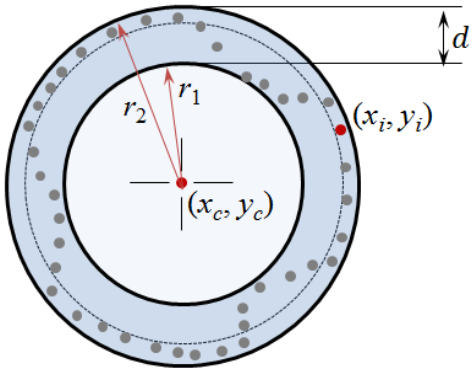

Figure 21. Determining Datum Axis

$$Minimize\ d = r_2 - r_1$$
$$Subject\ to\ \forall_{i=0}^{N}(x_i - x_c)^2 + (y_i - y_c)^2 \geq r_1^2$$
$$\forall_{i=0}^{N}\,(x_i - x_c)^2 + (y_i - y_c)^2 \leq r_2^2$$

Above is the required optimization. With $(x_i, y_i): i \in [0, N]$ and (x_c, y_c) represents the center datum, which for the 2D case is a point and not a line. r_1 is the radius of the circle less than all data points and $r_2$is the radius of the circle greater than all data points and the objective is their minimal difference. Once the reference datum is determined it can be used in the determination of several geometrical measures of interests. The datum provides the reference for all other measurements. The datum being calculated in this manner makes all measurements relative to the part and is fixture independent. This solves many conventional locating problems with precision measurement. This also allows for comparable measurements from different

mechanical systems, such as the Kansas State University's non-contact scanning system or a CMM in another lab.

2.5.1 Preprocessing of Point Cloud Data

The data is analyzed in incremental packets ranging consisting of one million point cloud data points. The packets can be analyzed as groups or individually. Doing this allows for simpler algorithms to be used in real-time. There are two pre-processing algorithms that need to be implemented prior to searching for the indent regions. The first is error removal and the second is alignment of a data reference axis. The data is collected using a non-contact laser displacement sensor. Highly polished surface can create sparse erratic errors with extremely off values. These erratic errors can be recognized as high frequency maximas and minimas. The error removal algorithm can be implemented in two different manners. A Fourier transform of the point cloud data is a simple initial solution for this error removal. This method provides the most sophisticate control of the errors to remove and provides the most robust solution possible.

However, a simpler method of error removal was found. By analyzing the local variation of one point from its nearest neighbor was found to be quick and only require one conditional on each data point which makes removing errors easy. The sparse erratic erroneous point cloud values have a high enough frequency variation from the average variation of the surface profile. A threshold, τ, is determined experimentally. When analyzing point p_i and p_{i+1} if the distance between the two exceeds τ then the point $p_{i+1}$is removed. This can be expressed as follows:

$$\forall_{i=1}^{I} |\overline{p_i p_{i+1}}| > \tau \rightarrow \ Remove\ P_{i+1}$$
$$\forall_{i=1}^{I} |\overline{p_i p_{i+1}}| \leq \tau \rightarrow \ i := i + 1$$

This simple algorithm effectively removes all erroneous data points for the data used in the current study once an ideal τ was determined. This algorithm only requires a set one other data point for to determine the current data point as erroneous. Because of this, this algorithm could be easily paralleled programmed on the cpu or gpu, allowing for a very short runtime.

The second preprocessing algorithm is to determine a reference axis for the reinforcement wire. This reference axis is to determine where the theoretical center of the wire exists. This is necessary for many geometrical feature calculations as a reference point. A common methodology for finding the center axis of a point cloud is a simple linear regression. However, given the guidelines of ANSI Y14.5 this does not meet geometrical dimensioning and tolerancing standards. Linear regressions are ideal when the variations between points are caused by probabilistic error, however, when the variation is deterministic as in surface profiling, a linear regression is a poor method of determining the reference axis or other geometrical features. However, a linear regression does provide a reasonable starting point for a Nelder-Mead algorithm.

The solution to this is to find the closest fitting concentric external and internal theoretical cylinders that contain all of the reinforcement wire data points. This problem formulation is as follows. Consider two concentric infinitely long cylinders. The first cylinder circumscribes all data points; the second cylinder inscribes all data points. Minimize the radial distance between these two cylinders. This minimization is a non-linear search and as such the Nelder-Mead algorithm is suitable for solving. Let Z_1represent the radius of the circumscribing cylinder. Let Z_2represent the radius of the inscribing cylinder.

$$\min\{Z_1 - Z_2\}$$
$$s.t. Z_1 \geq d_i \forall_{i=1}^{I}$$
$$Z_2 \leq d_i \forall_{i=1}^{I}$$
$$d_i = \frac{|(p_i - p_\alpha) \times (p_i - p_\beta)|}{|(p_\beta - p_\alpha)|}$$

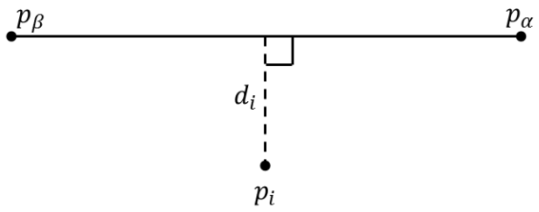

Figure 22. Definition of Variables for Reference Axis Determination

Where d_i is the radial distance of the data point from the theoretical line determined by the two points p_α and p_β. The objective function is subject to the radius Z_1being greater than radius of all data points from the center axis and the radius Z_2 being less than radius of all data points from the center axis. In order to minimize the objective function the concentric cylinders can be translated and rotated in an iterative manner to obtain the local minimum.

In order to solve this problem the position of the points $p_\alpha$and p_β are iteratively changed so by the Nelder-Mead method until convergence is reached. If we assume the two points are fixed to z-planes that are a constant distance apart then we only have four parameters that can be varied by the Nelder-Mead $(p_{\alpha x}, p_{\alpha y}, P_{\beta x}, P_{\beta y})$. This presents a four dimensional Nelder-Mead problem. The alternative method to define this model is with a single data points x and y values and then two angular values to represent pitch and yaw of the line.

Once this Nelder-Mead algorithm completes the result is the position of the center axis that adheres to the ANSI Y14.5 requirements for dimensioning and tolerancing. This reference axis will be used in determining the radial values of all data points from the center of the wire. This will provide a means of determining depth of the indented regions on the wire surface.

2.5.2 Removal of Non-Indent Data Points

In order to identify the indented regions of interest, the non-indented regions of data points need to be removed. This is done by thresholding. Any data point that exceeds a specified radial value from the reference axis is removed. This simple thresholding technique proved to be effective at leaving only data points that represent a minimal amount of indentation into the reinforcement wire surface. This thresholding condition from the predetermined threshold,T, is shown below.

$$\forall_{i=1}^{I} d_i > \mathrm{T} \rightarrow \ Remove\ P_i$$

This thresholding technique leaves clusters of data points. Each cluster of data points represents its own unique indent region. The next step for the algorithms is to identify the cluster regions that represent indents so that geometrical features may be measured.

2.5.3 Indent Identification via Clustering Algorithm

In order to identify the data point groups that represent indent regions, a marching rectangular prism clustering algorithm was design. This marching cube algorithm is as follows. Start with a seed data point, p_1, and assign it to a cluster, C_1. $C_1$is now a rectangular prism of an arbitrary size around point p_1. The size of the prism is predetermined by the rule that all faces of the prism must be distance l from all points within the cluster. Since there is only one point in the initialization, the cluster region is represented by a cube. Now for all subsequent points, if the point is within a cluster bound, add it to the given cluster and expand the walls of the cluster to be distance l from all points. If the point is not within a cluster region assign it to a new cluster. Once all data points have been checked, the algorithm is complete. The algorithm is intended to determine the clusters as simply as possible in order to minimize run time, the draw backs of this design is that the clustering algorithm is sensitive to l and it is must be determined carefully in order for the algorithm to succeed. In addition, it is possible for this algorithm to fail if two point cloud groups have relatively close faces that are oblique to the rectangular prism defining the cluster. In practice the algorithm ran successfully and is determined to be sufficient for the given application.

There exist many clustering algorithms that are far superior to this in terms of accuracy. As this algorithm was able to identify the indented regions, a more sophisticated clustering algorithm is not needed. The clustering algorithms simplicity allows for a fast run time and easy implementation in C programming.

Once the indent regions have been identified, the majority of the geometrical features described in Table 2 are ready to be measured. 14 of the 18 geometrical features in consideration can be measured without additional clustering and thresholding algorithms. These 14 geometrical features also provide enough information to make a strong prediction of the performance of the reinforcement wire.

2.5.4 Geometrical Feature Measurements

Some of the geometrical features in consideration can be measured without determining the indent regions. Other measurements require additional applications of the Nelder Mead algorithm, thresholding, and clustering in order to be determined.

2.6 Indent Depth

Now that the datum axis is determined the indent depth can be determined as well. The indent depth is the predominate measurement for reinforcement wire quality control. Conventional methods require using a depth micrometer traversed across the axis of the wire. Determining the maximum depth of the indent can be challenging to measure by hand have human bias.

In order to select the region of the wire that represents an indent, a predetermined threshold should be used. Any data point radii below the threshold is considered a part of the indent. Figure 23 illustrates the measurement. The indent depth is determined as the circumscribing circles radius minus the minimum radius of the indent.

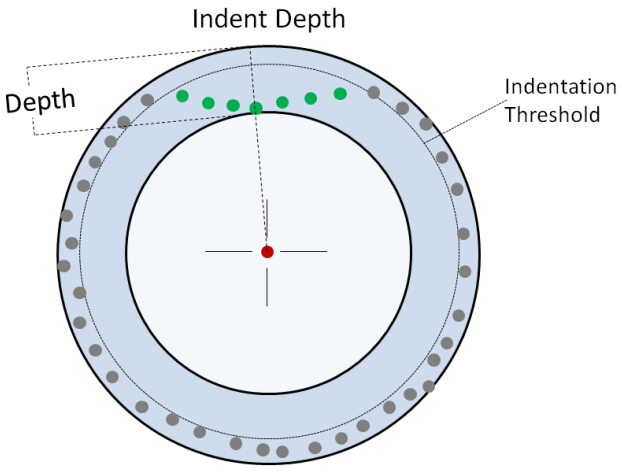

Figure 23. Indent Depth

Comparable metric to the average radial value yet only considers the indented regions. This metric considers each cluster of data points representing indent regions independently. The

equation below represents the measurement of one indent region consisting of a total of I_c data points.

$$\frac{1}{I_c}\sum_{i=1}^{I_c} Z_1 - d_i$$

2.7 Average Radial Value

The radial value is the simplest of all geometrical feature measurements. All data points have a radial distance d_i from the reference axis.

$$\frac{1}{I}\sum_{i=1}^{I} d_i$$

This metric has strong applications for providing real time quality control. Through testing it was found that variations in the Average Radial Value have a good correlation with the transfer length of the reinforcement wire in concrete. As all reinforcement wires start with the same nominal diameter the indents can be considered a reduction in the average radius of the wire. Larger indents correspond to a lower overall Average Radial Value. By monitoring this metric during the production of reinforcement wire, it is possible to detect meaningful changes in the wire geometry that may negatively influence the wires behavior. This simplicity of this metric makes it highly useful for real time industrial metrology.

2.8 Projected Surface Area

The projected surface area of the indented region can be calculated easily by knowing the resolution of the data acquired from the CMM and the number of the points that exist within the indent region. If the data points are taken at a uniform resolution, each data point represents a portion of the reinforcement wires surface which is constant. Notice that in Figure 24 the surface area shown is not the actual surface area of the indent only a close approximation. The indent surface area provides information into how large the cross section is of the concrete tooth that will fill the indented void once the wire is cast.

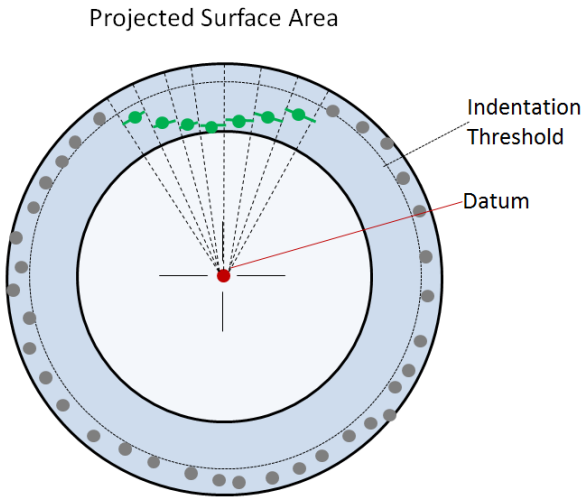

Figure 24. Indent Projected Surface Area

Figure 25 shows a top down view of the data points. Each green data point represents a point on the surface of the wire which radius from the center falls below the predetermined threshold. These data points are representative the surface area of the indent.

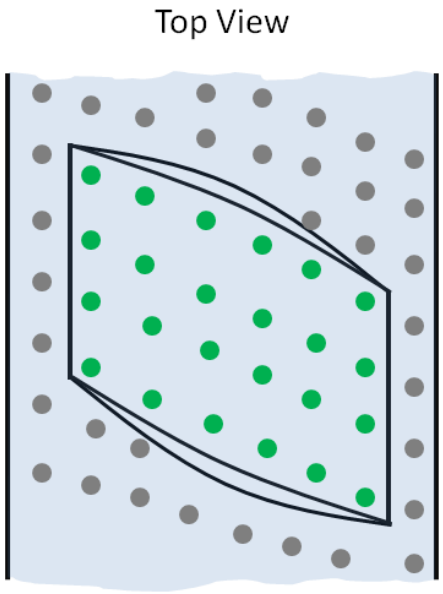

Figure 25. Indent Surface Area Top Down

The projected Surface Area of the indents is measured with the following metric. A is a constant that is the amount of surface area that one data point represents on the surface of the reinforcement wire. As the data points are spaced a known periodic distance apart, A is easily determined.

$$\sum_{i=1}^{I_c} Ad_i$$

The remaining geometrical feature calculations combine the principles discussed thus far to provide additional information on the indent edge wall which has been found to be an important factor in the indent geometries overall performance. For the application of pre-stressing steel reinforcement wire, the indent edge wall surface provides the primary resistive force against shear failure.

The edge wall can be isolated from the indent region by identifying areas where a large slope exists and running a clustering algorithm. One method of doing this is to use the Laplacian transform mentioned above to identify areas of large slope and threshold for a predetermined slope value.

Another method is to smooth the surface of the indent region by performing a moving average across the surface, and then identify neighboring pairs of points that have a slope between them above a predetermined threshold. The moving average is needed to minimize the influence of microscopic surface variations in-between pairs of data points.

Neither of these solutions has been determined to be robust enough to handle all chevron style reinforcement wire types. Rather, the threshold parameters within these methods must be modified for each reinforcement wire type. Additional work is needed to improve these algorithms implementations. Once the indent edge wall has been determined the projected surface area of the indent edge uses the same algorithm used in the projected surface area of the indented region.

2.9 Triangular Facet Surface Area

A more realistic calculation of the surface area is the Poly-Surface Area. This method of calculating surface area takes into the account the surface depth into the surface area measurement. Figure 26 illustrates the calculation. By using a piece-wise linear (2D) or a piece wise triangular mesh (3D), the surface can be segmented into many polygonal regions. By summing each of the polygons surface area the overall indent surface area is determined.

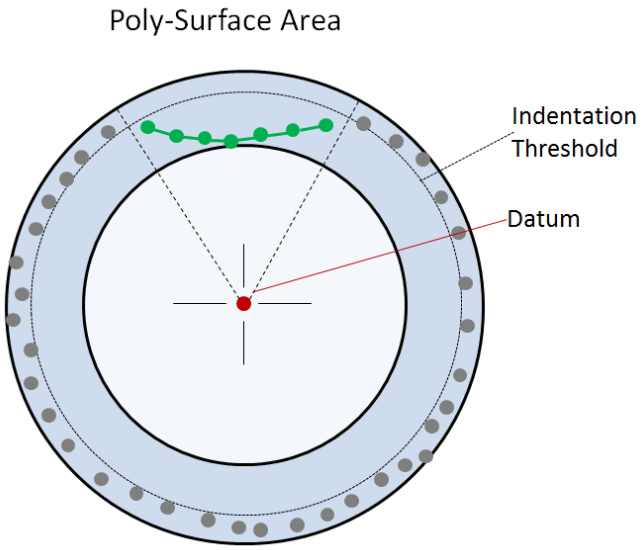

Figure 26. Indent Poly-Surface Area

Calculation of both the indent poly surface area and the indent projected surface area is not needed as the both provide very similar information about the indent. Where possible the poly-surface area method should be used as it is a more complete surface area measurement. However, statistical analysis has shown that the projected surface area measurement performs reasonably well, and from a process implementation perspective is easier to use [10].

The Indent Surface Area is a more accurate measurement of surface area than the projected surface area measurement. The projected surface area measurements do not consider the varying radius of the wire profile when determining the measurement. The Indent Surface Area measurement utilizes takes every neighboring group of three indents and sums the surface the

surface area between those three points. There is little difference between the performance of this metric and the performance of the projected surface area metric.

2.10 Volumetric Void

A new measurement tested within this research is the volumetric void [11]. The volumetric void of the indented region has been shown through statistical correlation to have a strong relationship with the transfer length and pull out force of a reinforcement wire. The volumetric void is represented in mm^3 and is the volume of the shape formed into the surface, which can also be interpreted as the amount of volume of concrete needed to fill the indentation of the surface. The volumetric void can be calculated by taking the projected surface area of the data points and then multiplying the projected surface area with the depth of each data point and summing across all data points. Figure 27 illustrates how the volumetric void is determined.

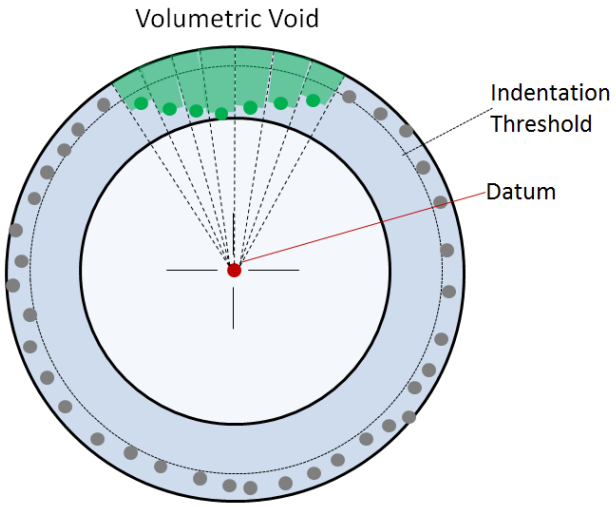

Figure 27. Indent Volumetric Void

The PSA metric and the Depth metric can be combined to create a single metric that represents the total volume of space the indented region takes on the surface.

$$A \sum_{i=1}^{I_c} Z_1 - d_i$$

2.11 Indent Projected Surface Area per CM and Indent Volumetric Void per CM

These metrics are the same as the PSA and the VV metrics, however also includes information on how far apart the indents are spaced or the indent frequency along the surface of the reinforcement wire. By summing up many indents PSA and VV metrics for an arbitrary length of reinforcement and then dividing by the length in centimeters the result is the PSAcm and VVcm metrics respectively. While the difference in metrics is subtle, the additional information about the frequency of indents per length of wire creates a statistically stronger correlation with the transfer length metric in the wires performance.

2.12 Indent Length and Indent Width

The length of the indented region and width can be difficult to determine as each wire manufacturer has its own unique geometry. Some wire types have oval shaped indent patterns; others have a more rectangular shape. What is needed is a generic means to measure the indent length and width for any given reinforcement type. A fitted ellipse is the best approach for this measurement. An ellipse can be fitted with a minimal zone technique. The ellipses location and size is such that the ellipse is its minimum circumference that circumscribes all data points. The major axis of the ellipse is the length of the indent; the minor axis is the width of the indented region.

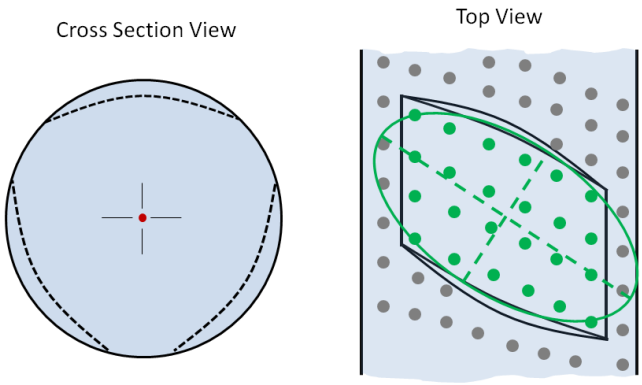

Figure 28. Indent Orientation

The Indent Length and Indent Width are the major and minor axi of the fitted ellipse, respectively. The indent axial length, and indent radial length represent the length of the ellipse down the reference axis and radially across the wire surface respectively. These first two metrics

and second two metrics are redundant. Until this study was performed there was no certainty of one of these metrics being superior to the other. The best metric of these four is the indent radial length. However, all of the reinforcement wires have strong correlations with the transfer length metric.

2.13 Indent Orientation

The following five geometrical features all require an additional application of the Nelder-Mead search algorithm in order to determine their values. For all clusters of data points representing indents C_j a minimal zone ellipse is fitted to the data. The fitted ellipse is designed to circumscribe all data points for the cluster while minimizing the ellipses surface area. This is done by rotating and translating the fitted ellipse and can be done with as few as three parameters, yet sometimes more. The three parameters consist of translation in x and y and also a rotation component θ representing the angle of the ellipse. The orientation of this ellipse (θ) is the metric used to determine the indents orientation. The following four geometrical features all utilize the results of this Nelder Mead solution to determine their measurements.

2.14 Indent Edge Wall Angle

The conventional measurement of the indent edge wall is to measure the indent with a depth micrometer at the center of the indent at its lowest depth to the top wire outside the indent region. This measurement however, is not representative across the entire indent. Most of the commercial reinforcement wires have a varying indent edge wall angle. The center of the indent is often the shallowest. While the edges have a steeper slope, there are several different methods of measuring the indent slope that can quantify the indent slope across the entire length. A simple method that can be used with a variety of different measurement hardware is to perform angular measurements at fixed distances down the length of the indent. Multiple measurements should be taken along the indent edge and the indent basin. Figure 29 shows how the angle of the indent should be sampled with multiple measurements on the edge wall and basin. An easy way to determine the two intersecting lines shown in the figure is to perform a least squares fit for the two lines. However, keeping with the conventions of ASME Y14.5-2009 a minimal planar zone is preferred.

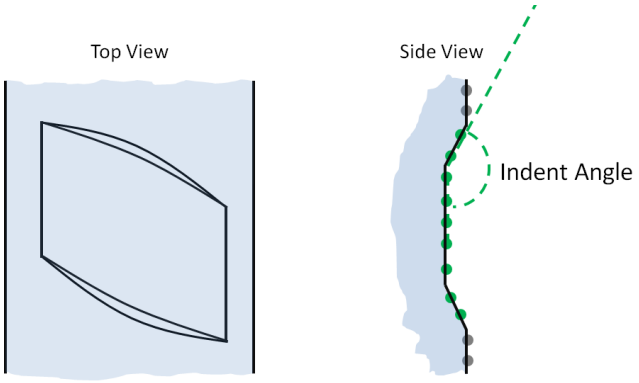

Figure 29. Indent Edge Wall Angle

Figure 30 illustrates the multiple sampling that is needed in order to acquire a measure of the indent edge slope. These multiple sample measurements should be averaged together to determine an average indent depth. The number of measurements taken should be the highest number that is practical. Within the given research the current surface profiling system can detect about 100 lines per wire indent.

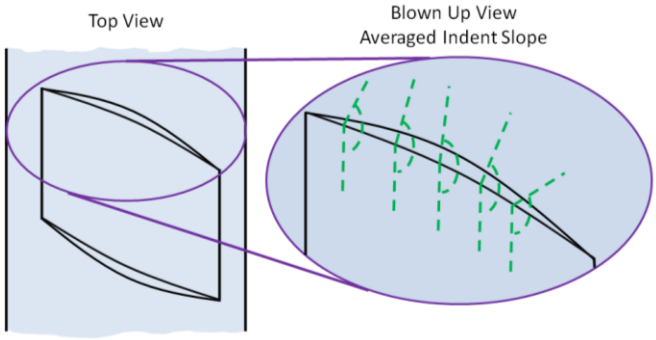

Figure 30. Sampling of Indent Edge Wall Slope

2.15 Indent Edge Average Slope and Indent Edge Slope

This two metrics have low statistical significance with the transfer length; however, they are hypothesized to be critical influential parameters of the concrete railroad ties propensity to crack. The average edge slope is measured as the ratio of the Indent Edge Projected Surface Area divided by the Indent Edge Triangular Facet Surface Area. The Indent Edge Slope is measured by calculating the slope at the axial center of the indent edge.

2.16 Indent Edge Surface Area

The surface area of the indent edge has been shown through previous testing to have a strong statistical relationship to the pullout force of the reinforcement wire. The indent edge surface area can be calculated in the same methods as that of the indent projected surface area or that of the indent poly surface area. Figure 31 shows the indent edge surface area measurement. By summing the representative surface area of each data point using a projection based method or the polygonal method the surface area may be determined.

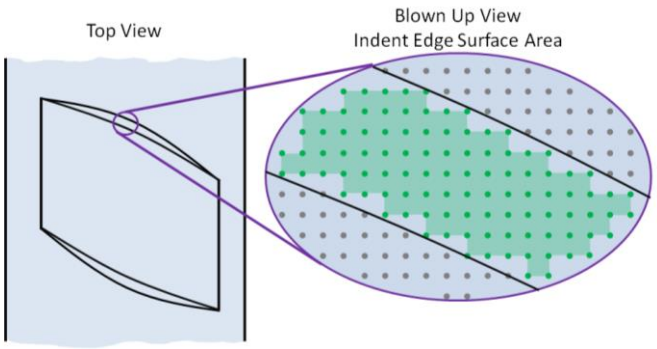

Figure 31. Indent Edge Surface Area

2.17 First Laplacian and Second Laplacian

A laplacian transform was used to calculate the first and second order derivatives of the surface profile. And then the average values of these profiles were determined using the same method as the Average Value metric. There are many different methods available for utilizing a laplacian transform to generate a measurement of overall surface roughness.

2.18 Current Implementations

Currently these methods for measuring indents in reinforcement wires have been implemented. Figure 32 shows the typical input data for these analyses. The data consists of 1 million data points across 1 cm length of reinforcement wire. The data points are uniformly spaced. The coloring of the point cloud is based off radial values of each data point. Data points closest to the datum axis are shown in dark blue and data points farthest away from the datum axis are shown in red and magenta.

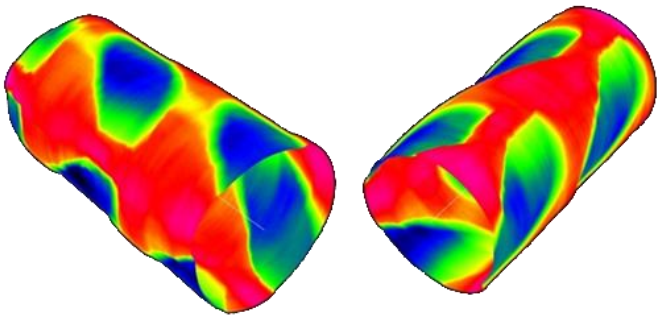

Figure 32. 3D Heat-Map of Indent Profile

By using the thresholding technique discussed in the earlier section, the resultant selection of indent regions is obtained as shown in Figure 33. Each indented region consists of several hundred thousand data points. From these selected regions all the measurements can be determined.

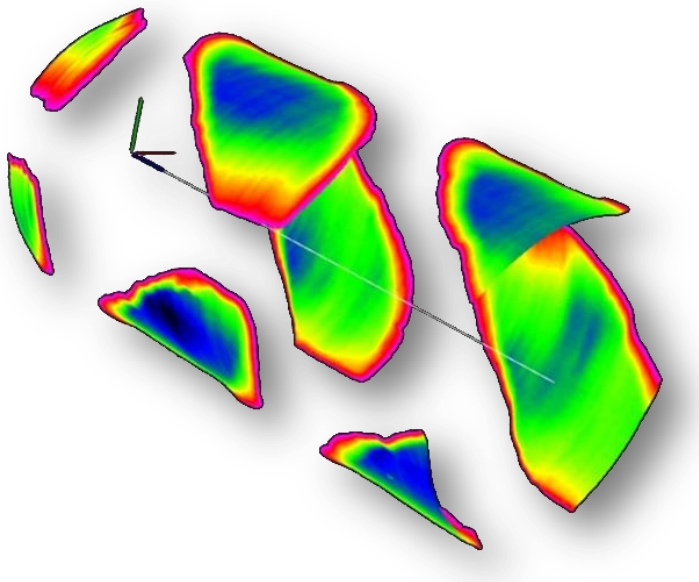

Figure 33. Isolated Indent Regions

2.19 Conclusions

These new measurement methods have been shown through statistical analysis to have stronge correlations to pull out force and transfer length than conventional measurements done by ASTM A881 and by combining these measurements into a multi-variant model and highly accurate predictions of the transfer length can be made. These multi-variant models are capable of providing much more information than any single geometrical feature can individually. By determining a method of measuring indent profiles that is more completely defining of the indent geometry and by doing so in a manner that agrees with ASME Y14.5-2009, improved reinforcement wire quality and improved concrete cross tie life span can be obtained.

The current developed 3D non-contact profilometry system has the potential to provide quality control during the production of reinforcement steel wires by scanning samples of the wire periodically. While the developed system is designed for pre-stressing steel reinforcement wires, the concepts and designs in this research and development can be reapplied to automated measurement and tolerancing in other surface metrology applications. Additionally with further research and development, it may be possible to apply this technology as a real-time solution providing quality control for 100% inspection during manufacture.

Chapter 3 — Non-Linear Search in GD&T

This chapter documents the research performed on non-linear search algorithms in solving the minimal zone calculations. Minimal zone calculations are necessary for the fitting of perfect geometrical forms to true surface profiles. The data sets considered in this study are relatively large to previous research applications of minimal zone. Within this study data sets as large as ten million data points have been used in the processing of pre-stressing reinforcement wire samples. In order to minimize software runtimes and develop measurement solutions that are practical for real world applications this research was necessary.

3.1 Introduction

This research addresses a class of non-linear search problems that are difficult to solve with traditional non-linear search methods. A specific class of applied non-linear problems has been found that have extensively long computation run times and the run times of the problems is currently prohibiting feasible applications of the non-linear search [8].

While researching applications of non-linear search for minimal zone algorithms in Geometric Dimensioning and Tolerancing (GD&T) a computational bottleneck was found with the non-linear search algorithm. As these algorithms are for real world applications it is critical that the run time of the algorithm falls within a reasonable bound for the given application. The GD&T research utilizes non-linear search to locate geometrical features. This is done for a variety of geometrical shapes such as circles, ellipses, cylinders, and planes. The determination of the position and orientation of these geometrical features provides datums that can be used in the measurement and analysis of the part [37].

3.2 Problem Statement

For this analysis of non-linear search modifications, the functional objective being solved is a minimal circular zone. The minimal circular zone is a commonly used nonlinear search for GD&T application, which makes it a perfect candidate for researching different search algorithms to determine which will solve the fastest for this problem class [24]. The minimal circular zone algorithm is used to determine the datum center of a circular data profile and the

size difference between the circumscribing and inscribing cirlces. Where $r_1$and $r_2$represent two concentric circles, the minimization determines the center point of the circles,(x_c, y_c). The center point is position such that the difference in radius of the two circles is minimized while the first circle $r_1$inscribes all data points $i \in [0, N]$ and the second circle $r_2$circumscribes all data points $i \in [0, N]$ [37].

$$\begin{aligned} &\text{minimize } d = r_2 - r_1 \\ s.t.\ &\forall_{\{i=0\}}^{N}(x_i - x_c)^2 + (y_i - y_c)^2 \geq r_1^2 \\ &\forall_{\{i=0\}}^{N}(x_i - x_c)^2 + (y_i - y_c)^2 \leq r_2^2 \end{aligned} \tag{1}$$

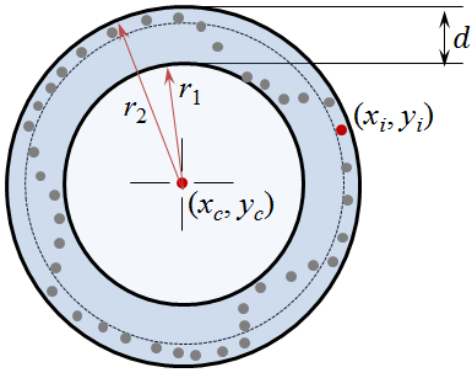

Figure 34. Circular Minimal Zone Problem

This non-linear search algorithm is often used to determine the reference of a circular surface profile. When N is small, the non-linear search can be solved relatively quickly. However, with improvements in GD&T systems large numbers of data points can be achieved for each surface profile, within the current research context problems are being solved where N ranges from 1 to 10 million data points. During each iteration it requires a significant amount of time to calculate the objective function. This brings forth the need for a non-linear search that maximizes the utilization of the currently existing calculation objective functions to best determine the gradient of the solution space and minimize the number of objective function computations required [8].

For the GD&T application within this study, the surface profiles considered are 3D scans from reinforcement steel rods. The 3D scans are high density and have 1 million data points within 1

cm length of rod. Figure 35 shows a sample of the 3D profiles used within this study, this is for wire WF. The model in the figure is 1 cm length of reinforcement steel rod scanned from a real rod used within industry. The coloring of the rod is the result of the circular minimal zone calculations. The rod is colored based off the radial distance of the surface from the center of the circular minimal zone calculation. Ten surface profiles like this were used to provide the raw data for the non-linear search [1, 2, 4, 6, 8].

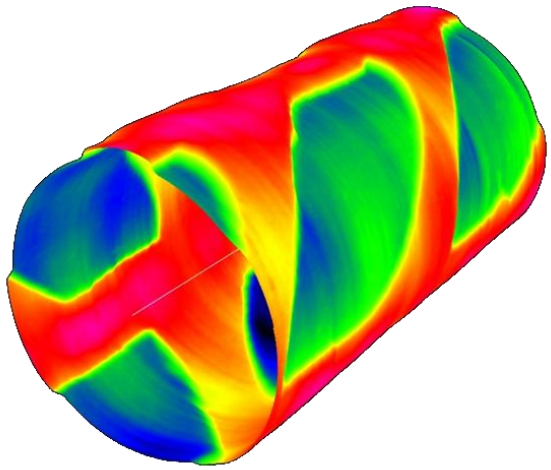

Figure 35. Actual Geometrical Body within Study

3.3 Assumptions

In order to control the scope of the problem type being solved within this research a few assumptions are made.

- The objective function computation time is extensively long
- The amount of time performing non-objective function computations is insignificant
- The objective is non-differentiable
- Any gradient information obtained must be made between at least two calculated objective values

3.4 Problem Initialization

For all non-linear search algorithms, any improvement that can be made to the starting point upon initialization can greatly decrease the run time of the problem. The non-linear search can be considered a two part process, the first part of the non-linear search identifies where the region of interest is that contains the local optimum, the second part converges upon that given local optimum. With a good enough approximation it is possible to start close to the local optimum.

One of the fastest ways to approximate the center of a circle is to determine its bounding box. By calculating the bounding box, the center of the circle can be guaranteed to lie somewhere within the bounding box. This can be even added as constraints to the original problem definition. The bounding box constraints will result in the following modified problem:

$$\begin{aligned} &\text{minimize } d = r_2 - r_1 \\ s.t. \forall_{\{i=0\}}^{N} (x_i - x_c)^2 + (y_i - y_c)^2 &\geq r_1^2 \\ \forall_{\{i=0\}}^{N} (x_i - x_c)^2 + (y_i - y_c)^2 &\leq r_2^2 \\ x_{min} &\leq x_c \\ x_{max} &\geq x_c \\ y_{min} &\leq x_c \\ y_{max} &\geq x_c \end{aligned} \tag{2}$$

Adding bounding box constraints to the non-linear search may not be necessary, however, a rough estimate can be made that the circle center lies at the point.

$$(x_c, y_c) = \left((x_{max} - x_{min}) + x_{min}, (y_{max} - y_{min}) + y_{min}\right) \tag{3}$$

For the minimal zone class of problems, there exists a least squares solution that can provide an improved starting location. The least squares fit of a circle, depending upon its implementation can still be time consuming. Possible methods of improving the least squares approximation would be to use only a small sample of the data points as it is not necessary to fit the least

squares circle to all 10 million data points to create an approximate start for the minimal zone. Rather a small sample size of 10-1000 data points can be used to give a quick least squares approximation for (x_c, y_c) [21, 41].

3.5 The solution space

Figure 36 shows a computer rendered visualization of the solution space of the minimum circular zone problem type. Visualizing the solution space provides insight into the complexity of the solution space. The image is of a 3D surface, the color of the surface and the vertical height of the surface represent the objective function value at different values of x_c and y_c for the circular minimal zone.

The solution space was created by calculating all solution values for x_c and y_c in a 1000 by 1000 value grid. Calculation of the solution space took approximately 16 hours. This would be representative of how long it would take to solve the minimal zone problem using an exhaustive search. This necessitates using a iterative search based non-linear search algorithm. Without an effective iterative non-linear search algorithm calculating the minimal zone would be impractical for real world applications.

The solutions space shown is a faceted convex region. This problem type has a single global optimum, which makes the circular minimal zone easier to solve as compared to other minimal zone problems such as straightness are subject to multiple local optima.

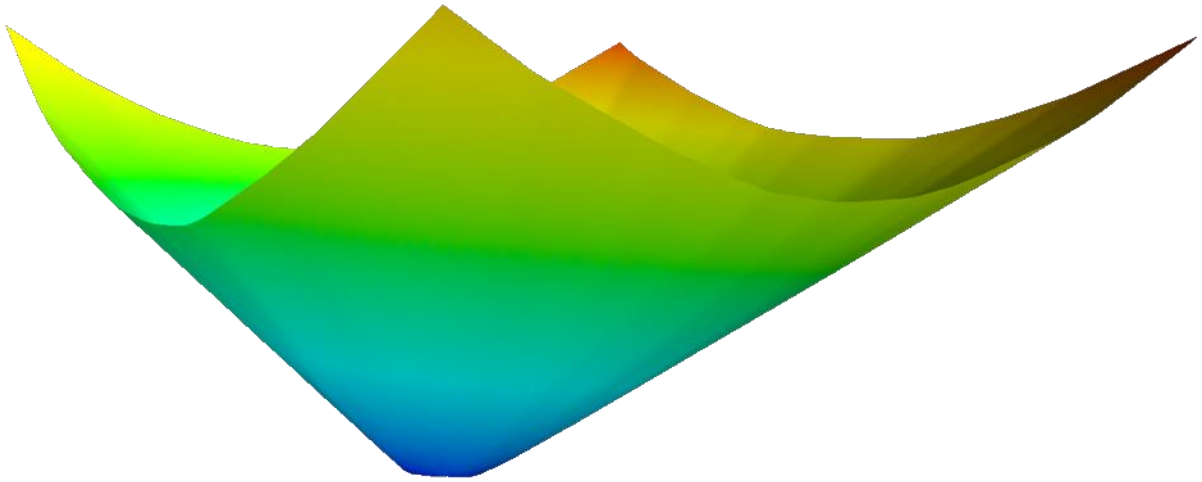

Figure 36. Solution Space for Circular Zone Problem

Zooming in on the solution space further in Figure 37 the faceted nature of the solution space can be seen in greater detail. In this image the solution space is viewed from an isometric position. From this image we can see that at the optimum location, the gradient between solutions has diminishes to zero. However, the region that has gradients near zero is elongated. The intersection of two facets with an intersection line gradient near zero can be difficult for certain types of non-linear search algorithms. Particularly, the traditional Gradient Descent algorithm would have a slow convergence at the location of the intersection of the two facets.

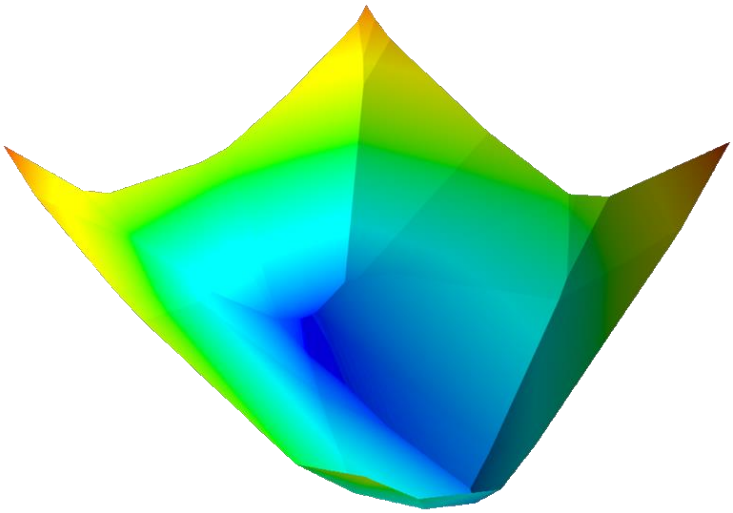

Figure 37. Circular Zone Problem Solution Space Facets

Zooming in even further into the solution space in Figure 38 the edges of the facets are easy to see. The local optimum is seen as dark blue in the middle right of the image.

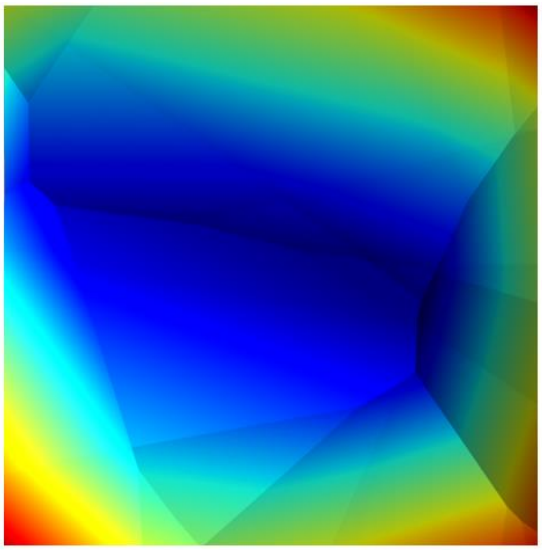

Figure 38. Circular Zone Local Optimum

3.6 Partial Objective Function Calculations

The primary reason for the large objective function computation time is the number of data points considered within the problem set. As GD&T data collection systems improve, the resolution and quantity of data points continues to increase. With process automation it is easy for high density data sets to be obtained with minimal effort. This creates a big data type problem where the amount of data available is in great excess of what is needed for determining the circular minimal zone solution.

The processing of 1 million to 10 million data points on a circular zone is not completely necessary. The GD&T data collection process provides 1 million to 10 million data points that need to be analyzed, however, the number of data points needed in the fitting of the circumscribed and inscribed concentric circles is actually quite small. It is possible for the circular minimal zone calculation to be solved with only the extrema radii data points, if they can be determined to be extrema with relative certainty.

For the circular minimal zone with such a large number of data points, many of the data points will be inactive or unused during the entire non-linear search. As an example, Figure 39 shows a circular minimal zone solution. All the data points shown in green are reasonably close enough the boundary layer of either the circumscribed or the inscribed circle that they have a reasonably chance of being actively used in some iterations of the non-linear search as the boundary data points. The points shown in gray however, will be un-used throughout the entire non-linearly search process. As such, for all iterations the data points are used in the calculation of the circumscribing and inscribing circles radii are completely unnecessary.

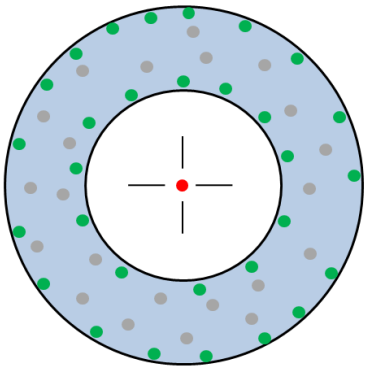

Figure 39. Extraneous Data Points

This presents an opportunity to improve algorithm run time, by reducing the objective function calculation complexity. If the gray data points can be removed prior to the non-linear search the objective function calculation time can be drastically reduced. This is dependent upon the problem initialization accuracy and the spacing of the data points.

First, we can consider the circumscribed circle as it is simpler. Theoretically, the circumscribe circle only requires the data points that define the convex hull of the data set. All other data points can be removed when considering the circumscribed circle. The best case scenario will be to determine the convex hull prior to the non-linear search. If a convex hull is too time extensive other approximations can be made. A percent radii method can be used for both the circumscribing and inscribing circles if they data is close enough aligned from a prior circular zone fit.

3.7 Non-Linear Search Algorithms

Of the many possible methods of performing non-linear search two of the most predominate algorithms are the Nelder-Mead Simplex and Powell's Method for when derivation is indeterminate. Both of these algorithms do not require objective function differentiation and they both make use of simultaneous decision variable change to achieve improved convergence. While Powell's method uses a method similar to that of a moving average to determine direction of steepest ascent, the Nelder-Mead Method utilizes the centroid of current best objectives to determine the direction of steepest ascent.

Original attempts at solving this class of problem were done with the Nelder-Mead simplex due to its simplicity and ease of implementation. The Nelder-Mead simplex has a variety of different variations that are used in practice and it dependent upon the end user how they Nelder-Mead algorithm handles decision criterion. Due to the large number of common Nelder-Mead implementations it is important to define the one used within this research.

3.8 Nelder-Mead Search Algorithm

The Nelder-Mead search algorithm was chosen as the primary non-linear search algorithm to identify search for these geometrical features. Originally developed in 1965 this algorithm is simple in practice yet effective [22, 29]. The Nelder-Mead search algorithm can be briefly defined by the following, consider a n dimensional function. The function refers to solution space, not the point cloud 3-dimensional space. A simplex in the solution space is defined by the convex region contained within $n+1$ points ($P_k^t : k \in 1..n+1, t \geq 0$). t represents the iteration of the simplex. F_k^t represents the objective function value at point P_k^t. Nelder-Mead attempts to transform the simplex by one of the following: reflect, contract, expand or shrink. The simplex is continuously transformed until it converges where the minimum points (P_{min}^t) have a difference less than δ. Where δ is an arbitrary constant.

$$P_{min}^t - P_{min}^{t+1} < \delta$$

The process for convergence to occur can be described as a three step procedure. The process is as follows:

1. **Find Minimum:** Identify p_{max}^{t} from points $P_1^t \ldots P_{n+1}^t$. This is the point that will be removed and replaced with a new point in iteration t
2. **Find Centroid:** Determine the centroid of the simplex, C^t, weighted by objective values F_k^t. The new point to be added will be placed on the line segment from P_{max}^t to C^t.
3. **Transformation:** Using one of the four previously described transformations: reflect, contract, expand, or shrink. Insert the new point P_k^{t+1} to create a new simplex.
4. **Check for Convergence:** If the algorithm has not yet converged proceed to step 1. Otherwise, the algorithm has completed.

There exist several variations of the Nelder-Mead algorithm. All off them rely on the basic principles discussed above. For this research the Nelder-Mead algorithms available in the GNU Scientific Library (GSL) were used. The focus of this research is the application of the algorithm not its detailed design or performance characteristics. The following sections will discuss how the Nelder Mead algorithm from the GSL was applied in the identification and extraction of geometrical features.

3.9 Nelder-Mead Transformations

For a $N-1$ dimensional solution space, there are N nodes of current solutions to the problem. For the circular zone problem described above we have a 2 dimensional problem, thus $N=3$ and we have three starting guesses for the optimal solution labeled $S_j(x_j, y_j): j \in N$. Where S_j is a function and has decision variables x_j and y_j for the minimal zone problem where (x_j, y_j) is the center of circumscribing and inscribing circle. The S_j are sorted from largest to smallest. As in solution S_0 is the worst and S_N is the best. For the initialization no two (x_j, y_j) can be the same.

The Nelder-Mead algorithm is comprised of four fundamental transformations that are used during the optimization. These transformations are the reflection, expansion, contraction, and $N-1$ point contraction where $N-1$ is the dimensionality of the solution space. The key determinate in these transformations is the center of mass, C_M, of points from S_2 to S_N and the coordinates of the C_M are expressed as (x_m, y_m) . In general this can be expressed within decision variables d_{jv} for all the decision variables V with the equation below.

$$\forall_{v=1}^{V} \frac{\sum_{j=2}^{N} d_{jv}}{N-1} \tag{4}$$

For the minimal zone problem with only two decision variables (x, y) for the center of the circle it can be expressed more simply with the following equation.

$$\left(\frac{x_3 + x_2}{2}, \frac{y_3 + y_2}{2}\right) \tag{5}$$

The Nelder Mead algorithm has many potential methods of optimizing. The Nelder-Mead has four internal coefficients traditionally labeled as α,β, γ, and δ. These parameters represent the coefficients for reflection, contraction, expansion, and shrinkage. Typical parameters for the transformations are $(\alpha, \beta, \gamma, \delta) = (1, .5, 2, .5)$

All transformations occur across the line from the S_1 to the C_M, except the $N-1$ point contraction. The first transformation is the reflection. Where the worst case objective, S_1, is removed from the solution space and replaced with the a new point at position S_r, S_c, or S_e for reflection, contraction, and expansion respectively. These points can be calculated by the following equations.

$$\begin{aligned} S_r &= C_M + (C_M - S_1)\,\alpha \\ S_c &= C_M - (C_M - S_1)\,\beta \\ S_e &= C_M + (C_M - S_1)\,\gamma \end{aligned} \tag{6}$$

If none of these transformations is effective at improving the objective, the algorithm resorts to the $N-1$ point contraction. This transformation rarely occurs in practice yet is a rare possibility that the previous transformations fail. Figure 40 and Figure 41 illustrate how these transformations place the next iterations node. In general the reflection and expansion transformations are primarily used in the first phase of the non-linear search as the algorithm searches for the region that contains the local optimum. Once that region is obtain the contraction transformations are used to converge on the local minimum. The green points

represent the center of mass for the set of data points not containing the worst. The dotted line is the path taken to determine the new point which crosses the C_M.

$$\forall_{k=2}^{N} S'_k = S_1 + (S_K - S_1)\delta \tag{7}$$

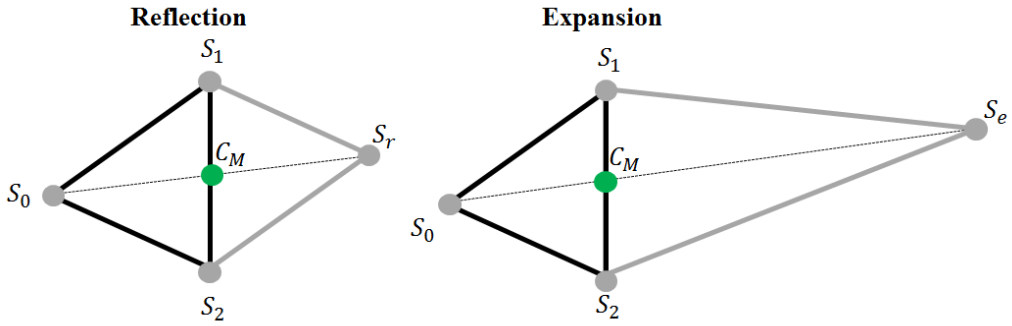

Figure 40. Reflection and Expansion

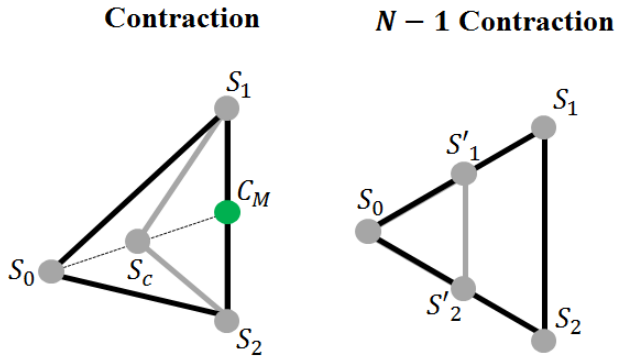

Figure 41. Contractions

The Nelder-Mead simplex has various different implementations as to how to decide which transformation is used. For this research the decision criterion as to when to perform the transformations is described as follows:

1. Attempt reflection
    a. If reflected objective is better than worse objective but not the best objective, keep reflection result. Iteration ends. Else, continue.

2. Attempt Expansion
    a. If the reflection is better than the best objective, perform expansion. If the expansion is better than the reflection, take the expansion as the new objective value. If it is not, take the reflected value. Iteration ends. Else, continue.
3. Attempt Contraction
    a. If the reflection was not better than the worse objective, perform contraction. If contracted objective value is an improvement on worst objective value. Accepted contraction and iteration ends. Else, continue.
4. Perform $N-1$ point contraction
5. Check for convergence
    a. If solution converged optimization ends. Else return to step 1.

This format for the Nelder-Mead simplex is conventional. The order and hierarchy of performing conditional checks with the Nelder-Mead are subject to investigation. The layout of the conditional checks makes logical since from a work flow perspective. However, there may be improved orderings to performing the conditional checks that can help minimize the overall number of iterations required for the Nelder-Mead simplex.

3.10 Nelder-Mead Modification

When first looking at potential improvements to the Nelder-Mead, there is the possibility of changing the coefficients $(\alpha, \beta, \gamma, \delta)$. However, this will only bring marginal benefits and the bisection coefficients that are traditionally used work provides a balanced approach to avoid over and under prediction the next iterations decision variables for S.

Given that the circular minimal zone can have a strong predicted initial start. The transformation format of the Nelder-Mead is not in an ideal order. If a least squares fit or a bounding box fit is performed prior to the non-linear search, the algorithm already has found the region where the local optimum will be obtained. The non-linear search needs to transition from the approximated started location to a point of convergence. For the traditional Nelder-Mead implementation at least two objective functions must be calculated before a contraction can be implemented. The Nelder-Mead normally performs a reflection and expansion objective function calculation prior

to the contraction. Modifications for improving convergence have been considered in the past to optimize the algorithm for given problem types [18, 23].

A new order for the Nelder-Mead transformations is proposed. The following order of transformations should allow for contractions to occur when possible without preforming a reflection or an expansion transformation.

1. Attempt Contraction
    a. If contracted objective value is an improvement on worst objective value. Accepted contraction if the contraction is better than reflection and iteration ends. Else, accept reflection continue.
2. Attempt reflection
    a. If reflected objective is better than worse objective but not the best objective, keep reflection result. Iteration ends. Else, continue.
3. Attempt Expansion
    a. If the reflection is better than the best objective, perform expansion. If the expansion is better than the reflection, take the expansion as the new objective value. If it is not, take the reflected value. Iteration ends. Else, continue.
4. Perform $N - 1$ point contraction
5. Check for convergence
    a. If solution converged optimization ends. Else return to step 1.

3.11 Numerical Analysis

For the Nelder-Mead modification, if the starting point is within the range of the local optimum the algorithm will only need to execute the contraction algorithm and potentially the reflection algorithm until convergence is found. This means that the expansion algorithm will be calculated only sparsely if ever at all. Since the minimum circular zone starting point can be reasonably approximated as mentioned prior, the non-linear search should calculate significantly fewer objective functions per iteration. Which will result in faster solve times.

In order to test the modified Nelder-Mead algorithm, 10 different problems were solved for the following three different scenarios:

Scenario 1: The first scenario is an experimental control where the objective function for all transformations is calculated prior to the iteration of the Nelder-Mead. This is known as the Standard Method calculation.

Scenario 2: The second scenario has the objective values for the transformations calculated only when they are needed and not in advanced, this results in about 1 less objective function calculations needed per each iteration.

Scenario 3: The third scenario is the Nelder-Mead modification described in section 8. The order of the transformations is such that the convergent transformations are calculated first. The objective values are calculated only when needed. This is labeled as an Aggressive Convergence Nelder Mead.

The first scenario serves as a baseline test to illustrate what influence calculating objective values in advanced have on processing time. Scenarios 2 and 3 both only calculated the objective values as needed which is preferred as it does not calculate objective values that are unused. The results from 10 different data sets are shown in Table 3. An example of the raw data set used is shown in Figure 35.All three scenarios get the exact same local optimum upon convergence for the 10 different problems. The best improvement seen within these 10 studies is a 10-fold improvement which occurred for the 3rd test set of data. The 3rd test set of data is very similar to that of the other 10. The difference in run-time is due to the convergence properties of the Nelder-Mead. In particular the scenarios 1 and 2 found a condition where they were unable to converge to an optimum and scenario 3 was impervious to this condition.

The standard Nelder-Mead implementation required 419 iterations, the modified Nelder-Mead algorithm required only 48 iterations. The Aggressive Convergence Nelder-Mead solved better for every scenario. With an average improvement of 220.2% comparing scenario 3 to scenario 2, the new algorithm required 45.4% of the number of iterations of the standard Nelder-Mead. In

addition to decreasing the total run-time the Aggressive Convergence Nelder-Mead has significantly less run-time deviation across multiple problem sets. The standard deviation of the Aggressive Convergence Nelder-Mead run-time is 2% of the Selective Objective Nelder-Mead and the Standard Nelder-Mead implementations.

Table 3. Nelder-Mead Modification Result

	Standard Method		Selective Objective		Aggressive Convergence	
Test #	**Iterations**	**Run-Time (s)**	**Iterations**	**Run-Time (s)**	**Iterations**	**Run-Time (s)**
1	70	33.423	70	28.305	50	20.540
2	78	37.203	78	31.167	48	19.699
3	419	198.596	419	146.289	48	19.684
4	84	40.260	84	33.439	47	19.294
5	70	34.201	70	28.190	48	19.682
6	83	39.575	83	32.798	50	20.469
7	61	34.778	73	29.480	50	20.511
8	84	29.236	61	24.798	53	21.705
9	73	40.140	84	32.999	49	20.470
10	68	32.473	68	27.290	52	21.291
Average	**109**	**51.988**	**109**	**41.475**	**49.5**	**20.334**
StdDev	**109.194**	**51.640**	**109.194**	**36.934**	**1.900**	**0.763**
Worst	**419**	**198.596**	**419**	**146.289**	**53**	**21.705**
Best	**61**	**29.236**	**61**	**24.798**	**47**	**19.294**

The Aggressive Convergence Nelder-Mead is ideal for this class of problem as the problem initialization is within close proximity to the local optimum. The Aggressive Convergence Nelder-Mead minimizes the number of objective function computations needed per each iteration and each iteration the algorithm favors converging upon a point verses expanded outward or reflecting to a new location. The minimum number of objective function calculations made within an iteration is two, as even though a contracting transformation may be beneficial it must be compared to a reflection in order to assure the algorithm converges unto a point that is a true local optimum.

3.12 Testing Additional Non-Linear Search Algorithms

In addition to the detailed analysis of the Nelder Mead algorithm and its modifications, other common non-linear search algorithms were tested and compared. Below is the list of alternative search algorithms used in the study.

- Polak-Ribiere Conjugate Gradient Algorithm (PR)
- Fletcher-Reeves Conjugate Gradient Algorithm(FR)
- Steepest Descent Algorithm (SD)
- Broyden-Fletcher-Goldfarb-Shanno Algorithm (BFGS)
- Nelder Mead (NM)

3.13 Newton's Method

Prior to understanding the conjugate gradient algorithm it is good to review gradient based root finding of Isaac Newton. Newton's method is an iterative search algorithm defined such that:

$$x_{i+1} = x_i - \frac{f(x_i)}{f'(x_i)}$$

The algorithm continues until the process converges.

3.14 Conjugate Gradient (Fletcher-Reeves and Polak-Ribiere)

The conjugate gradient algorithm starts in initialized in the same way as the steepest descent algorithm. For a given function $f(x)$ with derivative $f'(x)$ where x is a vector with dimension n. The problem is initialized at starting vector x_0 with a line search in the direction of steepest descent, d_0, where $d_0 = -f'(x_0)$ to determine the new vector x_1. In general for any iteration the x_{i+1} position can be determined from the x_i position by the following equation.

$$x_{i+1} = x_i + \lambda d_i$$

λ is the magnitude moved in the search direction determined by a line search. The line search can be performed by a variety of methods including Newton's root finding algorithm, bi-section algorithm, golden-ratio search, exhaustive search, and others. After the line search the next direction is calculated, this is expressed by

$$d_{i+1} = -f'(x_{i+1}) + \alpha_i d_i$$

Where α depends upon the variation of the conjugate gradient method that you choose to implement. For the Fletcher-Reeves algorithm:

$$a_i = \frac{\left||f'(x_{i+1})|\right|^2}{\left||f'(x_i)|\right|^2} = \frac{d_{i+1}^{\top} d_{i+1}}{d_i^{\top} d_i}$$

For Polak-Ribiere:

$$a_i = \frac{f'(x_{i+1}) \cdot (f'(x_{i+1}) - f'(x_i))}{\left||f'(x_i)|\right|^2} = \frac{d_{i+1}^{\top}(d_{i+1} - d_i)}{d_i^{\top} d_i}$$

After n iterations the problem is reset and then continued. This is done by on the n^{th} iteration $d_{i+1} = -f'(x_{i+1})$ where on the n^{th} iteration the $\alpha_i d_i$ term is ignored. The process is continued until the problem converges. Typically for the conjugate gradient method, the problem is considered to have converged when the gradient approaches close enough to zero within a reasonable tolerance, ε.

$$\left||f'(x_{i+1})|\right| < \varepsilon.$$

3.15 Steepest Descent

The Steepest Descent Algorithm starts in the direction of the gradient of the solution space and then performs a line search. Then the algorithm chooses an orthogonal direction and performs another line search and then continues the process until convergence. For a vector of decision variables x and a typical function $f(x)$ with derivative $f'(x)$. The problem is initialized at starting point x_0.

The direction of descent is set by

$$d_i = -f'(x_i)$$

The next position is determined by

$$x_{i+1} = x_i + \lambda d_i$$

Where λ is an optimal magnitude that minimizes $f(x_i + \lambda d_i)$. Next $i \coloneqq i + 1$ and the process repeats recalculating the direction of descent and the next position until$\left|\left|f'(x_i)\right|\right| < \varepsilon$, where ε is a predetermined stopping criterion.

3.16 Vector BFGS

The BFGS (Broydent-Fletcher-Goldfarb-Shanno) algorithm is a quasi-newton search algorithm. The BGFS utilizes an approximation of the hessian matrix, H, to improve the search direction. The search direction $d_{i+1} = -H_i^{-1} f'(x_i)$. Once the direction is determined, a line search is performed.

$$x_{i+1} = x_i + \lambda d_i$$

Given $y = f'(x_i) - f'(x_{i-1})$ and $s = x_i - x_{i-1}$

$$H_i = H_{i-1} + \frac{yy^\top}{y^\top s} - \frac{H_{i-1} s s^\top H_{i-1}}{s^\top H_{i-1} s}$$

3.17 Non-Linear Search Results Summary

The results of the above mentioned search algorithms are shown below in Table 4. These problems were run on a minimal circular zone problem on a data set of 1 million points. The test was run on 13 different data sets. The data was generated from real 3D scan data of pre-stressing steel reinforcement wire. These provide an indiciation as to which algorithm would be best suited for industrial applications. In general the nelder-mead algorithm has the shortest computation time. However both the conjugate gradient method of Polak-Ribiere and Flecther-Reeves required less total iterations. As the conjugate gradient method requires the calculation of a gradient and the gradient for the minimal zone problem is time consuming to compute, even though the conjugate gradient has fewer iterations the Nelder-Mead algorithm performs better in solve time as it does not require the calculation of a gradient. The method of steepest descent performed the worst at of all the computation methods as expected. The BFGS algorithm was the next worst performing algorithm. From these results we can see that the Nelder-Mead algorithm is the preferred algorithm for the calculation of minimal zone on applications with large data sets.

Table 4. Number of Iterations and Solve Times for Various Non-Linear Search

	PR		FR		SD		BFGS		NM	
	Iter.	Time (s)	Iter.	Time (s)	Iter.	Time (s)	Iter.	Time (s)	Iter.	Time (s)
WA	8	41.431	5	29.247	193	161.872	15	42.864	84	27.443
WB	35	83.610	25	67.018	1255	1030.187	124	217.985	49	16.080
WC	4	25.057	3	18.338	231	192.470	3	18.343	55	18.074
WD	9	38.885	7	30.377	237	196.987	17	51.181	78	25.037
WE	6	34.244	14	40.579	228	189.038	9	42.867	58	18.318
WF	52	112.839	14	46.317	236	196.213	10	36.147	96	31.426
WG	12	32.004	12	31.334	195	162.681	46	67.136	68	22.159
WH	7	33.607	7	31.831	154	129.904	8	30.234	60	19.918
WI	9	35.846	9	37.718	197	164.264	7	31.378	92	29.834
WJ	24	73.204	42	98.302	152	127.485	64	128.820	50	16.242
WK	5	24.191	9	38.979	232	193.001	10	41.769	58	18.480
WL	11	45.583	11	42.811	191	159.461	14	54.365	75	23.907
WM	6	31.225	49	93.001	473	391.150	34	95.754	53	17.198

3.18 Parallel Implementation Techniques

For the circular minimal zone algorithm one of the most time extensive aspects of the objective function is calculating the radial distance of a data point from(x_c, y_c). As the magnitude requires root and squared calculations the equation is non-trivial. Specifically for the minimal zone class of problems the vector magnitude is often required calculated between every data point. As this calculation is the exact same for every data point, it is ideal for parallel processing on the CPU (central processing unit) or the GPU (graphical processor unit). The only limitation to this calculation method is the memory space of allocable and the number of processors available for the parallel processing. Given the large number of equations that need to calculated, the parallel processing for this problem is best served by the functionality of the GPU with the non-linear search performed on the CPU.

By integrating GPU processing of the objective function, the large objective function computation time can be negated. However, a proper implementation of this contains both problem specific dependency and hardware dependency. The key factor as to why parallel processing is feasible is that for the minimal zone calculation has many independent computations that are needed. If the objective function has many interdependent computations that overlap, than parallel processing may not be as successful. While a circular zone search has

the potential for large scale parallel processing, it is not difficult to extrapolate a problem where the objective function has minimal potential for parallel processing.

For a GPU implementation, implementations can be done with either OpenGL shaders or with OpenCL. Given that much of the objective function is vertex manipulation, OpenGL implementation is preferred [3].

3.19 Benefits of Parallel Computing

Table 5 shows the benefits parallel computing can have as compared to the results from Table 4. The computation time for the Nelder Mead algorithm using GPU parallel processing allowed for were on average 3.3 times faster. The computation time for the conjugate gradient method from Polak-Ribiere was on average 2.86 times faster with GPU parallel processing.

Table 5. Benefits on GPU Parallel Computing

	Polak-Ribiere				Nelder-Mead		
	Serial (s)	Parallel (s)	Improvement		Serial (s)	Parallel (s)	Improvement
WA	41.431	7.898	81%	**WA**	27.443	8.496	69%
WB	83.610	10.860	87%	**WB**	16.080	4.919	69%
WC	25.057	5.693	77%	**WC**	18.074	5.163	71%
WD	38.885	33.976	13%	**WD**	25.037	8.283	67%
WE	34.244	6.395	81%	**WE**	18.318	5.440	70%
WF	112.839	6.393	94%	**WF**	31.426	9.601	69%
WG	32.004	23.699	26%	**WG**	22.159	6.691	70%
WH	33.607	52.879	-57%	**WH**	19.918	6.032	70%
WI	35.846	16.630	54%	**WI**	29.834	8.995	70%
WJ	73.204	11.706	84%	**WJ**	16.242	5.015	69%
WK	24.191	18.927	22%	**WK**	18.480	5.747	69%
WL	45.583	7.825	83%	**WL**	23.907	7.107	70%
WM	31.225	10.729	66%	**WM**	17.198	5.184	70%
Average Improvement:			**55%**	**Average Improvement:**			**70%**

The bottle neck for GPU parallel processing is in passing the large data sets to the GPU RAM. As the data sets consist of 1 million sets of a Cartesian x,y, and z double precision values, the write time to the video card significantly negates the potential benefits of parallel computing. For the implementation presented in this study, the system would have to write this data to the GPU RAM every iteration. Modifying the GPU processing code so that the data must only be

passed once to the GPU RAM, may allow for process improvement on the order of 10 to 100 fold.

3.20 Conclusion

A new non-linear search method is presented known as the Aggressive Convergence Nelder-Mead which has shown to perform significantly better than the standard Nelder-Mead algorithm for this class of problem. A two-fold improvement in the Nelder-Mead search algorithm was achieved for this class of problem.

A method of approaching non-linear search for problems with large objective function computations times has been addressed. When working with non-linear search where the objective function is large, the recommended procedure is as follows. First, determine the closest possible approximation that does not add significantly to the computational time. For the circular minimal zone this would be a least squares fit on a small subset of the data. Second, decrease the objective function computation to a close approximation. For the circular minimal zone this can be done by removing excess data points that are not value adding to the objective function computations. Third, solve the non-linear search. Finally, re-solve the non-linear search on the full objective and check if the answer is the same as the approximated search answer. If they are the same, then the local optimum has been found.

Additionally a modification to the Nelder-Mead simplex has been discussed that has the potential to reduce encourage faster convergence and reduce the total number of objective function calculations needed to find the local optimum for the Nelder-Mead simplex.

The Nelder-Mead algorithm was compared to four other non-linear search algorithms. The Nelder Mead algorithm had the shortest run time of all the algorithms and is recommend for use in industrial applications. The conjugate gradient method was able to solve the problem in fewer iterations, however, due to the computational time required to calculate the derivative it performed slower. Parallel processing was proven to show a significant benefit in the run time of these problems. The run time may be able to be improved even further with more advanced parallel programming techniques not used within this study.

Chapter 4 — Indent Profiling System Software and Algorithms

This chapter documents the research and findings of 3D processing algorithms for analysis and measurement of part point cloud data. The algorithms are applied to the analysis of pre-stressing steel reinforcement wire for testing and utilization. The algorithms have applications for general 3D point cloud analysis. The 3D processing algorithms are arranged in a linear workflow that includes data pre-processing, data alignment, shape correction, geometrical feature recognition, and automated measurement methods.

4.1 Automated Analysis & Measurement Workflow

The automated measurement algorithms follow a linear workflow. The workflow starts with inputting a raw 3D point cloud of the part. The output is a measurement report which provides measurement of key geometrical features required for the part. Figure 42 illustrates the workflow for processing the part point cloud.

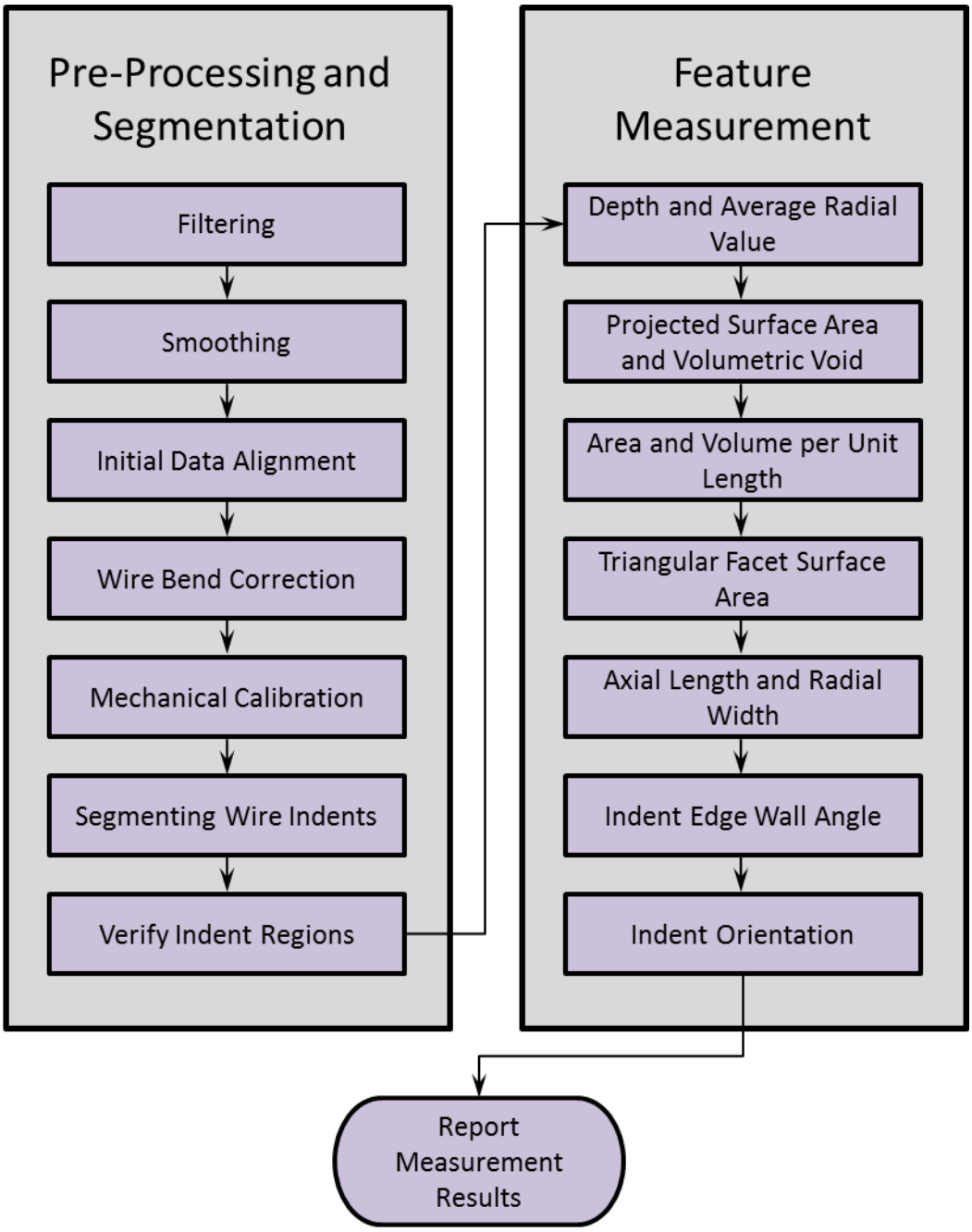

Figure 42. Algorithm Workflow

4.2 Pre-processing and Segmentation Algorithms

With raw data received from the non-contact profiling system, the data must be checked for quality. Errors must be removed and the data set needs to be aligned to the proper reference frame. The indent regions must be isolated from each other and from data points representing

the outside surface of the wire. Once preprocessing and segmentation algorithms are performed the indent features can be measured by their corresponding algorithms.

4.2.1 Filtering

Raw data received from a non-contact laser displacement sensor is subject to errors from specular reflection, beam splitting, signal noise, and other sources. The types of noise received depends on the profile and surface finish of the part being scanned, the types of laser optics used, and the types of laser source to digital signal conversion used. This filtering method that performs best will depend on the application and the hardware used.

Figure 43 shows the most common form of measurement error for the laser displacement sensors used within the study. The graph shows every laser measurement recorded with a tick mark. On the steep slope on the left of the graph the laser fails to record measurements. This is due to the reflectivity of the steel surface and its incident angle causing excessive amounts of specular reflection. When insufficient diffused laser intensity is detected from the sensor an error is output of the extreme most negative value.

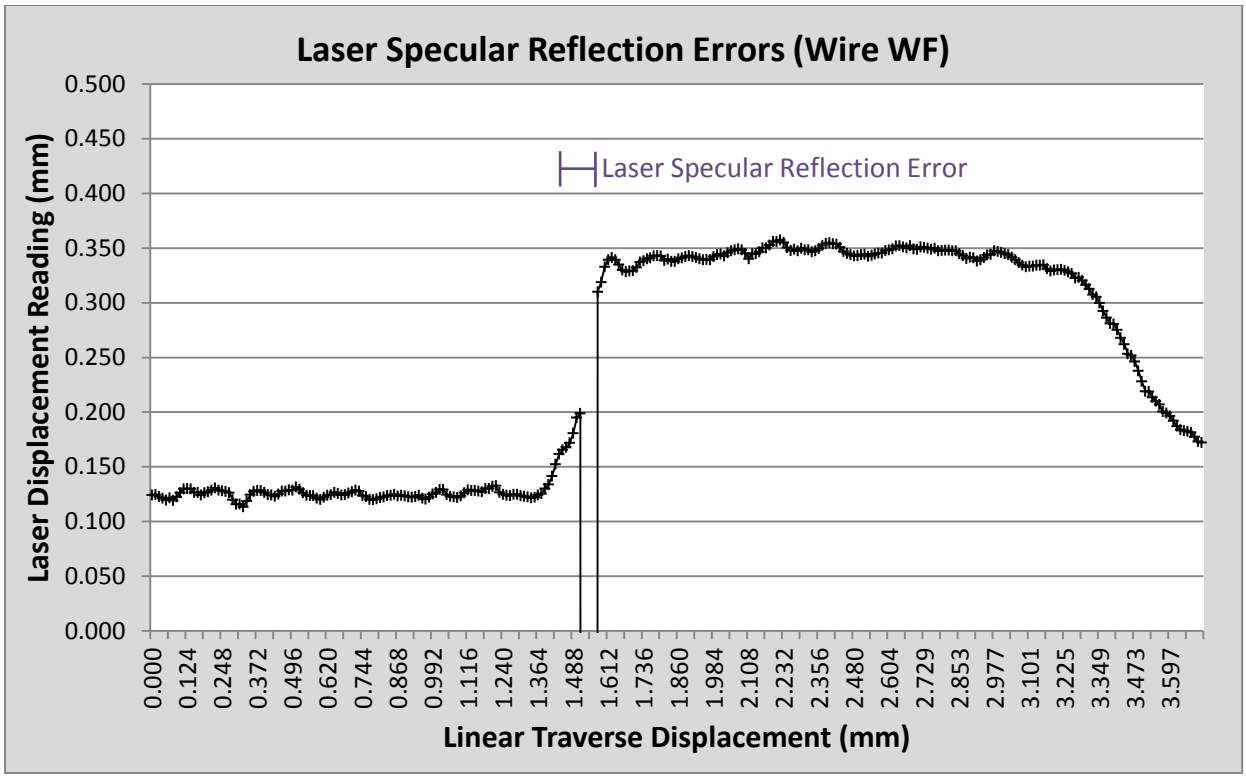

Figure 43. Laser Specular Reflection Errors

This form of error causes gaps in the collected scan data that must be resolved. One option is to omit the data from the point cloud which would result in a hole in the scanned profile, which causes processing difficulties for algorithms later in the work flow. A moving average or a frequency filter (Fourier Transform Thresholding) is inadequate at removing this error as it exists across a given patch of the data set. The frequency filter will result in a significant loss of positional information; the moving average will still show a large spike at the error location. The best found solution to this error is to detect the error range and use linear interpolation to approximate the positions of the missing data points.

Given a raw point cloud as a 2D array named $PC[l][i]$ with $L: l \in [0, L)$ scanlines and $I: i \in [0, I)$ data points per line, PC has a corresponding PC_x,PC_y, and PC_z for the respective x, y ,and z positions of the data point. PC also has a corresponding PC_r, PC_t, and PC_h for the cylindrical coordinate positions r,θ, and h. The rate of change threshold is T_{limit} and a temporary array $Errs$ to hold a consecutive group of erroneous values. Laser reflection errors have an

initial $PC_r = -\infty$. We will first remove any additional erroneous values from the data set by ensuring that they are within the threshold limit of their neighboring points.

```
//find all values outside threshold and mark as errors (−∞)
Get PC
Get T_limit
For all l in L
      For all i in I − 1
            If |PC_r[l][i] − PC_r[l][i + 1]| > T_limit
                  Set  PC_r[l][i] = −∞
                  Set  PC_r[l][i + 1] = −∞
```

Figure 44. Identify Erroneous Outliers

```
Get PC
Set C = 0      //counter for erroneous data points
For all l in L
      For all i in I − 1
            If |PC_r[l][i]| = ∞
                  While i in I And |PC_r[l][i]| = ∞
                        Increment C
                        Set Errs[C] to i
                        Increment i
                  Set initial = PC_r[l][Errs[0] − 1]
                  Set increment = (PC_r[l][Errs[C]+1] − PC_r[l][Errs[0]−1]) / Length(Errs)

                  For all C in Length(Errs)
                        Set PC_r[l][Errs[C]] = initial + increment ∗ C

//when error lines appear at the extremes of the data set additional
//accommodations must be made
```

Figure 45. Replace Error Points with Linearly Interpolated Points

4.2.2 Smoothing

Once the erroneous data values are corrected during the filter process, data smoothing is used to further reduce noise and improve the data quality. Aspects of the surface roughness of the part,

minor surface defects, and minor laser signal noise are not needed for measurement of the part geometrical features. These aspects can be removed with smoothing algorithms. Two smoothing techniques used within this study is a moving average and frequency filtering with fourier transforms.

For a M by M: $m \in [0, M)$ moving average of the cylindrical data set algorithm is as follows:

```
Get PC
//Pad the data set to handle edge of array
For all m_1 in M
      For all m_2 in M
            Set PC_r[L + m_1][I + m_2] = PC_r[L − 1][I − 1]
For all l in L
      For all m_2 in M
            Set PC_r[l][I + m_2] = PC_r[l][I]
For all m_1 in M
      For all i in I
            Set PC_r[L + m_1][i] = PC_r[m_1][i]
//Calculate the moving average
For all l in L
      For all i in I
            Set Tmp[l][i] = (Σ_{m_2=0}^{M} Σ_{m_1=0}^{M} PC_r[l+m_1][i+m_2]) / M^2
Set PC_r = Tmp
```

Figure 46. Moving Average Smoothing Filter

For the Fourier filter if an uninterrupted scanning method is used such as a spiral scanning path a Fourier Transform can be applied to the entire array at once. If the scanning has interrupts such as the line based scanning technique, the Fourier low pass filtering may be applied to each line.

For a typical function, $f(x)$, the Fourier Transform, $F(u)$ can be expressed by the following:

$$F(u) = \frac{1}{M} \sum_{x=0}^{M-1} f(x) e^{-i2\pi ux/M}$$

With the inverse Fourier Transform:

$$f(x) = \sum_{u=0}^{M-1} F(u) e^{i2\pi ux/M}$$

The low pass filter can be applied with the following pseudo code and mask T_{mask}.

```
Get PC
Get T_mask
//perform Fourier Transform
For all l in L
      For all i_1 in I
            For all i_2 in I
                  Set F^r[i_1]+= PC_r[i_2] cos(2πi_1 i_2/I)
                  Set F^i[i_1]−= PC_r[i_2] sin(2πi_1 i_2/I)
            Set F^r[i_1] = F^r[i_1]/I   //real component
            Set F^i[i_1] = F^i[i_1]/I   //imaginary component
            Set F[i_1] = F^r[i_1] + F^i[i_1]

//Apply filter
Set F = F&T_mask

//perform inverse Fourier Transform
For all l in L
      For all i_1 in I
            For all i_2 in I
                  Set PC_r^r[i_1]+= F[i_2] cos(2πi_1 i_2/I)
                  Set PC_r^i[i_1]+= F[i_2] sin(2πi_1 i_2/I)
            Set PC_r^r[i_1] = F^r[i_1]/I
            Set PC_r^i[i_1] = F^i[i_1]/I
            Set PC_r[i_1] = PC_r^r[i_1] + PC_r^i[i_1]

//In practice FFT processing libraries are used
//In practice data padding is also utilized
//This solution may be incomplete
```

Figure 47. Low Pass Fourier Transform Filter

4.2.3 Initial Data Alignment

The point cloud needs to be properly aligned to its datum reference frame for measurement purposes. For this application the data alignment is complete after the bend corrections are performed in the following section.

Aligning using cylindrical zone requires a minimum of four decision variables. If the data is aligned to the z axis the decision variables can be T_x, T_y, θ_x, and θ_y for translation and rotation about the X and Y axis. The decision variables define the translation matrix T and the rotation matrix R. With the zone defined by two concentric cylinders, the smallest circumscribing cylinder radius is Cyl_{max} and the largest inscribing cylinder radius is Cyl_{min}. The function that determines the current zone size about the z axis would be as follows:

```
//cylindrical zone size for current point cloud position

Function CylindricalZone (PC,T,R)
      Set PC = (PC + T)R
      For all l in L
            For all i in I
                  If PC_r > Cyl_max
                        Set Cyl_max = PC_r[l][i]
                  If PC_r < Cyl_min
                        Set Cyl_min = PC_r[l][i]
      Return Cyl_max − Cyl_min
```

Figure 48. Calculate Cylindrical Zone Size

In order to realign the point cloud to the z axis and find the minimum zone the pseudo code below generalizes the solution. Chapter 3 — Non-Linear Search in GD&T presents multiple methods for how the minimization may be performed. The Nelder-Mead search method was determined to be a reliable and fast converging solution.

```
//determine the minimum cylindrical zone
Get PC
Minimize CylindricalZone Using T_x, T_y, θ_x, θ_y
Set PC = (PC + T)R
```

Figure 49. Search for Minimal Cylindrical Zone Size

4.2.4 Wire Bend Correction

The wires analyzed in this study have a natural curvature due to being wound upon a spool during manufacture. As the wires are under large pre-tension loads during manufacture, the curvature is irrelevant for manufacture. The curvature causes difficulties for the measurement process as it prevents the theoretical datum axis from aligning with the true axis of the wire. A post-measurement straightening routine was developed to allow the wire to be "flexed" or straightened into alignment with the theoretical axis.

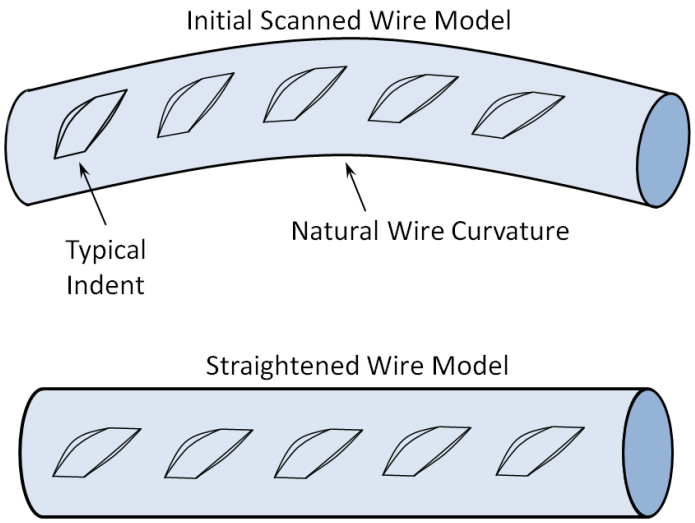

Figure 50. Before and After Bend Correction Algorithm

Figure 51 shows the results of aligning the data set and applying the bend correction algorithm. The left image shows an unaligned data set with wire bend. The right image shows the data set with datum alignment and bend correction applied.

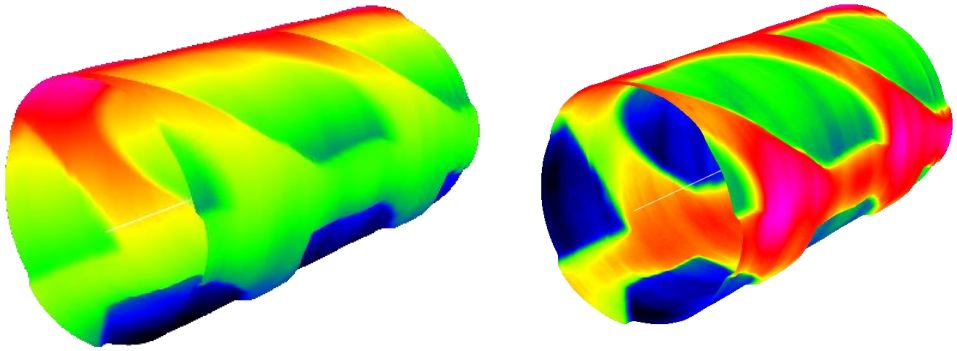

Figure 51. Unaligned Data Set(Left) verses Aligned and Bend Corrected(Right)

Figure 52 shows how the wire curvature can be compensated. The point cloud PC is segmented into a series of circular rings of data $PC[i][l]: i \in [0, I), l \in [0, L)$. For each circular ring, the center point is determined with circular zone calculation, which finds the minimum zone d by the two decision variables T_x and T_y which define the translation matrix T. The center points (x_c, y_c) are then moved to the nominal position (Z axis) to straighten the wire.

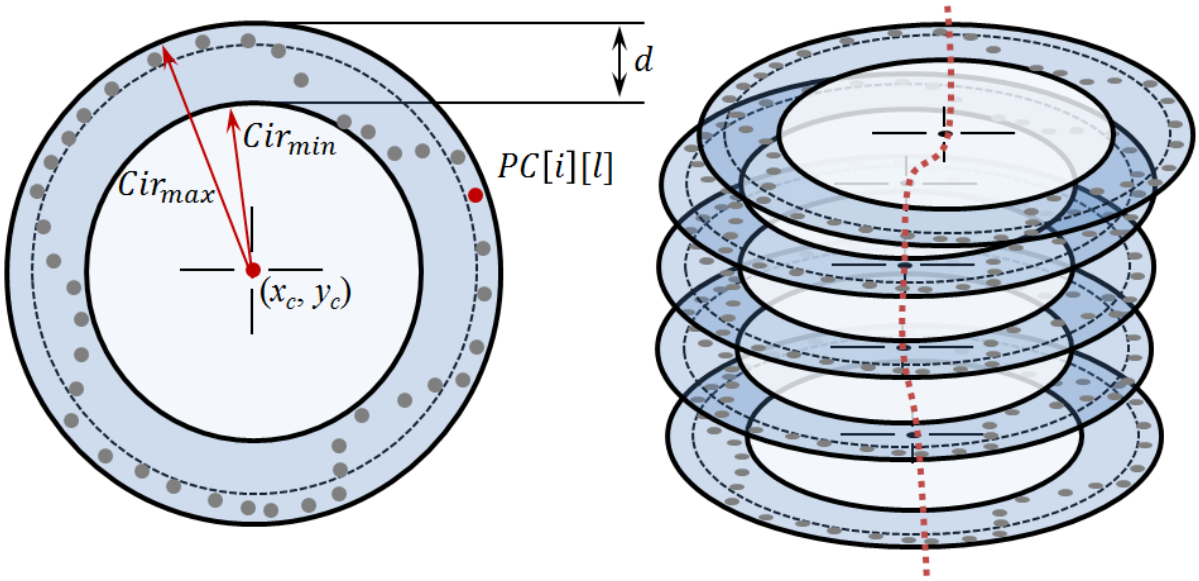

Figure 52. Wire Bend Corrections

The function for the circular zone size finds the difference in radii of the minimum circumscribing circle Cir_{max} and the maximum inscribing circle Cir_{min}.

```
//Circular zone size for current ring position
Function CircularZone (PC[i],T)
      Set PC = PC + T
      For all l in L
            If PC[i][l] > Cir_max
                  Set Cir_max = PC[i][l]
            If PC[i][l] < Cir_min
                  Set Cir_min = PC[i][l]
      Return Cir_max − Cir_min
```

Figure 53. Calculate Circular Zone Size

The following algorithm realigns each PC^{ring} to the Z axis by translation.

```
//Correct for wire bend
Get PC
For all i in I
      Minimize CircularZone Using T_x, T_y
      For all l in L
            Set PC[i][l] = PC[i][l] + T
```

Figure 54. Wire Bend Correction

This solution was found sufficient for practical application; however, at large bend deformations each $PC[i]$ would become more elliptical than circular. As the wires bend deformation is small relative to the scan length this issue is not present. A solution for this issue would be to rotate each $PC[i]$ into alignment, as opposed to the translation method shown above. A rotation matrix R would need to be created to rotate the remaining wire length the angle created from the Z axis to previous rings center point to the current rings center point. In this case R would be driven by R_x and R_y. As the rotation will occur about the origin, the center of rotation of each ring should be about the position of the previous ring.

```
//Correct for wire bend using rotation
Get PC
//First, Translate in z axis the step size in between rings
//This allows the first ring to be rotated into alignment.
For all i = 0; i < 2; i++
      Set Centroid_i = 0
      For all l in L
            Set Centroid_i += PC[i][l]
      Set Centroid_i /= L
For all i in I
      For all l in L
            Set PC[i][l]_z += Centroid_1,z − Centroid_0,z
//Realign circular rings using rotation
For all i in I
      Minimize CircularZone Using PC[i], R
      //Rotate all data points from current i to I by R
      For i' = i; i' < I; i'++
            For all l in L
                  Set PC[i'][l] = (PC[i'][l])R
      //If not at the last ring
      If i < I − 1
            //Calculate next two ring centroids
            For all i' = i; i' < i + 2; i++
                  Set Centroid_i' = 0
                  For all l in L
                        Set Centroid_i' += PC[i'][l]
                  Set Centroid_i' /= L
            //Translate points in Z axis for next rotation origin
            For all i' in I
                  For all l in L
                        Set PC[i'][l]_z += Centroid_i',z − Centroid_i'+1,z
```

Figure 55. Correct for Wire Bend Using Rotation

4.2.5 Mechanical Calibration (Conical Taper Correction)

The non-contact measurement system used to scan the reinforcement wire does not have perfect mechanical alignment. Achieving a mechanical alignment good enough to not need software calibration would be cost prohibitive and unreliable over the use of the measurement systems lifespan. An algorithmic mechanical calibration solution was made to correct for any

misalignment issues found with the scanning system. This allows for additional measurement systems to be made at a lower cost than physically calibrating the positioning of the measurement system. Figure 56 shows an exaggerated view of the mechanical misalignment between the axis of the rotary table and the axis of the linear traverse.

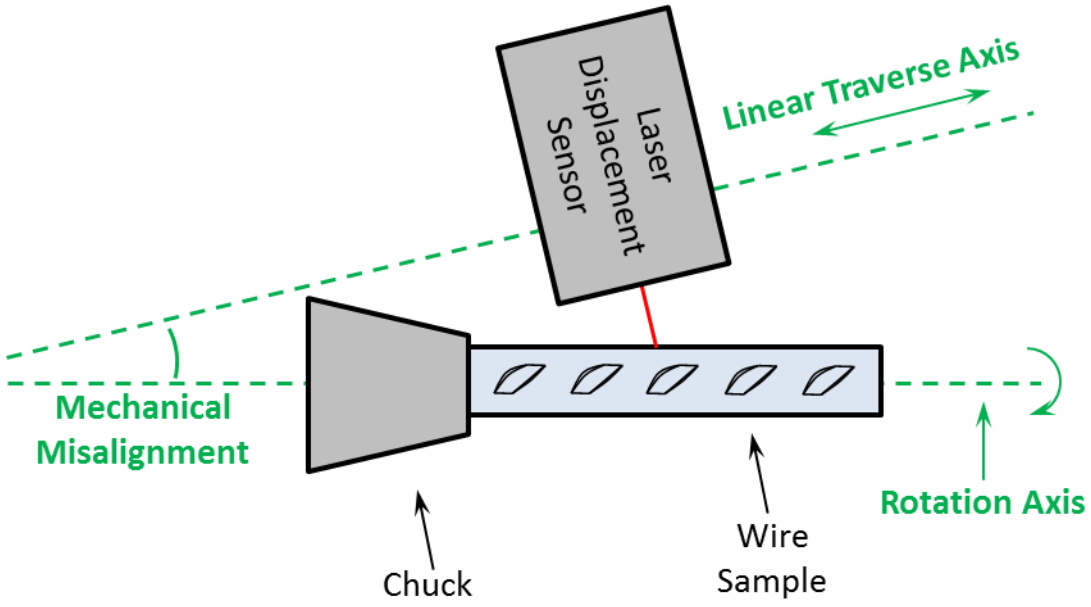

Figure 56. Mechanical Misalignment

The primary calibration step needed is aligning the axis of rotation of the rotary fixture to the directional axis of the linear traverse. This is possible as the wire diameter is known and constant through all the samples studied. With this assumption each ring of points collected can be resized to the proper diameter of the wire. This corrects for misalignment between the rotation axis and the directional axis of the linear traverse. Figure 57 shows the exaggerated impact in the 3D scan model of having the mechanical misalignment as the Initial Scanned Wire Model. The Calibrated Wire Model is after processing of the mechanical calibration algorithms.

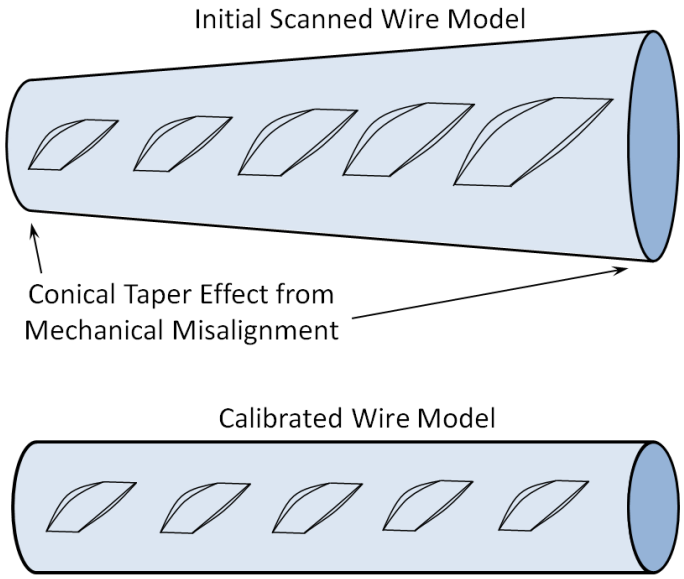

Figure 57. Resulting Conical Taper Effect

Figure 58 shows the results of the conical taper correction on a real data set. The result is subtle. However, the left image clearly has an overall larger wire radius at the back end. The right image shows a balanced overall radius from front to back.

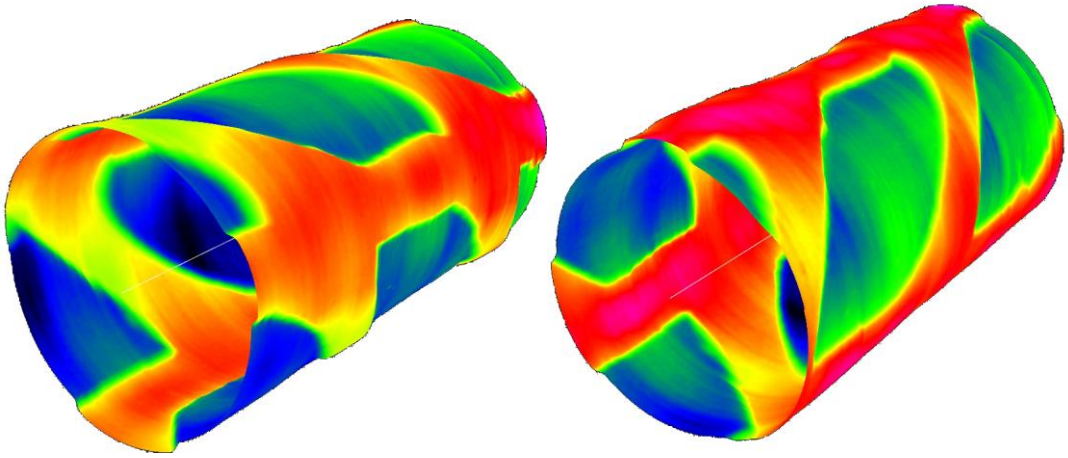

Figure 58 Before Conical Taper Correction (Left) and After (Right)

The result of the mechanical misalignment is the circular rings $PC[i]: i \in [0, I)$ increase in radius linearly as the traverse position is incremented. A linear regression was taken of the maximum radial values of each ring. The regression returns the slope M and offset B for the equation of the line. The regression function is named `LinearRegression()`. The rings are then rescaled to their nominal radius N_r which for the wires in the study is 2.66mm.

```
//Correcting for machine calibration
Get PC

//Get array of maximum ring radii
For all i in I
      For all l in L
            If PC[i][l] > Max[i]
                  Set Max[i] = PC[i][l]

//Get linear regression of maximum radii
Set M, B = LinearRegression (Max)

//Get ring radial size on regression line
For all i in I
      Set RadialSize[i] = M * i + B

//Rescale from regression line
For all i in I
      For all l in L
            Set PC_r[i][l] = cos(atan(M))(PC_r[i][l] − RadialSize[i]) + N_r

//for small angles cos(atan(M)) = 1 and can be ignored
```

Figure 59. Performing Mechanical Calibration (Correcting Conical Taper Effect)

4.2.6 Segmenting Wire Indents

For a given point cloud surface profile of a reinforcement wire, a one inch scan length contains 1,638,400 data points evenly dispersed across the wires surface. A large portion of these data points do not pertain to the indented region to be measured. Additionally the points for the indented regions need to be grouped by indent. A Cylindrical Flood Fill algorithm was created to cluster and identify indent regions.

The indent segmentation algorithm has three parts. Prior to searching for indents, the point cloud data set is padded on the boundaries by one data point. This prevents overflow at the array boundaries. Alternatively to padding the boundary, additional conditioning can be applied to prevent the overflow. This will prevent the need for redimensioning the data array, and allow for an overall faster processing time.

```
//Pad the border
Get PC
//stitch seam of cylinder
For all i in I
      Set PC_r[−1][i] = PC_r[L − 1][i]
      Set PC_r[L][i] = PC_r[0][i]
//Extend ends of cylinder
For all l in L
      Set PC_r[l][−1] = PC_r[l][0]
      Set PC_r[l][I] = PC_r[l][I − 1]
```

Figure 60. Padding Data Set Boundaries

The segmentation algorithm searches through all the possible data points. When the algorithm identifies a data point that is an indent, it uses that data point as a seed (si, sl). The seed is labeled with an indent identification number ($IndentID$). Starting from the seed point, a recursive algorithm tags all the surrounding data points that are a part of the indent with the same $IndentID$. The array that holds the identification number for every indent is $PC_i[l][i]: l \in [0, L), i \in [0, I)$.

Figure 61 illustrates the recursive flood fill procedure. The starting at the data point in yellow, the algorithm grows to consume all the green data points, data points in grey are outside the indent boundary and are not included. The algorithm in this example searches clockwise starting with the lower most point.

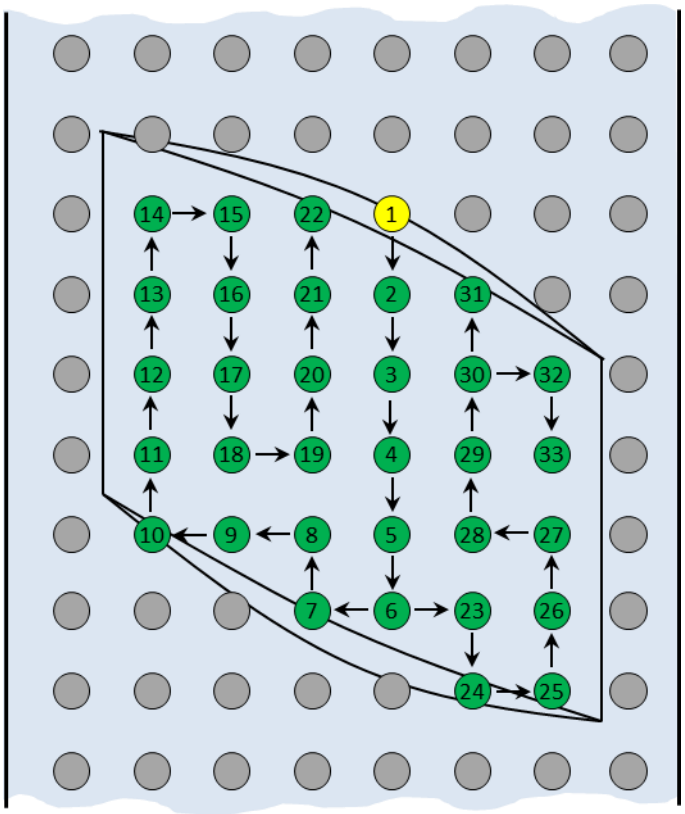

Figure 61. Recursive Flood Fill Algorithm

Figure 62 shows the results of the indent segmentation algorithm on a real data set. The Indented regions are highlighted in increasing shades of grey for the order that the indents were found.

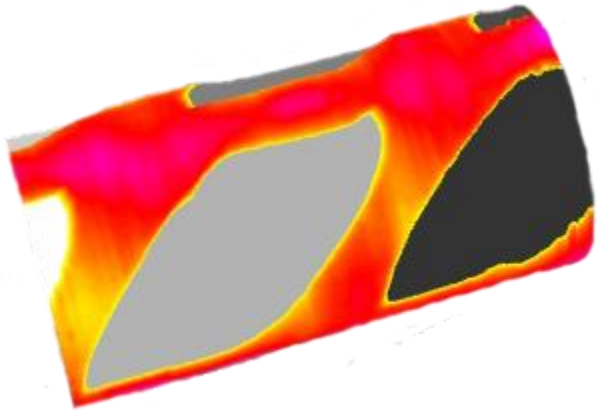

Figure 62. Indent Segmentation Result

The following algorithm shows the flood fill procedure. Starting at the seed location, all surrounding data points are checked that they are not part of an existing indent and that there radial value below the threshold used to identify an indent, T_{indent}. If the data point is an indent the algorithm calls itself using that point as the seed. There are a few exceptions, if the data point is at the edges of the cylindrical data it stops. Also, if the data point is at the seam line, the algorithm uses the data point across from the seam line as the seed. For example, if the data point has $sl = -1$ or L it respectively moves to position $L - 1$ or 0.

```
//Cylindrical Flood Fill
Get T_indent

Function CylindricalFloodFill(PC, sl, si, IndentID)
      If PC_i[sl][si − 1] ≤ 0 And PC_r[sl][si − 1] < T_indent
            Set PC_i[sl][si − 1] = IndentID
            If si − 1 > −1
                  CylindricalFloodFill(PC, sl, si − 1, IndentID)
      If PC_i[sl − 1][si] ≤ 0 And PC_r[sl − 1][si] < T_indent
            Set PC_i[sl − 1][si] = IndentID
            If sl − 1 = −1
                  CylindricalFloodFill(PC, L − 1, si, IndentID)
            Else
                  CylindricalFloodFill(PC, sl − 1, si, IndentID)
      If PC_i[sl][si + 1] ≤ 0 And PC_r[sl][si + 1] < T_indent
            Set PC_i[sl][si + 1] = IndentID
            If si + 1 < I
                  CylindricalFloodFill(PC, sl, si + 1, IndentID)
      If PC_i[sl + 1][si] ≤ 0 And PC_r[sl + 1][si] < T_indent
            Set PC_i[sl + 1][si] = IndentID
            If sl + 1 = L
                  CylindricalFloodFill(PC, 0, si, IndentID)
            Else
                  CylindricalFloodFill(PC, sl + 1, si, IndentID)
```

Figure 63. Perform Cylindrical Flood Fill (Indent Segmentation)

The algorithm to search for seed points is shown in the following pseudo code. All PC_i start at -1 representing a not yet calculated value. 0 represents data points on the surface of the wire but not a part of the indent. Values 1, 2, 3… for $IndentID$ represent the respective indent

number. At the end of algorithm all PC_i will be a number from 0, 1, 2, 3…. If a data point PC_r is less than T_{seed} – the threshold used to identify an indent seed – the flood fill of the indent begins.

```
//Search for Indents
Get PC
Get T_seed
Set PC_i = −1
Set IndentID = 0

For all l in L
      For all i in I
            If PC_i[l][i] = −1 And PC_r[l][i] < T_seed
                  Increment IndentID
                  Set PC_i[l][i] = IndentID
                  CylindricalFloodFill(PC, l, i, IndentID)
            Else
                  Set PC_i[l][i] = 0
```

Figure 64. Search for Seed Locations as Starting Points of Potential Indent Locations

In practice, a recursive flood fill algorithm will fail without proper memory management techniques. When working with 1-10 million data points or more, the stack on the processor will overflow. There are a couple ways to resolve this issue. The easiest method is to store the seed point locations on a stack or queue in memory to avoid recursion all together. The second method is to complete out each seed point if possible before recursively processing the next seed. This would be considered a breadth first search as opposed to a depth first search shown in the previous algorithm.

The value T_{seed} needs to be low enough to prevent false positive indent detection and high enough to capture all indents of varying depth. Using $T_{seed} = .5(\max[PC_r] - \min[PC_r]) + \min[PC_r]$ was found to be effective. T_{indent} needs to be high enough to capture all of the indent, but not capture the outer surface of the wire. This value is difficult to set to work universally across all wire types as there is so much different from one wire indent geometry to the next. Some wires have depressed outer surfaces from the rollers which are on the order of magnitude of some other wires indents. Because of the strong roller forces applied during manufacture,

some wire circumferences are more trilobal than circular. It is relatively easy to specify T_{indent} for a single wire type, but when some of the wires are trilobal and others are circular a constant radial threshold value does not work.

The solution to threshold all reinforcement wires with the same parameters is to use a dynamic threshold. Figure 65 shows how the dynamic thresholding technique. For every line scan, the threshold, T_{indent}, is set as the distance from the maximum radius of the line scan R_{max}.

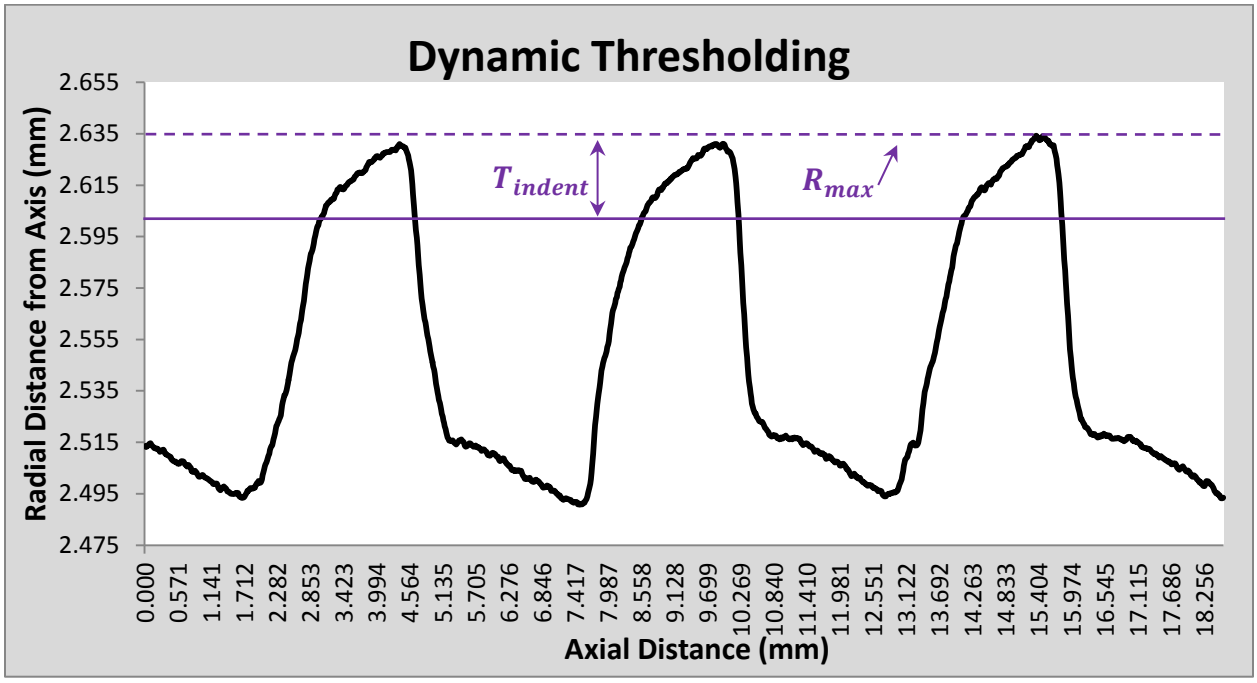

Figure 65. Dynamic Thresholding

Figure 66 shows the results of the dynamic threshold on an actual wire sample. The left image shows the use of dynamic thresholding, and the right image uses a fixed radius threshold on the same sample. Notice in the left image, the bright yellow region. This region is where the indent roller pressed a flat spot unto the surface of the wire.

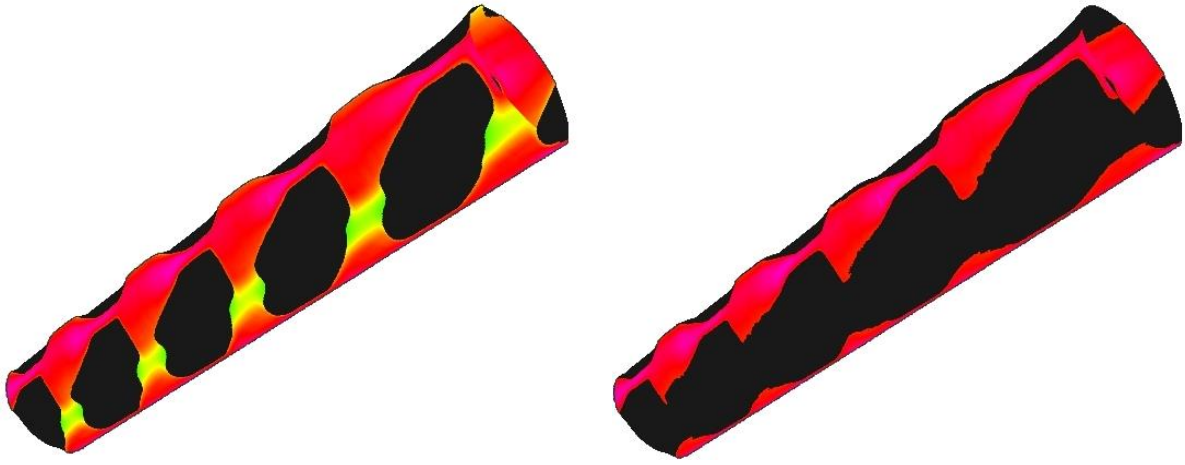

Figure 66. Dynamic Thresholding(left) verses Static Thresholding(right)

The dynamic thresholding technique was tested on all commercial reinforcement wire samples – a total of 50 point clouds. The dynamic threshold successfully isolated the indents for all 50 point clouds.

4.2.7 Verify Indent Regions

The reinforcement wires in the study have the potential to have surface marring, gouging, or depression. These regions appear in the segmentation algorithms as indents and must be isolated from the actual indent geometries to be verified by the measurement system. Small clusters of only a few data points around the indent boundary may appear as their own indent as the indent boundaries are not crisply defined for all wire types.

Figure 67 shows a typical indented wire. Indents at the ends of the scan are incomplete and are to be removed from the data set. Whole indents in the center of the scanned data set are kept and processed by the measurement algorithms.

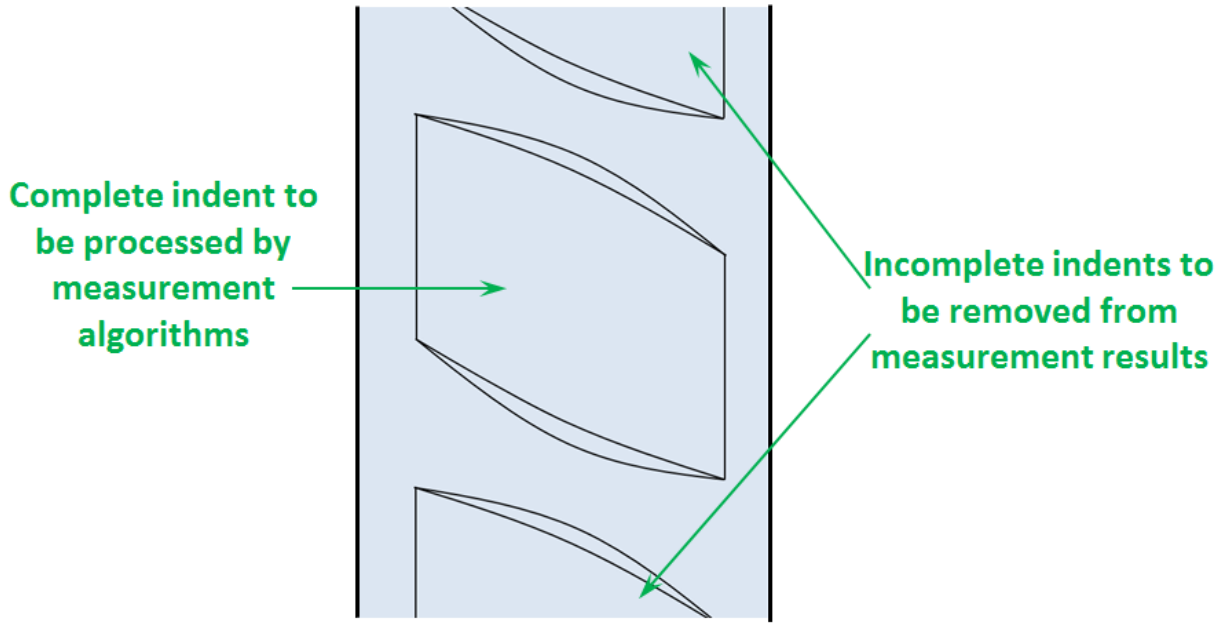

Figure 67. Removal of Incomplete Indent Regions

For each indent group $IG[n][d]: n \in [0, N), d \in [0, L * I]$. IG has the same subscripts as PC including (x, y, z, r, t, h, i). N is the last $IndentID$, and d is dynamic from 1 data point up to the size of the point cloud (unlikely). The size of the array is checked to make sure it is appropriate for an indent feature – pseudo code function notation `Size()`. Small groups of points are usually from surface marring. Large groups of indents indicate a failure with the threshold parameters and they need adjustment, this would trigger an abort in practice. $T_{minpoints}$ is the threshold for minimum number of data points in an indent region. $T_{maxpoints}$ is the threshold for maximum number of data points in an indent region.

```
Get PC
Get T_minpoints
Get T_maxpoints

//create an array of array of points to group indents
For all l in L
      For all i in I
            Push PC[l][i] on IG[PC_i[l][i]]

//Pop arrays of points too small or large to be indents
For all n in Size(IG)
      If Size(IG[n]) < T_minpoints
            Pop IG[n]
            Decrement n
      Else If Size(IG[n]) > T_maxpoints
            Pop IG[n]
            Decrement n
```

Figure 68. Removal of Incomplete and Non-Indent Regions

4.3 Measurement Algorithms

With the indents fully segmented from the raw point cloud data. Measurements of the indent geometrical features can now be made. Within the study a total of 18 geometrical features were analyzed via data processing algorithms that required some manual intervention. Manual intervention included data point selection in 3D heat maps and 2D scan line plots. With the critical geometrical features identified algorithms were developed to provide a fully automated measurement process. The following sections describe the algorithms for these automated measurements.

With the indented regions isolated, measurements can now be performed to determine the wires geometrical dimensions. For all $IG[n]: n \in [0, N)$ there is an $IG_d[n]$,$IG_{vv}[n]$, and $IG_{sa}[n]$ for the indents' depth, indents' volumetric void, and indents' projected surface area.

Table 6. Indent Geometrical Feature Variables

Variable	Geometrical Feature	Nomenclature
IG_d	Indent Depth	Depth
IG_{avgr}	Wire Average Radial	AvgVal
IG_{sa}	Indent Projected Surface Area	PSA
IG_{vv}	Indent Volumetric Void	VV
IG_{sacm}	Indent Projected Surface Area per cm	PSAcm
IG_{vvcm}	Indent Volumetric Void per cm	VVcm
IG_{al}	Indent Axial Length	axialdist
IG_{tfsa}	Indent Triangular Facet Surface Area	TFSA
IG_{rw}	Indent Radial Width	RotatDist
IG_θ	Indent Edge Wall Angle	EdgeSlope
IG_ϕ	Indent Orientation Angle	Ori
IG_L	Indent Length	EL
IG_W	Indent Width	EW

4.3.1 Indent Depth and Average Radial Value

For the indent depth, the calculation was made in comparison with the ASTM A881 standard for wire. The depth (IG_d) is measured from the outer surface of the wire to the location of maximum depth.

```
Get IG
Get T_indent
//Calculate indent maximum depth
For all n in Size(IG)
      Set Min = ∞
      For all d in Size(IG[n])
            If IG_r[n][d] < Min
                  Set Min = IG_r[n][d]
      Set IG_d[n] = T_indent − Min
```

Figure 69. Measure Indent Maximum Depth

The average radial value provides a generic quality check for the quality of the scan. The average radial value is correlated to the indent depth for a given wire type. Wires with deeper indents will have a lower overall average radial value. Wires with shallow indents have an overall greater average radial value, IG_{avg}.

```
Get PC
Set IG_avg = 0
//Calculate wire average radial value
For all l in L
      For all i in I
            Push PC[l][i] on IG[PC_i[l][i]]
            Set IG_avgr+= PC_r[l][i]
Set IG_avgr/= [L][I]
```

Figure 70. Measure Average Radial Value

4.3.2 Indent Projected Surface Area and Volumetric Void

For the indent surface area (IG_{sa}), a sum approximation is used. The data points are uniformly spaced, each data point takes up an approximate portion of the projected surface area. A constant C_{sa} is used to represent the amount of surface area from each data point. For the volumetric void (IG_{vv}), C_{sa} is multiplied by the data points depth for a sum approximation. In practice, a poly faceted surface area of the data points is highly correlated to the sum approximation shown.

```
Get IG
Get T_indent
Get C_sa
//Calculate indents surface area & volume
For all n in Size(IG)
      Set IG_sa[n] = 0
      Set IG_vv[n] = 0
      For all d in Size(IG[n])
            Set IG_sa[n]+= C_sa
            Set IG_vv[n]+= C_sa * (T_indent − IG_r[n][d])
```

Figure 71. Measure Indents Surface Area and Volume

4.3.3 Indent Projected Surface Area per cm and Volumetric Void per cm

The indent projected surface area per cm (IG_{sacm}) and volumetric void per cm (IG_{vvcm}) are very similar to their counterparts IG_{sa} and IG_{vv}. The IG_{sacm} and IG_{vvcm} can be calculated from the previously calculated values for IG_{sa} and IG_{vv}. The measure is intended to provide a metric of

the surface area and volumetric void for the length of the entire wire (L_{wire}) sample as opposed to each individual indent.

```
Get IG
Set IG_sacm = 0
Set IG_vvcm = 0

//Calculate indents surface area & volume per unit length of wire
For all n in Size(IG)
      Set IG_sacm += IG_sa[n]
      Set IG_vvcm += IG_vv[n]
Set IG_sacm /= L_wire
Set IG_vvcm /= L_wire
```

Figure 72. Measure Indents Surface Area per cm and Volumetric Void per cm

4.3.4 Indent Triangular Facet Surface Area

The indent triangular facet surface area (IG_{tfsa}) is a more precise surface area calculation that includes the effects of depth variation on the surface area measure. The projected surface area does not include the influence of depth. This solution requires calculating the surface area of a triangle defined by three vertices.

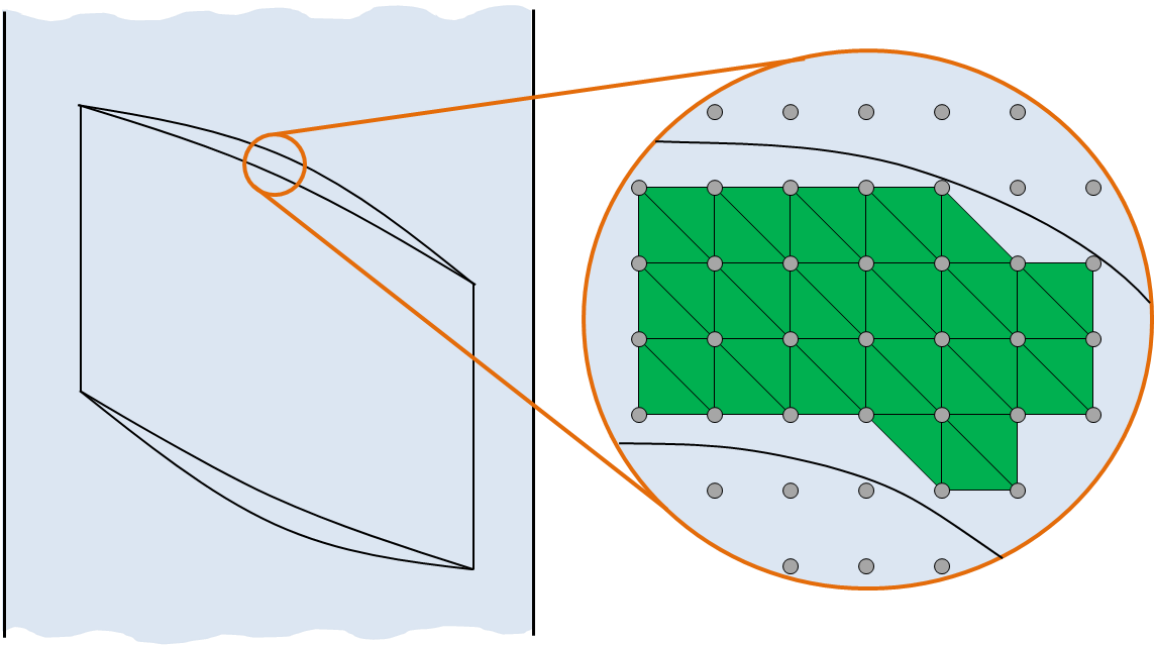

Figure 73. Indent Triangular Facet Surface Area

For a triangle with vertices v^1, v^2, and v^3 the surface area A can be expressed by the following equation.

$$A = \frac{|(v^3 - v^1) \times (v^2 - v^1)|}{2}$$

Using the vertex $PC_v = (PC_x, PC_y, PC_z)$ the surface area is calculated for every vertex in the indent by the use of the vertex neighbors

```
Get IG
Get PC
Set IG_tfsa = 0

//Calculate indents triangular facet surface area
For all l in L − 1
      For all i in I − 1
            If PC_i[l][i] > 0
                  Set IG_tfsa[n]+= |(PC_v[l][i+1]−PC_v[l][i])×(PC_v[l+1][i]−PC_v[l][i])| / 2

                  Set IG_tfsa[n]+= |(PC_v[l][i+1]−PC_v[l+1][i+1])×(PC_v[l+1][i]−PC_v[l+1][i+1])| / 2
//Compensate for the data seam in the cylindrical data set
Set l = L
For all i in I − 1
      If PC_i[l][i] > 0
            Set IG_tfsa[n]+= |(PC_v[l][i+1]−PC_v[l][i])×(PC_v[0][i]−PC_v[l][i])| / 2

            Set IG_tfsa[n]+= |(PC_v[l][i+1]−PC_v[0][i+1])×(PC_v[0][i]−PC_v[0][i+1])| / 2
```

Figure 74. Measure Indent Triangular Facet Surface Area

4.3.5 Indent Axial Length and Indent Radial Width

The indent axial length (IG_{al}) and indent radial width (IG_{sw}) define the length and width of the indented relative to the cylindrical coordinate frame of the wire. IG_{al} defines the length of the indent along the datum axis of the wire. IG_{sw} defines the angular width rotating about the datum axis. Let the variables $L_{max}[n], L_{min}[n], W_{max}[n], W_{min}[n]$ be used to define the extreme points of the indent.

```
Get IG
Set L_max, W_max = −∞
Set L_min, W_min = ∞
//Calculate indents axial length and radial width
For all n in Size(IG)
    For all d in Size(IG[n])
        If IG_h[n][d] > L_max[n]
            Set L_max[n] = IG_h[n][d]
        If IG_h[n][d] < L_min[n]
            Set L_min[n] = IG_h[n][d]
        If IG_t[n][d] > W_max[n]
            Set W_max[n] = IG_t[n][d]
        If IG_t[n][d] < W_min[n]
            Set W_min[n] = IG_t[n][d]
    Set IG_al[n] = L_max − L_min
    Set IG_sw[n] = W_max − W_min
```

Figure 75. Measure Indent Axial Length and Radial Width

4.3.6 Indent Edge Wall Angle

The indent edge wall angle(IG_θ) is the measure of the indent edge wall angle relative to the datum axis of the reinforcement wire. Each indent has two edge walls for the side of the indent facing forward during manufacture, $IG_{\theta f}$, and the side of the indent facing backward during manufacture, $IG_{\theta b}$. When forward or backward edge wall is irrelevant, IG_θ is used to represent the indent edge wall angle.

Figure 76 shows the profile of the indent along the axis of the wire. The measurement of the edge wall angle requires segmenting the edge wall from the indent basin. This is done by dividing the indent into the three sections: indent forward edge wall, indent basin, and indent backward edge wall. The division lines between the three section are determined during the minimal zone calculation. Each section has its own zone size Z_1, Z_2, and Z_3. The depth of the indent is found for the scan line, D_{line}. This is the distance from the bottom of zone Z_2 to the indent threshold T_{indent}.

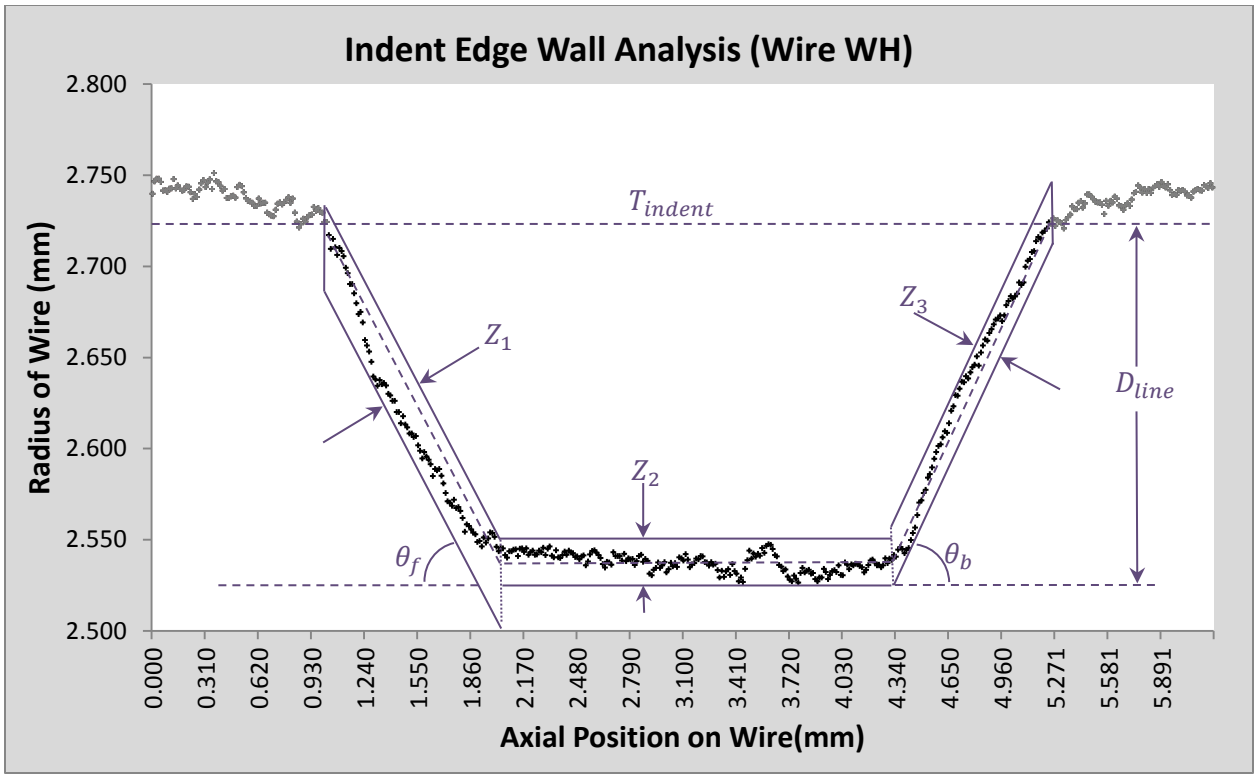

Figure 76. Indent Edge Wall Angle

The minimal zone for the indent profile can be expressed by three combined straightness zone problems. I_1 and I_2 are the cutoff locations separating Z_1, Z_2, and Z_3. The value for I_1 and I_2 are dynamic and determined by the values θ_f, θ_b, and D_{line} . The objective is the minimization of the sum of the three zones. The decision variables are θ_f, θ_b, and D_{line}.

$$Minimize\ d = (Z_{1H} - Z_{1L}) + (Z_{2H} - Z_{2L}) + (Z_{3H} - Z_{3L})$$

$$Subject\ to\ \forall_{i=0}^{I_1} LP_{hi} \sin(\theta_f) + LP_{ri} \cos(\theta_f) \geq Z_{1L}$$

$$\forall_{i=0}^{I_1} LP_{hi} \sin(\theta_f) + LP_{ri} \cos(\theta_f) \leq Z_{1H}$$

$$\forall_{i=I_1+1}^{I_2} LP_{ri} \geq Z_{2L}$$

$$\forall_{i=I_1+1}^{I_2} LP_{ri} \leq Z_{2H}$$

$$\forall_{i=I_2+1}^{I_3} LP_{hi} \sin(\theta_b) + LP_{ri} \cos(\theta_b) \geq Z_{3L}$$

$$\forall_{i=I_2+1}^{I_3} LP_{hi} \sin(\theta_b) + LP_{ri} \cos(\theta_b) \leq Z_{3H}$$

The algorithmic workflow to determine the indent slop is presented in Figure 77 and Figure 78. The algorithm starts with getting the isolated indent region IG. The indent region is then separated into scan line segments. Each scan line is then given an initial starting condition for the location of the forward indent edge wall, indent basin, and backward indent edge wall. For all scan lines an iterative minimum zone calculation is performed to determine the correct location of the forward indent edge wall, indent basin, and backward indent edge wall. Once the iterative search is complete the indent edge wall angle is defined by the angle between the indent basin and the forward and backward edge wall zones.

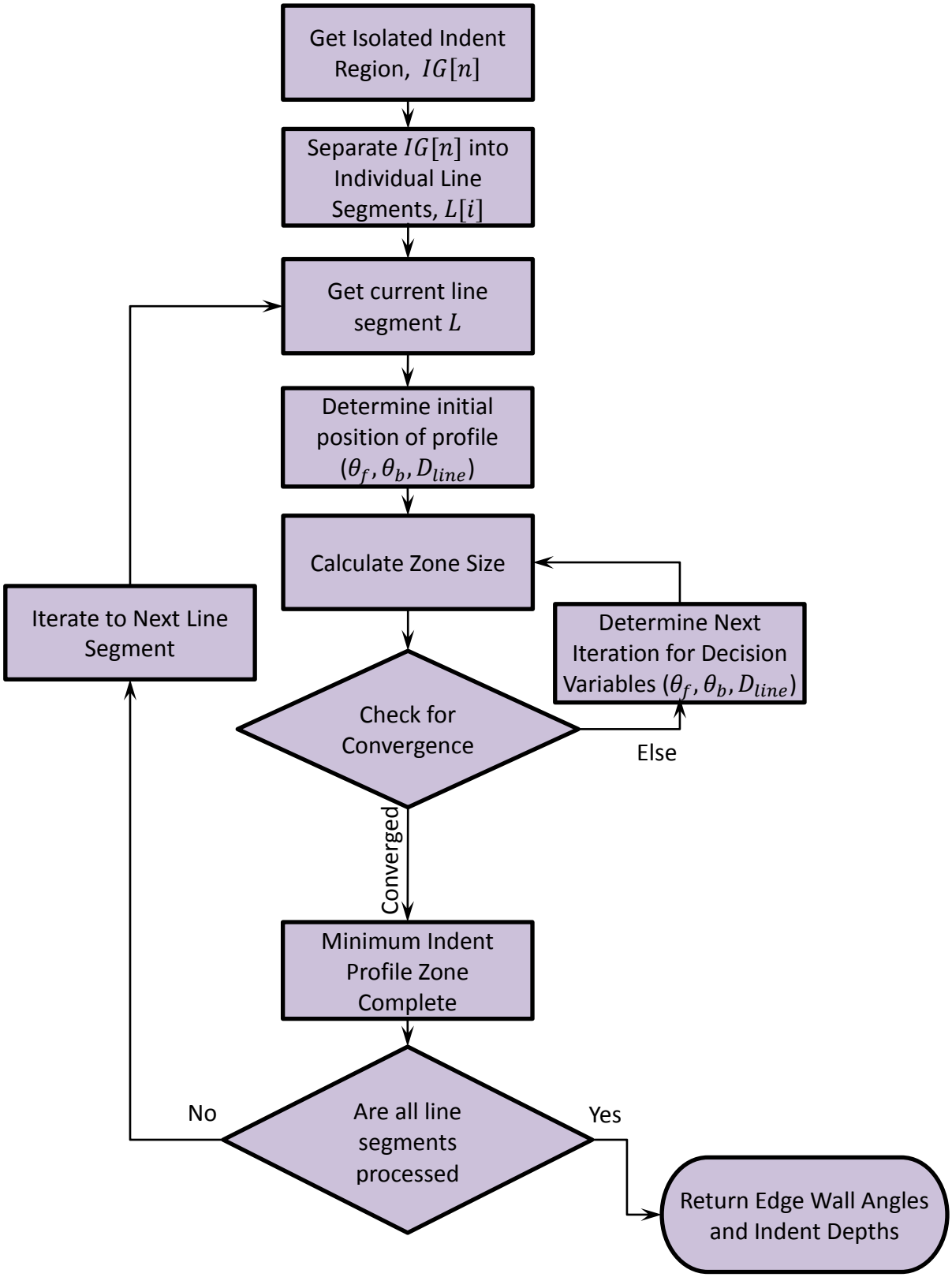

Figure 77. Indent Edge Slope Workflow

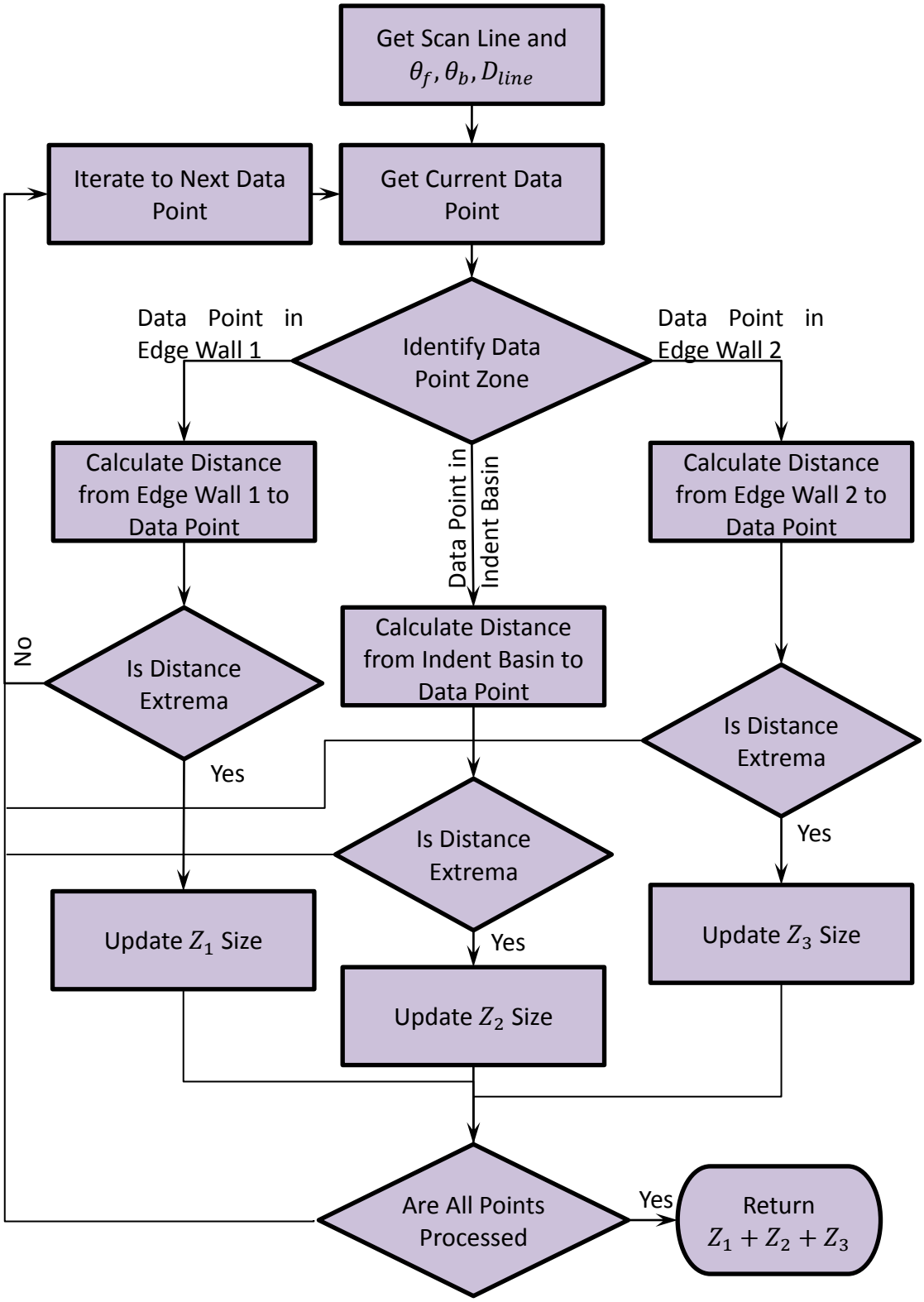

Figure 78. Calculate Zone Size Workflow

The determination of the edge wall angle can be presented by the sections of pseudo code. The first section shown below segments the indent region in an array of line segments $LP[p]_h : p \in [0, P)$. For each line segment, the slope is then calculated.

```
Get PC
//Get array representing points in scan line
For all l in L
      For all i in I
            If PC_i[l][i] > 0
            Set Current_i = PC_i[l][i]
            Clear LP
            While PC_i[l][i] = Current_i
                  Push PC[l][i] on LP
                  If i < I
                        Increment i
                  Else
                        Break
            CalculateSlope(LP)
```

Figure 79. Get Axial Line of Indent Points

The next section uses the previously defined indent profile zone minimization to determine optimized values for θ_f, θ_b, and D_{line}.

```
//Determine the minimum profile zone and edge wall angles
Function CalculateSlope (LP)
      Minimize IndentProfileZone Using θ_f, θ_b, D_line
```

Figure 80. Determine Minimal Profile Zone for Axial Line of Indent Points

The pseudo code for the indent profile zone determine which zone Z_1, Z_2, or Z_3 the data point lies within. Then it calculates whether or not the given data point is an extrema and resizes the zone accordingly.

```
//Calculate Indent Profile Zone
Function IndentProfileZone (LP, D_line, θ_f, θ_b)
      For all p in P
            //If data point on first edge wall
            If LP[p]_h < LP[0]_h + D_line / tan(θ_f)
                  If LP_h[p] sin(θ_f) + LP_r[p] cos(θ_f) < Z_1L
                        Set Z_1L = LP_h[p] sin(θ_f) + LP_r[p] cos(θ_f)
                  If LP_h[p] sin(θ_f) + LP_r[p] cos(θ_f) > Z_1H
                        Set Z_1H = LP_h[p] sin(θ_f) + LP_r[p] cos(θ_f)
            //If data point on second edge wall
            If LP[p]_h > LP[P − 1]_h − D_line / tan(θ_b)
                  If LP_h[p] sin(θ_b) + LP_r[p] cos(θ_b) < Z_3L
                        Set Z_3L = LP_h[p] sin(θ_b) + LP_r[p] cos(θ_b)
                  If LP_h[p] sin(θ_b) + LP_r[p] cos(θ_b) > Z_3H
                        Set Z_3H = LP_h[p] sin(θ_b) + LP_r[p] cos(θ_b)
            //Else data point in indent basin
            Else
                  If LP_r[p] < Z_2L
                        Set Z_2L = LP_r[p]
                  If LP_r[p] > Z_2H
                        Set Z_2H = LP_r[p]
      //Return Zone Size
      Return (Z_1H − Z_1L) + (Z_2H − Z_2L) + (Z_3H − Z_3L)
```

Figure 81. Measure Edge Wall Angle and Calculate Indent Profile Zone Size

4.3.7 Indent Orientation

The ellipsoidal zone determines the orientation of the indent, IG_ϕ. The ellipsoidal zone is calculated from the group of points that define the convex hull of the indented region. The fitted ellipse from the solution also provides the indent length IG_L and the indent width IG_W, these are determined by the length of major and minor axis of the ellipse. Figure 82 shows the measurements performed. IG_ϕ is the angle of the ellipse relative the axis of the wire. IG_L is the length of the major axis of the ellipse. IG_W is the length of the minor axis of the ellipse.

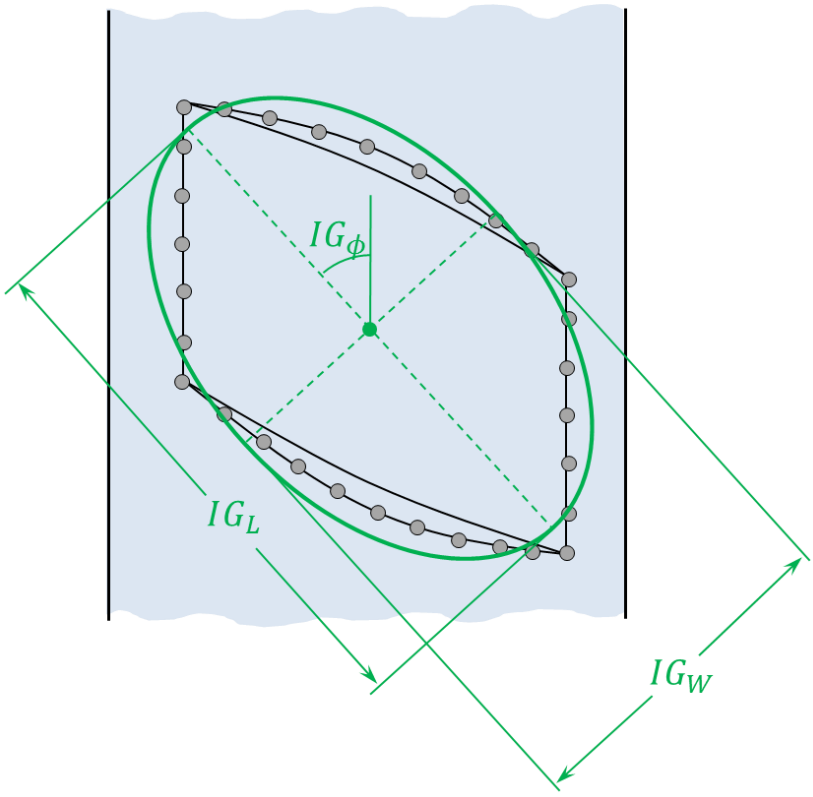

Figure 82. Indent Orientation

For all of the data points within the indent group, the only points that are significant for the fitted ellipse calculation are the data points along the border of the indent profile. The function `ConvexHull` is used to find the convex hull of the indent group IG. The ellipsoidal zone is then fitted to the convex hull vertices.

```
//determine the indent orientation
Get IG
Set IG = ConvexHull(IG)
Minimize EllipsoidalZone Using T_x, T_y, θ_z, a, b
```

Figure 83. Search for Ellipsoidal Zone with Indent Points

The pseudo code to determine the data points distance from the ellipse is shown below. The convex hull vertices are first translated and rotated to the current position. Then, every data

points distance from the ellipse is found with a root finding algorithm with decision variable θ_e. The size of the ellipse is reported as twice the maximum distance.

```
//Ellipsoidal zone size for current point cloud position
Function EllipsoidalZone (IG,a,b,T,R)
      Set IG = (IG + T)R
      Set Max = 0
      For all n in Size(IG)
            Minimize d = √((IG_t − a cos(θ_e))² + (y_i − b sin(θ_e))²) using θ_e
            If d > Max
                  Set Max = d
      Return Max*2
```

Figure 84. Measure Indent Orientation and Calculate Ellipsoidal Zone Size

4.3.8 Wire Surface Normal Vector Average

Besides measurement of the indent profile itself, other measures were used that are comprised of all data points from the scanned model. These measurements are easy to implement and were found to have strong correlations as in the case of the Laplacian transform measurements.

Measurements that use the entire scan data set do not require isolation of the indent region. Measurements that do not require indent isolation and are of the entire scan data set can be used for all wire types. This includes the spiral and dot type reinforcement wires. These algorithms ease of implementation make them great for production quality control metrics.

One such measurement is the average vector or angle of the wire surface relative to the datum axis. The pseudo code for the average vector is shown below. Each data point is associated with a triangular facet that makes up a portion of the wires surface. The normal vector for all triangular facets is calculated and then averaged together. Using the average as opposed to the sum allows for wire scans of different lengths to be compared. This could be considered an alternate measurement to indent edge wall angle that also includes any angularity effects of the indent basin. The pseudo code shows the surface normal vector average for the entire wire, this same algorithm can be applied to the isolated indent regions, IG, as well.

```
//Average wire surface normal
Get PC
Set N = 0
For all l in L-1
   For all i in I-1
      Set V1 = PC[l + 1][i] − PC[l][i]
      Set V2 = PC[l][i + 1] − PC[l][i]
      //Calculate Normal Vector
      Set N+= V1 × V2

      Set V1 = PC[l + 1][i + 1] − PC[l][i + 1]
      Set V2 = PC[l + 1][i + 1] − PC[l + 1][i]
      //Calculate Normal Vector
      Set N+= V1 × V2

//Divide sum by number of triangles
Set N /= 2(L − 1)(I − 1)
```

Figure 85. Measure Average Indent Wire Surface Normal

4.3.9 Wire Surface Roughness Average, R_a

The roughness of a surface, R_a can be described as the average error of all points from the mean line. As this data has been aligned to the datum axis, this can be calculated by the following pseudo code. The R_a is a commonly used measure in industry to describe surface roughness. Calculating the roughness across the entire wire provides a general metric to how deep and frequent the indents are on the wire. This could be considered an alternate measurement to replace indent depth.

```
//Wire surface roughness
Get PC
Set A = 0
Set R_a = 0
For all l in L
   For all i in I
      Set A+= PC_r[l][i]
//Get average radial value
Set A/= (L)(I)
//Get the average roughness
For all l in L-1
   For all i in I-1
      Set R_a+= |PC_r[l][i] − A|
Set R_a/= (L)(I)
```

Figure 86. Measure Wire Roughness, R_a

4.4 Report Results

With the indents within the point cloud sample measured, the processing algorithms are complete. The indent features are reported to the end user and the program is complete. Output formats for the report are varying and application specific. Most often a .txt file or .csv file format is used to report the individual measurement results. The average measurement and its standard deviation may also be reported along with other key statistical parameters.

4.5 Large Scale Point Cloud Visualization

With pre-existing 3D visualization software, the refresh rate of the modeling window would slow to an unusable state. While testing points clouds with 10 million data points refresh rates would drop to .3-.5 frames per second(fps). A refresh rate of 5 fps would be considered minimally acceptable for viewing 3D models for interrogation purposes. A custom 3D point cloud visualization program was created to maximize the number of data points displayed on screen while maintaining an acceptable frame rate. OpenGL was used for drawing the visualization. Figure 87 shows the developed visualization window rendering a model with 8,192,000 data points. The visualization appears as a smooth surface, but upon close examination in the visualization window each individual data point can be seen.

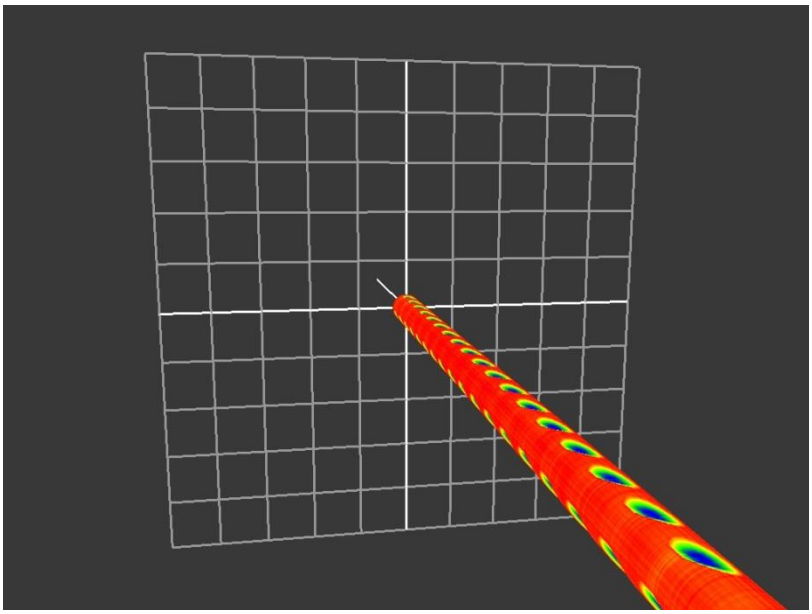

Figure 87. View of 8,192,000 Point Model in Custom Visualization Window

Figure 88 shows the algorithm workflow for rendering the 3D point cloud. The process is separated amongst Visualization Setup and Visualization Loop. Within the Visualization Setup all the necessary components of the 3D view are declared and initialized. The Visualization Loop is executed continuously, updating the window frame each time through the loop.

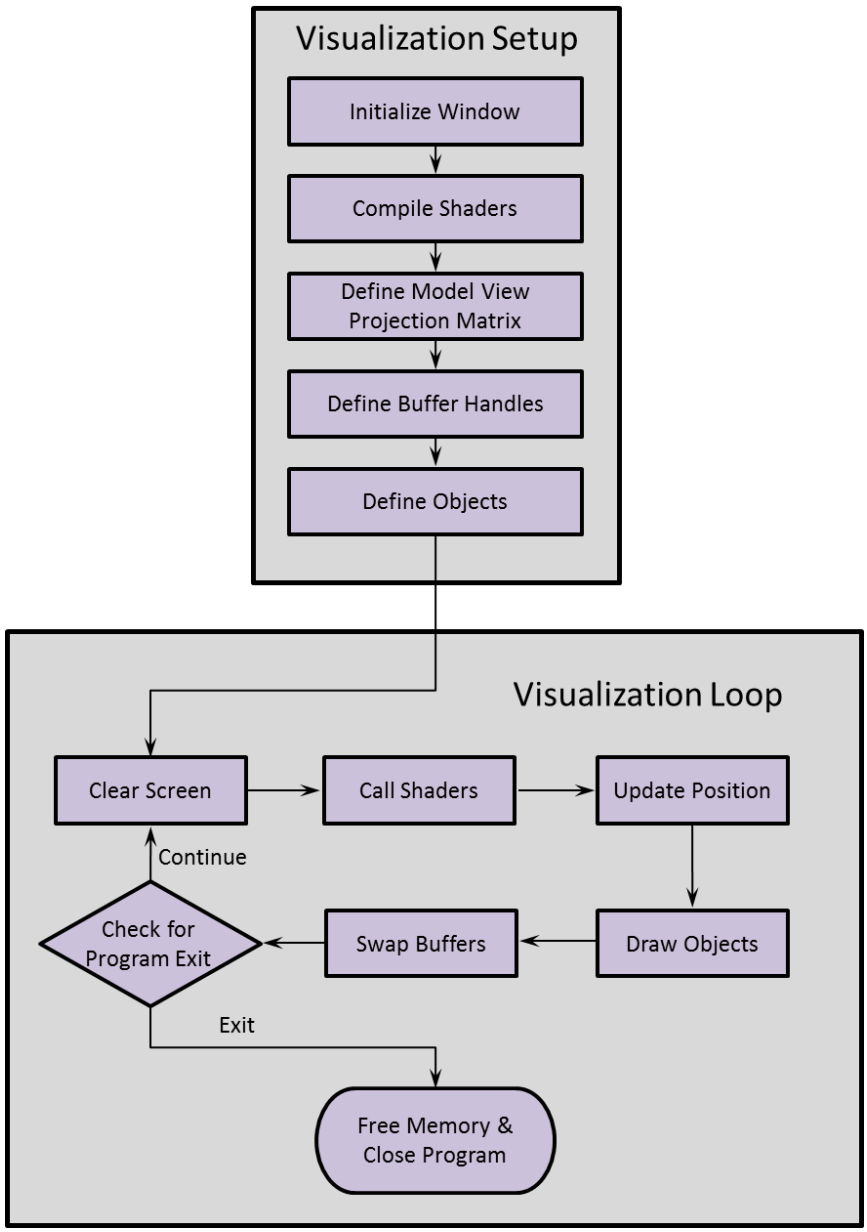

Figure 88. Point Cloud Visualization Workflow

4.5.1 Memory Efficient Graphic Shaders

Lean memory efficient shaders is what allows for rendering large point clouds that go beyond what typical 3D rending programs allow. By modeling point clouds with OpenGL point primitives as a single vertex buffer object there is a minimal amount of computational overhead. Each point in the vertex shader loop is multiplied by the Model View Project matrix to set vertex

position. The color of the data points is passed into the fragment shader to be loaded for every point.

The pseudo-code below shows the shader format. The shader contains information about the point position the MVP and the point color which is optional. The shader does not contain any additional information as any increase in shader size and complexity limits the overall number of frames per second that can be obtained.

```
//Vertex Shader
Attribute vec3 VertexPosition
Attribute vec3 VertexColor

Varying vec3 fragmentColor

//Model View Projection Matrix
uniform mat4 MVP

Function Main ()
      //Set vertex position with MVP matrix
      Set gl_Position = MVP * vec4(VertexPosition,1)
      Set fragmentColor = vertexColor
```

Figure 89. GPU Vertex Shader

```
//Fragment Shader
Varying vec3 fragmentColor
Function Main ()
      Set gl_FragColor = vec4(fragmentColor,1)
```

Figure 90.GPU Fragment Shader

4.5.2 Program Setup

The program setup is performed once prior to visualizing the point cloud and its processing time does not have a critical impact on the rendering window. Before the setup is performed the viewing window is defined with `InitializeWindow()`, this setups the graphical user

interface(GUI) and is dependent upon the GUI resources chosen. The setup process begins with compiling and attaching the shader programs to pointers in memory. The shader variables are attached to pointers as well. `DefinePointCloud()` Converts the point cloud array in memory into a vertex array object to be rendered later.

```
//Program Setup

//Get point cloud and color
Get PC_xyz
Get PC_rgb

//Get shader programs
Get MyVertexShader
Get MyFragmentShader

//Initialize Viewing Window and GUI
InitializeWindow()

Set MyProgramID = ReadCompileAttachShaders(MyVertexShader, _
                  MyFragmentShader)
Set MyMatrixID = glGetUniformLocation(MyProgramID, "MVP")

Set VertexPositionID = glGetAttribLocation(MyProgramID, _
                       "VertexPosition")
Set VertexColorID = glGetAttribLocation(MyProgramID, "VertexColor")

//Define Array Buffers
DefineReferenceGeometry(VAORefVertex, VAORefColor)
DefinePointCloud(PC_xyz, PC_rgb, VAOCloudVertex, VAOCloudColor)
```

Figure 91. Initialize Visualization Window

4.5.3 Visualization Loop

The visualization loop loads the window image for every frame. The processing time of the visualization loop is what determines the maximum amount of frames per second achievable. The pseudo-code below defines the visualization loop. The loop runs continuously while the `ProgramOpen()` function returns true. At the loop beginning the buffers are cleared, the shader programs are set, and the position updated. The point cloud object is then drawn.

```
//Visualization Loop
Get MyProgramID
Get MyMatrixID

Get VertexPositionID
Get VertexColorID

//Vertex Array Objects
Get VAORefPositionVertex
Get VAORefColorVertex
Get VAOCloudPositionVertex
Get VAOCloudColorVertex

Do
      //Clear screen, call shaders, update position
      glClear(GL_COLOR_BUFFER_BIT|GL_DEPTH_BUFFER_BIT)
      glUseProgram(MyProgramID)
      UpdatePosition(MyMatrixID)

      //Draw Axis System and Any Desired Background Objects
      DrawReferenceObjects (VertexPositionID, _
            VertexColorID, _
            VAORefPositionVertex, _
            VAORefColorVertex )

      //Draw Point Cloud
      DrawPointCloud (VertexPositionID, _
            VertexColorID, _
            VAOCloudPositionVertex, _
            VAOCloudColorVertex )

      glDisableVertexAttribArray(VertexPositionID)
      glDisableVertexAttribArray(VertexColorID)

      //Event Handling Library Call – Not OpenGL, GLFW Library
      glfwSwapBuffers()
While(ProgramOpen())
```

Figure 92. Visualization Loop

4.5.4 Visualization Results

The point cloud rendering software was compared to commercially available software and was found to perform significantly better. The commercially available software averaged about .6 frames per second while the point cloud was moving on screen. The new visualization software averaged at least 42 frames per second while the object was on screen. The new software is significantly faster than what is needed for the human eye to see a smooth continuous transition as the cloud is moved across the screen.

Table 7. Large Scale Point Cloud Visualization Results

Point Cloud Rendering Frame Rate: 8,192,000 Points		
	Commercially Available Alternative	New Visualization Program
Frame Rate (fps)	0.6	42

4.6 Mesh Generation

When working with point clouds it can be beneficial to view the data as a 3D surface or 3D model. This is done by creating a mesh from the point cloud. There are limited software resources available for working directly with point clouds in comparison to 3D models. There is no-standardized point cloud file format which greatly limits the software resources available. Converting the point cloud to a standardized 3D model format such as .stl, .stp, or .obj provides another means of interpreting the data. The .stl file format was chosen as it has a simple file structure.

Typical 3D meshes rely on representing complex surfaces by a summation of small triangular facets. By creating a point to point relationship between all neighboring points in the data set, the data can be viewed as a continuous surface. Figure 93 is a simplified illustration of how the points in the indented wire data sets were meshed together. The grey points represent the measured data points, these become the triangle vertices. The green line shows the triangular segments created from neighboring points. For every group of four points in the data set two triangles are created.

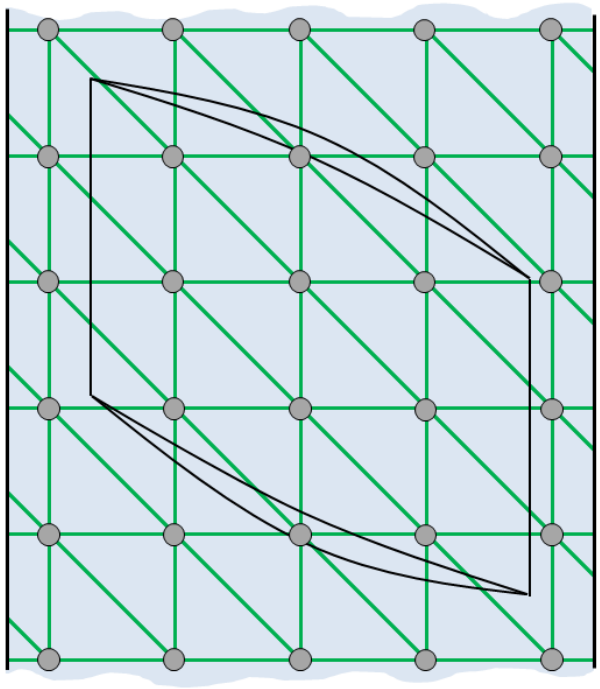

Figure 93. Triangular Facet Surface Meshing

The result of the meshing algorithm can be seen in Figure 94. This mesh was imported into and rendered on Blender v2.74. Being able to create a surface mesh from the point cloud as a .stl file allows for other software packages to be able to manipulate the data. The mesh also allows for visualizing the surface contours, something that is difficult to achieve via point clouds.

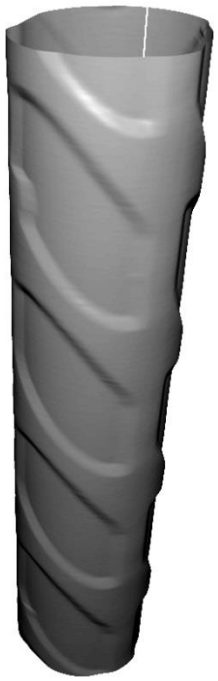

Figure 94. Resultant Mesh Rendered via Blender v2.74

By knowing the sequence the data points were collected a simple meshing algorithm is used to create a .stl file with the wire surface. Figure 95shows the pseudo code to create the .stl file. The .stl file can be in binary or ASCII format, the ASCII algorithm is shown below. The normal vector to each triangle can either be ignored or calculated using the three vertices of the triangle. As long as the right hand rule is followed the normal is redundant. The equations to calculate the normal for the triangles would be the following.

$$N_1 = \frac{(PC[l+1][i] - PC[l][i]) \times (PC[l][i+1] - PC[l][i])}{|(PC[l+1][i] - PC[l][i]) \times (PC[l][i+1] - PC[l][i])|}$$

$$N_2 = \frac{(PC[l+1][i] - PC[l][i+1]) \times (PC[l+1][i+1] - PC[l][i+1])}{|(PC[l+1][i] - PC[l][i+1]) \times (PC[l+1][i+1] - PC[l][i+1])|}$$

```
Get PC
//Mesh Points
Print “solid [Wire Name]\n”
For all l in L-1
   For all i in I-1
      //Let facet normal be defined by right hand rule
      //alternatively calculate normal N1 from the 3 vertices
      Print “          facet normal 0.0 0.0 0.0\n” //10 spaces
      Print “            outer loop\n” //12 spaces

      //print 3 vertices of first triangle
      Print “              vertex ”
      Print PC[l][i] & “\n”
      Print “              vertex ”
      Print PC[l+1][i] & “\n”
      Print “              vertex ”
      Print PC[l][i+1] & “\n”

      Print “            endloop\n” //12 spaces
      Print “          endfacet\n” //10 spaces

      //Let facet normal be defined by right hand rule
      //alternatively calculate normal N2 from the 3 vertices
      Print “          facet normal 0.0 0.0 0.0\n” //10 spaces
      Print “            outer loop\n” //12 spaces

      //print 3 vertices of second triangle
      Print “              vertex ”
      Print PC[l][i+1] & “\n”
      Print “              vertex ”
      Print PC[l+1][i] & “\n”
      Print “              vertex ”
      Print PC[l+1][i+1] & “\n”

      Print “            endloop\n” //12 spaces
      Print “          endfacet\n” //10 spaces

Print “        endsolid\n” // 8 spaces
```

Figure 95. Convert Mesh Point Cloud into Triangular Facet .stl File

4.7 Graphical User Interface

Figure 96 shows the graphical user interface setup to collect perform the analysis of scanned data and report the measurement results. The interface allows the user to select the input data file and the output report location. The analyze button performs the pre-processing and segmentation algorithms as well as the measurement algorithms.

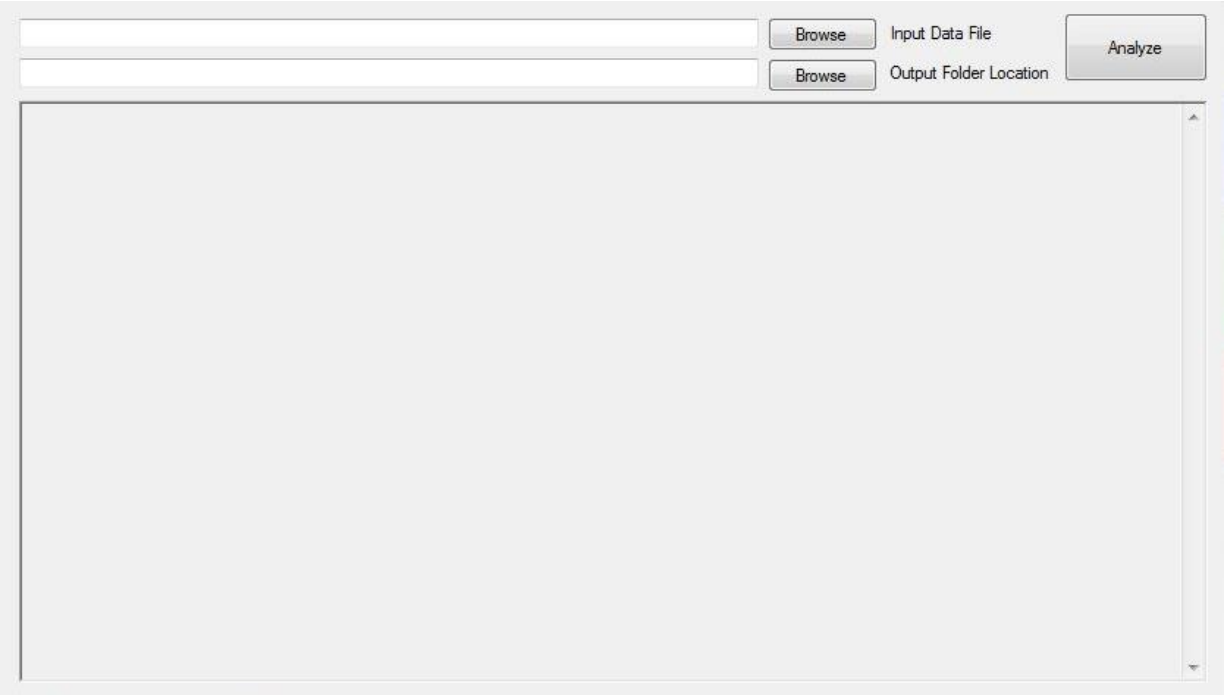

Figure 96. Point Cloud Analyzer Graphical User Interface

Chapter 5 — Indent Profiling System Hardware and Electronics

This chapter documents the hardware, electronics, and controls systems software used for the indent profiling system. Through-out this research project four indent profiling system prototypes were developed. Each prototype was used to address specific aspects of the research project objects. Each prototype developed has unique advantages and disadvantages associated with the design. The four different prototypes are documented within this section.

5.1 Introduction

Geometrical dimensioning and inspection are critical for manufacturing quality control. Coordinate Measurement Machines (CMM) are the industry standard for geometrical dimension quality control. Modern industrial CMM machines do not offer a feasible method of performing 100% inspection on produced parts due to the cost, limited data collection rates, and lack of autonomous feature recognition and measurement systems. This explorative research attempts to establish a means of providing autonomous geometrical dimensioning and inspection at a high processing rate and high scan resolution while keeping costs within practical range for industrial application.

5.2 Objectives

The list below describes the primary objectives to be achieved through the research and design of an indent profiling system.

- Acquire a sub-micron resolution point cloud of part geometries
- Develop autonomous processing algorithms to detect and measure surface geometries
- Achieve data acquisition rates practical for application in industrial production facilities
- Develop system at feasible price point for wide scale industrial application
- Use the developed prototype for the quality control and analysis for the Federal Railroad Association on real manufacturing quality control problems

5.3 Data Collection

The first aspect of the development is identifying a proper depth probe to provide the non-contact measurements. A custom development was not chosen, due to the amount of already commercial available solutions in the market. What was chosen is an industrial grade laser displacement sensor. Laser displacement sensors use relatively simple optics and imaging tools to triangulate the position of a laser spot, making for a robust sensor with very high accuracy. The sensor chosen for this research has a resolution of ± 25 microns. This sensor is capable of taking surface measurements at 392 kHz. However, in order to collect surface data at this rate precision motion control solutions needed to be developed.

In order for the indent geometrical feature measurements to be performed, a high detail surface profile must be obtained. Shown in Figure 97 the system uses a single laser displacement sensor to take depth measurements. A rotary table with a 6 jaw chuck fixates the wire sample and provides controlled angular displacement. A linear traverse is used to provide controlled displacement along the axis of the wire sample. The setup requires few components and provides surface profile measurements resolvable to within a micron. All four 3D scanning prototypes developed at rely on this concept to collect high resolution surface profiles.

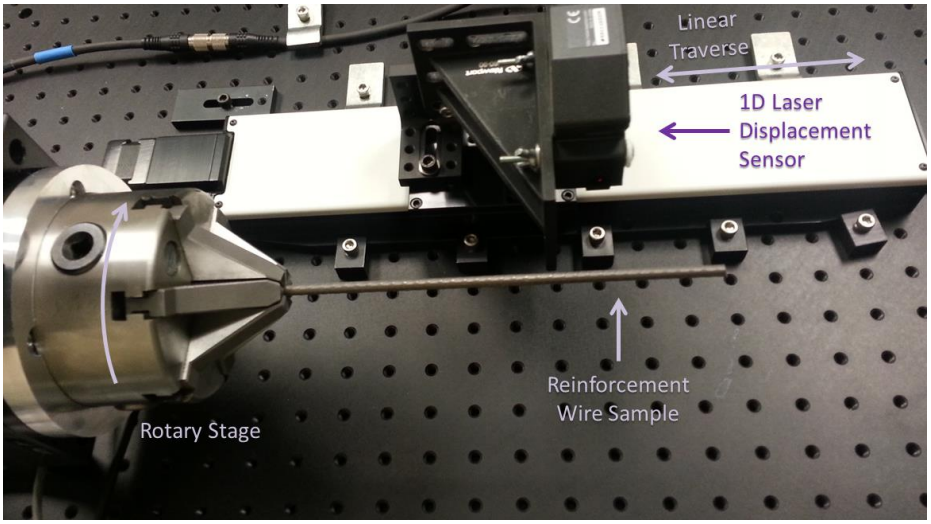

Figure 97. Reinforcement Wire Scanning System

5.4 Prototype 1: Indent Profiling Proof of Concept

For validating the initial prototyping concept, precision motion control hardware that was readily available at the university was used. Figure 5 shows the first prototype developed. A Programmable Logic Controller (PLC) was used to control the laser displacement sensor and the motion control. Due to limitations in the PLC's ability to communicate with the laser displacement sensor and the slow speeds of the traversing hardware a second prototype was developed.

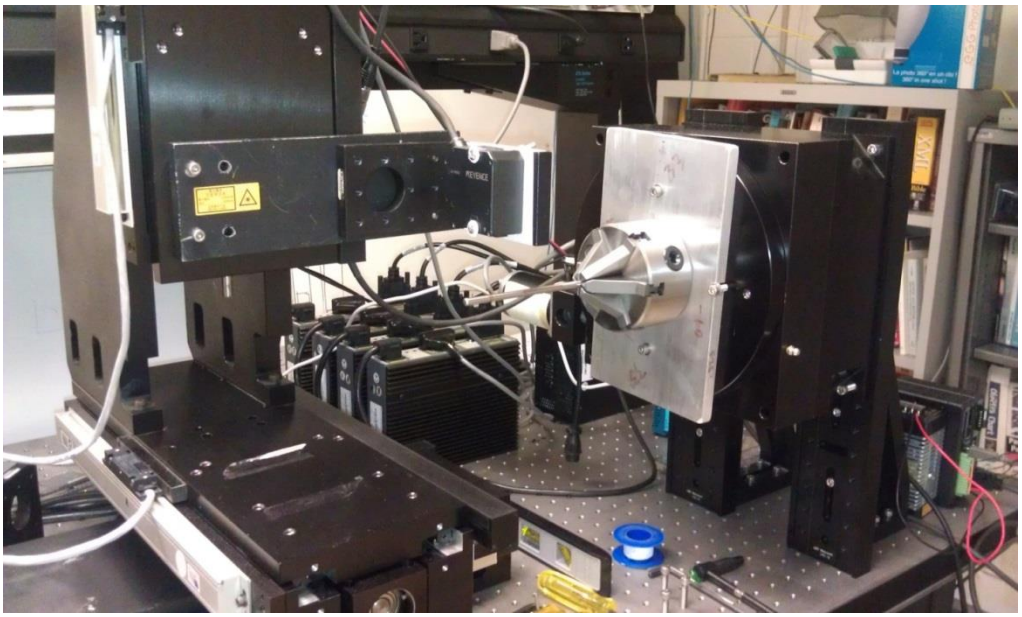

Figure 98. First Indent Profiling System (Proof of Concept)

5.5 Prototype 2: Indent Profiling with Cost Effective Components

The second prototype developed involves a custom motion control circuit using an 8-bit microcontroller for communication with the laser displacement sensor and the motor drivers. This allows for a more integrated system design, which can run at faster speeds and has greatly flexibility on how the data collection process occurs. After reviewing the capabilities of the first prototype, it was found that the prototype had excessively high tolerances and over sampling of data. The second prototype developed, uses a lower cost linear and rotary traversing system, and

maintains sufficient accuracy scans for resolving indent patterns. Figure 99 shows the second prototype arrangement.

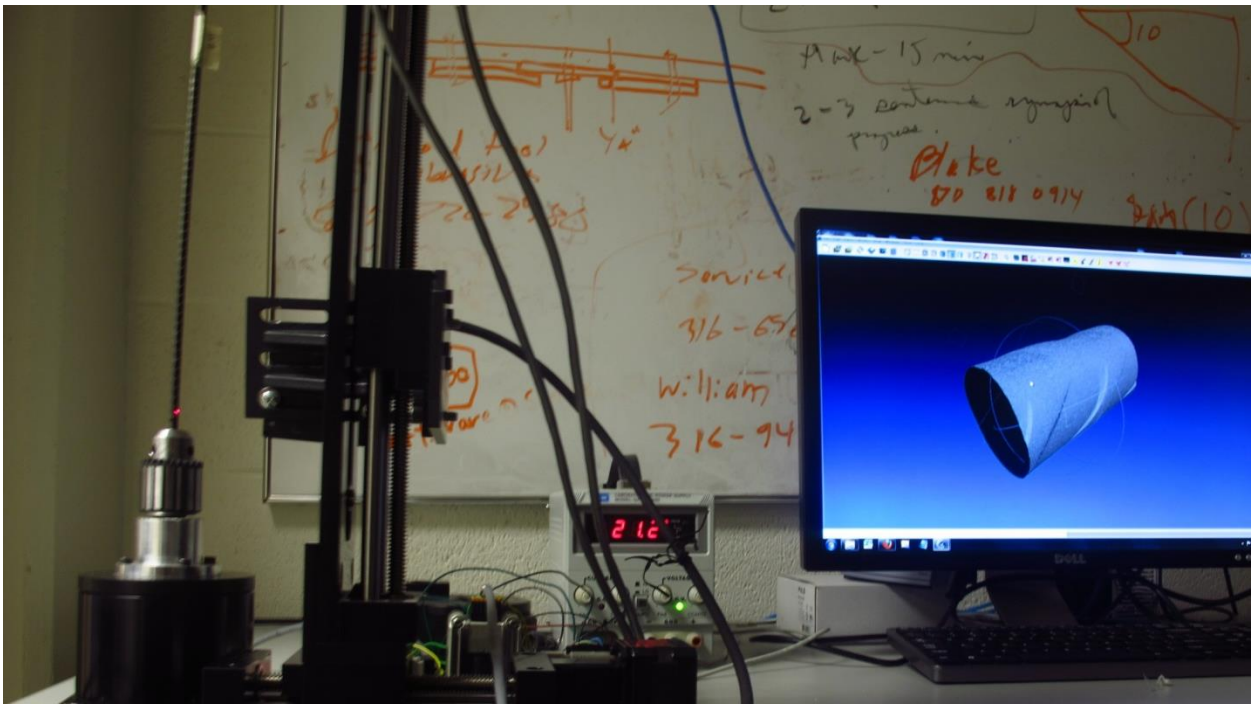

Figure 99. Second Indent Profiling System (Minimal Cost and Practical Sampling Rates)

5.5.1 Motion Control Hardware

The motion control hardware consists of a mixture of industry available components and custom built components. The industrial components used simplified the development process and dramatically decreased time of development. Below is a list of all the key components in the design of the second prototype.

- 3 axis linear traverse
- Rotary table
- Bipolar Stepper Motors
- Stepper Motor Drivers
- Laser Displacement Sensor
- Laser Displacement Sensor Controller

- Desktop Computer
- ATMega2560 8-bit Microcontroller Unit
- Max232 Integrated Chip
- Desktop PC

The microcontroller unit is used to cross communicate between the multiple components and control the timing and synchronization of the laser displacement sensor and the motors. The communication flow for the system is shown in Figure 100.

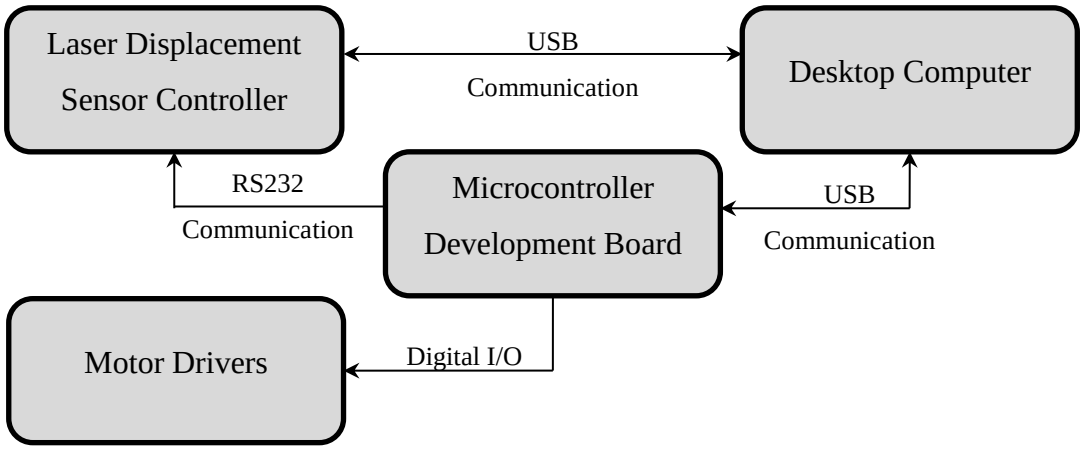

Figure 100. Prototype 2 Communication Network

The data collection process begins with the user selecting the type of scanning process they want to run on the computer and begin the scan. The computer transmits the users input to the microcontroller unit over serial USB at a baud of 115,200Hz. The microcontroller deciphers the motion commands and begins sending commands to the stepper motor drivers to accelerate them to the user's predefined speed. Once the steppers motors have reached a constant velocity, the microcontroller sends a command to the laser displacement sensor to begin data collection. When the laser displacement sensor controller reaches the on board storage limit, then the microcontroller brings the stepper motors to a temporary halt. Next the laser displacement sensor exports the collected data to the desktop computer. When the on board storage empties, the microcontroller starts the motors and the scanning process continues. When the desktop

computer receives the data from the laser displacement sensors controller, it can begin processing the data and initiate the feature identification and extraction software.

5.5.2 Motion Control Software for Scanning Patterns

The software for the ATMega2560 microcontroller was written as a procedural program in C. The microcontroller is critical for achieving the real time programming need for the motors and laser displacement sensor. The stepper motor drivers require two signals per motor, the first is for direction, the second is for when the motor increments position. A timer interrupt routine (TIR) clocked at 100 microseconds is used for generating the pulses needed to drive the stepper motor. In addition the timer interrupt executes any commands necessary for the RS232 connection to the laser displacement sensor. In between execution of the timer interrupts, the microcontroller unit processes movement commands that it receives from the desktop computer in a G-code style format which is typical for computer numerical control CNC based systems. The microcontroller determines the acceleration rate and velocity of the system and all sequences of necessary movement commands from this G-code formatted data from the desktop computer. The G-code formatted data allows for easy modifications of the scanning process by the user. This design allows for more accurate timing of the overall system and is significantly cheaper than the first prototypes PLC type motion control solution.

5.6 Prototype 3: Indent Profiling at Fastest Possible Sampling Rates

The third prototype differed greatly from the previous two designs. The sampling rates of the second prototype were fast enough for practical application and use. However, the overall amount of data collected was still limited by the sampling of the machine. This third prototype was designed to address the following question: what is the fastest possible data collection speed possible for profiling the indents of 5.32mm pre-stressing steel? The result was a data collection rate of 10 million data points in 4 minutes and 50 seconds – a data collection rate of 34,480 Hz. Mechanical limitations prevented the system from performing at faster rates. Additionally vibrations in the rotary table were found to deteriorate the measurement quality. The measurement data while usable for quality control was non ideal for collecting measurements for research and analysis. With proper rated mechanical components that are in excess of this

research budget, this prototype would be a valid solution for high speed data collection for production quality control.

5.6.1 Limitations of Prototypes 1 and 2

The first system prototype developed was to prove the feasibility and concept of developing a low cost profiling system while maintaining high data resolution. The first system was built using an industrial programmable logic controller (PLC) and using a single point laser displacement sensor to provide the sub-micron resolution measurements. The first system was able to successfully generate 3 Dimensional point clouds of the scanned surface at a fraction of the cost of commercially available CMM equipment. The first prototype had a data acquisition rate of 100 data points per second which while feasible was too slow for the data collection desired within this research. The proof of concept relied heavily on already owned components that were available at the research lab to keep a cost to a minimum. The second prototype would present practical data collection rates and using components that are affordable for wide scale industrial use.

The second prototype developed replaced the expensive PLC with an ATMega168 eight bit microcontroller. With design improvements the new prototype was able to achieve 1000 data points per second. Issues with the commercial laser displacement sensor controller limited the overall number of data points that could be collected as well as created timing issues.

The third prototype utilizes an AM335x 1GHz ARM Cortex-A8 processor running a linux OS along with a custom developed analog to digital converter to acquire data from the laser displacement sensor. With this design, data collection speeds have been achieved at 28,000 samples per second during operation and the maximum possible collection rate has been computed to be 200,000 samples per second. The low cost ARM processor enables the developed system to sustain complete synchronization between the laser displacement sensor data acquisition and positioning of the 3 axis traverse system.

5.6.2 Design Overview

The third prototype development and design can be segregated into the following three sections, mechanical hardware design, electrical circuit design, and software design. For each aspect of the design process analyses were made to determine whether the needed component should be custom design or that commercially available components are available that meet the objective requirements.

5.6.3 Hardware Design

The hardware design needed to achieve the following:

- Securely locate the part to be scanned by the profiling system
- Locate and control the position of the laser displacement sensor relative to the part
- Provide a smooth scanning path that allows for the entire part to be scanned continuously

The hardware chosen was specific to the needs of the parts scanned during the research. Two linear traverses and one rotary table were used to locate and control the motion of the part relative to the laser displacement sensor. The application of this research is the surface profiling of pre-stressing steel reinforcement wires used in concrete members. The wires in question are hardened steel with a diameter of 5.32mm. The surface of the reinforcement wire is covered in indentations which geometrical features are critical for the reinforcement steels performance in concrete members. In Fig. 1 the hardware layout is shown. The part in yellow is the 5.32 mm diameter wire to be scanned by the profiling system. The linear traverse and rotary table are shown in blue and the laser displacement sensor in green. During data collection the vertical linear traverse and rotary table are moved synchronously to achieve a helical scan path allowing the laser displacement sensor to cover the entire surface of the part.

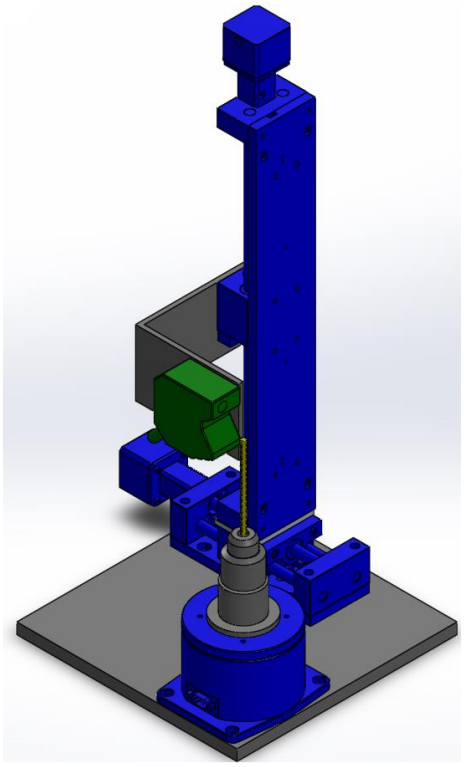

Figure 101. Hardware design

Figure 102 shows the layout of the third indent profiling system prototype. A significant amount of custom circuitry and software were required in order to achieve high speed synchronization of the data collection and the motion control system. In the image the system power supply is shown to the right. The three green control boxes in the middle are for stepper motor drivers. To the left of that is the microcomputer development board (which controls all data collection and movement commands). Towards the bottom is the wiring for the custom ADC circuit and control buttons. At the edge of the image on the left is the reinforcement wire sample mounted to the rotary table.

Figure 102. Third Indent Profiling System (Fastest Data Collection Rates)

5.6.4 Circuit Design

The mechanical hardware for the non-contact profiling system is application specific. However, the circuit design and software is universally applicable for any given part geometry and size. The circuit design needed to achieve the following:

- Support high speed analog to digital conversion (ADC) of at least 16 bit resolution.
- Synchronize ADC control with control of traverse motor positions
- Output the data to a personal computer for analysis

Figure 103 shows the functional block diagram for the circuit design. The scanning process is initiated by a user at the desktop interface. The desktop computer communicates to the AM335x processer via an Ethernet connection. The AM335x begins the scanning process by sending the scanning instructions to the Programmable Real-time Unit Sub-System (PRUSS). The PRUSS consists of two 32 bit microcontroller coprocessors dedicated to real time applications. The PRUSS then communicates with the AD997A ADC converter via Serial Peripheral Interface (SPI) while simultaneously sending step and direction signals to the stepper motor drivers synchronizing the rotary table and linear traverse to the ADC conversion. A buffer is used to

pass the retrieved ADC data from the PRUSS to AM335x processor which can either store the information in a USB storage device or send via Ethernet to the desktop computer.

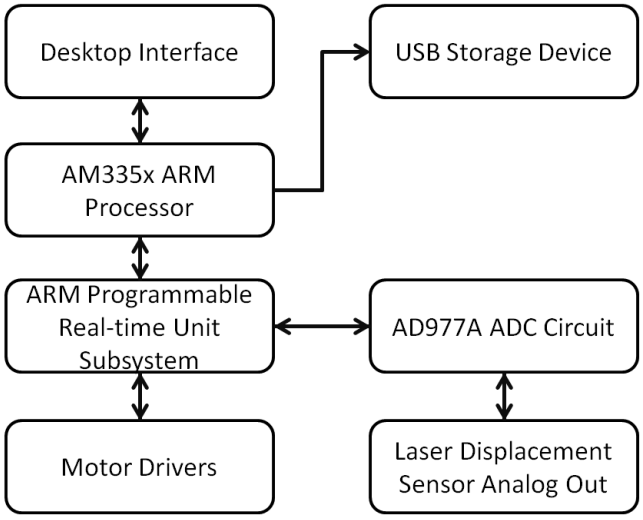

Figure 103. Function block diagram

Prior to this design, prototypes had limited buffer spaces limiting the amount of data that could be collected within a single scan. Due to the high resolution and spatially dense point clouds generated by the profiling process, the data requirements are relatively large compared the performance capabilities of modern industrial laser displacement controllers. By developing a custom ADC circuit, limited buffer space problems are mitigated. In addition the custom ADC allows for a high speed synchronization of the laser sampling with the motion control system, this is also not achievable with modern single point laser displacement sensor controllers.

Figure 104 shows the circuit used with the AD977A. The circuit utilizes the AD8031 – a high speed op amp – to configure the AD977A for bipolar operation between ± 10 volts. This voltage range is a standard for industrial analog output which is used on the output of the laser displacement sensor utilized within this development. The data clock and R/C (read/convert) pins are driven by the PRUSS. Data received by PRUSS is stored in a temporary buffer until it is retrieved by the AM335x processor.

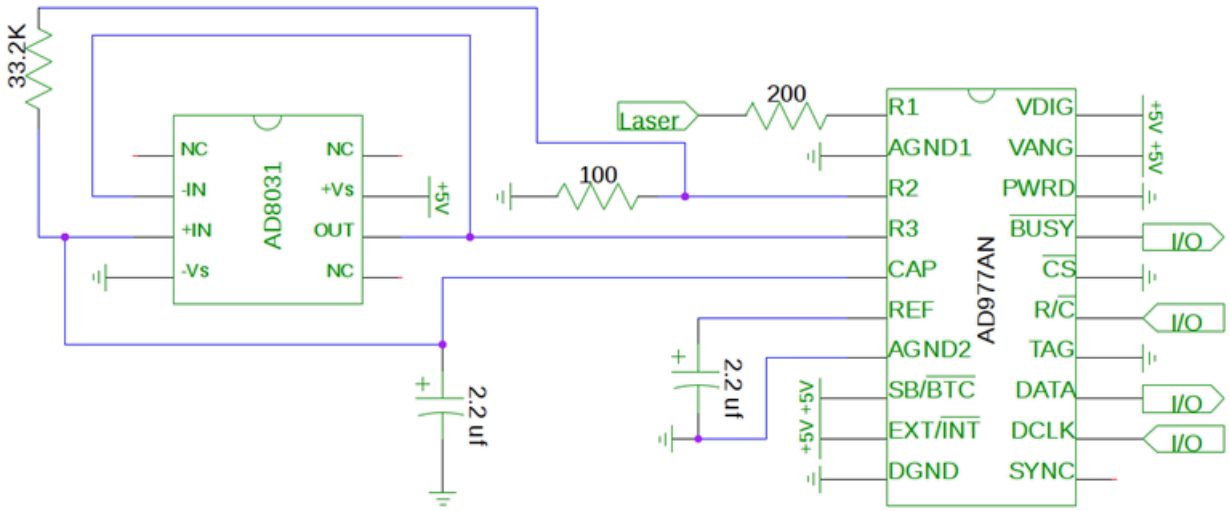

Figure 104. ADC circuit diagram

Figure 105 shows the circuit board designed and created by Levi DeLissa. The circuit board follows the schematic from Figure 104. The coaxial analog plug SMA was located away from the digital circuitry to minimize electrical noise. Circuit board designed to mount directly to a microcomputer development board.

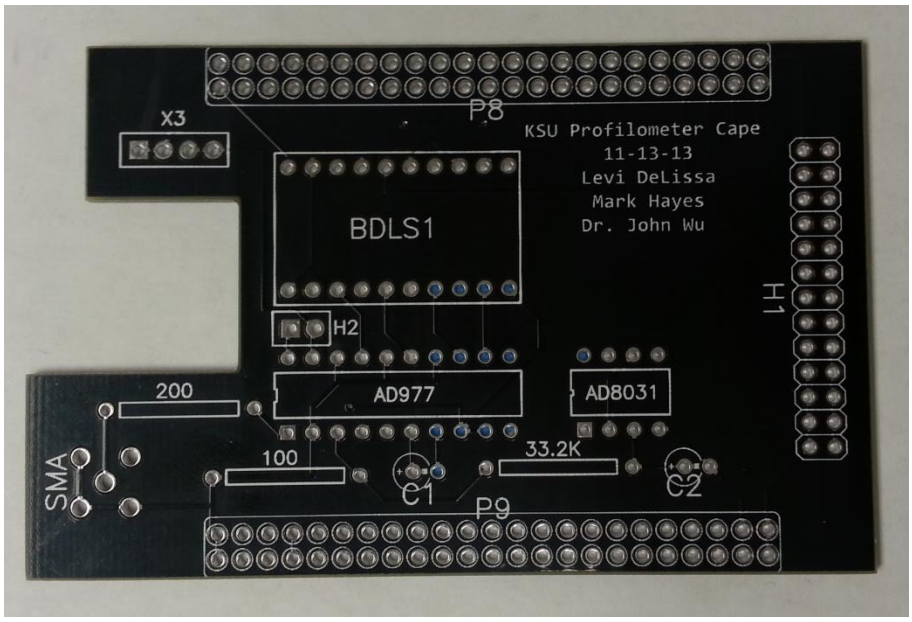

Figure 105. KSU Profilometer Circuit Board

Figure 106 shows the electronic control box created for prototype 3. Housing was used to protect wiring and provide a means of transport. Motor drivers powered via relay after microcomputer boot is stabilized and scanning code is executed. A medical grade DC power supply with low noise characteristics was used to power AD977 and microcomputer. This was done to fully minimize the amount of noise possible from the analog to digital conversion.

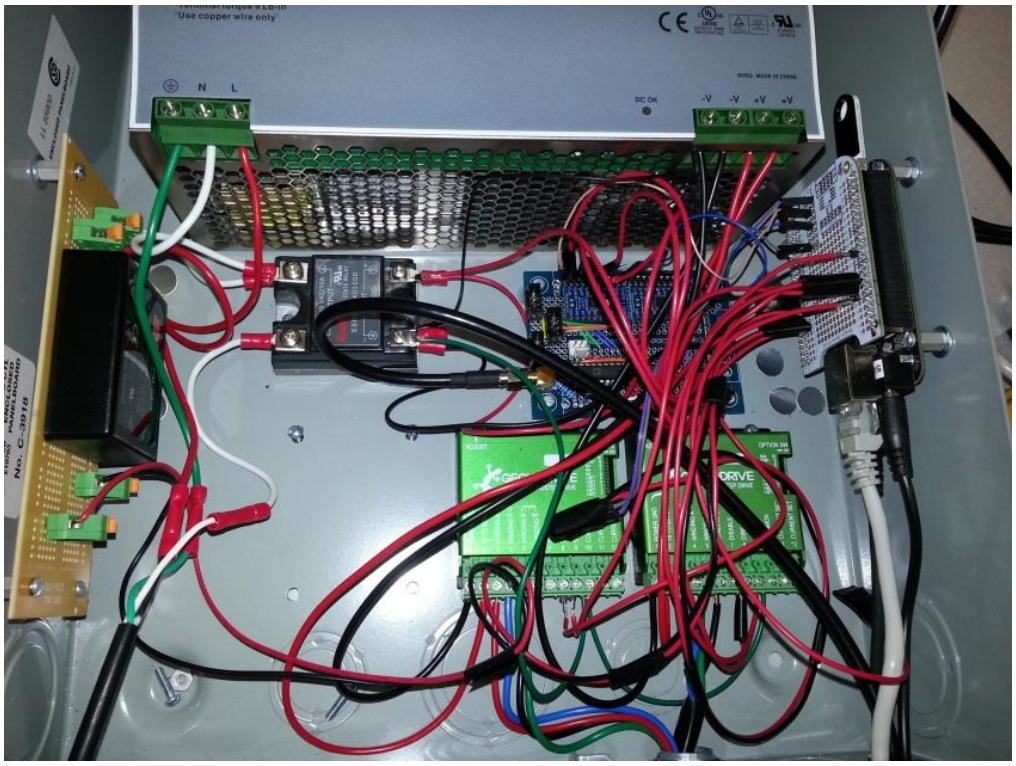

Figure 106. Prototype 3 Electronic Control Box

5.6.5 Software Design

The designed software can be separated into the following three categories.

- PRUSS assembly for data acquisition and motion control
- AM335x C code for data transfer and interfacing the desktop computer
- Desktop C/C++ code for processing collected data and performing autonomous geometrical feature measurements

The PRUSS assembly instruction set is specifically tailored for developing real time systems where precise timing is critical. The assembly code developed for the PRUSS assembly code is written to receive instruction sets via a buffer from the AM335x processor. Upon receiving instructions for a scan the assembler code generates the necessary step and direction signals for the stepper motors while processing the SPI for the ADC. The assembly code stores ADC data in a buffer to be retrieved by the AM335x processor.

The AM335x C code provides a means of communication and data storage in-between the desktop computer and the PRUSS. Data pulled from the PRUSS buffer is stored on a flash memory device until it is unloaded to the desktop computer. The AM335x software additionally receives and processes all commands from the user and desktop computer.

The last and most intricate of the software development is in creating autonomous geometrical feature measuring algorithms capable of processing the data and obtaining surface profile measurements. Much of this development can be seen in greater detail in "Automated real-time search and analysis algorithms for a non-contact 3D profiling system".

Each geometrical feature to be measured requires unique processing to obtain the desired measurement. A combination of spatial correlation, non-linear search algorithms, and procedural programming methodologies leads to automated measurement extraction.

5.7 Prototype 4: Indent Profiling System Ready for Industry and Field Use

The fourth indent profiling system was developed to provide a solution that was affordable, robust, and replicable. The fourth design replaced the custom circuit designs of prototypes 2 and 3 with an industrial motion controller that is designed with the ability of accurate synchronization between data collection and system position. While the industrial motion controller does not allow precision control at the speeds of prototype 3, the use of an off the shelf available industrial controller makes the system design more robust for long term use and easier to replicate if additional indent profiling systems are desired.

This iteration of prototype design used a new mechanical traverse and rotary table. The rotary table and linear traverse in prototype 1 were two expensive for practical industrial application. The rotary table and linear traverse in prototypes 2 and 3 were not robust enough to minimize vibrations in a non-lab environment and their life expectancy was not long enough for routine use. The rotary table and linear traverse in prototype four are still cost effective yet significantly more robust. Figure 107 shows the new components that provide more stable positioning.

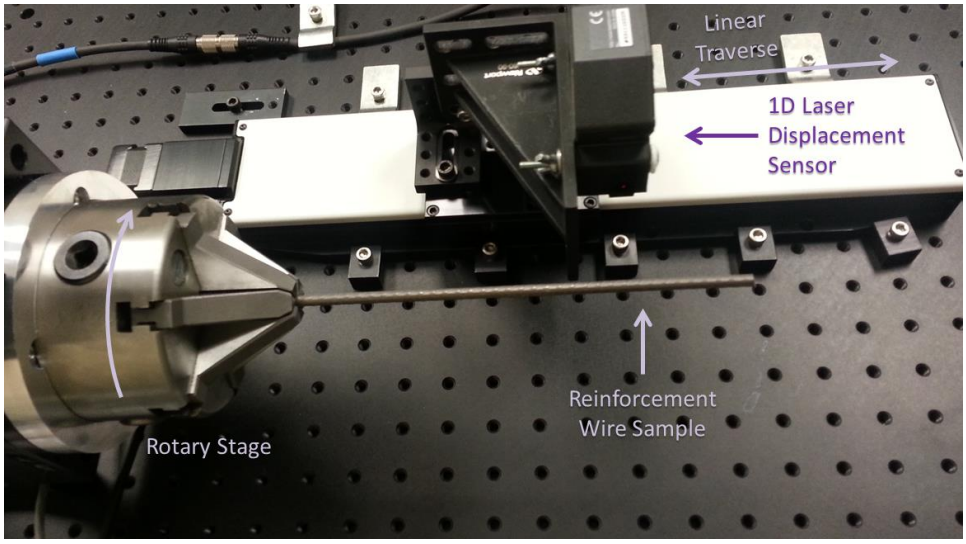

Figure 107. Fourth Indent Profiling System Components

The scan direction was changed in Prototype 4 from the scan direction used in prototypes 1 through 3. The first three prototypes scanned the wire in a spiral helical path. This allowed for smooth motion without varying acceleration and backlash. With the fourth prototype collected scan data down the axis of the reinforcement wire while the rotary table was stationary. At the end of the scan the linear traverse would return to its starting position and the rotary table would rotate to align the wire for the next scan line. These individual scan lines allowed for easy 2D plotting of the wire profile and also removed the motion of the rotary table during data collection which reduces the overall system vibrations creating cleaner surface profiles.

Figure 108 shows prototype 4 in its early development stage. The scanner was kept on a rubber mat to dampen acoustical vibrations. All electronic controls were stored on the shelving above.

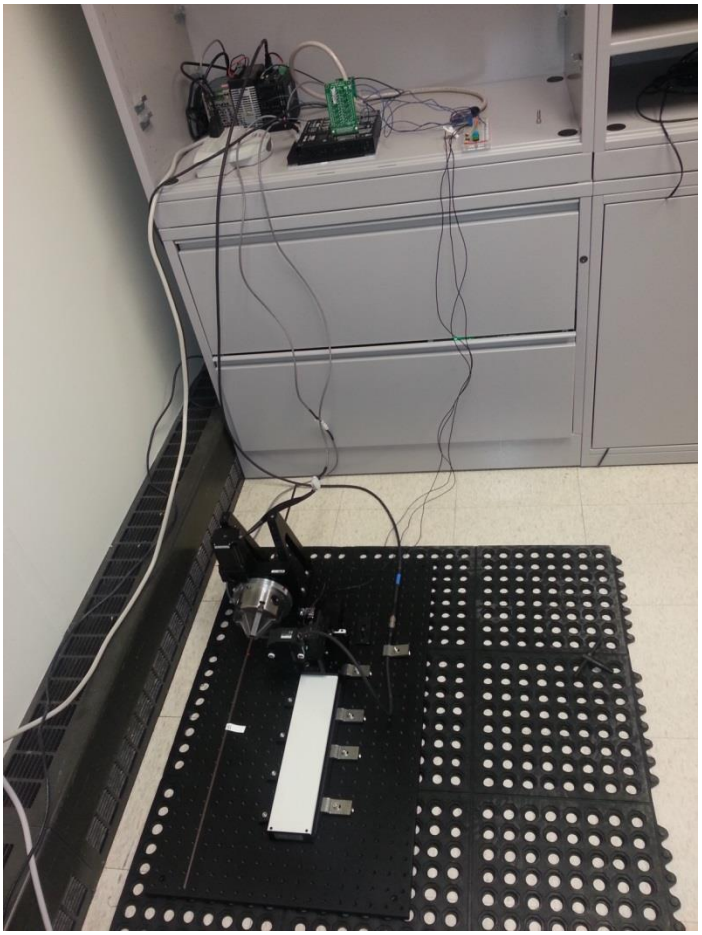

Figure 108. Prototype 4 Early Development Phase

Figure 109 shows the initial concept art for the intended design of prototype 4. The design intent was to make a standalone prototype capable of production use. Some characteristics included in the concept are: a horizontally mounted traverse for increased support, changed scan path from helical to line based scans, and a secondary free-spinning chuck for additional wire support.

Figure 109. Prototype 4 Initial Concept Art

Figure 110 shows the final prototype. All electronics are enclosed and wired within the aluminum enclosure. The linear traverse and rotary table are mounted unto a .5" aluminum breadboard. The breadboard allows for easy change and reconfiguration of components if desired. The system is connected via Ethernet to a computer (laptop in top left). The control software is an installable application developed in Visual Basic. The software controls the homing of the machine and the start and stop of the scanning process. During the scanning operation, the software actively records each scan line one segment at a time to a predesignated file.

The system was configured to scan 2048 data points per inch and 800 scan lines per revolution. The entire process takes about 50 minutes to scan a 1 inch section of reinforcement steel. Lengths of up to 6 inches can be scanned as well. Distances greater than 6 inches would require an additional support to locate the opposite end of the reinforcement wire.

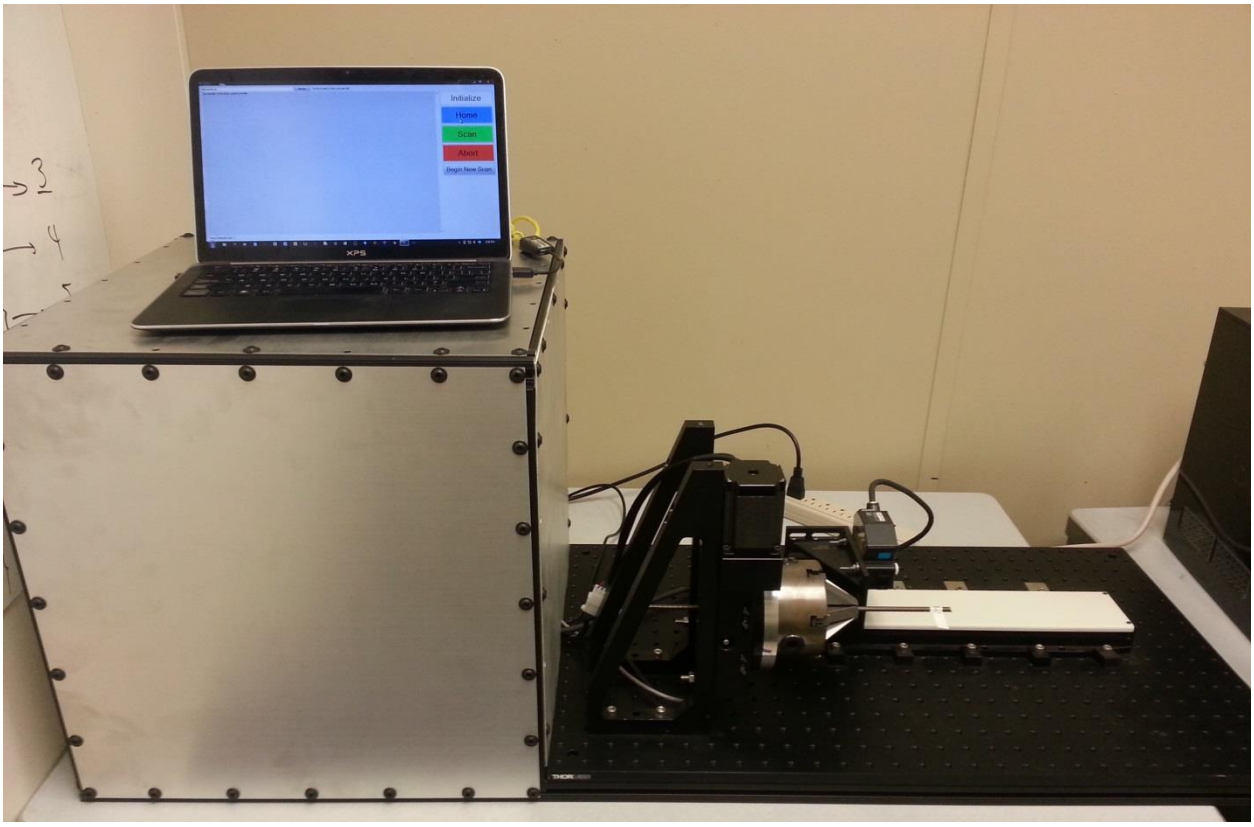

Figure 110. Final Indent Profiling System (Industry Ready)

Figure 111 shows the graphical user interface used to control the indent profiling system. The interface has been simplified from previous prototype versions. The user first selects the location for where to store the scanned data output file. The user initializes the system, this establishes a connection between the desktop and the profiling hardware. Then the user homes the machine and begins the scan.

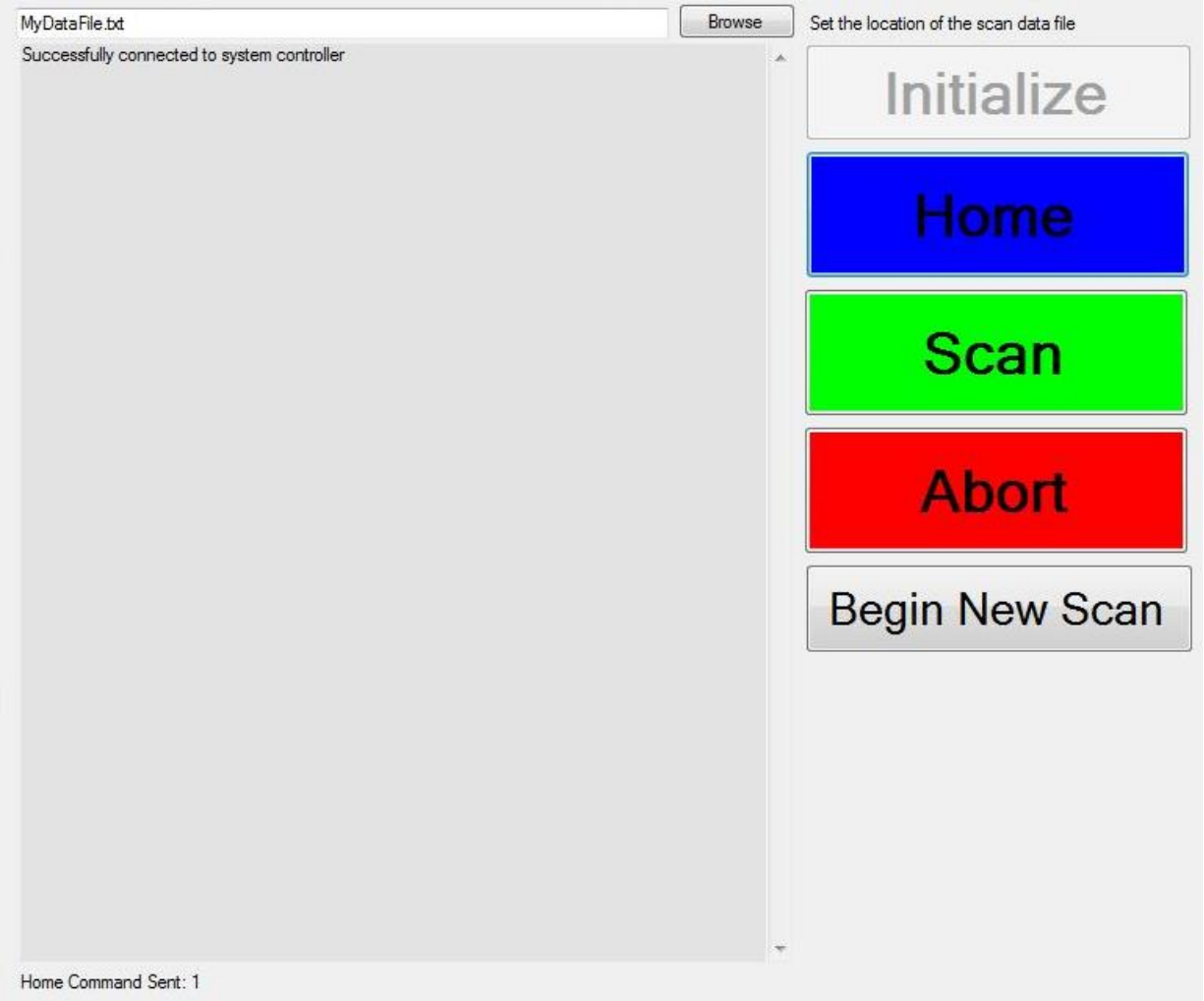

Figure 111. Wire Scanning Graphical User Interface

5.7.1 Results

The developed systems were utilized for the surface profiling of pre stressing steel reinforcement wires to determine the geometrical features that influence performance when the steel is used in concrete members. With this system new geometrical features were discovered as having critical influences on concrete members which have never been measured until this research. Figure 112 below shows a typical resulting 3D model (right) of a microscope image capture of the same wire (left).

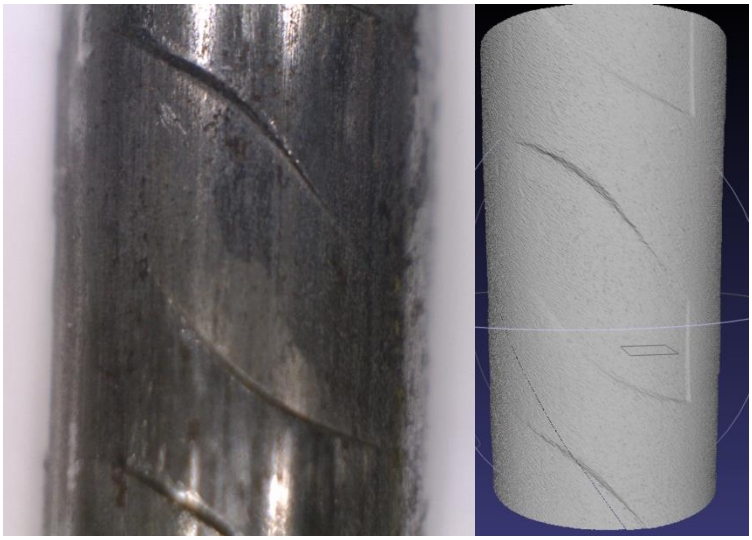

Figure 112. Results of Indent Profiling

Figure 113 shows the results of scanning 1 inch long sections. The coloring accentuates the surface variation making even minute changes in profile visible. All data sets used in this study were visually rendered to provide a confirmation that there exist no visible issues with the data. Additionally preprocessing algorithms were used to verify that the data was clean and without defect.

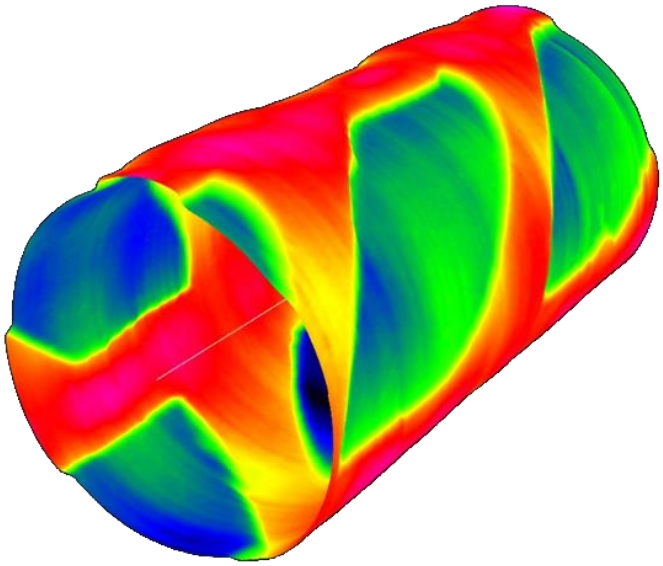

Figure 113. 3D Heat Map of 1 Inch Profile

Figure 114 shows the results of scanning 5 inch long sections. The coloring accentuates surface variations. In general the surface profile looks detailed and accurate. However, small vibrational build up can be seen. The end of the wire shown in the bottom right is that of the unsupported end during scanning. As the wire is of a small diameter and the unsupported end is a minimum of 5 inches from the chuck, minute vibration effects appear in the data. Fixating the wire at both ends during scanning would resolve this issue. Meaningful measurement data can still be obtained from these long scan lengths, yet for the research of developing models from geometrical feature measurements a conservative approach was used. Due to these minute vibrations only 1 inch scans were used during this study to create geometrical feature measurement data. Tests were performed to confirm that vibrational influences for the 1 inch scan lengths were negligible and are discussed in a later chapter.

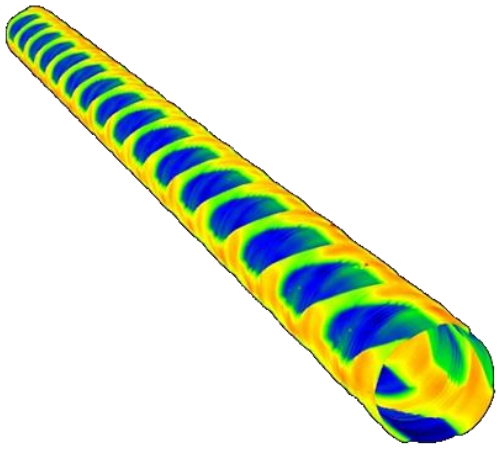

Figure 114. Results of Indent Profiling

5.8 Conclusion

Table 8 summarizes the features of the four different prototypes developed. The first prototype offered a proof of concept that validated the ability to meet the research requirements. The second prototype was the first prototype used for testing and experimentation of different wire types. With prototype 2 the first confirmations were made about the strong correlation between transfer length and wire geometry. The third prototype was the fastest scanning system, and offered the largest amount of data to be collected in the least amount of time. At these high

operating speeds, mechanical vibrations induced noise into the scanned data set that would require more expensive hardware than what was available to correct. The fourth prototype offered a complete solution in a single package. Being made with industrial components it is the easiest to duplicate. The line based scans and the machine setup provide a very stable and repeatable result. This prototype is ready to be used for industrial quality control applications.

Table 8. Prototype Summary

Prototype Summary				
	Prototype 1	**Prototype 2**	**Prototype 3**	**Prototype 4**
Description	Proof of Concept	Most Affordable	Fastest Profiling	Industry Ready
Samples per Second	100	1,000	30,000	1,350
Scanning Direction	Spiral Scan	Spiral Scan	Spiral Scan	Line Scan
Scanning Trigger	Event Driven	Time Based	Event Driven	Event Driven
Industry Affordable	No	Yes	Yes	Yes

Table 9 lists the pros and cons to the four different prototypes. The first prototype was too costly for practical implementation in industry and was eventually disassembled when the rotary table for the system failed. The second prototype was a cost effective solution. The timer based sampling method of this prototype limited the utility of the collected data as the data collection interval was not aligned to the wire axis. The third prototype offers the most capable data collection rate. While the scanned data from this prototype was usable for quality control, the noise from mechanical vibrations made the system non-ideal for lab testing and experimentation of different wires. The fourth prototype is the most well rounded and complete solution. This prototype has an easy to use interface and stable and consistent scanning result. Being made of industrial components this system is easiest to duplicate and reproduce.

Table 9. Pros and Cons of Different Prototypes

	Pros	Cons
Prototype 1	• Validated project feasibility • Clean scans from slow sampling rate	• Most expensive • Rotary table failed • Difficult development interface • Unstable programming environment • Slow data collection rate
Prototype 2	• Most affordable • Data collection rates feasible for wire testing	• Timer based sampling limited data accuracy
Prototype 3	• Fastest scanning rates	• Custom circuitry required • High speeds induced scanning vibrations with current hardware
Prototype 4	• Ready for industrial use • Integrated homing system • Simple user interface • System packaged in a portable setup • Line based scans offers alternative analysis methods • Most stable and repeatable scanning results	• Made with off the shelf industrial components only

The developed systems were used successfully for the analysis and quality control of pre-stressing steel reinforcement wire geometry [4]. The non-contact profiling system was able to identify critical geometrical features and their influence on reinforcement wire performance in concrete members [40, 33]. The designed system maintains a sub-micron resolution and state of the art sampling rates while being at a fraction of the cost of commercially available systems. Additionally, the developed software allows for autonomous geometrical feature measurements making autonomous 100% inspection of geometrical measurements practical for industrial applications. System limitations consist of the mechanical hardware and the specialization

requirements for the autonomous geometrical feature measurements. The mechanical hardware is part-specific and performing automated surface profiling on different part geometries will require a different hardware arrangement. Each geometrical feature measurement extracted by the software requires specialized software development to achieve robust feature extraction.

Chapter 6 — Wire Analysis and Measurements

This chapter summarizes the measurement findings of the pre-stressing steel reinforcement wire. This section documents the geometrical features analyzed, the measurement results, qualitative and quantitative analysis of the reinforcement wire surface profile.

6.1 Commercial Reinforcement Wire

Figure 115 shows the variety of commercial reinforcements used within the industry. From left to right the reinforcement wires in the study were given a number to a code WA, WB, WC, … , WM. Within the study there is one smooth wire WA. Wires WC and WE were spiral type reinforcements. Wires WK and WL are dot type reinforcements. All remaining wires are a chevron type reinforcement wire. Chevron type are the most predominately available type within the industry. An additional wire WN, which is the wire that failed in plant is not shown in this picture.

Figure 115. Commercially Available Pre-Stressing Steel Reinforcement Samples

6.2 Measurement Results

Using the fourth prototype indent profiling system, five 1 inch long scans were used to collect measurements of geometrical features. Each 1 inch long scan contained approximately 12 indents for the chevron style reinforcement.

Figure 116 shows the individual measurement values for the indent depths for the reinforcement wires shown. Wire WE had the overall largest indent depths, which is due to its unique surface profile. Wires WC, WF, WH, and WN had the next largest indent depths. Wire WG has the shallowest indents of all.

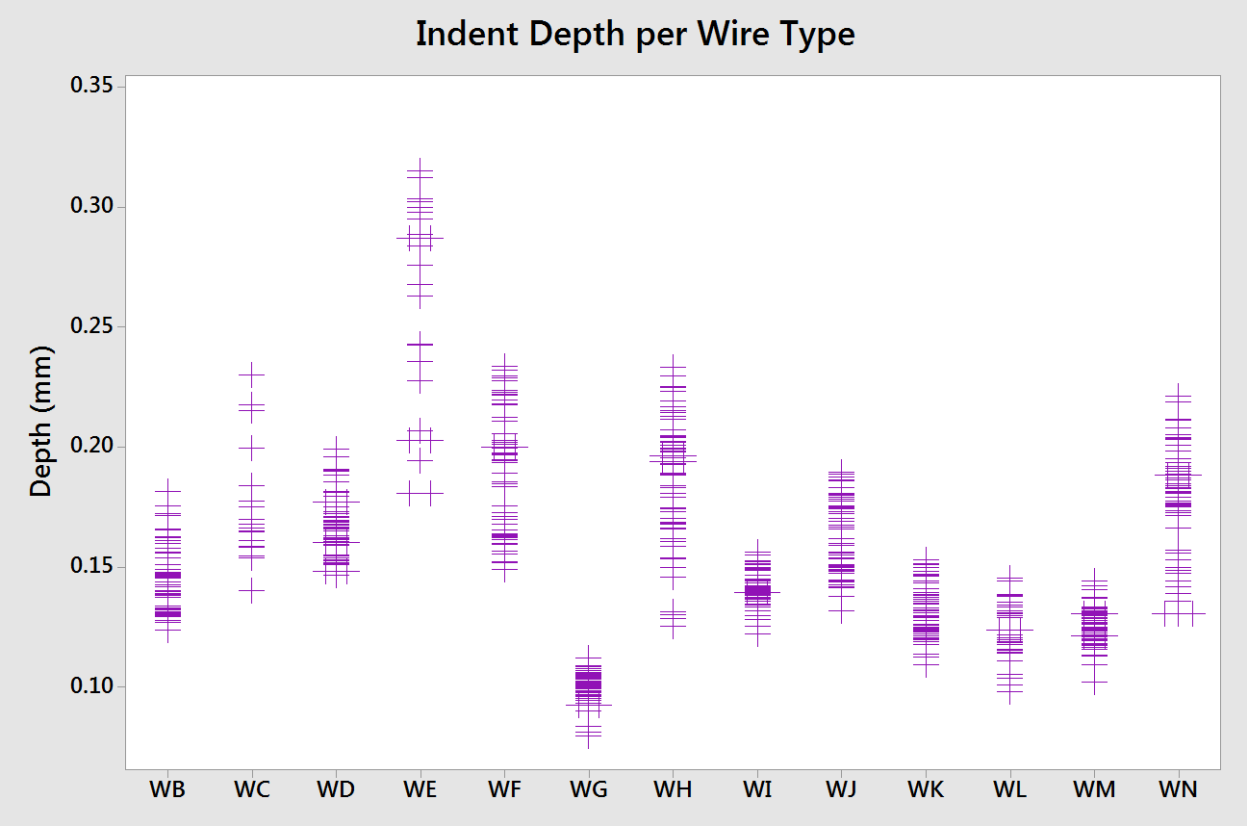

Figure 116. Individual Measurements of Indent Depth

Figure 117 shows the box plots for the indent depth measurements. The box plot shows the average depths as well as the first and third quartile ranges. Astericks at the box plot tails represent outlier results.

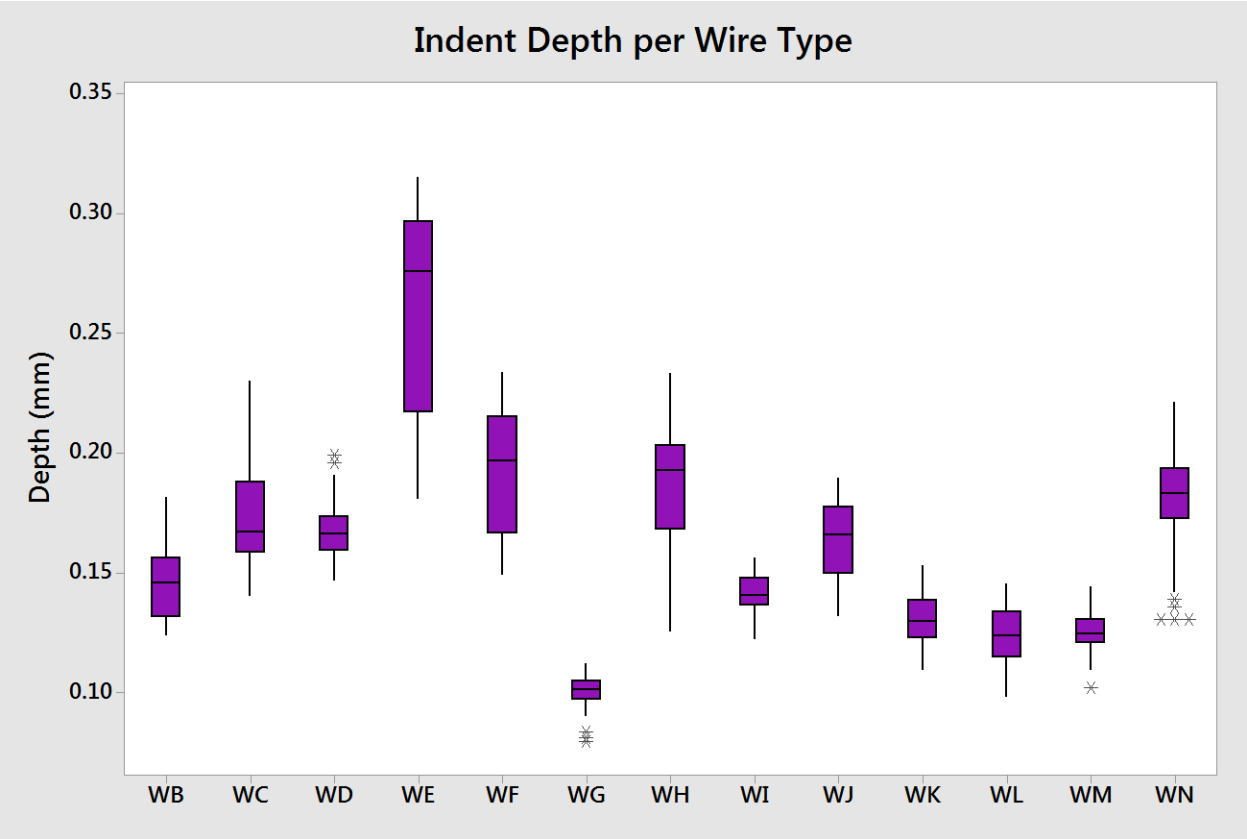

Figure 117. Box Plots of Indent Depth Measurements

Figure 118 shows the individual plots of the indent width per wire type. Wire WE has indents that are by far the largest. Many of the chevron style indents have comparable indent widths, with a few exceptions. The dot wire types have small indent widths.

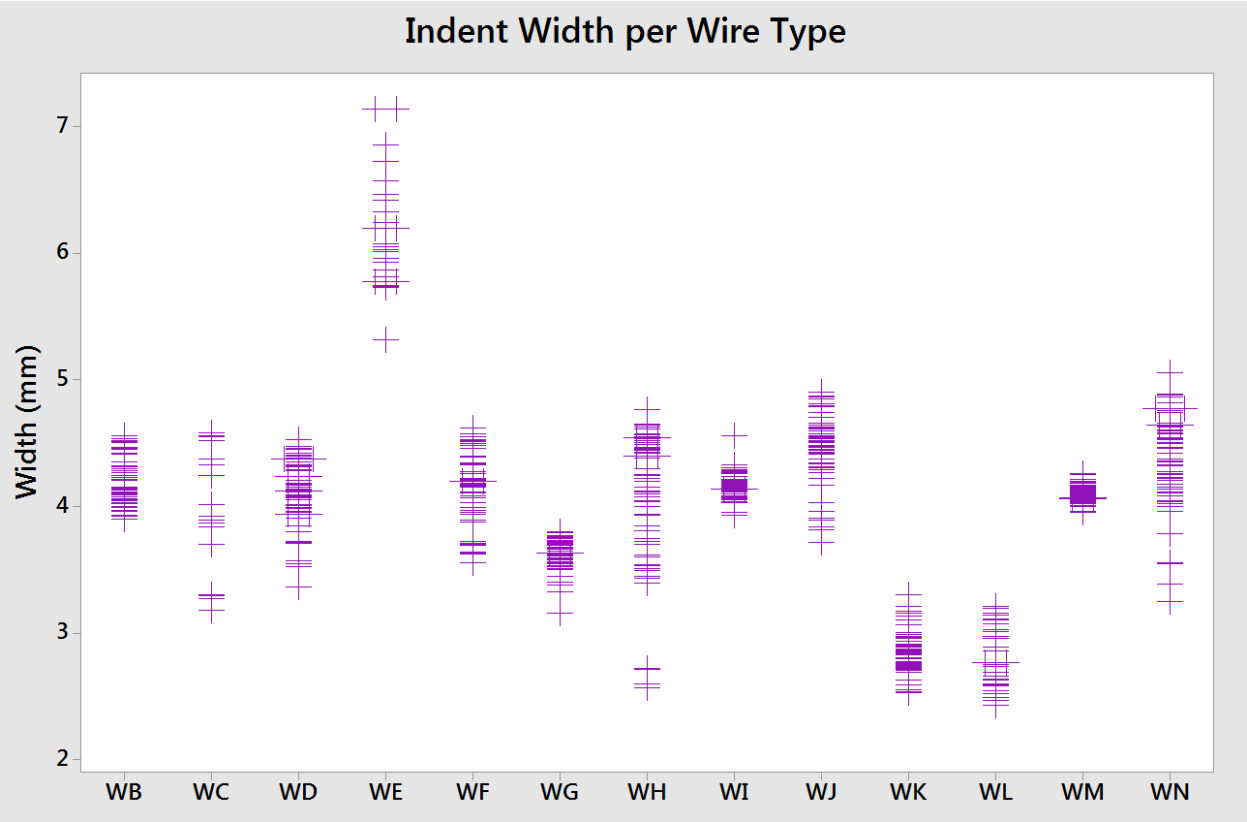

Figure 118. Individual Measurements of Indent Width

Figure 119 shows the box plots for the indent width. The indent widths have overall less variation from one wire type to the next. Wire WG has the lowest indent of all the chevron style indents. Wire WJ has the widest of all the indents. Given the amount in similarity of the indent widths, this geometrical feature would not be as well suited for predictive models of only chevron wires.

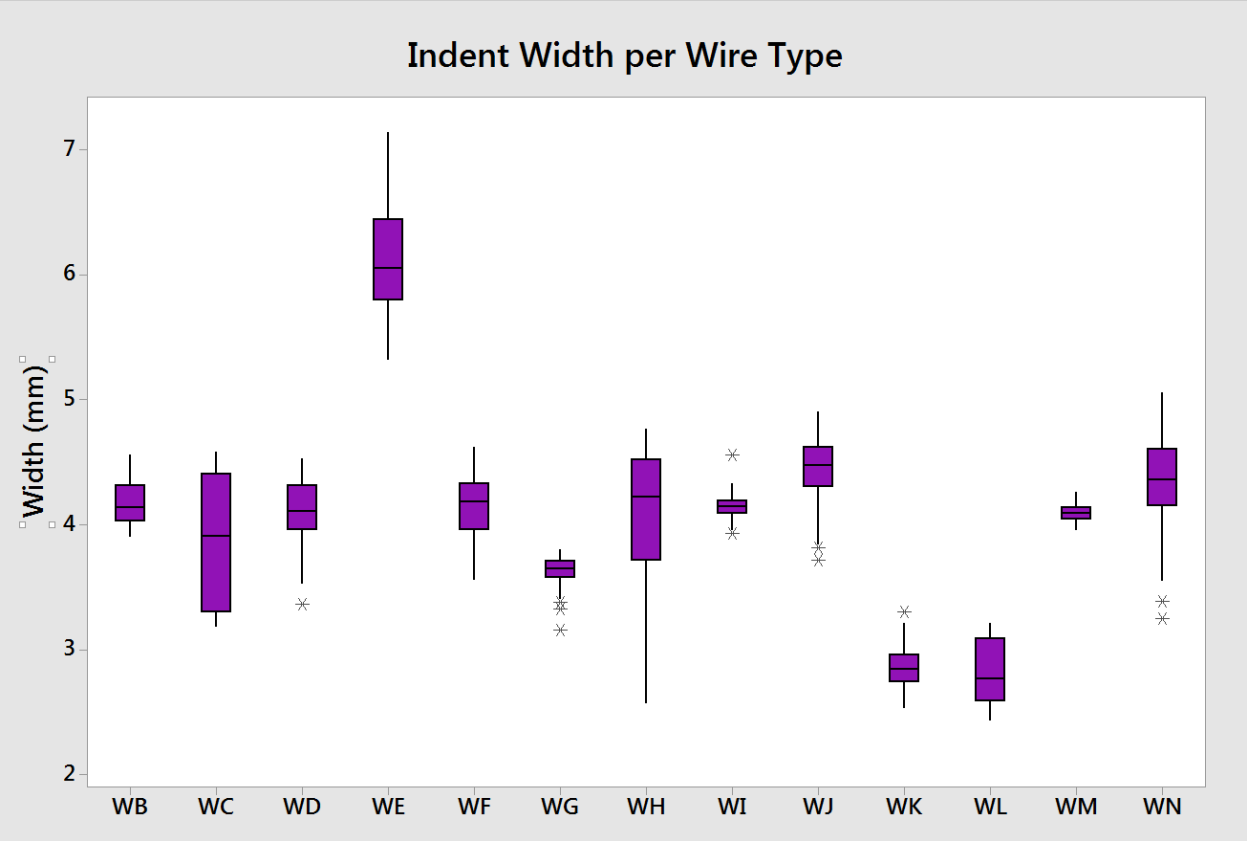

Figure 119. Boxplots of Indent Width

Figure 120 shows the indent edge wall angles for both sides of the indent. There variation in the indent edge wall angle is large. Indent's width steeper edge wall angles have more variation than indents with shallower edge wall angles. This is due to challenges in regards to determining the start and stop of the indent edge wall. Small variations at the top of the indent and at the indent basic, such as built up base metals, or faded transitions from the top of the indent to the bottom of the indent can create big variations in the overall indent edge wall angle.

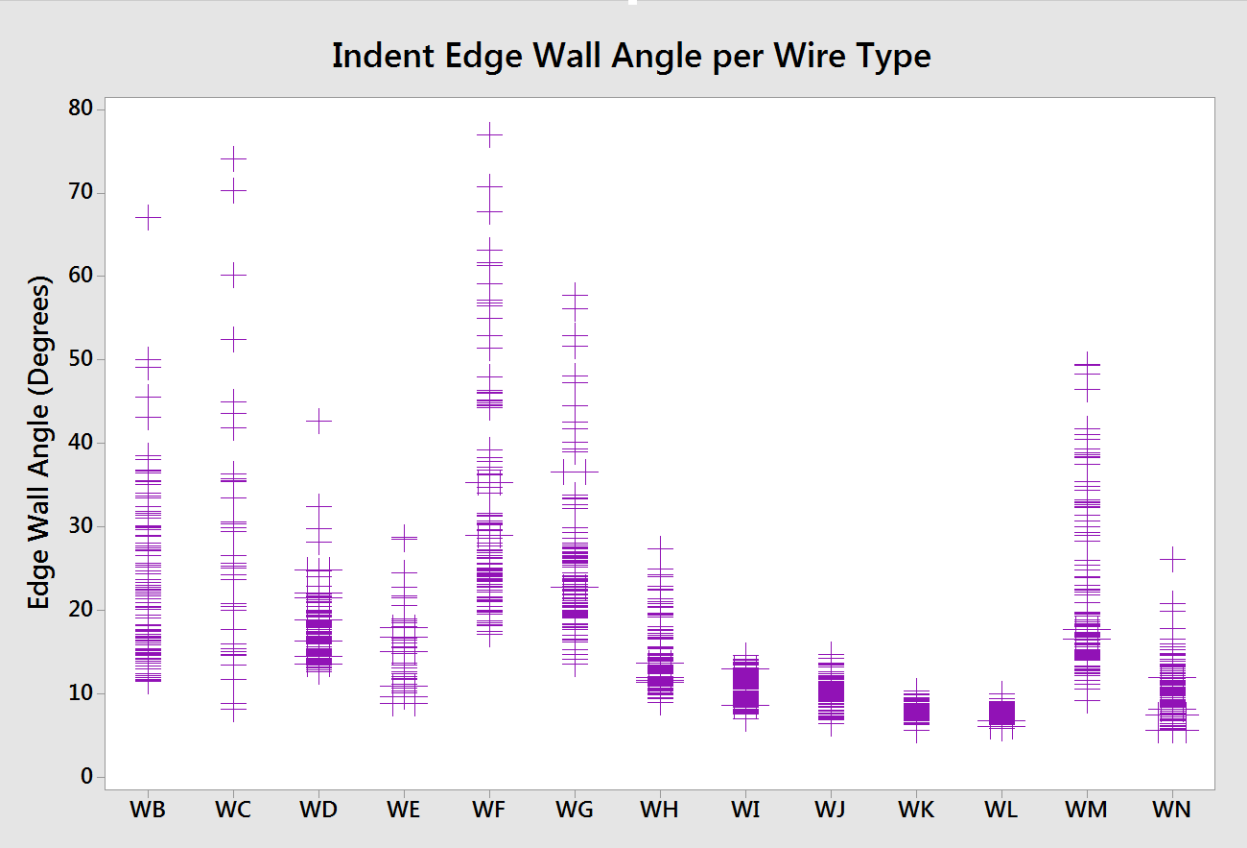

Figure 120. Individual Measurements of Indent Edge Wall Angle

Figure 121 shows the boxplots of the indent edge wall angle. The box plot shows that there is a clear correlation to steeper indents and greater indent edge wall variation. This makes any predicative models that rely on indent edge wall variation to be convoluted with the average indent edge wall. The steepest indent edge wall is from wire WF, and it is visibly clear that it is the steepest of all wire types. Wire WN – the wire that failed at the plan – has the shallowest of all the chevron style indents with only the dot reinforcement wire types having a shallower indent edge wall angle. The boxplot also highlights how indent profiles with imperfections can vary significantly from the mean. The steep indents of WC, WF, and WG have outliers that are exceptionally steep.

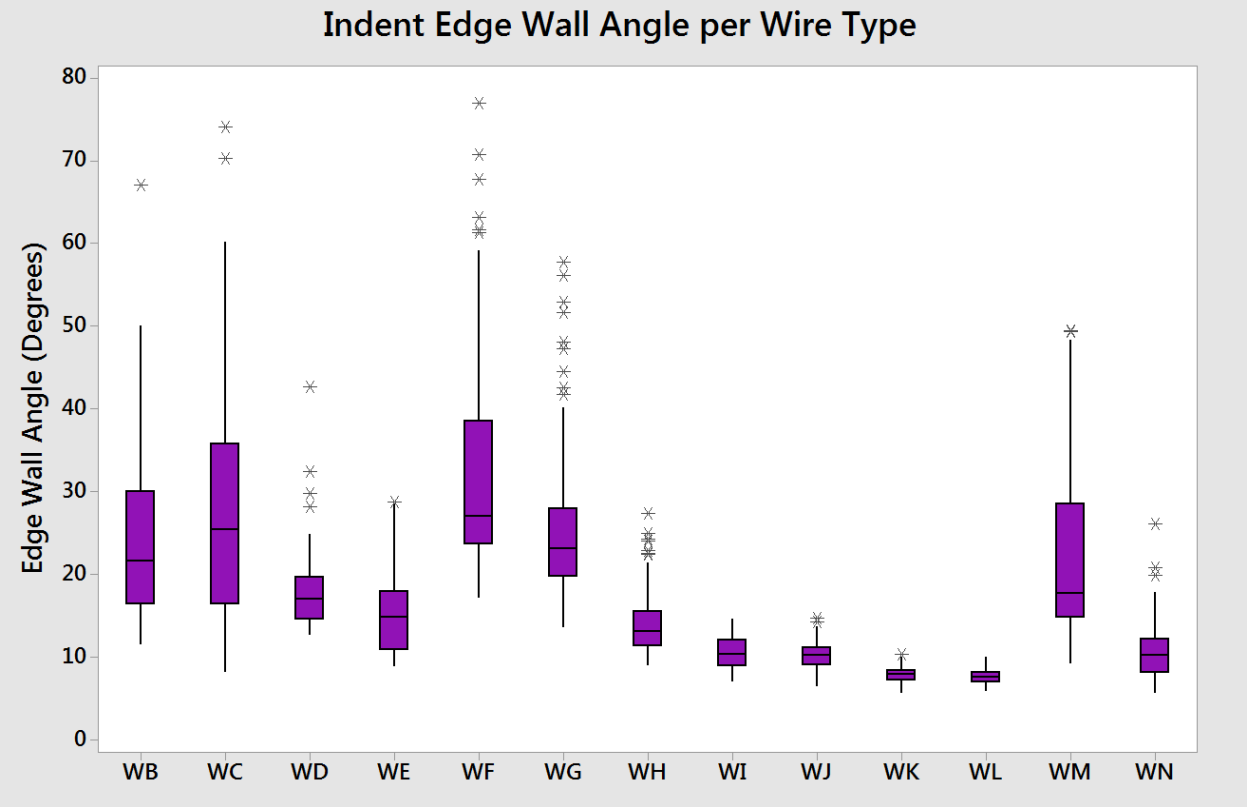

Figure 121. Box Plots of Indent Edge Wall Angle

Table 10 shows the summary of basic geometrical feature measurements of all the reinforcement wires within this study. For all reinforcement types five 1 inch long sections were used for this data. There are 50-60 indents that were profiled and measured for the chevron type reinforcements. The indent edge wall angle contains information about the indent edge wall on both sides of the indent. This data was collected with the fourth prototype scanner.

Table 10. Basic Indent Geometrical Features

	Depth (mm)		Width (mm)		Edge Wall Angle (Deg.)	
	Average	Std. Dev.	Average	Std. Dev.	Average	Std. Dev.
WA	0.000	0.000	0.000	0.000	0.0	0.0
WB	0.146	0.014	4.191	0.186	23.6	9.7
WC	0.176	0.025	3.932	0.501	29.3	16.0
WD	0.167	0.013	4.097	0.258	17.9	4.3
WE	0.259	0.044	6.164	0.455	15.1	4.8
WF	0.192	0.025	4.143	0.272	32.6	13.4
WG	0.100	0.006	3.629	0.119	25.7	8.9
WH	0.186	0.026	4.078	0.545	14.2	3.9
WI	0.141	0.007	4.157	0.097	10.6	1.8
WJ	0.164	0.015	4.445	0.279	10.2	1.7
WK	0.132	0.011	2.860	0.167	8.0	0.9
WL	0.124	0.013	2.826	0.251	7.7	0.9
WM	0.126	0.008	4.097	0.070	21.8	9.6
WN	0.180	0.023	4.355	0.362	10.7	3.3

Table 11 shows additional indent measurements performed in regards to the orientation and size of the indent. The orientation is the angle of the indent in respects to the axis of the wire. Little difference is seen for the orientation of the chevron style reinforcements. The dot reinforcements are oriented at nearly the same direction as the axis of the wire. The length of the indent (EL) along its direction vector and the width of the indent (EW) perpendicular to its direction vector are shown. This data was collected on the second prototype indent profiling system. This data is from a 1cm long scan of each reinforcement wire type. About 3 indents per chevron wire type can be obtained within this length of wire. The indents were profiled with 1 million data points per cm of wire. The data set used also provided the information for Table 12.

Table 11. Additional Indent Geometrical Features

	Orienation (Deg.)		EL (mm)		EW (mm)	
	Average	Std. Dev.	Average	Std. Dev.	Average	Std. Dev.
WB	41.5	1.1	7.465	0.390	3.016	0.073
WD	45.0	1.1	5.703	0.264	2.783	0.004
WF	43.2	2.0	7.258	0.095	3.163	0.051
WG	45.4	0.5	6.328	0.329	2.612	0.013
WH	46.0	0.4	6.895	0.247	3.082	0.019
WI	45.1	2.0	6.798	0.208	2.810	0.060
WJ	43.4	1.2	6.658	0.210	2.923	0.085
WK	3.2	1.1	2.929	0.066	2.160	0.071
WL	2.9	3.1	3.436	0.002	2.536	0.203

Table 12 shows the results for indent geometrical features that are newly found within this study. These geometrical features provide detailed information about the indent surface profiles that were previously unmeasurable. These measurements are the indent projected surface area(PSA), the indent volumetric void(VV), the indent surface area(TFSA), and the indent edge wall surface area (EdgeTFSA). The VV, PSA, and TFSA all have strong correlations to the transfer length created by the wire.

Table 12. Advanced Indent Geometrical Features

	PSA (mm2)		VV(mm3)		TFSA (mm2)		EdgeTFSA (mm2)	
	Avg.	Std. Dev.	Avg.	Std. Dev.	Avg.	Std. Dev.	Avg.	Std. Dev.
WB	17.58	1.02	2.69	0.58	16.62	1.08	1.72	0.17
WD	12.99	0.49	2.08	0.17	11.97	0.72	1.72	0.12
WF	16.97	2.44	3.46	0.72	17.25	0.24	1.90	0.10
WG	13.50	1.40	1.26	0.08	12.41	1.02	0.65	0.15
WH	16.92	0.77	2.85	0.04	16.71	0.71	3.16	0.02
WI	14.26	0.02	1.70	0.21	13.76	0.15	2.23	0.32
WJ	16.00	1.13	2.30	0.13	14.65	1.14	2.39	0.97
WK	4.36	0.06	0.40	0.04	3.96	0.11		
WL	5.59	1.11	0.61	0.10	5.52	0.41		

6.3 Commercial Wire Types

This section provides a general summary of all the wire commercially available reinforcement wires in the study. General discussions of the wires within this study are provided. All 3D models provided within this section are from the fourth indent profiling system. The microscope images were captured at approximately 40x magnification.

6.3.1 WA

Wire WA in Figure 122 was the control test within the study. Pre-stressing steel wire was acquired before indent patterns were die pressed into the surface. This control wire has the same material properties and diameter as that of the other commercially available wires, the only difference of this wire was that it was removed from production prior to indent forming.

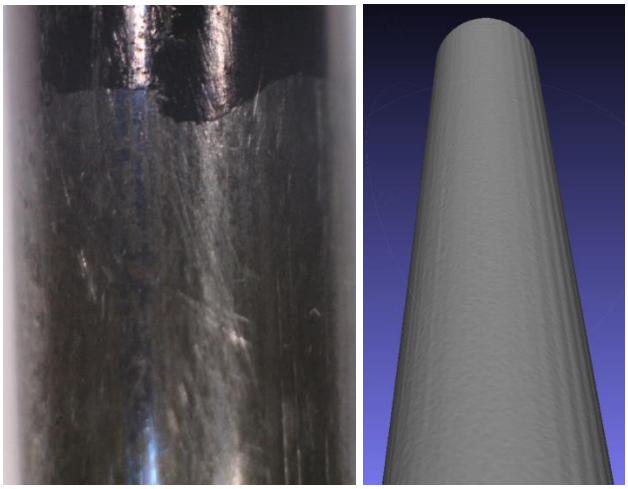

Figure 122. WA Microscope Image and 3D Model

6.3.2 WB

Wire WB in Figure 123 is a typical representation of the chevron style reinforcement wires. Wire WB indent profile is close to the average of all the chevron indent types.

Figure 123. WB Microscope Image and 3D Model

6.3.3 WC

Wire WC in Figure 124 is a spiral type reinforcement wire. This wire has an surface profile in-between indents that is unlike other wire types. In-between indentations the wire surface bulges outward. This rounding effect makes determining the depth and the overall indent edge wall angle difficult for this wire. In addition, this reinforcement wire type had surface rust build up

that was unlike the other wire types. The rust seen is thick and in concentrated regions. All wires were stored throughout the study within a controlled environment to prevent oxidation.

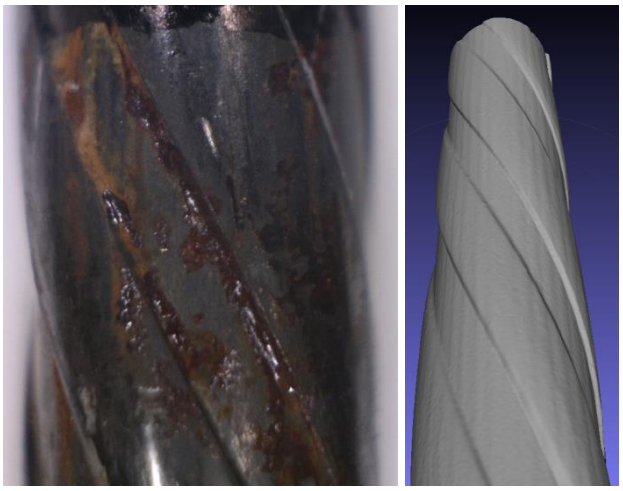

Figure 124. WC Microscope Image and 3D Model

6.3.4 WD

Wire WD in Figure 125 has chevron style indents that are more rounded than the typical wire type. While most indent are shaped like a parallelogram, wire WB has a more elliptical shape. This elliptical shape creates for a non-consistent edge wall angle. The angle is shallow at opposing ends of the indent and along its length the indent gradually steepens. This make determining the indent edge wall angle with traditional methods not representative of the overall profile.

Figure 125. WD Microscope Image and 3D Model

6.3.5 WE

Wire WE in Figure 126 is a spiral type reinforcement. This wire has a very different profile the that of wire WC. Wire WC has relatively the same axial length in-between indents as the axial length of the indent. Wire WE has a much larger indent axial length than the axial length in-between indents. Wire WE has a flat indent basin and a flat top between indents.

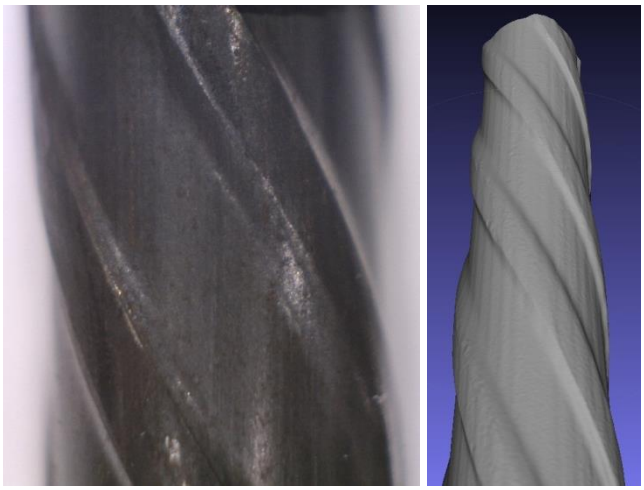

Figure 126. WE Microscope Image and 3D Model

6.3.6 WF

Wire WF in Figure 127 is the most unique of all wire types within the study. The wire has a noticeable different surface finish from that of the other wires. A dark black oxide color appears on this wire while most others are grey. Bright purplish colors around the indent edge may be from tempering and steel hardening effects. The indents of this wire are the deepest of all the chevron style reinforcements and this wire has the steepest of all indent edge wall angles. While most chevron indents have a gradual transition from the indent basin to the area in-between indent rows, wire WF has a crisp defined edge wall at this location.

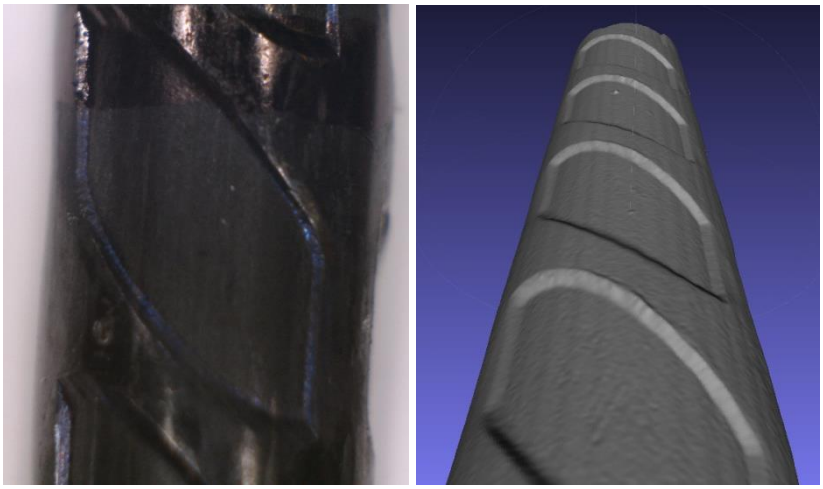

Figure 127. WF Microscope Image and 3D Model

6.3.7 WG

Wire WG in Figure 128 is the shallowest of all the indents. This wire has an indent depth of 100 microns. This wire along with WF was used to represent the range of possible indent types in the development of coefficients of friction and adhesive bond in the theoretical model.

Figure 128. WG Microscope Image and 3D Model

6.3.8 WH

Wire WH in Figure 129 is second deepest of all the chevron style reinforcement types, with WF being the deepest buy a small amount. Unlike WF, wire WH has a shallow indent edge wall angle. This indent edge wall angle for wire WH varies down the length of the edge wall. The

deep indentations in wire WH have created a flattened face at the top surface of the wire. This effect made determining an adequate threshold for indentation difficult when developing automated measurement algorithms.

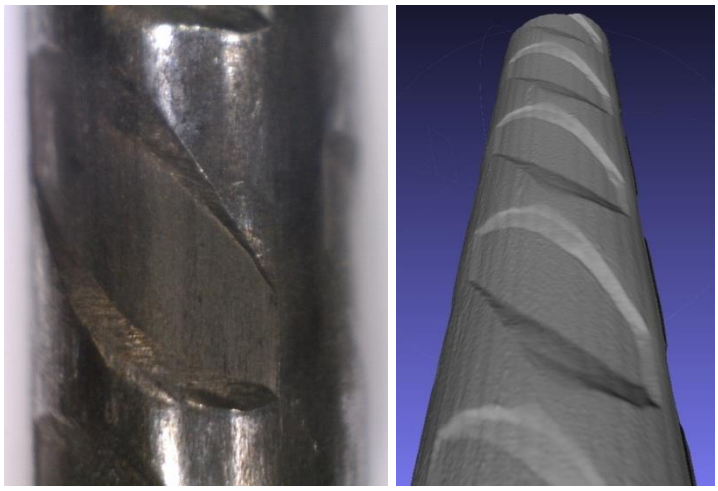

Figure 129. WH Microscope Image and 3D Model

6.3.9 WI

Wire WI in Figure 130 is very similar to that of wire WJ. The indent is of an average depth and is of a shallow edge wall angle like that of WJ. These two wires have the shallowest edge wall angles of the chevron style reinforcements.

Figure 130. WI Microscope Image and 3D Model

6.3.10 WJ

Wire WJ in Figure 131 is very similar to that of wire WI. The indent is of an average depth and has the shallowest average edge wall angle of all the reinforcement wire types.

Figure 131. WJ Microscope Image and 3D Model

6.3.11 WK

Wire WK in Figure 132 is the only 4 dot reinforcement wire type in the study. The dots have a shallow indent depth with a very gradual edge wall angle. As the dots have a continuously curved profile, no clear definition between indent edge wall and indent basin exists.

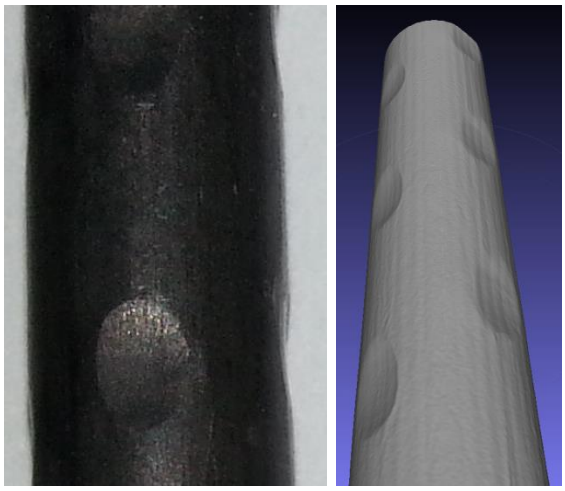

Figure 132. WK Microscope Image and 3D Model

6.3.12 WL

Wire WL in Figure 133 is the only 2 dot reinforcement wire type in the study. The main difference between wire WK and WL is wire WK has 4 rows of indents at 90 degrees to each other around the wire. Wire WL has 2 rows of indents at 180 degrees of each other on the wire. Wire WL produces the shallowest indent edge wall angle of all the reinforcement wire types. The dot type indentations in this wire are of shallow depth. This wire is the closest to the control wire WA of all other wire types.

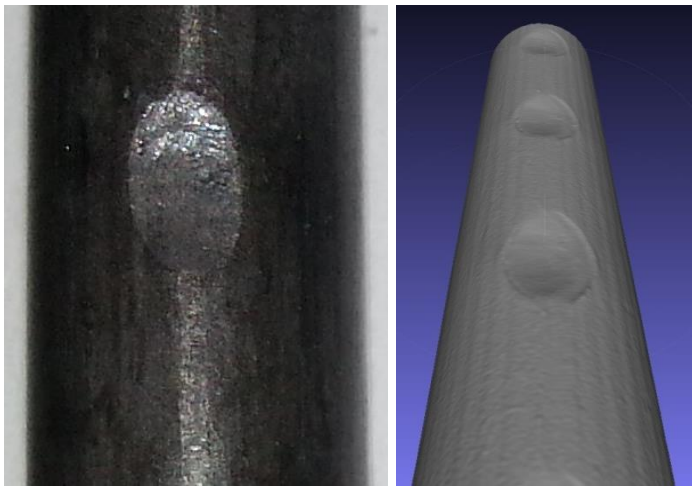

Figure 133. WL Microscope Image and 3D Model

6.3.13 WM

Wire WM in Figure 134 is an additionally added wire not available at the beginning of the research study. This wire is very unique, the indents are very crisp with good definition to indent edge wall and indent basin. The chevron indents on this wire are a near average depth with that in comparison to the other wire types. The indent edge wall angle is also near the average of the other chevron style reinforcements. The average geometrical feature measures and the crisp and clearly discernable profile made it an excellent wire for test non-contact scanning system setups. This wire was used extensively as a control subject in the design of automated indent measurement algorithms. In additional to a crisp indent profile the surface finish of this wire was cleaner and of less color variation and marring as that of other wire types. This wire is the best single representation of the industry mean.

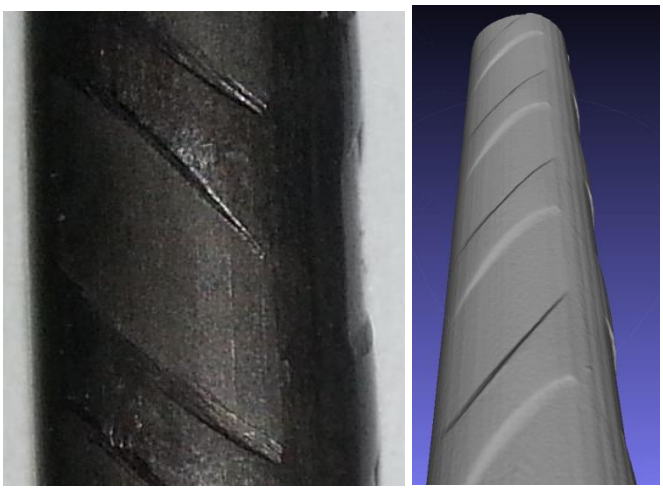

Figure 134. WM Microscope Image and 3D Model

6.3.14 WN

Wire WN in Figure 135 is a wire that was pulled from concrete cross ties that failed in plant. During the cure of the concrete ties, fractures propagated and destroyed the tie. Work was done to remove and preserve the reinforcement wire for profiling and analysis. The wire has an unusual gold yellow coloring to its finish. This is most likely from casting the wire into the concrete tie. The indents from this wire are both very shallow and very deep. The combination of the two conditions increases the propensity of fracture for this wire. The indents from this wire have no crispness to their definition and each indent has very visible pitting and sporadic deformation. This wire is investigated further in the next section.

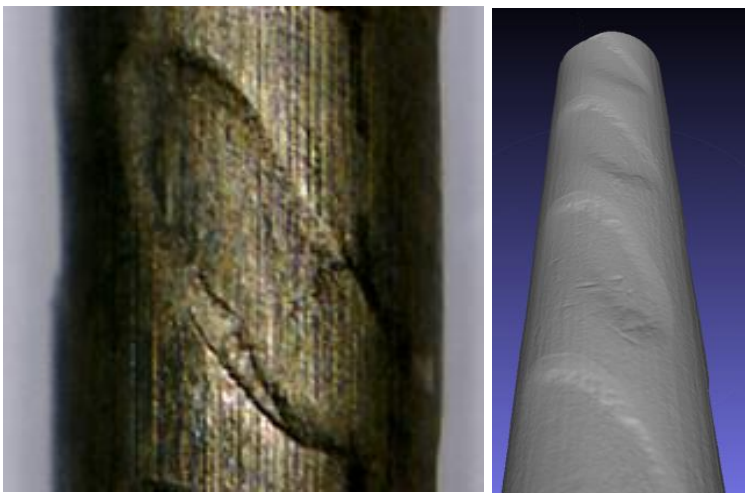

Figure 135. WN Microscope Image and 3D Model

6.4 Wires that Failed in Plant

Figure 136 is a microscope image of the wire that failed during manufacture. This reinforcement wire sample was pulled from a concrete crosstie that failed at the manufacturing plant from fracture propagations.

Figure 136. Microscope Image of Wire that Failed During Manufacture

Twelve samples of this reinforcement wire were analyzed. Figure 137 shows microscope image captures of the twelve samples. The samples are visibly varying from one to the next. Some indents have gradual transitions at the indent edge wall other indents have more clear indent

shapes. Several indents have unique surface deformations that are either the resulted of being cast in the tie or the result of warn indent profile dies during the manufacture of the wire.

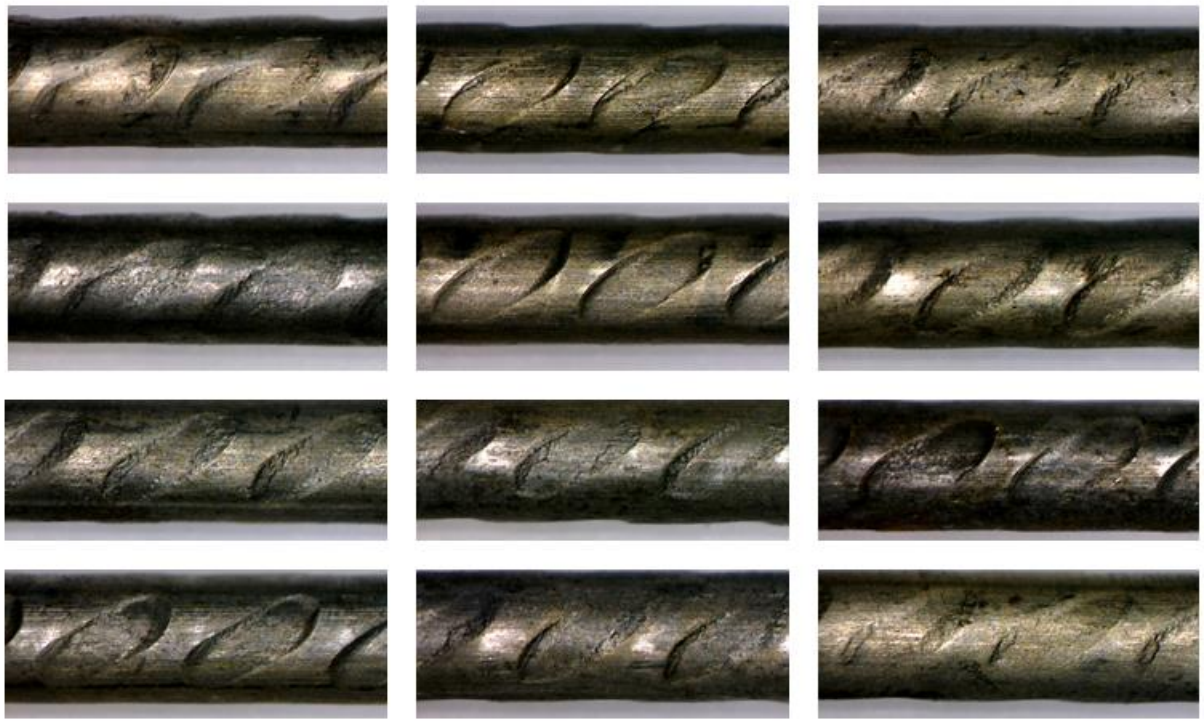

Figure 137. All Sample Images of Wire that Failed During Manufacture

6.4.1 Heat Maps of Wire WN

2D heat maps were generated of all the samples data sets to further visual investigate for visual variations. Figure 138 shows the heat map of one sample. The blue dark regions represent areas of smaller wire radii the red areas represent regions of greatest wire radii.

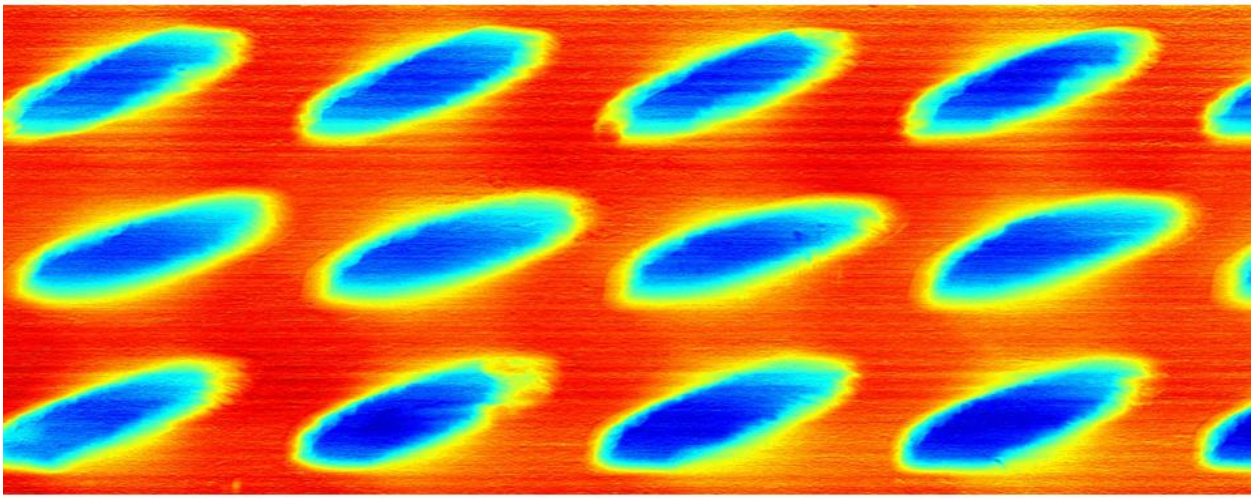

Figure 138. Heat Map of Wire that Failed During Manufacture

Figure 139 shows the heat map images of all the samples. The heat map images help show protrusions and areas with voids in the wire. Surface marring can be seen in one of the heat maps (center column third row from the top).

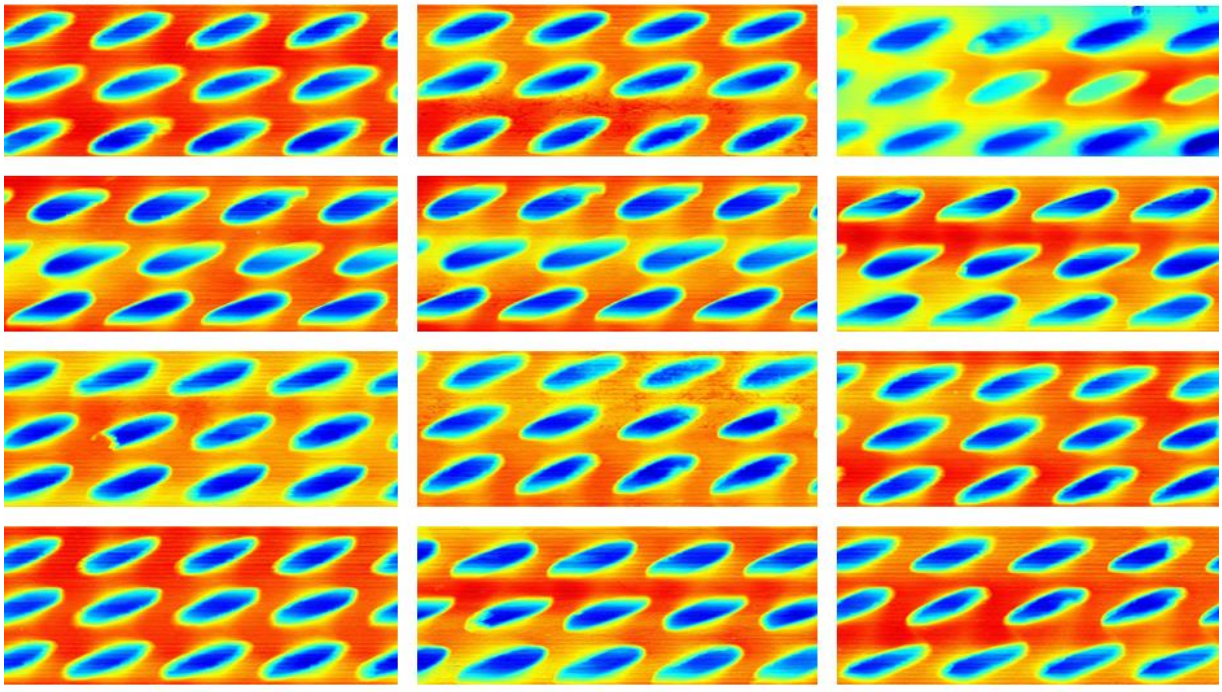

Figure 139. Heat Maps of All Samples that Failed During Manufacture

Figure 140 is a 3D model of one of the wire WN samples. Viewing the 3D model allows for viewing surface variations without influences from lighting and wire color. The indent at the top left shows a large section of the indent was never pressed into the wire. This is most likely due to warn dies during the manufacture of the wire.

6.4.2 Visualizing the Profile of Wire WN

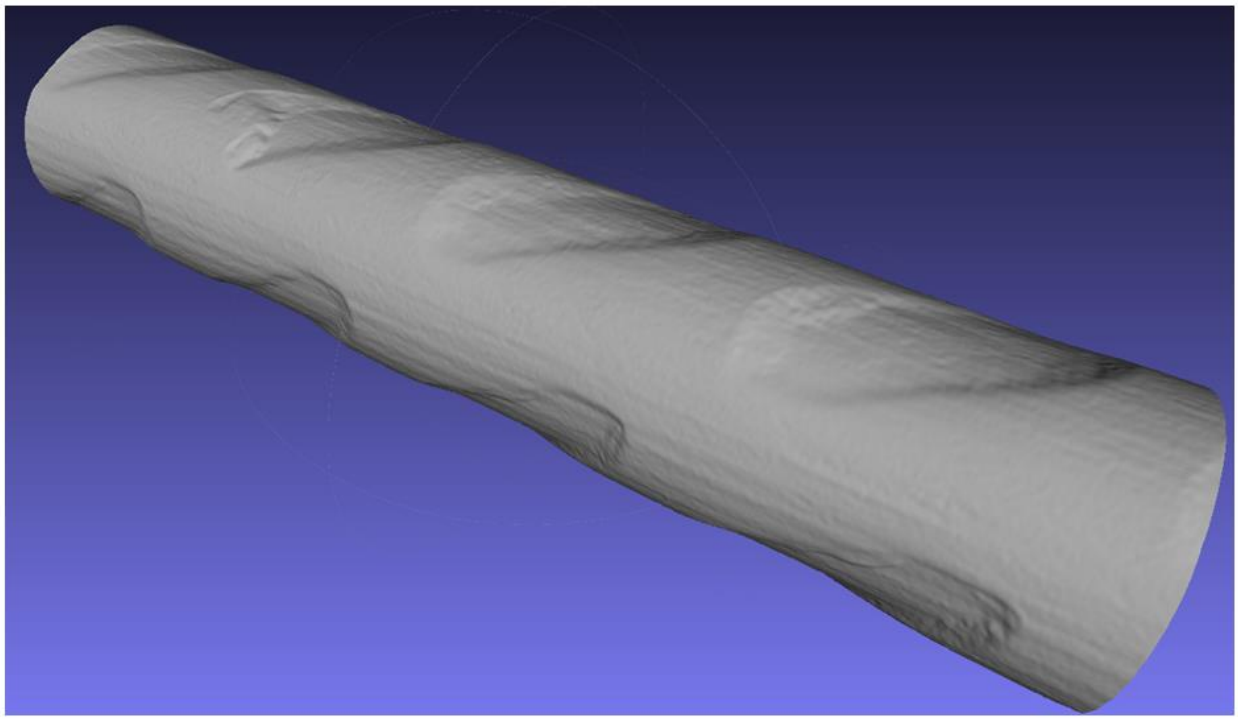

Figure 140. 3D Model of Wire that Failed During Manufacture

Figure 141 is a 2D profile of the indent. The top section of the graph shows a zoomed in illustration of the indent. The 2D profile makes it clear that the indent edge wall has a very gradual transition and its overall edge wall angle is low.

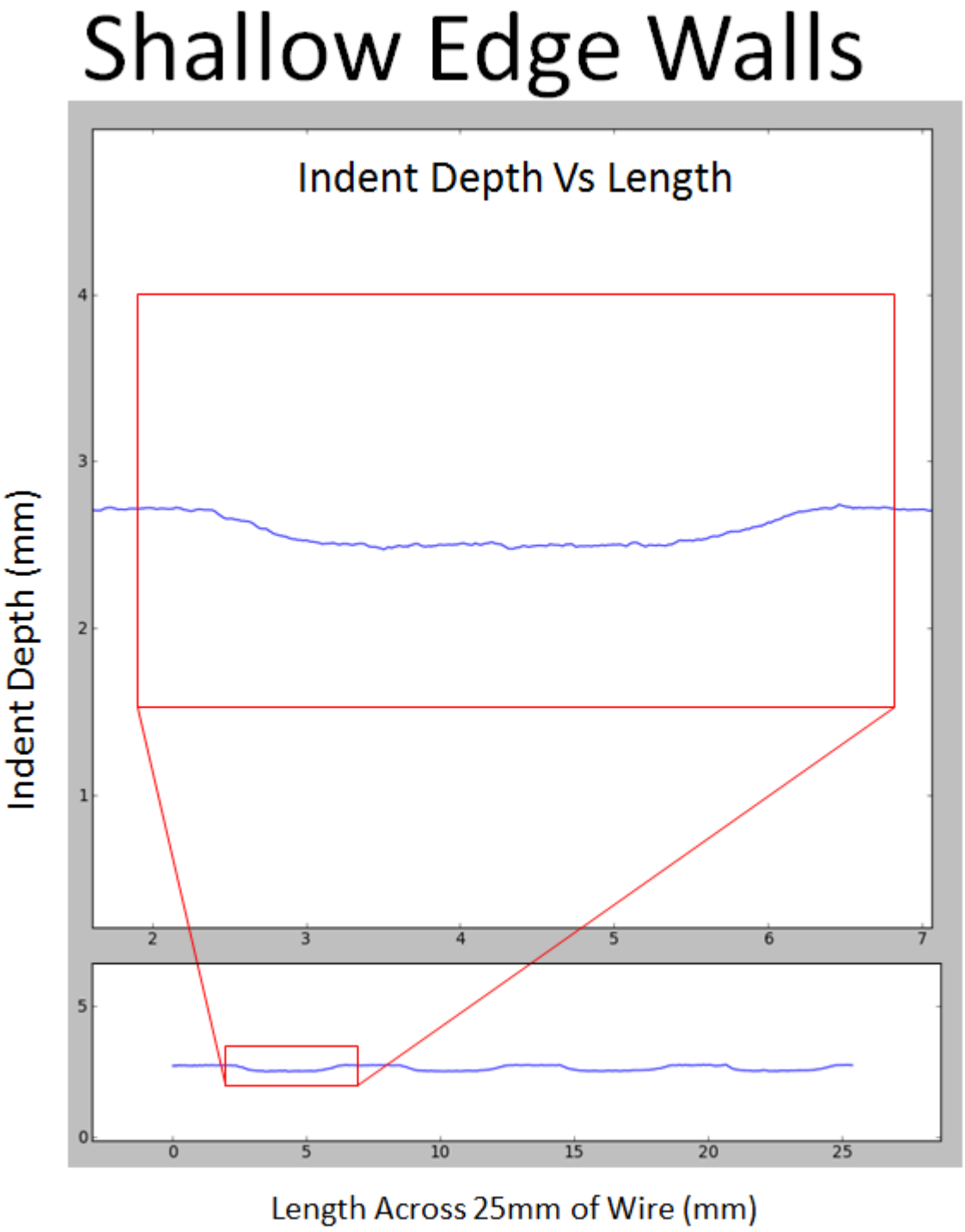

Figure 141. 2D Plot of Wire that Failed During Manufacture

6.4.3 Measurements of Wire WN

For all the indents measured from the 12 one inch long scans of the wire. A total of 100 indents were sampled. Figure 142 shows a histogram of the measured indent edge wall angle for this wire. The distribution appears to be a skewed normal The dual peaks in the histogram may be from difference in the side the indent edge wall is on. The mean edge wall angle shown is 11.52°.

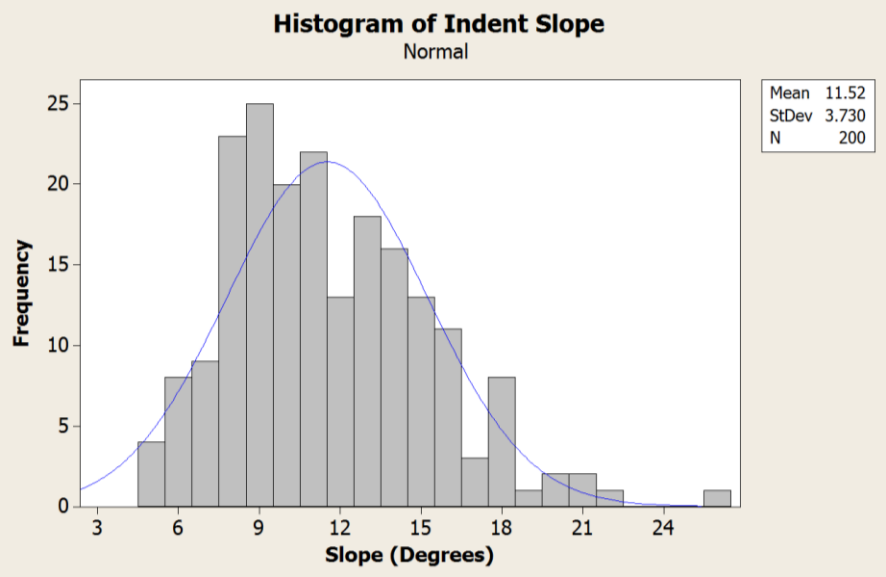

Figure 142. Histogram of all Indent Edge Wall Angles Measured for WN

Figure 143 shows a histogram of the indent depths for this wire. The indent depths have a mean of 180 microns which is towards the high end of the range of wires studied.

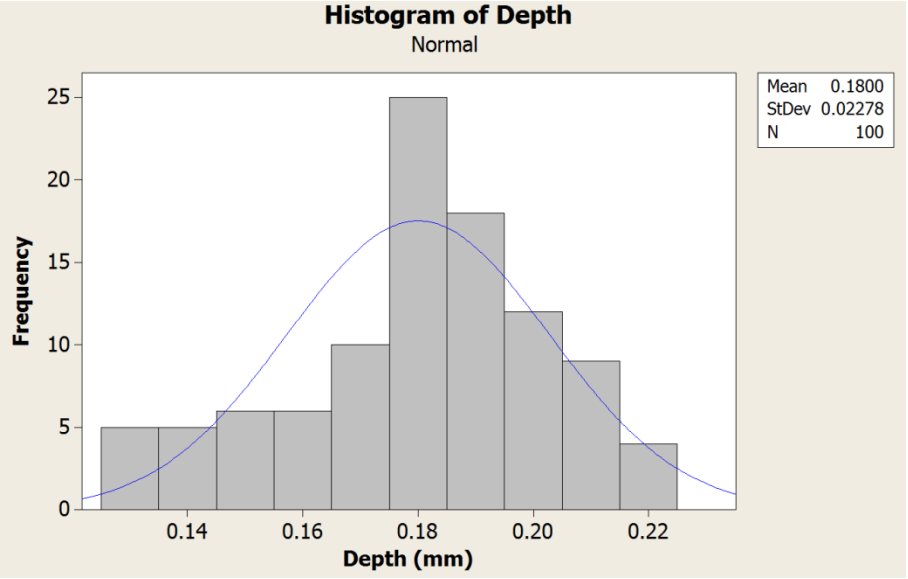

Figure 143. Histogram of all Indent Depths Measured for WN

6.4.4 Comparison of WN to Other Commercial Wires

The wires that failed in plant were compared to other wires in the study. Figure 144 shows boxplots comparing the indent depth of the failed wire to that of other wires in the study. Its depth is comparable to that of WF and WG.

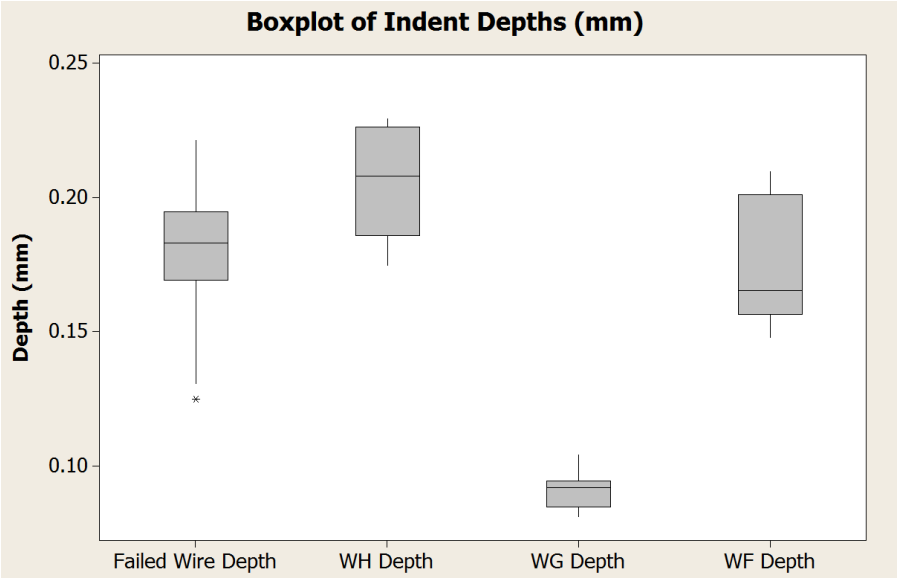

Figure 144. Boxplots of Indent Depths for WN

Figure 145 shows the boxplots comparing edge wall angle of the failed wire to other wires in the study. Wire WN had shallower indent edge wall angles than the other wires. The only chevron style wires that had a shallower edge wall angle were wires WI and WJ, yet these indents also had shallow depths. The combination of shallow edge wall angle and deep indents is unique to wires WH and WN and these wires have known splitting issues.

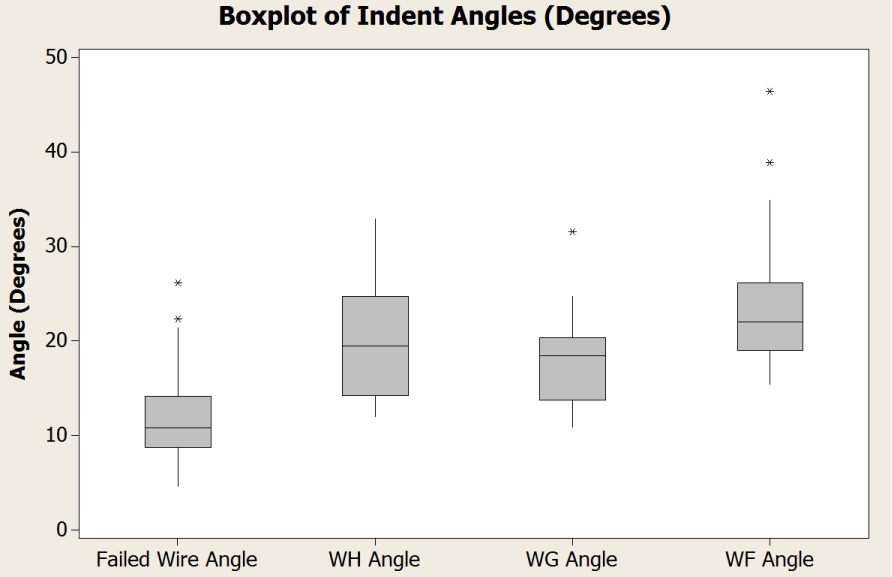

Figure 145. Boxplots of Indent Edge Wall Angle for WN

Figure 146 shows a visual comparison between the failed wire, WN, and other wires in the study. WN clearly stands out from the other wires as have a more smoothed gradual indent profile. The most similar wire to WN is that of WH with large indents with shallow edge wall angles.

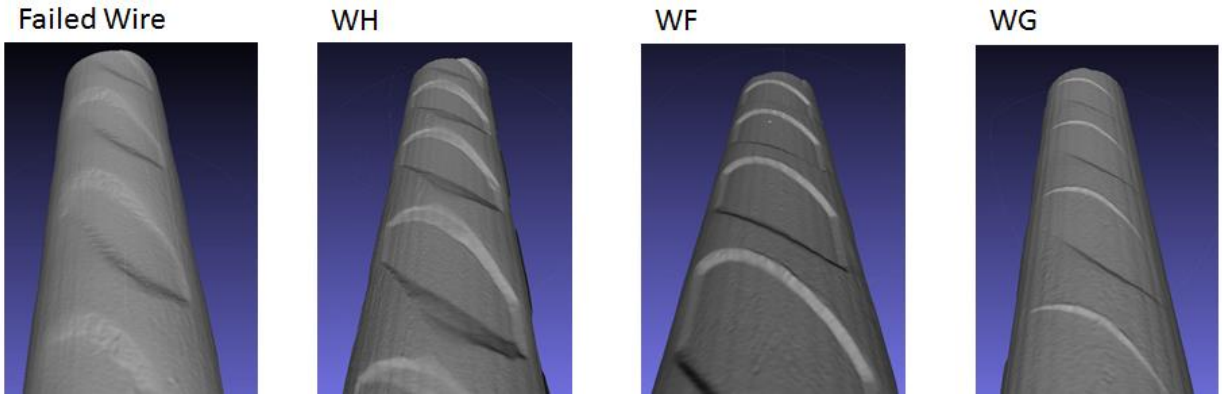

Figure 146. Comparison Between Failed Wire and Commercial Alternatives

6.4.5 Hypothesized Influential Indent Basin Angle

One hypothesis into the failure of wire WN is that the indent basin has an angle that is non-parallel to the axis of the wire. As the indent profile rolls in and out of the surface of wire WN, a gradually slope is formed at the indents of the indent. These gradual slopes could create large radial forces inside the concrete member.

Figure 147 illustrates the issue of the indent. The 2D plot is of four indents in a 1 inch long section of the wire. The graphs units are in mm. The 2D plot passes through the section circled in red on the 3D model. This area near the edge of the indent has a notable indent basin angle. The angles of the indent basin were measured and ranged from 1.6° to 2.3°.

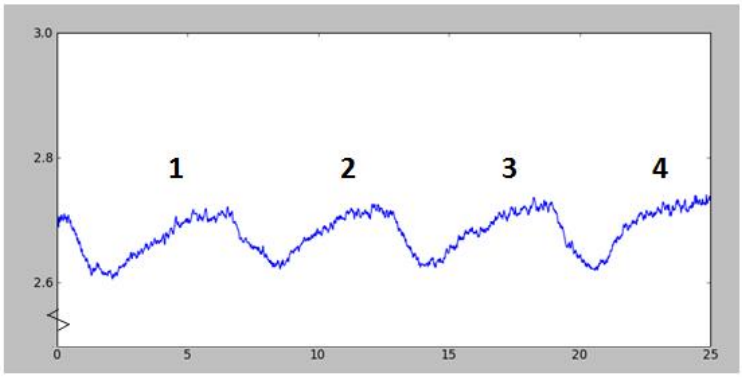

Indent	Angle (Deg)
1	1.8
2	1.9
3	1.6
4	2.3

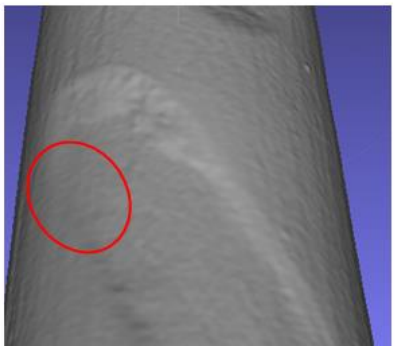

Figure 147. Potential Cause of Cross Tie Failure

The failed wire was compared to the machined reinforcement wires within the study. The failed wire is most comparative of the large depth 15° edge wall machined wires. This machined wire was proven through testing to have a high splitting potential. Figure 148 compares the failed wire to the two machined wires that slip during pre-tensioned pull out tests without fracture. These wires indent profiles are visibly different from that of the failed wire.

Figure 148. Comparison of Failed Wire to Machined Geometries

6.4.6 Conclusion of Failed Wires

The wires that failed in plant is a result of the combination of deep indents and shallow edge wall angles. With an average indent depth of .18 mm and an average indent edge wall angle of 11 degrees, the indents generated large splitting forces that caused the concrete member to fail. In addition the shallow edge wall angle, the indent basin was discovered to have a shallow slope as well. This further magnifies the splitting forces generated by the wire.

Visually, the wire can be seen to have a non-distinct indent profile. The gradual curvature of the indent is a clear indicator that the edge walls and indent basin are not well defined and have shallow sloping. Future reinforcement wires that have this visually appearance should not be used without testing and validation of the indent geometry.

6.5 Custom Machined Wires

Within this study, custom machined pre-stressing reinforcement indent profiles were made. Custom machined reinforcement allowed for controlled testing of the geometrical features of the indent that was not possible with the commercial reinforcements. As the commercial reinforcements had many varying geometrical features from one wire to the next, these geometrical features were often convoluted with each other making it difficult to identify which geometrical feature has a causal relationship with the wires performance.

Custom machined reinforcements provide a means of determining which range of geometrical features parameters will provide optimum performance. These wires provide a chance at creating an improved reinforcement wire design that creates a short transfer length while minimizing the fracture propensity of the wire.

Figure 149 shows the machined indent geometries created within the study. The indents are shiny from the milling operations. From left to right in the image the indents range from edge wall angles of 15°,30°,45°,60°,75°, and 90°. With two wires of each edge wall angle the wire to the left being of a shallower depth than the wire on its right.

Figure 149. Machined Indent Geometry Samples

Figure 150 shows the fixture designed and used for the machining of the reinforcement wires. The fixture was designed to have a uniform clamping force across the entire length of the reinforcement wire. The clamp edge was ground to a slight angle so that the horizontal clamping forces also generated a downward holding force for the wire. This ensured that natural bend of the wire was straightened for the machining operation.

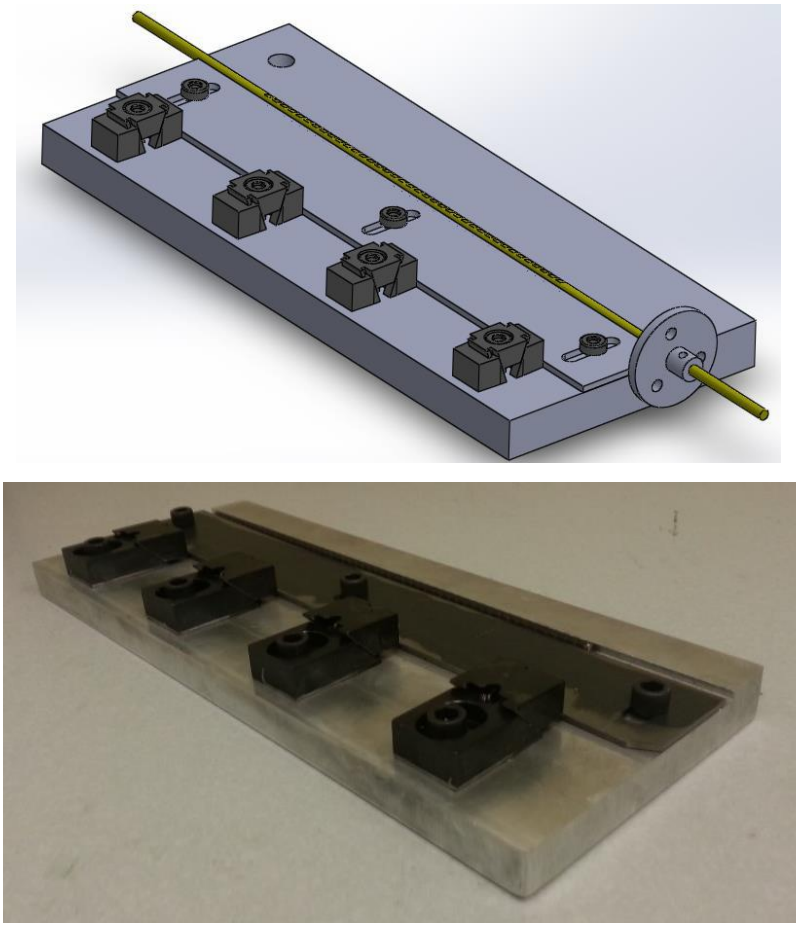

Figure 150. Reinforcement Wire Fixture

Figure 151 shows the dimensions of the end mills used. The end mills were custom 1/8" diameter mills made of tungsten carbide with an aluminum-titanium-nitride (AlTiN) coating. These six end mills were used along with a standard end mill with a no chamfer. Two end mills were used at the 15° angle as the depth of cut is limited by the height of the chamfer.

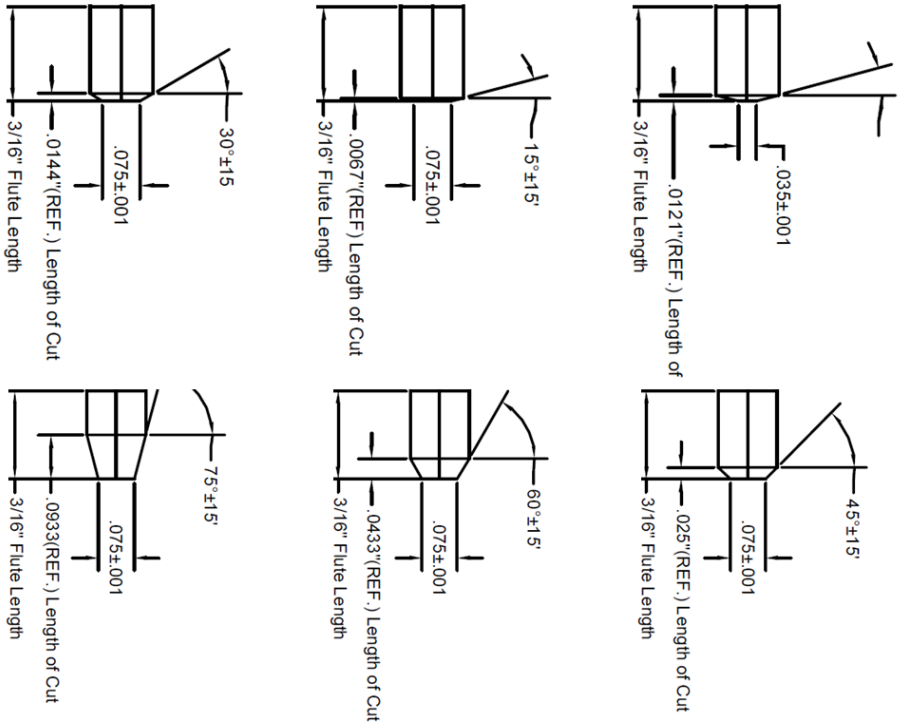

Figure 151. End Mill Dimensions

Figure 152 shows the machining process used. The indents were machined on a 3 axis HAAS VF-2 CNC mill. The cutting path of the tool was calibrated through iterative testing to ensure the wires were parallel to the machining operation. Two rows of indents were machined at a 45° angle to the axis of the wire which closely matches the orientation of the indents in commercially available wires. The third row was machined at an angle of 135°, to keep the indent orientations the same as that of commercially available chevron style reinforcements. The direction of the cutting tool was kept constant. For every indent cut the end mill began in front of wire axis and traversed behind the wire axis to keep the loading of the wire the same for every cut and remove any effects of machine backlash.

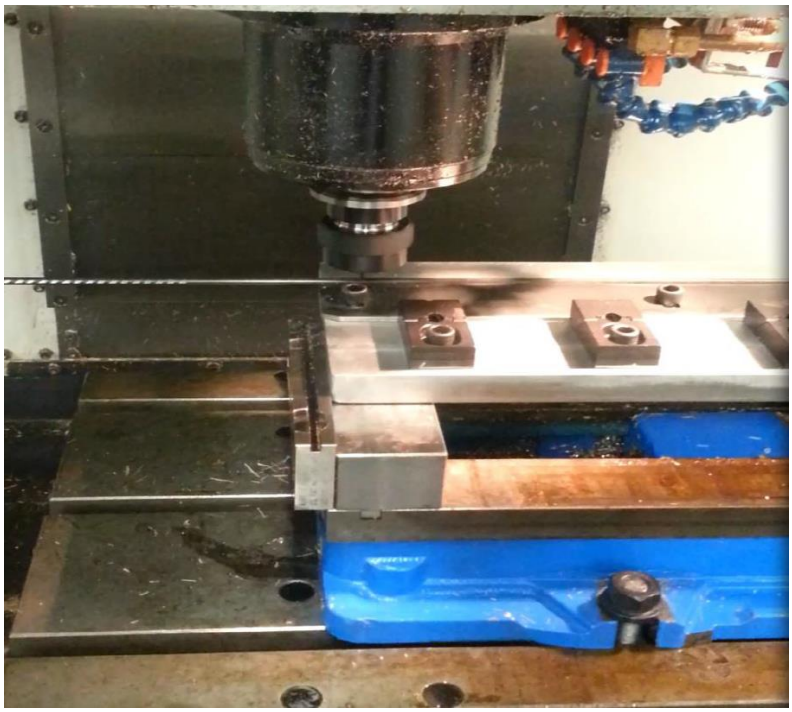

Figure 152. Machining Setup

Figure 153 shows the machined indent profiles underneath a microscope. All the machined wires have the same coloration, but under the microscope image exposure variations caused varying colors. The wires were attempted to be machined at a depth low depth comparable to the small commercial indents and a large depth attempted to be machined at a comparable to the large commercial indents. The CNC tool depth was varied a total height of 0.004" (101 microns)

from small to large depth during cutting. The CNC machined had to be calibrated via iterative testing in order to refine the process and produce consistent indent geometries for each wire.

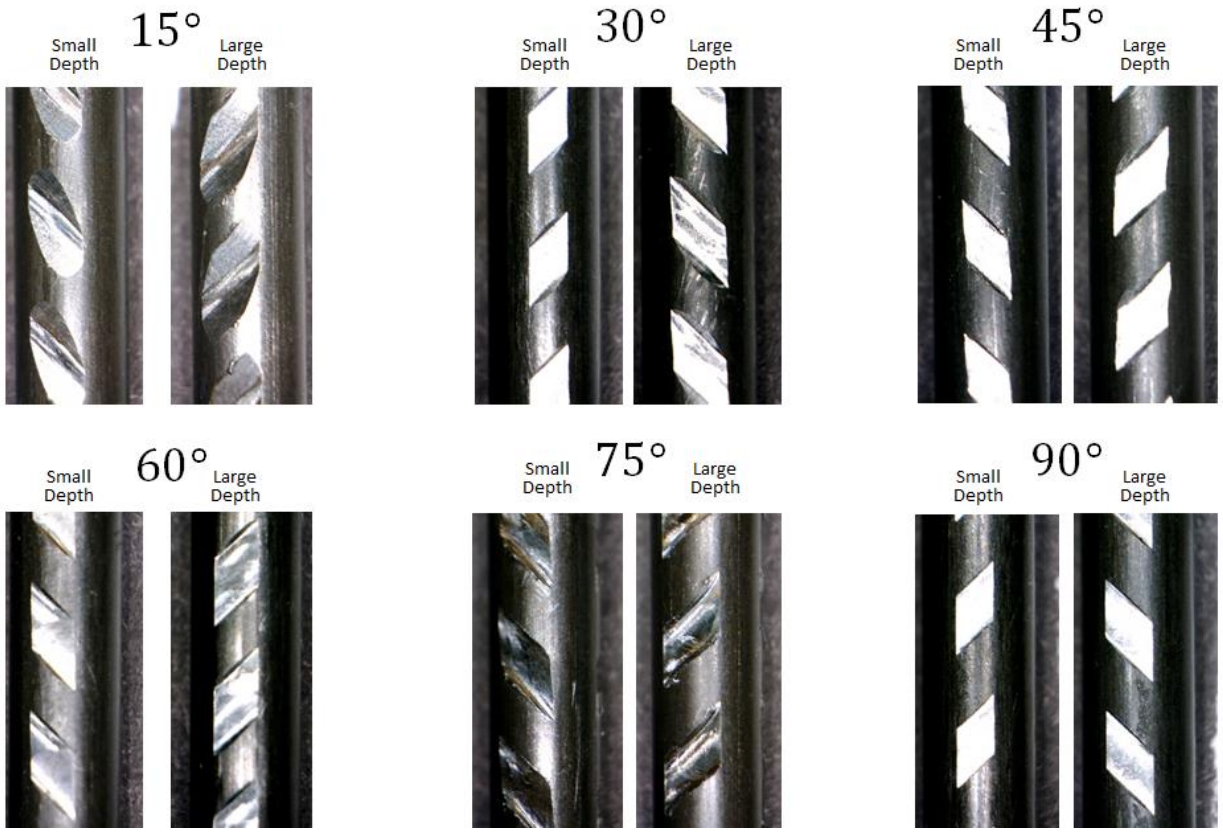

Figure 153. Machined Indent Geometries Under Microscope

Figure 154 shows the 3D models generated from the indent profiling system. All machined reinforcement wire samples were scanned with the indent profiling system prior to being used in pre-tensioned pull out tests. The profile data provides confirmation of the machined indent profile geometry.

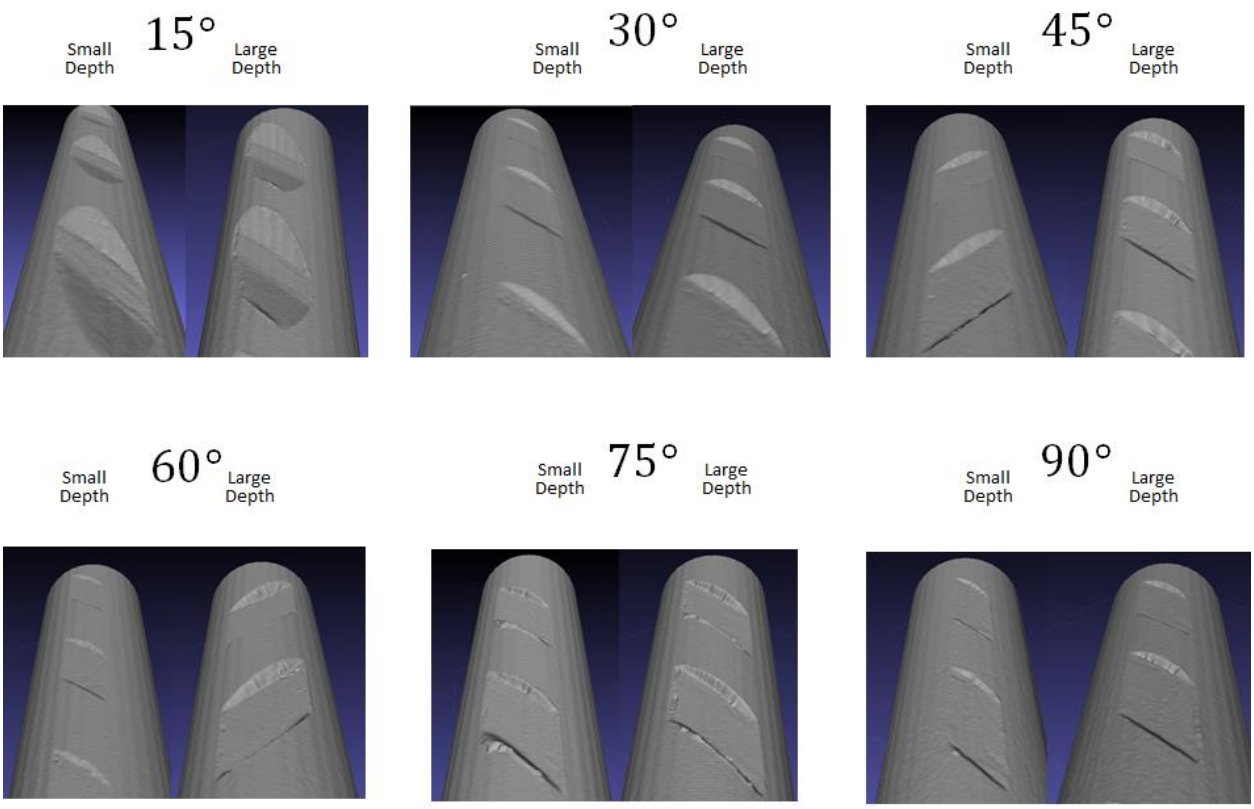

Figure 154. Machined Indent Geometries 3D Models

Table 13 shows the measurement summary for machined reinforcement wires. The indent edge wall angles were cut close to the anticipated edge wall angle. The largest difference from the anticipated was 6.6 degrees. The difference could be related to tool error or measurement error as no validation to the true chamfer of the tool existed. The actual depths machined were consistent for the 30°,45°,60°, and 90°. The 15° and 75° had to be used with different tooling a zeroing processes from the others do to limitations of the CNC available. These results provide controlled geometrical features that can be used for testing the testing of indent depth and edge wall angle in a controlled manner without convolution of other features.

Table 13. Machined Wire Measurement Summary

Tool Chamfer (Deg.)	Tool Depth (mm)	Actual Depth (mm)		Indent Width (mm)		Angle 1 (Deg.)		Angle 2 (Deg.)	
		Avg.	Std. Dev.	Avg.	Std. Dev.	Avg.	Std. Dev.	Avg.	Std. Dev.
15	0.305	0.310	0.015	4.516	0.119	11.1	0.8	10.6	0.9
15	0.406	0.140	0.015	4.669	0.139	13.1	0.8	13.5	1.5
30	0.305	0.158	0.022	3.631	0.078	20.4	4.0	17.7	4.7
30	0.406	0.261	0.021	4.059	0.076	23.1	4.1	19.5	3.9
45	0.305	0.156	0.022	3.181	0.078	30.1	7.4	24.5	6.2
45	0.406	0.245	0.019	3.379	0.093	28.6	7.3	33.5	5.9
60	0.305	0.142	0.026	3.130	0.042				
60	0.406	0.245	0.028	3.294	0.044				
75	0.305	0.286	0.012	3.145	0.084				
75	0.406	0.387	0.024	3.148	0.140				
90	0.305	0.142	0.027	3.664	0.071				
90	0.406	0.217	0.024	3.856	0.103				

These machined reinforcement wire geometries were used in pre-tensioned pullout tests. The findings from this study found that an optimal indent edge wall and indent depth range exists. The indents that did induce splitting were the shallow depth indents with edge wall angles varying between 35 and 50 degrees. All the large depth machined wires induced splitting in the pre-tensioned pullout tests [11, 25].

Table 14. Machined Wire Pre-Tensioned Pullout Testing

Cutting Tool	Effective Edge Wall Angle (Deg.)	Depth (mm)	Result
15	10.7	0.31	Fractured
30	22.2	0.158	Fractured
45	35.2	0.156	Slipped
60	50.7	0.142	Slipped
75	69.2	0.286	Fractured
90	90	0.142	Fractured

6.6 Optimal Wire Parameters

An indent with an edge wall angle between 35 and 50 degrees and a depth of about 140 to 170 microns deep, has the ideal bonding characteristics for minimizing transfer length and minimizing propensity for fracture. As seen in Table 15, the optimal indent parameters presented are a determined from the accumulation of results from the wires that were seen to have failed in plant, the machined wires, and the commercially available reinforcement wires in the industry. The deeper the indent the greater influence it will have on the concrete structure and the more likely it will cause fracture to occur. Shallower indents reduce the propensity for fracture, yet the indent must be deep enough for the desired transfer length to be achieved.

Table 15. Optimal Indent Parameters

Optimal Indent Parameters	
Indent Depth (microns)	140-170
Indent Edge Wall Angle (degrees)	35-50

Chapter 7 — Statistical Modeling

This chapter documents the statistical models developed that provide a multi-variant regression between geometrical features of the reinforcement wire and the pull out tests and transfer length measurements. The model was tested to predict the transfer length of reinforcement not used in the model design and was found to provide an accurate prediction of the transfer length of the concrete member.

7.1 Introduction

The objective of this research is to develop a means of providing real time quality control to the manufacture of reinforcement wires and to provide a means of assessing and improving performance characteristics of reinforcement wire. This has been achieved developing a system to measure sub-micron resolution surface profiles and extracting geometrical features autonomously. From this system, a statistical model has been created to predict how well a reinforcement wire will perform given its known geometry. For this study the metric to measure the pre-stressing steel reinforcement wires performance is the transfer length. This was chosen as the pre-stressing steel reinforcement wires in consideration are intended to be used in pre-stressed concrete rail road ties where transfer length is a critical quality control metric.

7.2 Nomenclature

In Table 16. Nomenclature a list the list of geometrical features considered in this study and their abbreviations is shown. In total eighteen different geometrical features were considered in the development of this mathematical model.

Table 16. Nomenclature

Abbreviation	Name
AvgVal	Average Value
Axialdist	Axial Distance of Indent
Depth	Indent Depth
EdgePSA	Indent Edge Projected Surface Area
EdgePSAtfsa	EdgePSA divided by EdgeTFSA
EdgeSlope	Indent Edge Slope
EdgeTFSA	Indent Edge Triangular Facet Surface Area
EL	Ellipsoidal Length
EW	Ellipsoidal Width
Lap1	Laplacian Filter Single Application
Lap2	Laplacian Filter Double Application
Ori	Indent Orientation
PSA	Projected Surface Area
PSAcm	Projected Surface Area per cm
RotatDist	Rotational Distance of Indent
TFSA	Triangular Facet Surface Area
TL	Transfer Length
VV	Volumetric Void
VVcm	Volumetric Void per cm
ZL	Zhao-Lee Transfer Length

7.3 Bond Index Number

The goal of this research is to develop a Bond Index Number (BIN) and a means to calculate the number for the current pre-stressing steel reinforcement wire types in the market. The BIN is a metric to describe the performance of a pre-stressing reinforcement wire given its geometrical characteristics. For this study the Transfer Length (TL and ZL) of the pre-stressing wire in a concrete prism was used as the performance metric that the BIN would predict. The BIN is defined by the following characteristics:

- A single number that is scaled to the performance of the pre-stressing wire
- The number is determined by the geometrical features that define the wire
- The number is applicable for commercially available wire types

By developing a statistical model that predicts the transfer length using the wires geometrical features as input parameters the bond quality can be assessed. For this study the transfer length serves as the BIN. Throughout this paper the transfer length is denoted as both TL and ZL.

7.4 Input Data

In order to convert the data from the 3D models to statistics on useful geometrical features, automated feature extraction algorithms were developed. These algorithms capture features such as the depths of the indents, their lengths, widths, surface area, and etc. Table 17 shows the average measurement values and transfer length values for the data used in the statistical models.

Table 17. Averaged Input Data for Statistical Models

Measurement	Units	WB	WD	WF	WG	WH	WI	WJ	WK	WL
ZL	**(in)**	11.5	11.0	8.2	13.3	7.1	10.9	9.0	14.2	19.0
AvgVal	**(mm)**	2.573	2.574	2.557	2.644	2.555	2.583	2.581	2.707	2.682
Depth	**(mm)**	0.153	0.160	0.203	0.094	0.169	0.120	0.144	0.091	0.109
PSA	**(mm^2)**	17.579	12.985	16.973	13.497	16.919	14.263	16.003	4.359	5.594
VV	**(mm^3)**	2.688	2.079	3.457	1.257	2.847	1.701	2.296	0.398	0.607
PSAcm	**(mm^2)**	93.263	72.429	94.514	67.264	88.658	86.551	79.311	26.405	16.781
VVcm	**(mm^3)**	13.959	11.361	18.531	5.365	14.737	10.209	10.469	2.207	1.822
Ori	**(Deg.)**	41.490	45.035	43.181	45.398	46.006	45.149	43.449	3.156	2.903
EL	**(mm)**	7.465	5.703	7.258	6.328	6.895	6.798	6.658	2.929	3.436
EW	**(mm)**	3.016	2.783	3.163	2.612	3.082	2.810	2.923	2.160	2.536
RotatDist	**(mm)**	6.501	5.476	6.593	5.791	6.501	6.206	6.084	1.972	2.290
axialdist	**(mm)**	8.193	6.547	8.090	6.890	7.670	7.407	7.430	3.080	3.590
TFSA	**(mm^2)**	16.619	11.967	17.245	12.407	16.713	13.763	14.645	3.957	5.518
Lap1		2.431	2.395	2.422	2.561	2.415	2.480	2.466	2.574	2.566
Lap2		2.436	2.400	2.426	2.566	2.420	2.485	2.470	2.578	2.569
EdgePSA	**(mm^2)**	1.535	1.581	1.538	0.585	2.925	2.117	2.265	-	-
EdgeTFSA	**(mm^2)**	1.716	1.720	1.897	0.651	3.160	2.232	2.392	-	-
EdgePSAtfsa	**(mm^2/mm^2)**	0.892	0.919	0.810	0.892	0.926	0.949	0.941	-	-
EdgeSlope	**(mm/mm)**	0.264	0.237	0.249	0.218	0.145	0.140	0.136	0.114	0.096

7.5 Geometrical Feature Correlations

In total 18 different geometrical features were considered within this study. 16 of the 18 geometrical features had strong correlations with the transfer length. The following section covers the details on these geometrical features and their correlation to the transfer length. Table 18 shows the correlation matrix relating one geometrical feature to another.

Table 18. Correlation Matrix for Geometrical Features

Pearson Correlation Coefficients																			
	AvgVal	Depth	PSA	VV	PSAcm	VVcm	Ori	EL	EW	RotatDist	axialdist	TFSA	Lap1	Lap2	EdgePSA	EdgeTFSA	EdgePSAtfsa	EdgeSlope	ZL
AvgVal	1.00	-0.86	-0.27	-0.74	-0.47	-0.80	-0.04	-0.25	-0.68	-0.40	-0.33	-0.55	0.98	0.99	-0.34	-0.41	0.07	-0.14	0.64
Depth	-0.86	1.00	0.53	0.96	0.57	0.92	-0.16	0.43	0.81	0.55	0.51	0.71	-0.80	-0.80	0.19	0.29	-0.42	0.37	-0.74
PSA	-0.27	0.53	1.00	0.74	0.75	0.69	-0.66	0.89	0.70	0.81	0.89	0.82	-0.28	-0.28	0.17	0.25	-0.43	0.28	-0.49
VV	-0.74	0.96	0.74	1.00	0.69	0.94	-0.36	0.63	0.86	0.69	0.70	0.82	-0.69	-0.69	0.18	0.28	-0.51	0.41	-0.74
PSAcm	-0.47	0.57	0.75	0.69	1.00	0.85	-0.56	0.92	0.89	0.92	0.95	0.93	-0.52	-0.52	0.34	0.43	-0.27	0.22	-0.58
VVcm	-0.80	0.92	0.69	0.94	0.85	1.00	-0.34	0.72	0.94	0.80	0.79	0.91	-0.79	-0.79	0.27	0.37	-0.41	0.37	-0.74
Ori	-0.04	-0.16	-0.66	-0.36	-0.56	-0.34	1.00	-0.57	-0.31	-0.34	-0.59	-0.35	-0.06	-0.06	-0.01	-0.06	0.31	-0.14	0.07
EL	-0.25	0.43	0.89	0.63	0.92	0.72	-0.57	1.00	0.77	0.96	0.99	0.91	-0.32	-0.32	0.16	0.24	-0.41	0.34	-0.42
EW	-0.68	0.81	0.70	0.86	0.89	0.94	-0.31	0.77	1.00	0.87	0.83	0.95	-0.69	-0.69	0.49	0.59	-0.21	0.14	-0.86
RotatDist	-0.40	0.55	0.81	0.69	0.92	0.80	-0.34	0.96	0.87	1.00	0.96	0.97	-0.47	-0.47	0.28	0.37	-0.33	0.29	-0.59
axialdist	-0.33	0.51	0.89	0.70	0.95	0.79	-0.59	0.99	0.83	0.96	1.00	0.94	-0.39	-0.39	0.21	0.30	-0.40	0.32	-0.50
TFSA	-0.55	0.71	0.82	0.82	0.93	0.91	-0.35	0.91	0.95	0.97	0.94	1.00	-0.59	-0.59	0.32	0.42	-0.35	0.30	-0.72
Lap1	0.98	-0.80	-0.28	-0.69	-0.52	-0.79	-0.06	-0.32	-0.69	-0.47	-0.39	-0.59	1.00	1.00	-0.38	-0.45	0.01	-0.10	0.62
Lap2	0.99	-0.80	-0.28	-0.69	-0.52	-0.79	-0.06	-0.32	-0.69	-0.47	-0.39	-0.59	1.00	1.00	-0.38	-0.45	0.01	-0.10	0.62
EdgePSA	-0.34	0.19	0.17	0.18	0.34	0.27	-0.01	0.16	0.49	0.28	0.21	0.32	-0.38	-0.38	1.00	0.99	0.73	-0.79	-0.74
EdgeTFSA	-0.41	0.29	0.25	0.28	0.43	0.37	-0.06	0.24	0.59	0.37	0.30	0.42	-0.45	-0.45	0.99	1.00	0.65	-0.71	-0.80
EdgePSAtfsa	0.07	-0.42	-0.43	-0.51	-0.27	-0.41	0.31	-0.41	-0.21	-0.33	-0.40	-0.35	0.01	0.01	0.73	0.65	1.00	-0.96	-0.12
EdgeSlope	-0.14	0.37	0.28	0.41	0.22	0.37	-0.14	0.34	0.14	0.29	0.32	0.30	-0.10	-0.10	-0.79	-0.71	-0.96	1.00	0.22
ZL	0.64	-0.74	-0.49	-0.74	-0.58	-0.74	0.07	-0.42	-0.86	-0.59	-0.50	-0.72	0.62	0.62	-0.74	-0.80	-0.12	0.22	1.00

7.5.1 Average Value (AvgVal)

The data in the profilometer is initially retrieved in a cylindrical coordinate format. For each data point there exist a radial, angular, and height value. The radial value represents how far the surface of the reinforcement wire is from the central reference axis. All reinforcement bar types analyzed are made with a 5.32 mm diameter. However, depending on the types of indents pressed into the wire, the average value of the wire diameter may be less than the initial 5.32 diameter. By averaging all the radial values in the heat map it is hypothesized that there may be some correlation of this average value to the transfer length. A lower average value represents a wire with more indentation and as would be expected the transfer length correlates directly proportional to the average value from the profilometer. The graph in Figure 155. AvgVal vs. ZL shows a reasonably good correlation. The R-Squared of the regression is 99.95% and with a minute p-value – less than .0001 – we know that the correlation is statistically significant.

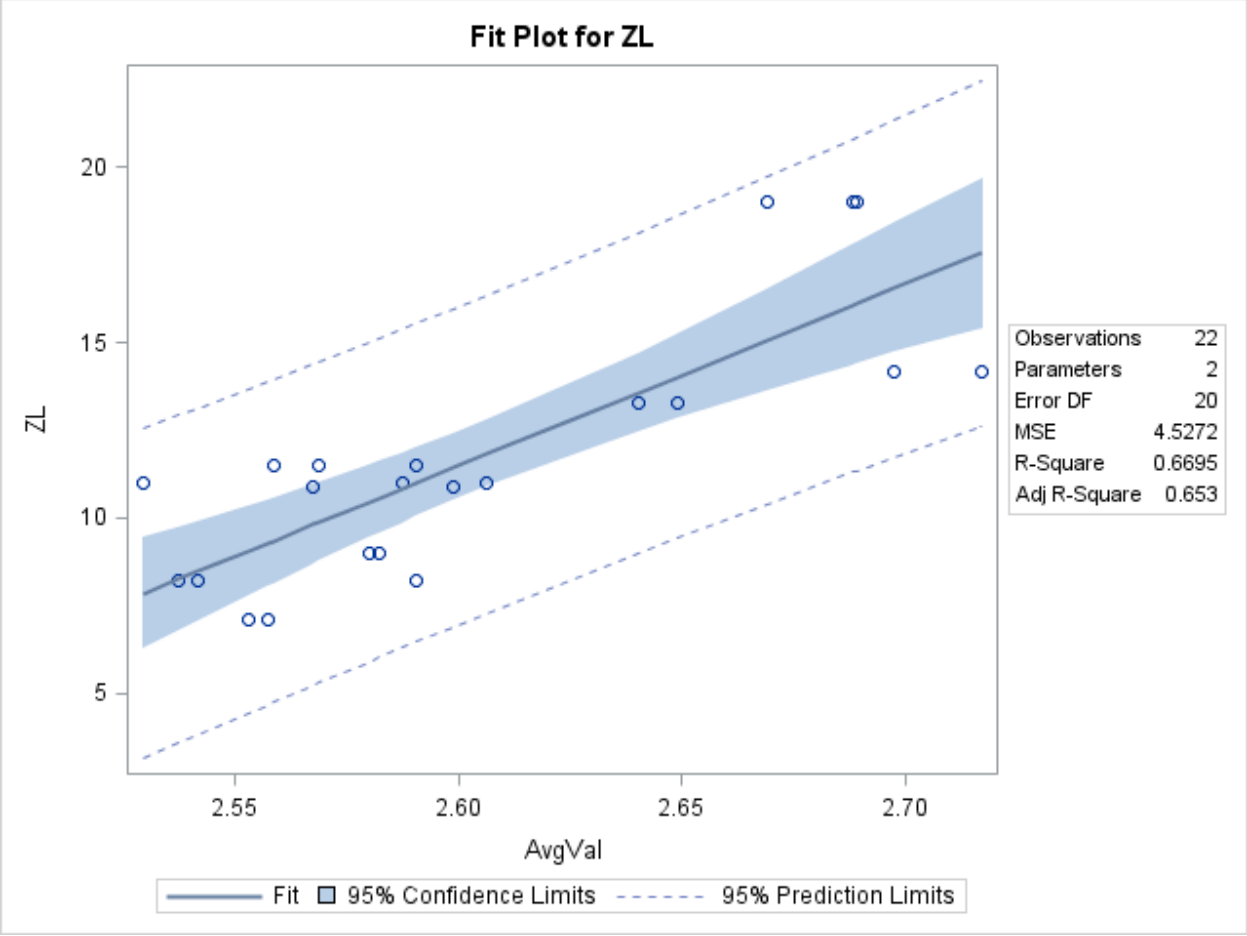

Figure 155. AvgVal vs. ZL

7.5.2 Depth (Depth)

The indent depth is calculated by taking the maximal radius value in the indent region and subtracting all other radial values in the indent from that maximum. These values are averaged together to provide an average depth value across the entire indent. The ASTM-881 standard for measuring indent depth only a few points at the indent basin are compared to the top of the indent edge wall. This new method of averaging all the data points considers the entire indent region as a whole consisting of several thousand data points. The graph in Figure 156. Depth vs. ZL shows a strong fit of indent depth to the transfer length. However, the AvgVal has better correlation than the Depth metric. This is most likely due to the AvgVal metric being all inclusive considering the entire wire surface while the indent depth only considers the regions around the indent.

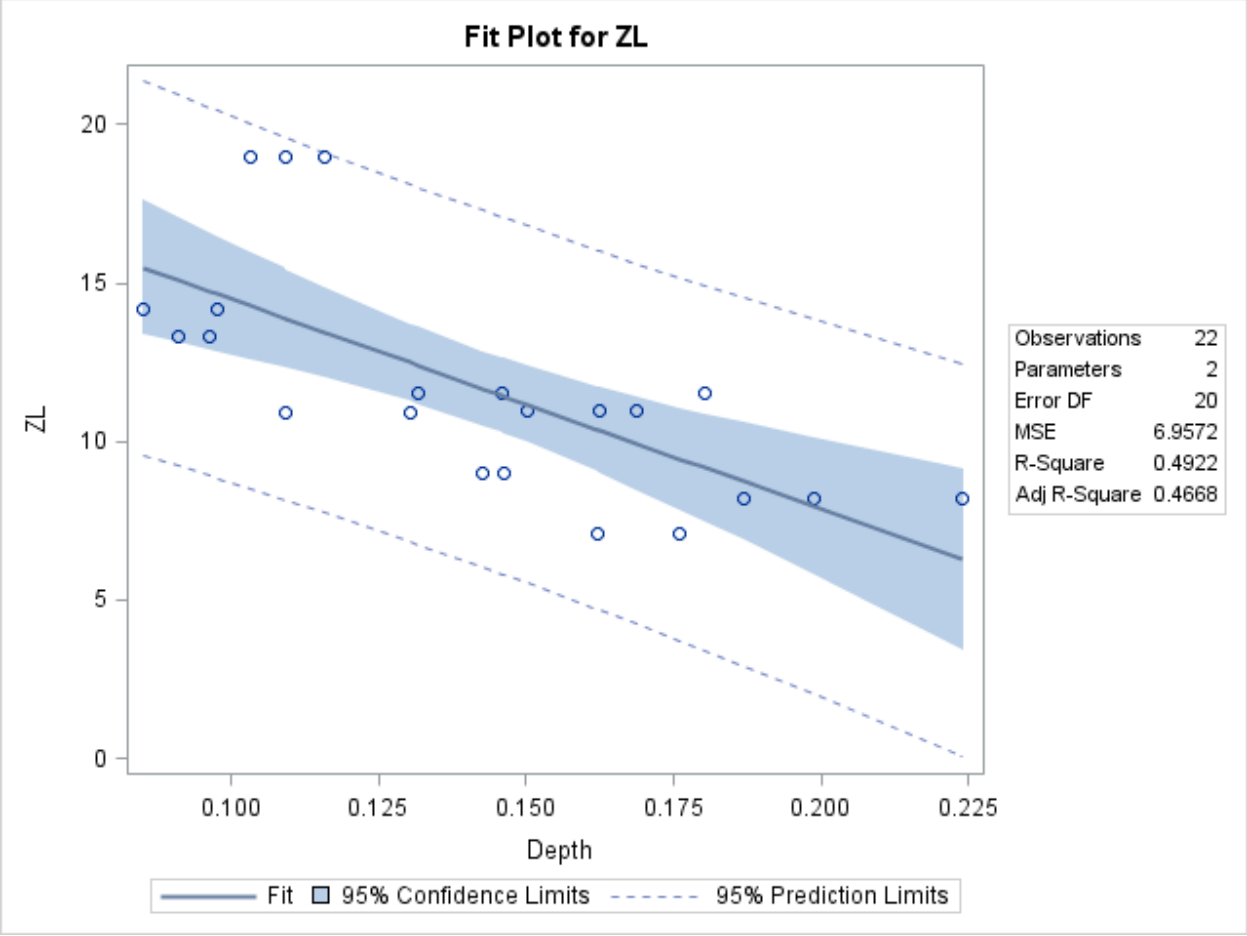

Figure 156. Depth vs. ZL

7.5.3 Projected Surface Area (PSA)

The Projected Surface area measurement is performed by summing the number of data points in the indented region and multiplying them by a constant that represents how much of the indented area each data point represents. The term "Projected" is used as the surface area in this metric does not include the impact of variations in indent depths on surface area. The projected surface area metric performs significantly better than the indent depth measurement. However, looking at the graph of the PSA, there exist two distinctly separate groups of indents. The group with higher transfer length on the left of the graph represents the dot reinforcement wire types, while the cluster of data points on the right represent the chevron style reinforcement wire types and spirals. The R-square for this correlation is 67.28%.

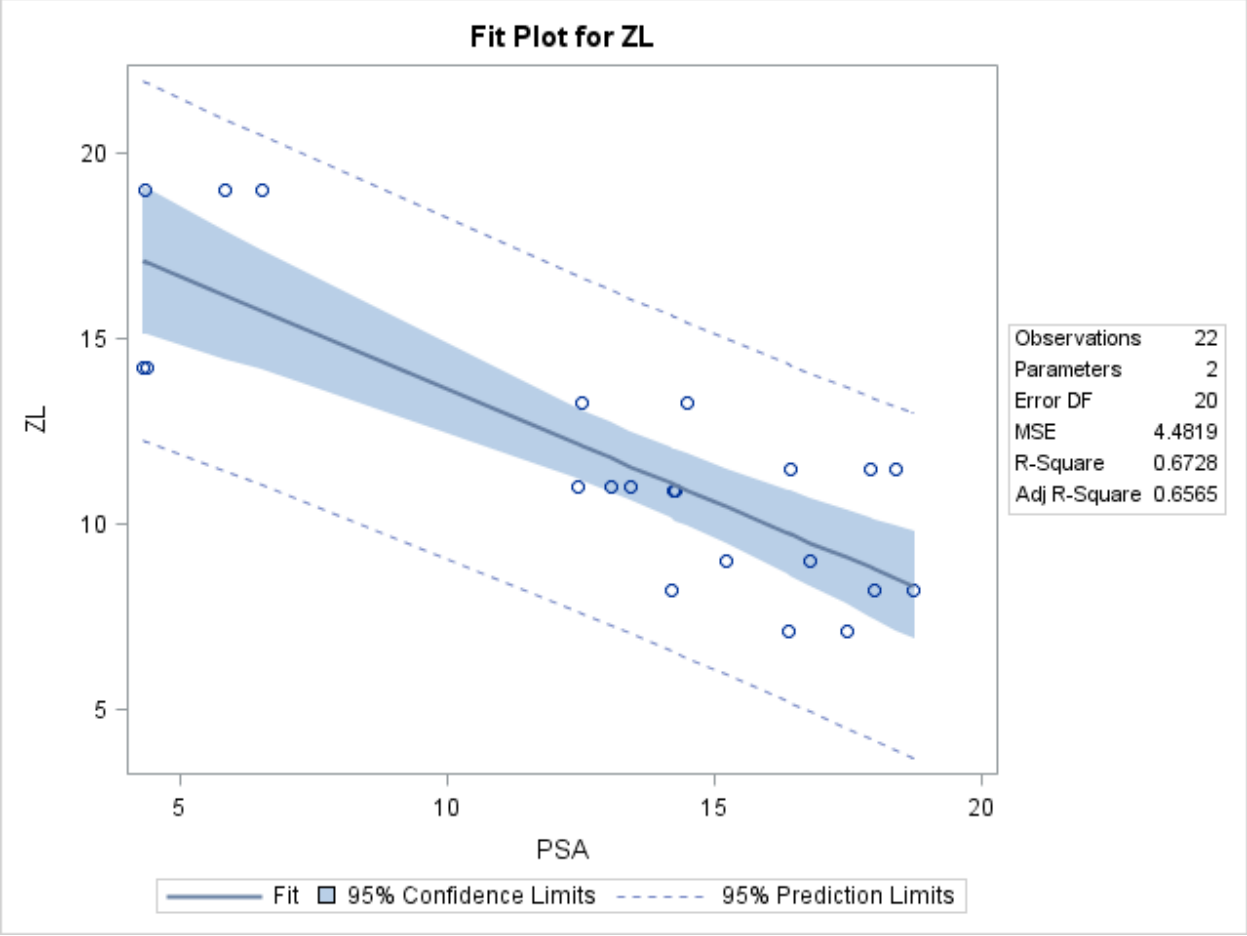

Figure 157. PSA vs ZL

7.5.4 Projected Surface Area (PSAcm)

The projected surface area per cm is measured by summing all the PSA regions within a one cm length of reinforcement wire. By analyzing the surface area per unit length wire we are able to remove some bias against small frequent indents as opposed to large and sparse indent patterns. This metric considers how much of the surface area of the reinforcement wire has been indented and performs significantly better than the PSA metric as expected. The graph in Figure 158. PSAcm vs ZL shows slightly better linearity than the PSA metric and with an R-squared of 75.46% from the ANOVA it is a better metric than PSA.

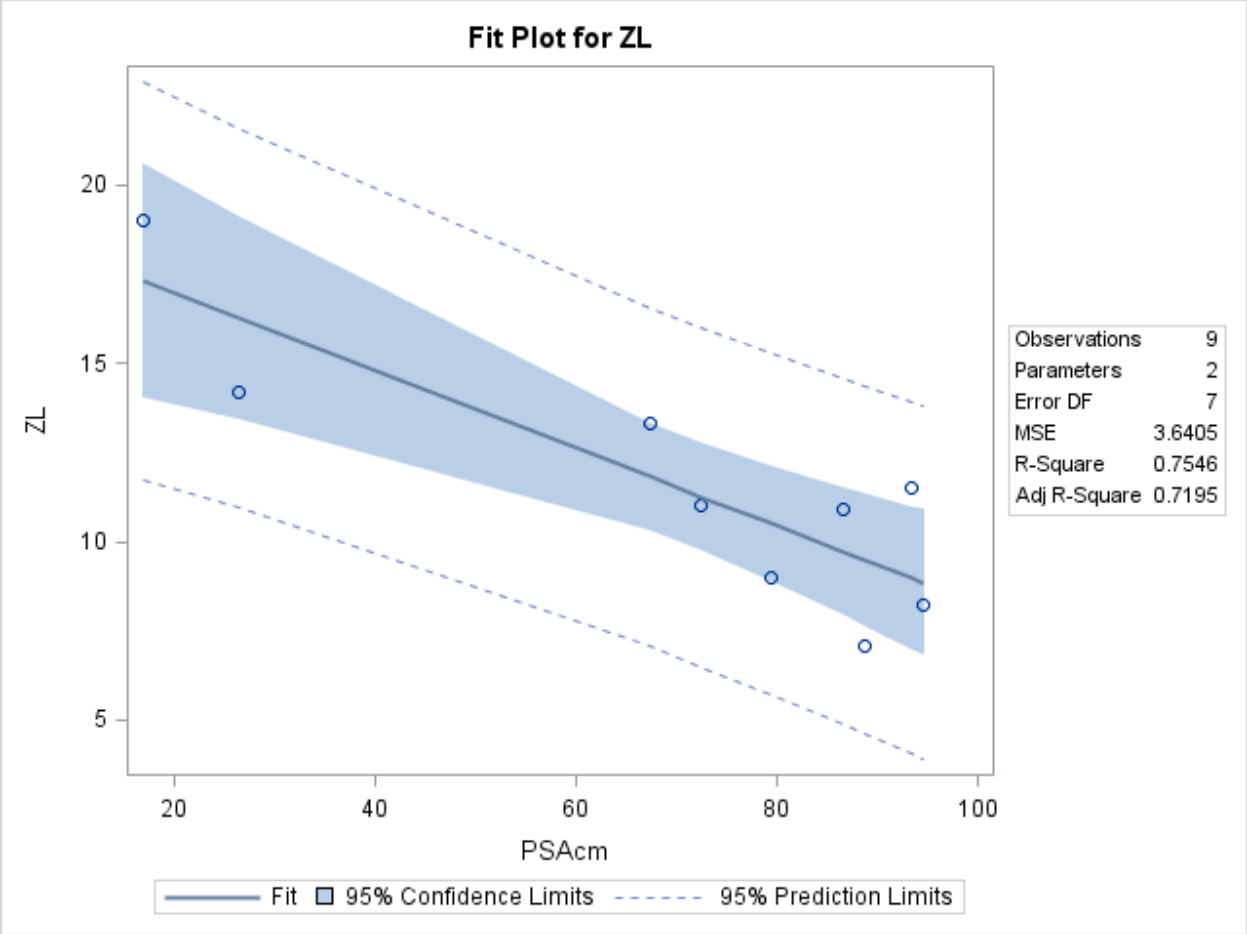

Figure 158. PSAcm vs ZL

7.5.5 Volumetric Void (VV)

The volumetric void is measured by multiplying the average indent depth by the projected surface area. The goal of this metric is to create a quantitative measure of how much concrete will be embedded into the reinforcement wire indent when the wire is used in a concrete railroad tie. The hypothesis for this metric is that larger amounts of concrete embedded passed the convex hull of the wire will lead to stronger bonds and lower transfer lengths. This metric is much more ideal the PSA or PSAcm metrics. This can be seen in the graph. There is a much more uniform and spread than what is seen in the surface area metrics. The R-square in addition is better than the PSA metric yet not better than the PSAcm. However, given the graphical spread, this metric is more preferable than the surface area measurements.

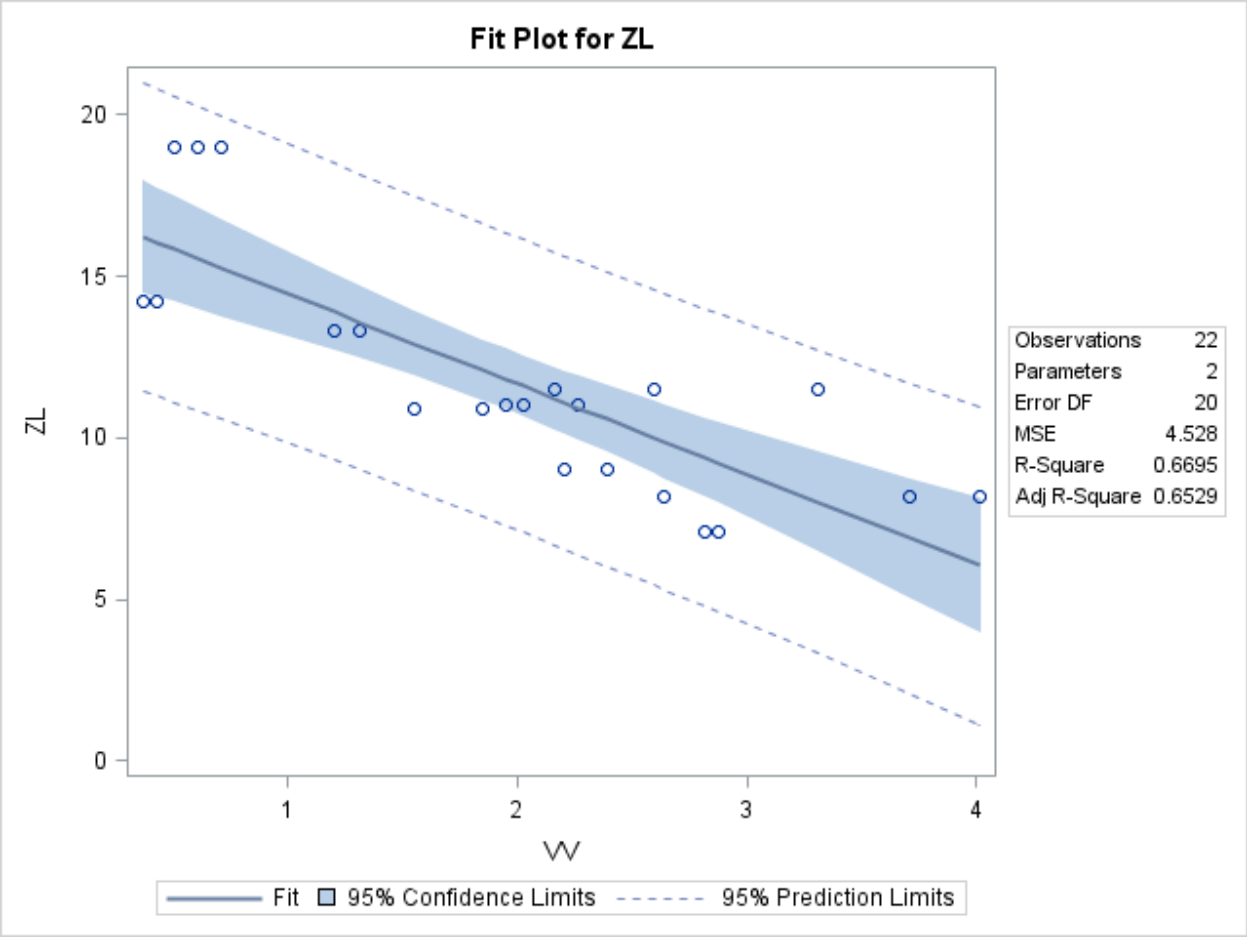

Figure 159. VV vs. ZL

7.5.6 Volumetric Void (VVcm)

The volumetric void is measured by summing all VV regions within a 1 cm length of reinforcement wire. This metric is extremely similar to the PSAcm metric for the PSA. The intent of this metric is to consider the entire surface of the reinforcement wire and remove bias against small and frequent indents. In the same way that the PSAcm metric improved on the PSA metric, the VVcm metric is an improvement on the VV metric. This graph in Figure 160. VVcm vs ZL shows a good data spread and the R-squared of 73.72% is significantly better than the VV metric. It is important to note that the VVcm metric cannot be a complete replacement for the VV metric. The two metrics provide distinctly different information about the wire geometry and as such it is not certain which geometrical feature will be more adequate in creating a complete statistical model of the reinforcement wire behavior.

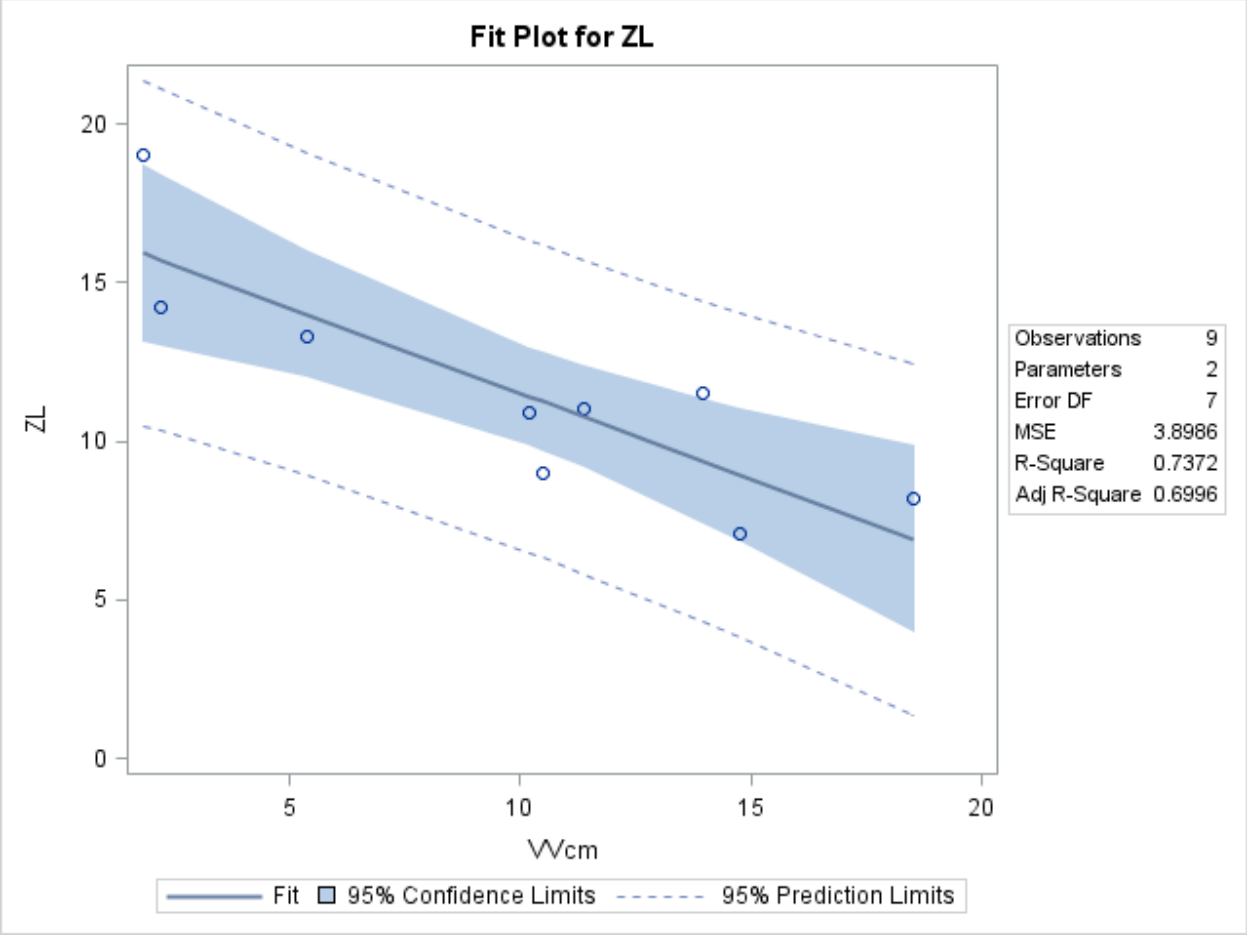

Figure 160. VVcm vs ZL

7.5.7 Indent Orientation (Ori)

The indent orientation is measured by a least squares ellipsoidal fitting on the data points that represent the indent geometry. The orientation of the fitted ellipse is then used as the orientation of the indent. All of the chevron style indents are oriented off axis from the axis of the reinforcement wire. This orientation is hypothesized to have a direct impact on the overall load bearing forces of the wire. A more off axis indent orientation is assumed to create more radial forces than an indent with edges perpendicular to the axis of the wire. However of the reinforcement wires available, nearly all of chevron style reinforcements had a nearly identical orientation angle. The dot reinforcement wire types have orientation angles aligned to the axis of the reinforcement wire. In comparison to the other metrics this one is rather poor and misleading. The result shown in Figure 161. Ori vs ZL is the same bipolar clustering of data as seen in the PSA measurements. The correlations shown are more in a practical sense the correlation between dot and chevron reinforcement wire type. It is still a strong correlation and it may have significant potential in the development of the statistical model.

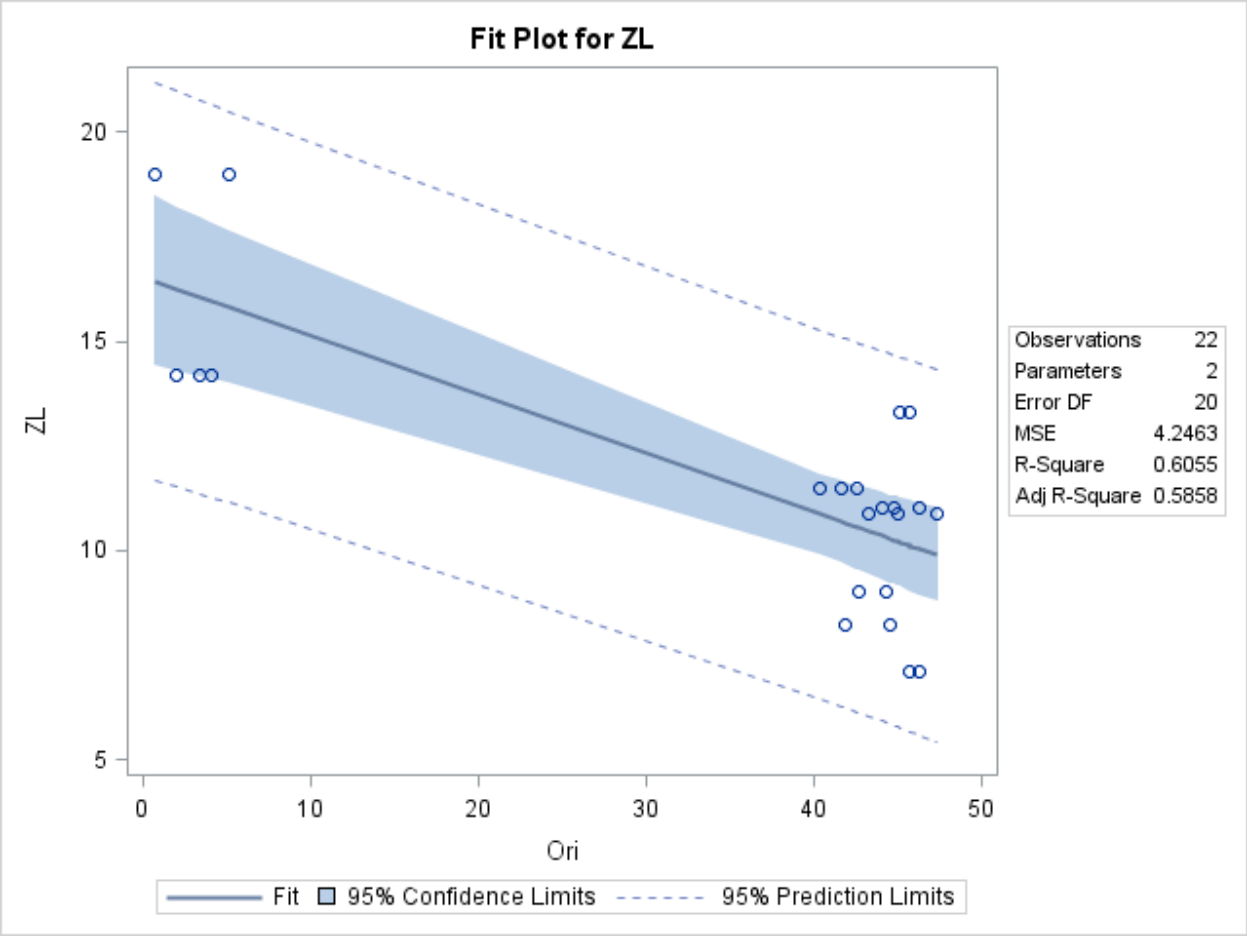

Figure 161. Ori vs ZL

7.5.8 Ellipsoidal Length (EL)

The fitted ellipse algorithm as mentioned in the Ori measurement provides several metrics. One of which is the ellipsoidal length; the ellipsoidal length is the long axis of the above mention fitted ellipse. This provides a measurement to the length of the indented region. The length of the indent is a required measurement by the ASTM-881 protocol. The measurement suffers the same issues that the Ori measurement has in the bipolarity created by differences in dot type reinforcements verse chevron type. However, looking at just the data samples representing the chevron type, a tread is still visible within the data. The R-square is 55.76%.

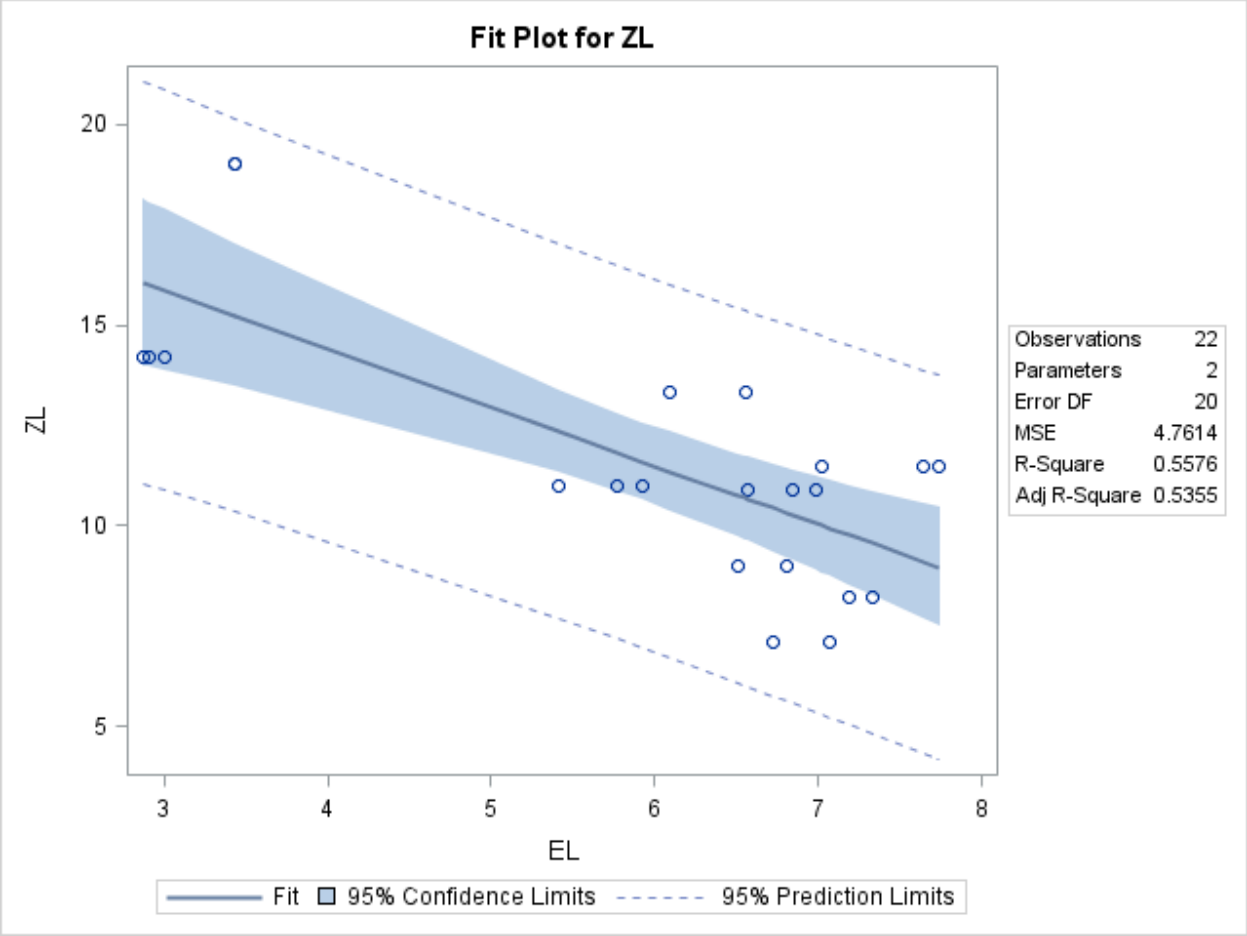

Figure 162. EL vs ZL

7.5.9 Ellipsoidal Width (EW)

The ellipsoidal width is the short axis of the above mentioned fitted ellipse. This measurement appears to be the most useful of the fitted ellipse measurements. There is a significant amount of variation within the chevron wire type ellipsoidal width that we can see the trend is not based on the division of chevron verse dot reinforcements. The R-squared is 51.43%, which is not as good as that from the EL. However, the spread of the data within the correlation makes this geometrical feature a much more desirable metric for developing the statistical model.

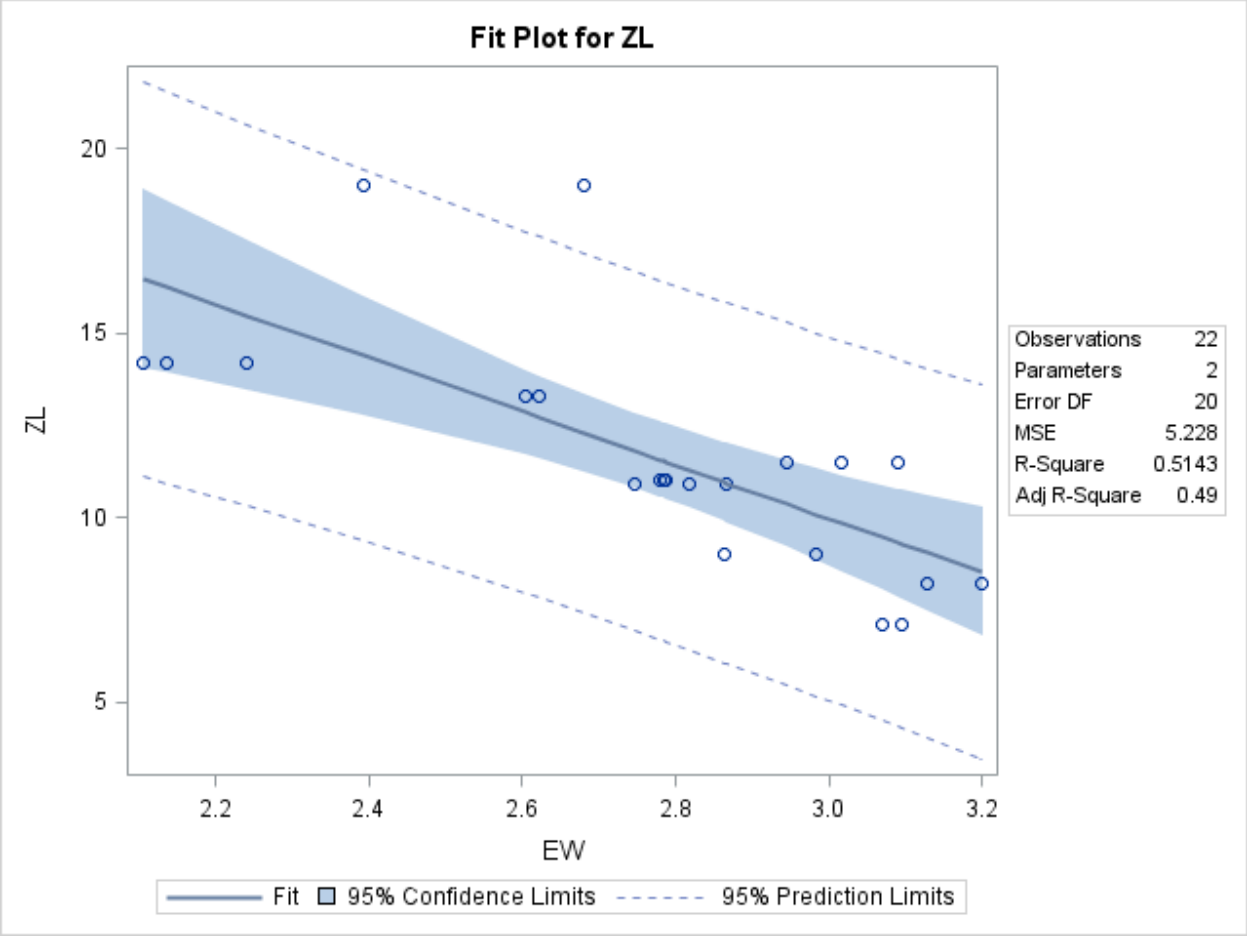

Figure 163. EW vs. ZL

7.5.10 Rotational Distance of Indent (RotatDist)

The rotational distance is the distance the fitted ellipse runs around the rotational arc of the reinforcement wire. Given that all the chevron wires are oriented off axis from the reinforcement wire by about 45 degrees the width of the indent when measured around the circumference of the wire provides a better representation of how much concrete around the circumference of the wire is embedded into the surface. This metric has a much stronger correlation to transfer length than the ellipsoidal width. The R-squared of 61.25% is great, yet the correlation of the data again represents a bipolar effect which is much stronger than in the EW measurements.

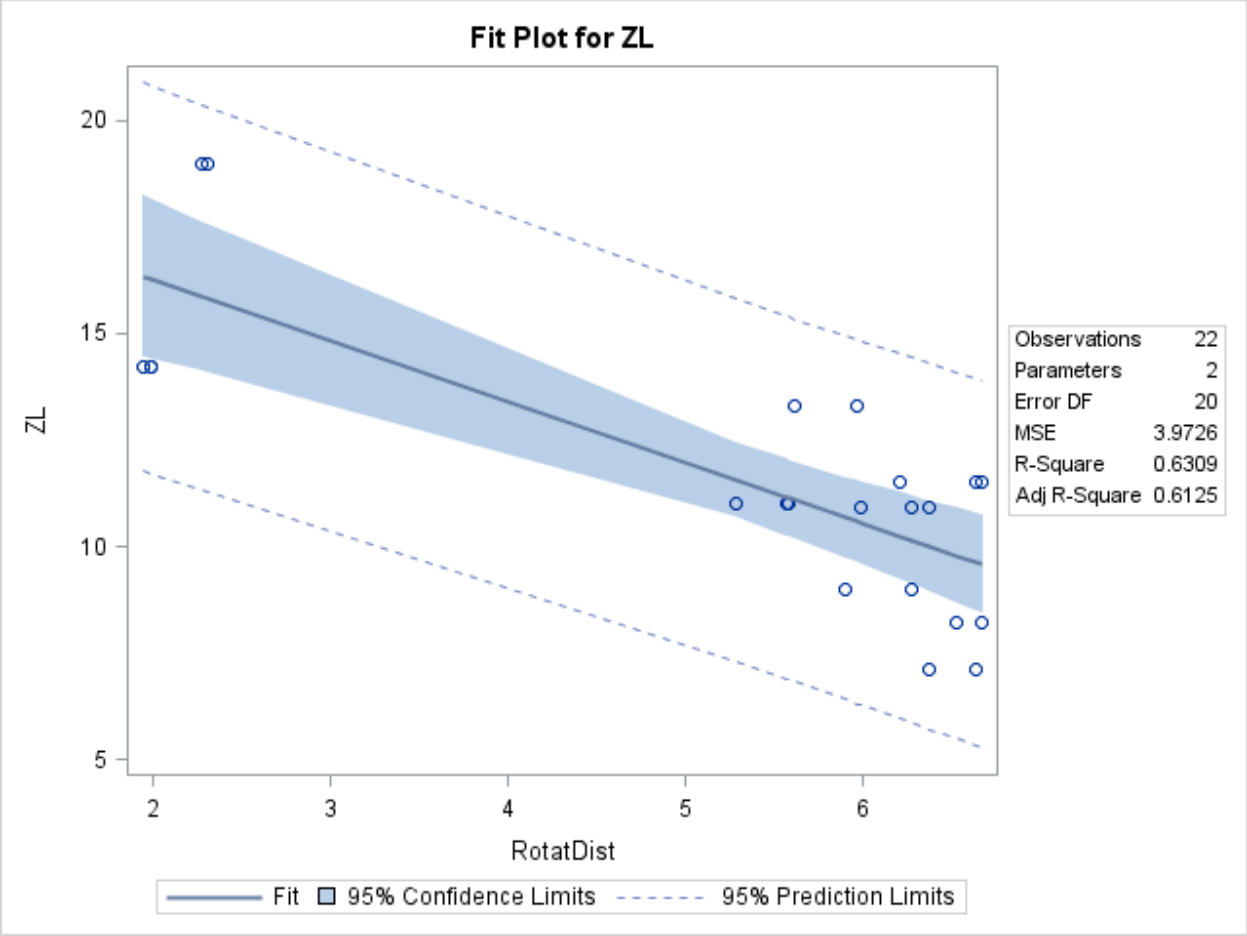

Figure 164. RotatDist vs. ZL

7.5.11 Axial Distance of Indent (axialdist)

The axial distance is the distance the fitted ellipse runs down the length of the reinforcement wire. Similar to the rotational distance of the indent, this metric describes the length of the indent running down the axis as opposed to its off axis orientation. There is little difference from this result and the result as mentioned in the RotatDist.

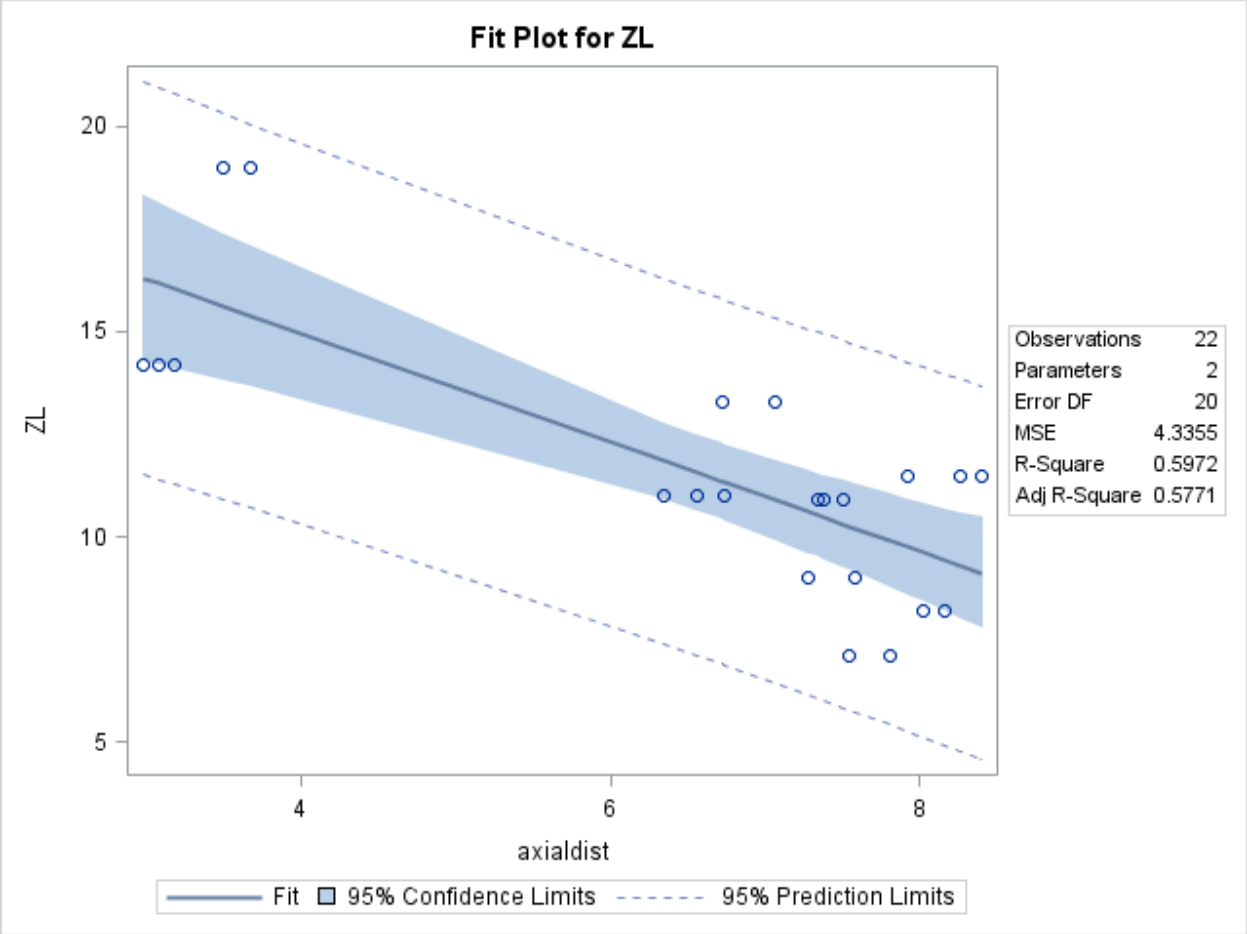

Figure 165. axialdist vs. ZL

7.5.12 Triangular Facet Surface Area (TFSA)

The triangular facet surface area is calculated by summing the individual triangular polygons that represent the surface area between 3 neighboring data points. This calculation expands upon the PSA and PSAcm measurements. The hypothesis behind this measurement is that the amount of surface bonding the indent to the concrete is a critical factor in transfer length. The difference between this measurement and PSA is that it considers the varying height effects on surface area while PSA does not. The result however, shows an almost negligible difference from the TFSA and the PSA.

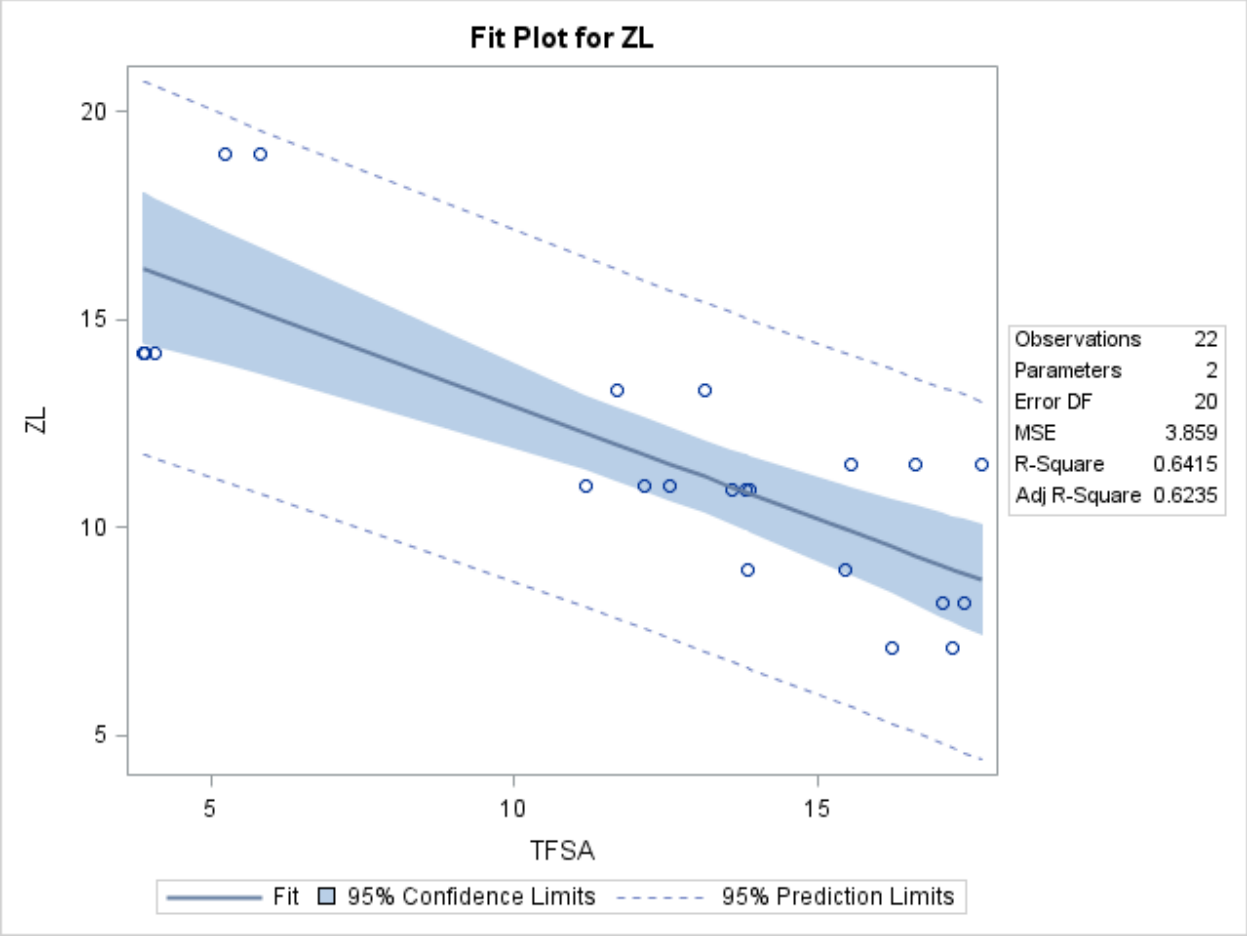

Figure 166. TFSA vs. ZL

7.5.13 Indent Edge Project Surface Area (EdgePSA)

The EdgePSA is calculated in the same manner as the PSA yet it is applied only to the indent edge wall region. Metrics about the indent edge are particularly important. The indent edge walls provide the primary surface for pre-tensioning forces to be exerted unto the surrounding concrete. The EdgePSA is the same projected surface area calculation as PSA yet looking at only at the indent edge, as this metric is "projected" area and the indent edge wall is typically rather steep, the difference between projected surface area and triangular facet surface area is more substantial that on the PSA and TFSA metrics. These edge metrics are important when developing a statistical model as they provide a unique set of information compared to metrics on the indent as a whole. The correlation is fairly strong at 54.71% and the spread of the data in the regression in Figure 165. axialdist vs. ZL looks fairly good except for a few outliers.

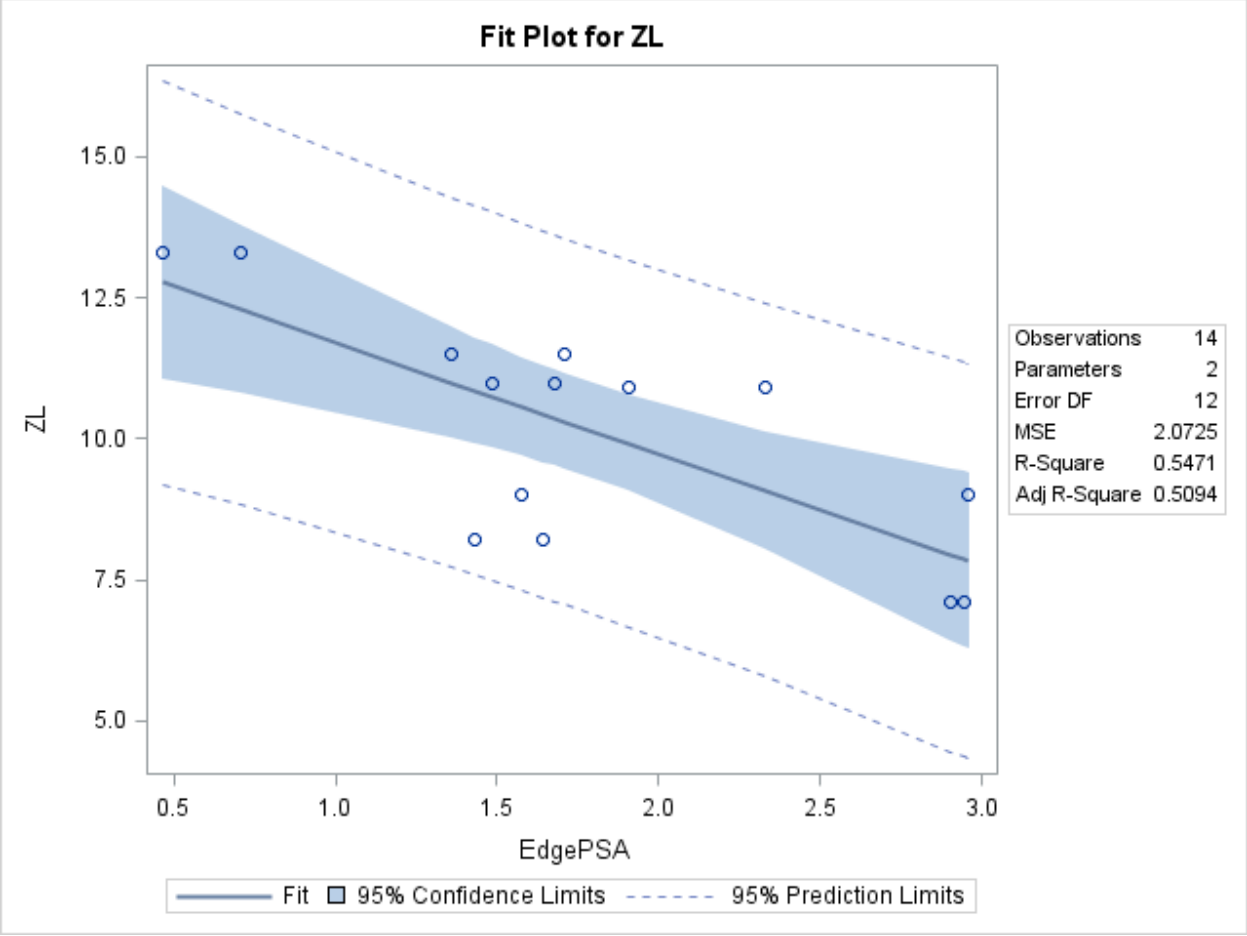

Figure 167. EdgePSA vs. ZL

7.5.14 Edge Triagular Facet Surface Area (EdgeTFSA)

The EdgeTFSA is calculated in the same manner as the TFSA yet it is applied only to the indent edge wall. The hypothesis for this metric is that a larger surface area of the indent edge wall that the shorter the transfer length. As anticipated the triangular facet surface area is better metric that the EdgePSA metric. Both the EdgePSA and EdgeTFSA have low enough correlations with the other geometrical features in this study that they make for strong factors within the statistical model. The R-squared of the EdgeTFSA is 64.15% the spread of the data in the regression is very similar to that of the EdgePSA.

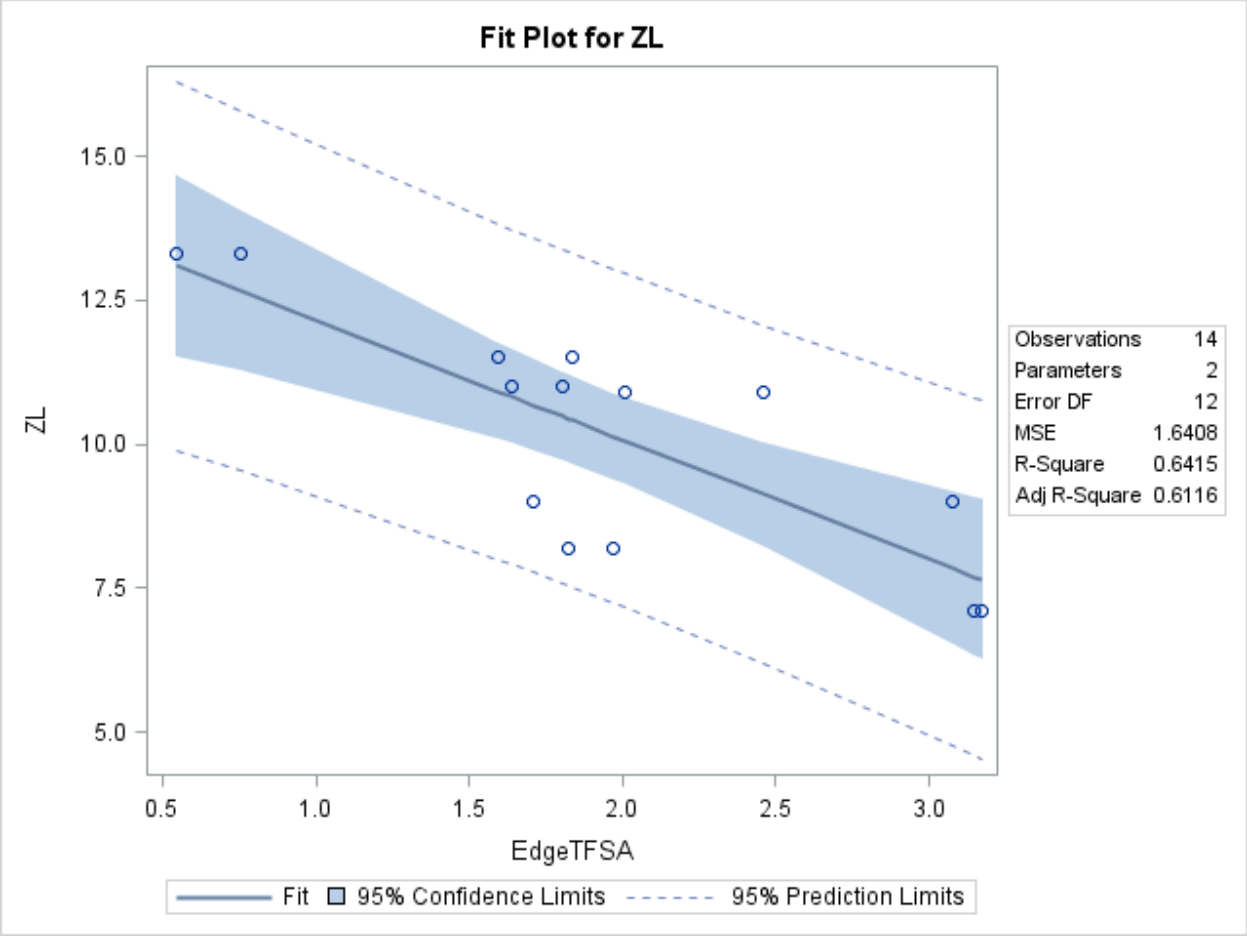

Figure 168. EdgeTFSA vs. ZL

7.5.15 Indent Edge Slope (EdgeSlope)

The indent edge slope is found by averaging a cluster of data points at the top and bottom of the indented region. The difference in the height is then divided by the difference in projected distance of the two clusters. Similar to the problems with the edgePSAtfsa there is low correlation between indent angle and transfer length.

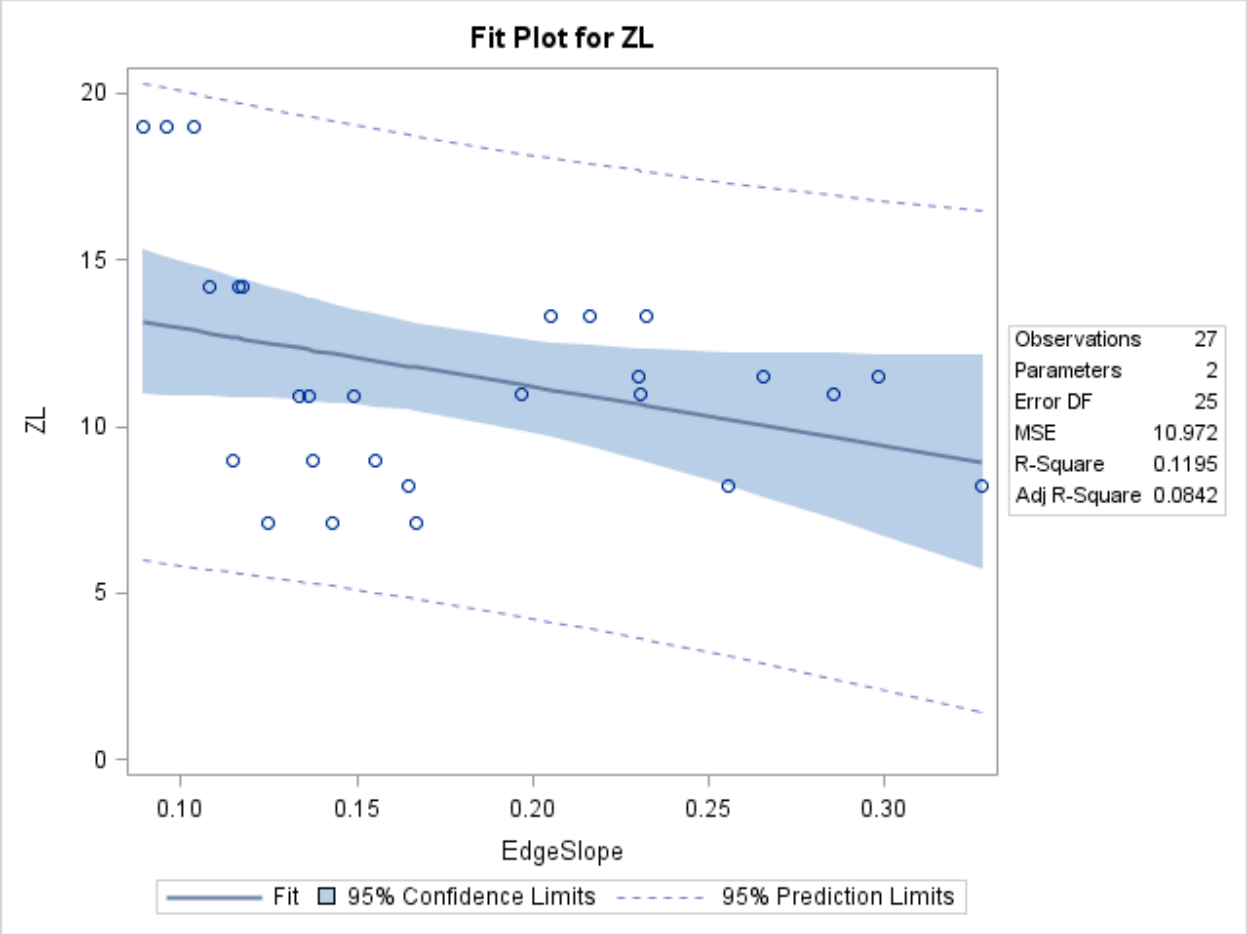

Figure 169. EdgeSlope vs. ZL

7.6 All-Possible Regression Analysis

In order to develop a statistical model to serve as a Bond Index Number of the reinforcement wire an All-Possible Regression Analysis was performed. The All-Possible Regression Analysis creates linear regressions of all combinations of geometrical features. The results from this

analysis make it easy to determine which statistical models will be the best fitting as a bond index model. [61]

The All-Possible Regression Model is broken into four sections: one factor, two factor, three factor, and four factor regressions. Going beyond four factors causes over fitting to occur in the model. The one factor model is nearly identical to single variable correlations to transfer length. There are some slight differences that occur as certain outlying and non-applicable portions of the data are left out in single variable correlations that are not left out in the All-Possible Regression Analysis. Table 19. One Factor Regression Analysis summarizes the results of the single feature model. The best fitting single variable correlation is ellipsoidal width, followed by the indent edge surface area. These two parameters describe different information about the reinforcement wire and as such have are likely to work well together in the multivariable models.

Table 19. One Factor Regression Analysis

R-Square	MSE	SSE	Variables in Model
0.7416	1.4190	7.0952	EW
0.6408	1.9728	9.8637	EdgeTFSA
0.5512	2.4645	12.3227	Depth
0.5489	2.4770	12.3851	VV
0.5458	2.4943	12.4717	VVcm
0.5416	2.5170	12.5851	EdgePSA
0.5123	2.6780	13.3901	TFSA
0.4062	3.2607	16.3037	AvgVal
0.3824	3.3916	16.9579	Lap2
0.3824	3.3917	16.9587	Lap1
0.3525	3.5557	17.7786	RotatDist
0.3337	3.6588	18.2939	PSAcm
0.2545	4.0941	20.4705	axialdist
0.2440	4.1515	20.7574	PSA
0.1799	4.5035	22.5175	EL
0.0497	5.2184	26.0922	EdgeSlope
0.0136	5.4169	27.0846	EdgePSAtfsa
0.0048	5.4651	27.3254	Ori

For the two factor All-Possible Regression analysis, many strong models are generated. All of the models shown in Table 20. Two Factor Regression Analysis have an R-Squared over 80%. The best performing model for two factors is the Indent Edge Triangular Facet Surface Area (EdgeTFSA) and the indent Volumetric Void (VV). These two factors work well together both statistically and as a verbal explanation of the bond index. When considering which factors are most likely to correlate well with transfer length, the amount of concrete within the indent and the amount of surface area opposing the axial tension of the pre-stressing forces are logically important. However, there are several models that are still very good without these parameters. The PSAcm and EW is still above 90% R-Squared and distinctly different metrics. These metrics do however describe similar information as VV and EdgeTFSA. This model helps reaffirm the importance of the VV and EdgeTFSA as predictors of a Bond Index Number.

Table 20. Two Factor Regression Analysis

R-Square	MSE	SSE	Variables in Model
0.9284	0.4915	1.9659	VV EdgeTFSA
0.9274	0.4985	1.9940	VV EdgePSA
0.9259	0.5083	2.0333	Depth EdgeTFSA
0.9194	0.5536	2.2143	Depth EdgePSA
0.9189	0.5567	2.2270	PSAcm EW
0.9161	0.5758	2.3033	EdgeTFSA EdgePSAtfsa
0.9132	0.5961	2.3844	EdgePSA EdgePSAtfsa
0.9040	0.6590	2.6361	EdgePSA EdgeTFSA
0.8881	0.7681	3.0724	EdgeTFSA EdgeSlope
0.8868	0.7770	3.1080	VV EdgeSlope
0.8827	0.8054	3.2216	EW axialdist
0.8787	0.8328	3.3311	EdgePSA EdgeSlope
0.8769	0.8453	3.3813	EL EW
0.8756	0.8537	3.4148	VV EdgePSAtfsa
0.8746	0.8609	3.4437	EW EdgeTFSA
0.8710	0.8852	3.5410	EW EdgePSA
0.8660	0.9201	3.6805	VVcm EdgeTFSA
0.8643	0.9315	3.7258	EW EdgeSlope

For three factor models in the All-Possible Regression analysis shown in Table 21. Three Factor Regression Analysis, there is a good balance between strong fitting models and not over fitting the model to the data. All of the models generated in the three factor analysis are considered very strong. The lowest ones still have an R-squared over 96%, while the highest one is 99%. With these good fitting models, any of them are adequate solutions for serving as a Bond Index Number prediction. To select the best available model, it is important to assess the statistical significance of the results. This is covered in more detail later.

Table 21. Three Factor Regression Analysis

R-Square	MSE	SSE	Variables in Model
0.9910	0.0825	0.2475	PSAcm EW EdgeSlope
0.9878	0.1115	0.3344	PSAcm EW EdgeTFSA
0.9873	0.1161	0.3482	PSAcm EW EdgePSA
0.9827	0.1584	0.4752	PSAcm EdgePSA EdgeTFSA
0.9788	0.1937	0.5811	axialdist EdgeTFSA EdgePSAtfsa
0.9781	0.2003	0.6009	Depth VVcm EW
0.9769	0.2110	0.6331	AvgVal Depth EdgePSA
0.9764	0.2157	0.6470	Ori EdgePSA EdgePSAtfsa
0.9762	0.2178	0.6534	AvgVal Depth EdgeTFSA
0.9738	0.2397	0.7190	PSAcm EdgeTFSA EdgePSAtfsa
0.9737	0.2411	0.7233	axialdist EdgePSA EdgePSAtfsa
0.9734	0.2431	0.7292	Ori EdgeTFSA EdgePSAtfsa
0.9725	0.2515	0.7546	EL EdgeTFSA EdgePSAtfsa
0.9720	0.2564	0.7693	PSAcm EW EdgePSAtfsa
0.9700	0.2746	0.8237	Depth Lap2 EdgeTFSA
0.9692	0.2818	0.8453	EL EdgePSA EdgePSAtfsa
0.9692	0.2821	0.8461	Depth Lap1 EdgeTFSA
0.9669	0.3030	0.9089	Depth Lap2 EdgePSA

For the four feature models, over fitting occurs. All of the models generated in Table 22. Four Factor Regression Analysis the data have incredibly high R-Squared values exceeding 99%. These models are acceptable to be used as a Bond Index Number; however, they will most likely lose their strong fit when additional wires are analyzed with the model. Because of this over fitting it is not recommend using these models as a Bond Index Number predictor.

Table 22. Four Factor Regression Analysis

R-Square	MSE	SSE	Variables in Model
0.9999	0.0008	0.0016	PSAcm EW EdgePSAtfsa EdgeSlope
0.9996	0.0053	0.0106	Depth VVcm EW EdgeSlope
0.9996	0.0061	0.0122	Ori RotatDist EdgePSA EdgePSAtfsa
0.9995	0.0067	0.0134	Ori EL EdgePSA EdgePSAtfsa
0.9994	0.0089	0.0177	Ori TFSA EdgeTFSA EdgePSAtfsa
0.9993	0.0095	0.0189	Depth VVcm EW EdgeTFSA
0.9993	0.0096	0.0191	Ori axialdist EdgePSA EdgePSAtfsa
0.9993	0.0097	0.0194	Depth Lap1 Lap2 EdgePSA
0.9992	0.0111	0.0221	Depth VVcm EW EdgePSA
0.9992	0.0112	0.0223	PSAcm EW EdgePSA EdgePSAtfsa
0.9991	0.0121	0.0242	RotatDist axialdist EdgeTFSA EdgePSAtfsa
0.9990	0.0137	0.0275	Depth PSA EW axialdist
0.9989	0.0144	0.0289	PSAcm EW EdgeTFSA EdgePSAtfsa
0.9989	0.0148	0.0297	PSA VVcm EW axialdist
0.9989	0.0150	0.0299	Ori axialdist EdgeTFSA EdgePSAtfsa
0.9989	0.0154	0.0309	axialdist TFSA EdgePSA EdgePSAtfsa
0.9987	0.0173	0.0346	EL TFSA EdgePSAtfsa EdgeSlope
0.9987	0.0180	0.0360	Ori RotatDist EdgeTFSA EdgePSAtfsa

7.7 Results for Transfer Length by Geometrical Features

From the results of the All-Possible Regression analysis, each possible model was tested with an Analysis of Variance (ANOVA) for statistical significance. Several models were found to have stronger statistical significance than others. It is from these models that a recommendation for a Bond Index Number model is presented. An ideal model should have the following: a strong statistical significance, a strong fit to the data, and as few factors as possible.

The first model considered is shown below along with its ANOVA table in Table 23. ANOVA for Model 1 This model is very acceptable as a predictor of the Bond Index Number. The equation consists of only two factors and the p-value is negligibly small. Any p-value below .05 is considered acceptable.

$$TL = -1.35VV - 1.5EdgeTFSA + 16.28$$

Table 23. ANOVA for Model 1

Analysis of Variance					
Source	**DF**	**Sum of Squares**	**Mean Square**	**F Value**	**Pr > F**
Model	2	48.34007	24.17003	40.44	<.0001
Error	11	6.57422	0.59766		
Corrected Total	13	54.91429			

Root MSE	0.77308	**R-Square**	0.8803
Dependent Mean	10.14286	**Adj R-Sq**	0.8585
Coeff Var	7.62194		

Parameter Estimates					
Variable	**DF**	**Parameter Estimate**	**Standard Error**	**t Value**	**Pr > |t|**
Intercept	1	16.27509	0.71902	22.64	<.0001
VV	1	-1.35489	0.28923	-4.68	0.0007
EdgeTFSA	1	-1.49519	0.29732	-5.03	0.0004

The second model considered is shown below. This model builds upon the previously mentioned one by adding one more factor. This three factor model provides a slight increase in the R-squared while keeping a strong statistical significance of the model. The variable added, Ori, was known to have a low correlation to transfer length.

$$TL = -1..50\,VV - 1.45\,EdgeTFSA - .25\,Ori + 27.72$$

Table 24. ANOVA for Model 2

Analysis of Variance					
Source	**DF**	**Sum of Squares**	**Mean Square**	**F Value**	**Pr > F**
Model	3	50.34027	16.78009	36.69	<.0001
Error	10	4.57401	0.4574		
Corrected Total	13	54.91429			

Root MSE	0.67631	**R-Square**	0.9167
Dependent Mean	10.14286	**Adj R-Sq**	0.8917
Coeff Var	6.66789		

Parameter Estimates					
Variable	**DF**	**Parameter Estimate**	**Standard Error**	**t Value**	**Pr > |t|**
Intercept	1	27.71769	5.50791	5.03	0.0005
VV	1	-1.50090	0.26248	-5.72	0.0002
EdgeTFSA	1	-1.44717	0.26111	-5.54	0.0002
Ori	1	-0.25295	0.12096	-2.09	0.0630

The third model considered does not use the VV factor. This model is significantly better than the second model. The R-squared of 98% is very strong and the P-value of the model and the individual factors are all within the industry standard threshold of .05. This model equation is shown below; the parameters used are the Projected Surface Area per Unit Length (PSAcm), Ellipsoidal Width (EW), and Indent Edge Triangular Facet Surface Area (EdgeTFSA).

$$TL = .158\,PSAcm - 15.98\,EW - .78\,EdgeTFSA + 44.9$$

Table 25. ANOVA for Model 3

Analysis of Variance					
Source	**DF**	**Sum of Squares**	**Mean Square**	**F Value**	**Pr > F**
Model	3	27.12278	9.04093	81.12	0.0023
Error	3	0.33437	0.11146		
Corrected Total	6	27.45714			

Root MSE	0.33385	**R-Square**	0.9878
Dependent Mean	10.14286	**Adj R-Sq**	0.9756
Coeff Var	3.29147		

Parameter Estimates					
Variable	**DF**	**Parameter Estimate**	**Standard Error**	**t Value**	**Pr > |t|**
Intercept	1	44.90381	3.39953	13.21	0.0009
PSAcm	1	0.15797	0.02991	5.28	0.0132
EW	1	-15.98320	1.92896	-8.29	0.0037
EdgeTFSA	1	-0.77956	0.18918	-4.12	0.0259

The fourth model considered uses a total of four factors. This model has the lowest P-values all around and has a very high R-Squared of 99.99%. This model has the best results from the ANOVA, however, as mentioned previously to many factors in the model cause over fitting. In general simpler and more elegant models are preferred as opposed elaborate models with many factors. The equation for the model is shown below; this model includes all the factors in model three and has one additional factor indent edge slope (EdgeSlope).

$$TL = .16PSAcm - 18.68EW + 11.74\,EdgePSAtfsa + 26.44\,EdgeSlope + 35.36$$

Table 26. ANOVA for Model 4

Analysis of Variance					
Source	**DF**	**Sum of Squares**	**Mean Square**	**F Value**	**Pr > F**
Model	4	27.45550	6.86388	8363.64	0.0001
Error	2	0.00164	0.00082068		
Corrected Total	6	27.45714			

Root MSE	0.02865	**R-Square**	0.9999
Dependent Mean	10.14286	**Adj R-Sq**	0.9998
Coeff Var	0.28244		

Parameter Estimates					
Variable	**DF**	**Parameter Estimate**	**Standard Error**	**t Value**	**Pr > |t|**
Intercept	1	35.36408	0.85975	41.13	0.0006
PSAcm	1	0.16158	0.00254	63.69	0.0002
EW	1	-18.67894	0.14634	-127.64	<.0001
EdgePSAtfsa	1	11.73817	0.67820	17.31	0.0033
EdgeSlope	1	26.43876	0.86447	30.58	0.0011

7.8 Results for Transfer Length by Geometrical Features and Release Strength

For the reinforcement wires types considered within this research five of the types were used in the testing of 4 wire concrete prisms at 3 different release strength levels. The release strengths were 3,500; 4,500; and 6,000 PSI. This presents a unique opportunity to create a single statistical model that combines factors of both the wire design and concrete design to give an overall prediction of the performance of the concrete member transfer length. By creating a

model relying on both wire design and concrete design the model has greater utility for pre-stressed concrete manufacturers as a method of maintaining quality and predicting the performance from their controllable inputs [31].

The abbreviations for models using release strength and standard deviations is shown in Table 27.

Table 27. Nomenclature for Models with Release Strength and Standard Deviations

Abbreviation	Description
AvgAngle	Average Indent Edge Wall Angle
AvgDepth	Average Indent Depth
AvgWidth	Average Indent Width
CosSqAngle	Cosine of the Squared Edge Wall Angle
DevAngle	Standard Deviation of Indent Edge Wall Angle
DevDepth	Standard Deviation of Indent Depth
DevWidth	Standard Deviation of Indent Width
KSI	Kilo Pounds per Square Inch
PSI	Pounds per Square Inch
REL	Release Strength
TL	Transfer Length

Table 28 shows the input data used to generate these models. This data set comes from a different collection of wire measurements from that of the previous section as the previous section results were generated at an earlier phase of the indent profiling system. The wires chosen represented a variety of different commercial reinforcements. Wire WE is a spiral, wire WK is a 4-dot reinforcement type, Wires WG and WH are chevron type with shallow and deep indents respectively, and wire WA is a smooth wire. As these wires are uniquely different geometrical features had to be chosen that are ubiquitous to all wire types. Therefore the indent depths, widths, and edge wall angles were used. Other wires could not be added to the development of the model due to the costs of the performing prism tests. The standard deviations of the sampled measurements were also used. The CosSqAngle ($\cos(\theta^2)$) was also added as it was found to have a more linear relationship with the transfer length than just the indent edge wall angle alone.

Table 28. Input Data for Statistical Models with Release Strength

Wire	TL (in)	REL (ksi)	AvgDepth (mm)	AvgWidth (mm)	AvgAngle (Deg.)	CosSqAngle	DevWidth (mm)	DevDepth (mm)	DevAngle (mm)
WA	16.3	4.5	0.000	0.000	0.000	1.000	0.000	0.000	0.000
WE	7.4	4.5	0.259	6.164	15.078	-0.678	0.455	0.044	4.782
WG	11.8	4.5	0.100	3.629	25.677	0.489	0.119	0.006	8.877
WH	7.5	4.5	0.186	4.078	14.226	-0.925	0.545	0.026	3.862
WK	14.0	4.5	0.132	2.860	7.959	0.449	0.167	0.011	0.858
WA	21.4	3.5	0.000	0.000	0.000	1.000	0.000	0.000	0.000
WE	10.5	3.5	0.259	6.164	15.078	-0.678	0.455	0.044	4.782
WG	11.9	3.5	0.100	3.629	25.677	0.489	0.119	0.006	8.877
WH	11.2	3.5	0.186	4.078	14.226	-0.925	0.545	0.026	3.862
WK	17.7	3.5	0.132	2.860	7.959	0.449	0.167	0.011	0.858
WA	13.5	6	0.000	0.000	0.000	1.000	0.000	0.000	0.000
WE	7.1	6	0.259	6.164	15.078	-0.678	0.455	0.044	4.782
WG	9.8	6	0.100	3.629	25.677	0.489	0.119	0.006	8.877
WH	7.3	6	0.186	4.078	14.226	-0.925	0.545	0.026	3.862
WK	11.1	6	0.132	2.860	7.959	0.449	0.167	0.011	0.858

The correlation matrix shown in Table 29 includes the parameters for the multivariate regressions. The release strength, REL, has the lowest correlation to TL. However, previous analysis has shown that the release strength has a consistent relationship [31].

Table 29. Correlation Matrix for Statistical Models

Pearson Correlation Coefficients									
	TL	**REL**	**AvgDepth**	**AvgWidth**	**AvgAngle**	**CosSqAngle**	**DevWidth**	**DevDepth**	**DevAngle**
TL	1.00	-0.41	-0.78	-0.81	-0.58	0.79	-0.77	-0.74	-0.53
REL	-0.41	1.00	0.00	0.00	0.00	0.00	0.00	0.00	0.00
AvgDepth	-0.78	0.00	1.00	0.96	0.45	-0.89	0.88	0.95	0.35
AvgWidth	-0.81	0.00	0.96	1.00	0.66	-0.81	0.79	0.88	0.58
AvgAngle	-0.58	0.00	0.45	0.66	1.00	-0.37	0.32	0.27	0.97
CosSqAngle	0.79	0.00	-0.89	-0.81	-0.37	1.00	-1.00	-0.89	-0.28
DevWidth	-0.77	0.00	0.88	0.79	0.32	-1.00	1.00	0.88	0.23
DevDepth	-0.74	0.00	0.95	0.88	0.27	-0.89	0.88	1.00	0.22
DevAngle	-0.53	0.00	0.35	0.58	0.97	-0.28	0.23	0.22	1.00

Table 30 shows a summary from all-possible regression analysis from the data set in Table 28 for two parameters. Only select models are shown as to simplify the output. The best models that use the release strength reach an R-squared of 91%. These are not as good as some of the previous models that did not use the release strength. This is primarily due to not including all geometrical feature types. As only the indent depth, width, and edge wall angles are considered the benefits of a geometrical features such as volumetric void and indent surface area are not included. The R-square is not the only defining factor in a good model. A high statistical significance is needed ($p < \alpha: \alpha = .01$). A good model utilizes the fewest number of parameters to achieve the desired R-square. The model should have a relationship that is intuitive to users and is no more complicated than necessary to predict the transfer length. Models should avoid using parameters that have a high correlation with respects to each other.

Table 30. All-Possible Regression Summary for Additional Models (2 Parameters)

2 Parameter Models	
R-Square	**Variable in Model**
0.82	REL AvgWidth
0.80	REL CosSqAngle
0.78	REL AvgDepth
0.76	REL DevWidth
0.73	CosSqAngle DevAngle
0.73	DevWidth DevAngle
0.73	CosSqAngle DevWidth
0.72	AvgAngle CosSqAngle

The three variable models shown in Table 31 have a good balance between the number of parameters used and resulting R-square. These models are all used a combination of REL and geometrical features, which is desired as it provides a better overall prediction of the transfer length from the available design parameters that must be controlled.

Table 31. All-Possible Regression Summary for Additional Models (3 Parameters)

3 Parameter Models	
R-Square	**Variable in Model**
0.90	REL CosSqAngle DevAngle
0.90	REL DevWidth DevAngle
0.89	REL CosSqAngle DevWidth
0.89	REL AvgAngle CosSqAngle
0.89	REL AvgAngle DevWidth
0.88	REL AvgWidth CosSqAngle
0.87	REL AvgAngle DevDepth
0.87	REL AvgWidth DevWidth

Table 32 shows the results from the 4 variable models. Notice that the R-square is only marginally better than that of the 3 variable models. This makes the 4 variable models unnecessary as little additional value is obtained for the increase in model complexity. These models while have the best R-square are as practical for implementation as the 3 variable models.

Table 32. All-Possible Regression Summary for Additional Models (4 Parameters)

4 Parameter Models	
R-Square	**Variable in Model**
0.91	REL DevDepth DevWidth DevAngle
0.91	REL CosSqAngle DevDepth DevAngle
0.91	REL AvgDepth AvgWidth CosSqAngle
0.91	REL AvgDepth AvgWidth DevWidth
0.91	REL AvgWidth CosSqAngle DevAngle
0.91	REL AvgDepth CosSqAngle DevAngle
0.91	REL AvgAngle CosSqAngle DevDepth
0.91	REL AvgWidth DevWidth DevAngle

The equation below is the model found that had the highest R-squared while still maintaining statistical significance. This model uses a good variety of unique parameters. The model predicts the transfer length using the release strength(REL),indent depth($AvgDepth$), indent width($AvgWidth$), and the $cos(\theta^2)$:θ is the edge wall angle. The $\cos(\theta^2)$ was used because testing found it provided a more linear relationship to transfer length than just θ alone. Table 33 below shows the analysis of variance for the model. Although the model has a high R-squared the use of the $\cos(\theta^2)$ could be considered over fitting of the data and requires further investigation before application. Other models with good R-squared are shown later that do not rely on the use of this parameter.

$$TL = -1.86\,REL + 38.125\,AvgDepth - 2.035\,AvgWidth + 3.374 CosSqAngle + 22.132$$

Table 33. ANOVA for Model 5

Analysis of Variance

Source	DF	Sum of Squares	Mean Square	F Value	Pr > F
Model	4	298.78550	74.69638	51.82	<.0001
Error	20	28.83079	1.44154		
Corrected Total	24	327.61629			

Root MSE	1.20064	**R-Square**	0.9120
Dependent Mean	12.15200	**Adj R-Sq**	0.8944
Coeff Var	9.88019		

Parameter Estimates

Variable	DF	Parameter Estimate	Standard Error	t Value	Pr > |t|
Intercept	1	22.13166	1.65248	13.39	<.0001
REL	1	-1.86073	0.30016	-6.20	<.0001
AvgDepth	1	38.12522	13.43405	2.84	0.0102
AvgWidth	1	-2.03462	0.45514	-4.47	0.0002
CosSqAngle	1	3.37439	0.75486	4.47	0.0002

The model below provides the most basic solution that combines both a geometrical feature and release strength. The model uses the indent depth ($AvgDepth$) and the release strength (REL). The model has a descent R-Squared and strong statistical significance. Table 34 shows the analysis of variance for the model.

$$TL = -32.679\ AvgDepth - 1.86\ REL + 25.136$$

Table 34. ANOVA for Model 6

Analysis of Variance					
Source	**DF**	**Sum of Squares**	**Mean Square**	**F Value**	**Pr > F**
Model	2	255.35029	127.67514	38.87	<.0001
Error	22	72.26600	3.28482		
Corrected Total	24	327.61629			

Root MSE	1.81241	**R-Square**	0.7794
Dependent Mean	12.15200	**Adj R-Sq**	0.7594
Coeff Var	14.91447		

Parameter Estimates					
Variable	**DF**	**Parameter Estimate**	**Standard Error**	**t Value**	**Pr > |t|**
Intercept	1	25.13576	2.19024	11.48	<.0001
REL	1	-1.86073	0.45310	-4.11	0.0005
AvgDepth	1	-32.67921	4.18854	-7.8	<.0001

The equation below was the best performing model that utilized the fewest number of parameters while still including the release strength and the indent width. The simplicity of this model along with the strong R-Squared make it a good candidate for application. Table 35 below shows the analysis of variance for the model.

$$TL = -1.465\, AvgWidth - 1.86\, REL + 25.614$$

Table 35. ANOVA for Model 7

Analysis of Variance					
Source	**DF**	**Sum of Squares**	**Mean Square**	**F Value**	**Pr > F**
Model	2	269.90359	134.95179	51.44	<.0001
Error	22	57.71270	2.62330		
Corrected Total	24	327.61629			

Root MSE	1.61966	**R-Square**	0.8238
Dependent Mean	12.15200	**Adj R-Sq**	0.8078
Coeff Var	13.32836		

Parameter Estimates					
Variable	**DF**	**Parameter Estimate**	**Standard Error**	**t Value**	**Pr > |t|**
Intercept	1	25.61354	1.96676	13.02	<.0001
REL	1	-1.86073	0.40492	-4.60	0.0001
AvgWidth	1	-1.46496	0.16201	-9.04	<.0001

The model below uses the indent edge wall angle($AvgAngle$) and the release strength(REL). The ANOVA in Table 36 uses the release strength in PSI which is a thousandth of the release strength in KSI. The R-Squared is low and as such this model would not be fit for application. As been found in the individual correlations the indent edge wall angle has an overall poor correlation to transfer length.

$$TL = .248\,AvgAngle - 1.86\,REL + 23.828$$

Table 36. ANOVA for Model 8

Analysis of Variance					
Source	**DF**	**Sum of Squares**	**Mean Square**	**F Value**	**Pr > F**
Model	2	165.78620	82.89310	11.27	0.0004
Error	22	161.83008	7.35591		
Corrected Total	24	327.61629			

Root MSE	2.71218	**R-Square**	0.5060
Dependent Mean	12.15200	**Adj R-Sq**	0.4611
Coeff Var	22.31878		

Parameter Estimates					
Variable	**DF**	**Parameter Estimate**	**Standard Error**	**t Value**	**Pr > |t|**
Intercept	1	23.82830	3.26647	7.29	<.0001
REL	1	-1.86073	0.67804	-2.74	0.0001
AvgWidth	1	-0.24762	0.06392	-3.87	<.0001

The model below is similar to the previous. The only difference is that the $\cos(\theta^2)$ is used as opposed to just θ. This is a significantly better model than the previous, however, as stated earlier the use of $\cos(\theta^2)$ was needed in order to linearize the relationship between θ and transfer length. Given that the surface area of the indent edge wall varies in a non-linear relationship to variations in the edge wall angle, it is not surprising that a non-linear relationship exists between θ and transfer length. Table 37 shows the ANOVA for the below model.

$$TL = 3.877\ CosSqAngle - \ 1.86\ REL + 20.451$$

Table 37. ANOVA for Model 9

Analysis of Variance					
Source	**DF**	**Sum of Squares**	**Mean Square**	**F Value**	**Pr > F**
Model	2	260.78372	130.39186	42.92	<.0001
Error	22	66.83257	3.03784		
Corrected Total	24	327.61629			

Root MSE	1.74294	**R-Square**	0.7960
Dependent Mean	12.15200	**Adj R-Sq**	0.7775
Coeff Var	14.34283		

Parameter Estimates					
Variable	**DF**	**Parameter Estimate**	**Standard Error**	**t Value**	**Pr > |t|**
Intercept	1	20.45122	2.03471	10.05	<.0001
REL	1	-1.86073	0.43574	-4.27	0.0003
CosSqAngle	1	3.87734	0.47155	8.22	<.0001

7.9 Results for Transfer Length by Geometrical Features and Feature Variation

With a larger sample set of data acquired from the development of fourth indent profiling system, models were generated that used the standard deviation of geometrical features as parameters. The hypothesis tested with these parameters is if a wire is produced with a high amount of variation and is therefore uncontrolled, will it influence transfer length.

The model below covers uses the standard deviation of the indent width($WidthDev$) and the release strength of the concrete member. The model has a descent R-squared and shows that it is possible to utilize the standard deviation of the geometrical features as a parameter to predict transfer length.

$$TL = -13.414\, WidthDev\ - 1.86\, REL + 24.164$$

Table 38. ANOVA for Model 10

Analysis of Variance					
Source	**DF**	**Sum of Squares**	**Mean Square**	**F Value**	**Pr > F**
Model	2	249.44526	124.72263	35.10	<.0001
Error	22	78.17103	3.55323		
Corrected Total	24	327.61629			

Root MSE	1.88500	**R-Square**	0.7614
Dependent Mean	12.15200	**Adj R-Sq**	0.7397
Coeff Var	15.51186		

Parameter Estimates					
Variable	**DF**	**Parameter Estimate**	**Standard Error**	**t Value**	**Pr > |t|**
Intercept	1	24.16409	2.24935	10.74	<.0001
REL	1	-1.86073	0.47125	-3.95	0.0007
WidthDev	1	-13.41470	1.81526	-7.39	<.0001

By adding the indent depth ($AvgDepth$) to the previous model the R-squared is improved.

$$TL = -6.345\ WidthDev\ - 19.278\ AvgDepth\ - 1.86\ REL + 24.955$$

Table 39. ANOVA for Model 11

Analysis of Variance					
Source	**DF**	**Sum of Squares**	**Mean Square**	**F Value**	**Pr > F**
Model	3	265.14625	88.38208	29.71	<.0001
Error	21	62.47004	2.97476		
Corrected Total	24	327.61629			

Root MSE	1.72475	**R-Square**	0.8093
Dependent Mean	12.15200	**Adj R-Sq**	0.7821
Coeff Var	14.19314		

Parameter Estimates					
Variable	**DF**	**Parameter Estimate**	**Standard Error**	**t Value**	**Pr > |t|**
Intercept	1	24.95471	2.0867	11.96	<.0001
REL	1	-1.86073	0.43119	-4.32	0.0003
AvgDepth	1	-19.27883	8.39157	-2.30	0.0320
WidthDev	1	-6.34540	3.49673	-1.81	0.0839

This final model combines the feature variation from the 3 primary indent features indent edge wall angle($AngleDev$), indent depth($DepthDev$), and indent width($WidthDev$). With using only the standard deviations of the wire geometrical features and the release strength a model with an R-squared of 91% is obtained.

$$TL = -.426\,AngleDev - 61.543\,DepthDev\ - 7.859\,WidthDev\ - 1.86\,REL + 25.3754$$

Table 40. ANOVA for Model 12

Analysis of Variance

Source	DF	Sum of Squares	Mean Square	F Value	Pr > F
Model	4	298.95106	74.73777	52.15	<.0001
Error	20	28.66523	1.43326		
Corrected Total	24	327.61629			

Root MSE	1.19719	**R-Square**	0.9125
Dependent Mean	12.15200	**Adj R-Sq**	0.8950
Coeff Var	9.85179		

Parameter Estimates

Variable	DF	Parameter Estimate	Standard Error	t Value	Pr > |t|
Intercept	1	25.37540	1.44492	17.56	<.0001
REL	1	-1.86073	0.29930	-6.22	<.0001
WidthDev	1	-7.85930	2.39056	-3.29	0.0037
DepthDev	1	-61.54351	31.59154	-1.95	0.0656
AngleDev	1	-0.42608	0.07806	-5.46	<.0001

The models using the geometrical features of the wire and the release strength of the concrete provide a single model that can predict the performance of the concrete member using its overall key design characteristics. Developing a singular model to relate these design parameters to transfer length has great potential to serve as a quality control and design tool for manufacture of pre-stressed concrete elements, including concrete railroad ties. The models using the standard deviation of the geometrical features prove that production variation of the indent geometries can have a direct relationship to the quality of the pre-stressed concrete element.

7.10 Recommended Bond Index Number

After reviewing the previously mentioned models generated from the All-Possible Regression Analysis, model three is the best candidate for the Bond Index Number predictor (BIN). Model three meets the previously mentioned criteria of a good statistical model. With only three factors relating to the geometry of the wire, the model has an R-squared of 98% and is statistically significant. This model is able to perform well as a predictor of transfer length given the known geometry of a typical commercial wire. The equation below is a multi-variable linear regression that will accurately predict the performance of pre-stressing steel reinforcement wires currently within the market.

$$TL = .158\,PSAcm - 15.98\,EW - .78\,EdgeTFSA + 44.9$$

7.11 Conclusions

Through this statistical analysis a model was successfully developed to predict the transfer length of the wire given its known geometry. This output of the linear regression can serve as a Bond Index Number predicting how well the given wire will perform given its known geometrical parameters.

Being able to develop a BIN has significant impacts in the quality control of pre-stressing reinforcement wire manufacture and design. Being able to non-destructively assess the quality of the reinforcement wire has the potential to provide real-time quality control during manufacture and prevent defective wires being used within concrete members.

Chapter 8 — Theoretical Modeling

This chapter documents the theoretical models developed during this research. The theoretical model developed provides a mathematical representation of the interaction between pre-stressing reinforcement steel and the concrete member. The theoretical model defines the relationship between steel and concrete with fundamental physics principles. The theoretical model provides a means of calculating the coefficient of friction and the adhesive bonding forces between the reinforcement and concrete member.

8.1 Introduction

The developed model is built upon the work of W. Yeih on determining the relationship of steel rebar geometries effect on bond strength in a pullout test [38]. W. Yeih's work expands on the models generated by H. Stang on modeling the pullout force of a single fiber in a brittle matrix [19]. The model was first developed by defining in detail the geometry of the reinforcement steel. Next the detailed geometry is broken into sections and calculations are made on each of the sections to determine how much force is being applied to the concrete structure in the axial direction and radial directions relative to the reinforcement steel wire. In order to develop a model that accurately fits the performance of the wire in a pullout test, the adhesive shear stress and the coefficient of static friction between the steel and concrete surfaces must be determined. This was performed by setting up a system of linear equations and solving for the two variables. Once these are determined the model can then be used to predict the pullout force on any other reinforcement wire. In this study seven different pre-stressing steel reinforcement wires were used that have a chevron style indentation pattern.

8.2 Nomenclature for Theoretical Model

The list below contains the variables used in defining the theoretical model.

L_t: Period length of repeating indent patterns in the steel reinforcement wire

L_w: Embedment length of the reinforcement wire in the concrete cylinder during pullout tests

R: Maximum radius of the reinforcement wire

r: Radius of reinforcement wire at the indent basin

L_e: Length of the indent edge

L_{eaxi}: Length of the indent edge down the axis of the reinforcement wire

h: L_{eaxi}

L_b: Length of the indent basin

β: Indent edge wall angle

α: Orientation of indent relative to axis of reinforcement wire

P_y: Y value for the point of intersection between indent edge, indent basin, and non-indent area

P_x: X value for the point of intersection between indent edge, indent basin, and non-indent area

w_b: Width of indent basin

A_e: Surface area of indent edge wall

A_b: Surface area of indent basin

A_a: Surface area portion around the indent edge wall

A_t: Surface area between indented regions

A_s: Surface area in-between indent rows

f: Pull out force applied

d: Depth of indent

θ: β

l_{indent}: Length of the indent as measured from the top

P: L_t or axial fiber load when referencing stang's model

S: Effective yielding shear stress of reinforcement wire

μ_s: Static coefficient of friction of reinforcement wire

q_y: Critical pullout force of reinforcement wire

k: Shear stiffness of shear lag in matrix

L: Fiber embedment length

E_f: Young's modulus of fiber

A: Cross sectional area of fiber

ω: $\sqrt{k/(E_f A)}$

a: Length of debonded zone

Γ: Specific work of fracture of fiber/matrix interface

q^*: Frictional shear force per length of fiber

8.3 Background

The origin of this research traces back to Stang's development and analysis comparing a fracture mechanical approach to a stress based model for the pullout of a single fiber in a brittle matrix. This is the foundation to the geometrical model generated by W. Yeih in his analysis of a pullout experiment considering two different types of rebar cast into a concrete cylinder [38]. This research builds upon those models in the analysis of several pre-stressing steel reinforcement wires commercially available in the market and used in pre-stressed concrete railroad tie manufacture. For this study there exist seven chevron-indent reinforcements, two spiral-indent reinforcements, two dot-indent reinforcements, and one smooth wire. The key components of the model are developed and tested on the seven chevron indents as they are the most commonly used and provided the largest sample of data for testing purposes. The geometrical models generated can ideally be applied to a reinforcement wire of any geometry.

8.3.1 Stang's Model

Stang's study consisted of two models [19]. The first of which uses a stress criterion; such that debonding occurs when the shear force per length reaches the critical value, q_y. Where $P^*$is the pullout load, q^* is the frictional shear force per length of fiber, a is length of debonded zone, L is length of embedded fiber, and ω represents the constant. ω represents $\sqrt{k/E_f A}$ where k is the shear stiffness of shear lag in matrix, $E_f$is Young's modulus of the fiber, and A is the cross sectional area of the fiber. Debonding occurs at:

$$P^* = q^* a + \frac{q_y}{\omega}\tanh\big(\omega(L-a)\big) \qquad 1$$

The load where debonding first occurs is when $a = 0$. The initial pullout load,P_y^*, is expressed by:

$$P_y^* = q_y \frac{\tanh(\omega L)}{\omega} \qquad 2$$

These two equations provide a means of determining q_y through experimentation. Once q_y is determined the models can be used to predict the pullout loads for different conditions. These equations are derivations of the work from Lawrence and Laws [27,28].

The second model is based upon energy equilibrium and a fracture mechanics approach. This is represented as the ratio $\frac{q^*}{q_y} = D$. The model is applicable when $D \leq 1$. Stang concludes the following two interpretations of D:

$$D_u = \left[\left(\frac{1}{2}\right) + \sqrt{\left(\frac{1}{2}\right)^2 + \frac{2kp\Gamma}{(q^*)^2}}\right]^{-1} \qquad 3$$

$$D_q = \left[1 + \sqrt{\frac{2kp\Gamma}{(q^*)^2}}\right]^{-1} \qquad 4$$

Where Γ is the specific work of the interface between fiber and matrix. p is the perimeter of the fiber. It is important to note that Stang's model does not include the Poisson effect which occurs and has a significant effect in a traditional pull out test. Stang's model was tested on pull out tests with a steel strip bonded to a concrete matrix. The experimental data coincides well with the model, yet is limited to bond failure only and does not consider the effects of different geometries of steel.

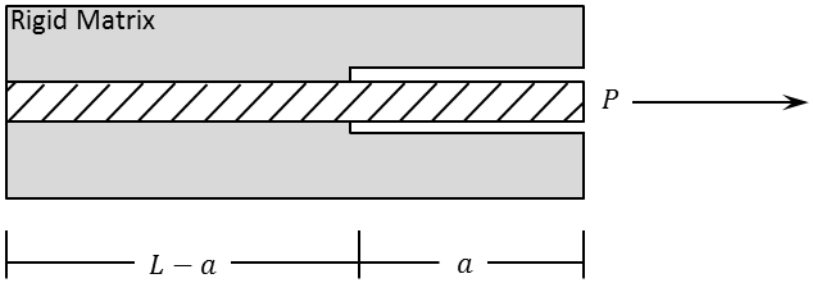

Figure 170. Stang's Experiment Design

8.3.2 Pullout Test for Determining Interface Properties between Rebar and Concrete

The experiments performed by W. Yeih were done on two different steel rebar geometries. The table of the rebar parameters is shown below. The two rebar types in W. Yeih's experiments are of a very different geometry then the pre-stressing steel reinforcement wires examined in the current study. Most notably the diameter of the reinforcements is considerably larger. These reinforcements were used in pull out tests. The shear stress of the concrete steel interface and the coefficient of friction between concrete and steel were determined in this study by using a system of two equations based on the two different rebars.

The model used in the study was a simplified model of the actual geometry of the reinforcement. In order to achieve this simplified model, an assumption is made that the effective yielding shear stress, τ_{eff}, and the coefficient of friction, μ, are constant across the surface of the reinforcement surface. The diagram below summarizes the primary forces across the rebar considered in their simplified model. S_r denotes the period length of repeating indent patterns.

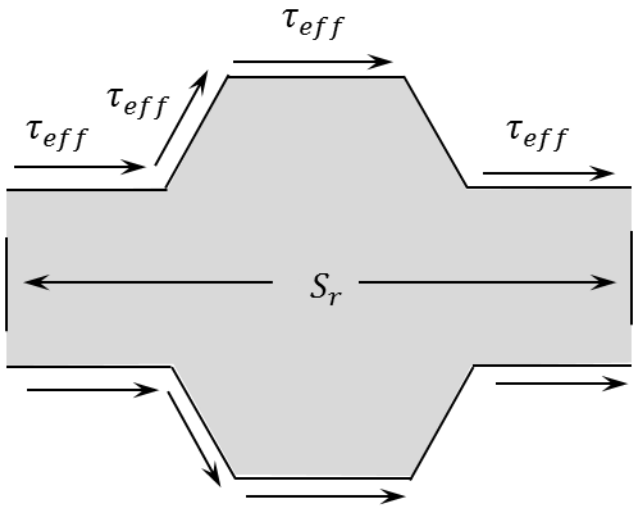

Figure 171. W. Yeih's Reinforcement Geometry

The indent edge bears a force normal to its surface denoted, N. The force parallel to the edge surface is $N\mu$. The force N also generates forces parallel to the axis of the reinforcement. The faces that are parallel to the axis of the reinforcement bar exert no frictional forces on the

assumption that they have no normal force applied. The only faces that bear load from friction are the angled surfaces. The force that is experienced on the faces parallel to the axis of the reinforcement is adhesive bonding forces.

The parameters obtained from measuring the reinforcement bars profile is shown below. The most significant difference between the two reinforcement bars in their nominal diameter, d_n, the depth of the indentation, h_r, and the indent period, S_r. The edge wall angle, β, and orientation of the indent, α, show very little variation.

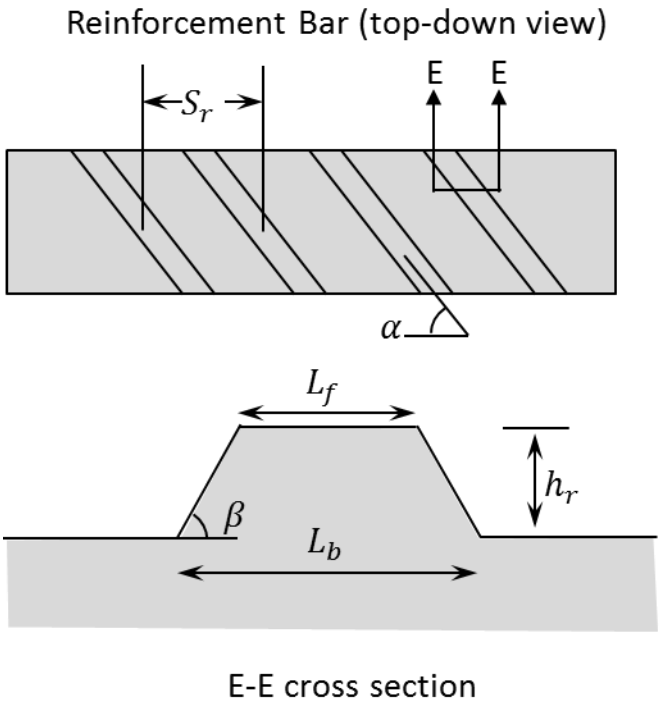

Figure 172. Two Reinforcement Bars Measurements

The pull-out tests were performed three times for each reinforcement bar. The sample reinforcement bars were cast into 10cm diameter by 20cm length cylindrical concrete members with a steel shell outside the concrete cylinder. Linear Variable Differential Transformers (LVDT) was used to measure the displacement during the pullout test. The table below summarizes the result from their experiments.

Table 41. W. Yeih's Pullout Test Results

	Rebar Number					
Parameters	**#3**			**#4**		
q_yKN/cm	3.522	3.702	3.508	4.619	5.158	5.371

From the previous figure, an equation was derived to relate the effective yielding shear stress, τ_{eff}, to the coefficient of friction, μ. The equation developed is shown below. With the two reinforcement bars available in their study, they were able to create a system of two equations using the different parameters of the reinforcement bars to determine τ_{eff} and μ. The underlying assumption is that τ_{eff} and μ are constant for the two reinforcement bars.

$$\frac{q_y S_r}{\pi} = \left[L_r(d_n + 2h_r) + (S_r - L_b)d_n + \frac{h_r^2 + h_r d_n}{\sin(\beta)}\left(\frac{\sin(\beta)}{\mu} + \cos(\beta)\right)\right]\frac{\tau_{eff}}{\sin(\alpha)} \qquad 5$$

Only having two reinforcement bars available does not allow for much analysis on how effective the above equation is on predicting the shear stress and coefficient of friction. With the two unknown variables and only two samples, μ and τ_{eff} can be determined but there is not enough data to verify the results. The current study consists of seven chevron style reinforcements. This allows for five measurements to be used in validating the model.

8.4 Model Design

The reinforcement wire geometries in the current study are different from that of the reinforcement bars used in W. Yeih's study, thus a new model needs to be made. A simplified two-dimensional model was made first, followed by a three-dimensional model. The first step is developing some reasonable assumptions of the model; the second is outlining how the geometry of the wire should be defined in a mathematical form.

8.4.1 Assumptions

The first assumption coincides with the assumption made by W. Yeih. The coefficient of friction of all reinforcement wires shall be constant. Additionally, the shear stress of all reinforcement wires shall be constant. These assumptions allow for a basis of comparing only geometrical differences in the wires. However, from previous research, it is known that the surface finishes

of each reinforcement wire is different at they all come from different manufacturing facilities. Residual lubricants on the wire surface from manufacturing as well as pitting and corrosion can have significant impacts on both shear stress and friction coefficient. Ideally, the model will still have a reasonably acceptable fit even with the variations in surface finishes. [59]

The next assumption made is that the mathematical expression of the model need not be exact. The objective of the mathematical expression is to provide a relationship between the geometry parameters to the friction coefficient and shear stress. The expression is considered sufficient for all practical purposes as long as it relates the interaction between these parameters in a manner that serves as a good predictor of reinforcement wire performance.

8.4.2 Model Considerations

First we start off with a two dimensional design to explain the concept and layout additional assumptions that may be applied in the three dimensional model. The diagram below shows how the reinforcement wire design is considered in the two-dimensional model. Figure 173 shows an image of typical chevron style reinforcement. There exist three rows of indents around the reinforcement wire. The simplified 2D model contains the primary features of the indent such as its depth, width, period, and edge wall angle.

Figure 173. 2D Simplification of Reinforcement Bar

This geometry of the two-dimensional reinforcement wire can be considered in four parts: the forward facing indent edge wall, the indent basin, the backward facing indent edge wall, and the top surface of the wire. For the sake of simplifying the model the top surface of the wire and the indent basin are considered to exert load in the same manner. Figure 174 below describes the

forces exerted at the concrete steel interface of the reinforcement wire. S_l is the length of the considered region, $F_A$is the force that is exerted unto the reinforcement wire during the pullout test. $F_l$is the adhesive between concrete and reinforcement steel per unit length. Given that the surface is in static equilibrium the forces applied at F_A must be balanced with the adhesive forces thus:

$$F_A = F_l S_l \qquad 6$$

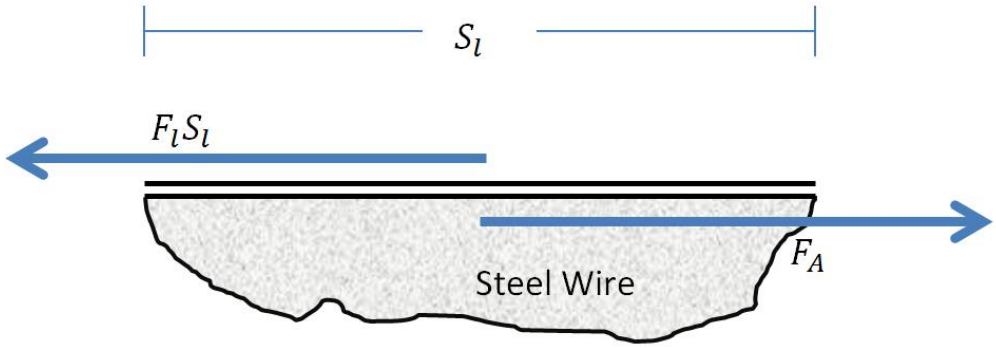

Figure 174. Force Diagram, Top Surface of Wire and Indent Basin

The next region considered is that of the backward facing indent edge. Here the two surfaces are under tension between each other. Using the principles of the first model, the adhesion forces between the concrete and steel would bear the load. However, it is known that the adhesion forces between the concrete and steel are relatively weak in comparison with the forces applied from the pullout experiment. In order to help simplify the model, it forces generated from this surface are negligible and not considered in the model. Figure 175 illustrates the forces considered for the backward facing indent edge.

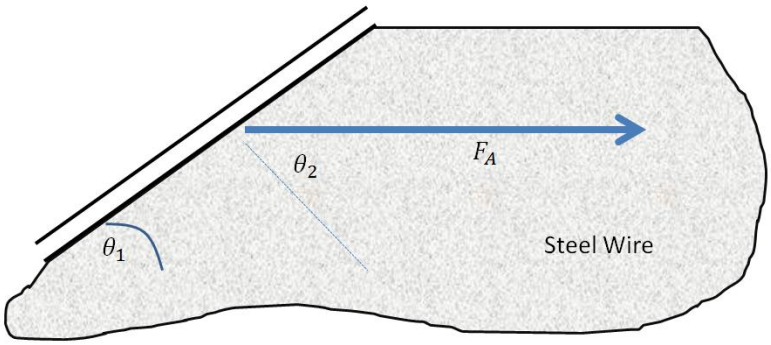

Figure 175. Force Diagram, Backward Facing Indent Edge

Figure 176 illustrates the forward facing indent edge diagram. This is the most important section of the four considered. For this free body diagram we can see that the force generated by F_N has a vertical and a horizontal component. This would correspond to radial and axial forces respective to the cylindrical prism of the concrete during the pull out tests. In this current free body diagram the vertical upward component of F_n is cancelled by the vertical downward component of F_C. However, we can assume that cohesion is not providing this cancelling force, as much of the radial component of the reinforcing wire is compensated by tension forces of the surrounding concrete.

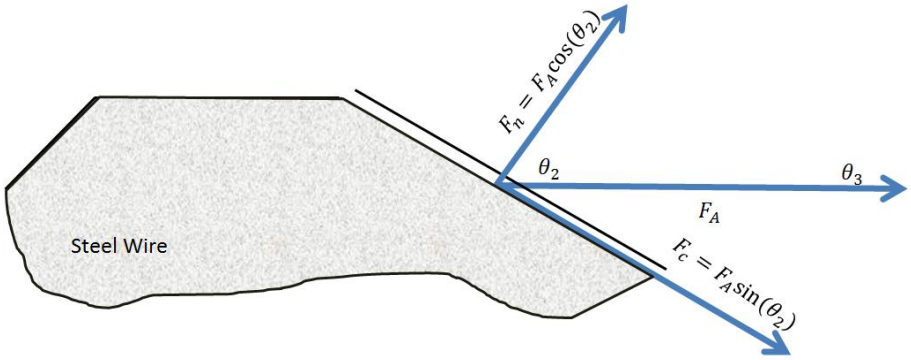

Figure 176. Force Diagram, Forward Facing Indent Edge

8.4.3 3D Model Design Simplified

The first model tested relates closest to the development model of W. Yeih. Figure 177 shows the simplified 3D models geometry. Instead of model the individual indents around the

circumference of the wire, the indents are considered to be one continuous revolution around the surface of the indent. This allows the same four sections discussed in the previous section, to be reapplied in three-space.

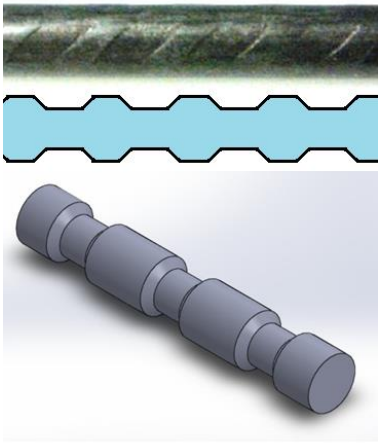

Figure 177. Simplified model geometry

The simplified 3D model consists of two conical regions and two cylindrical regions. Figure 178 defines the key variables that describe the geometry of the simplified 3D model. Within the figure, the force being applied on the section is $F_A \frac{L_t}{L_w}$; where F_A is the critical force applied during the pull out test. L_t is the period length of repeating indent patterns, and L_w is the embedment length of reinforcement wire in concrete. The diagram shows the wire in four segments, the cylindrical segments are 1 and 3. The conical segments are 2 and 4.

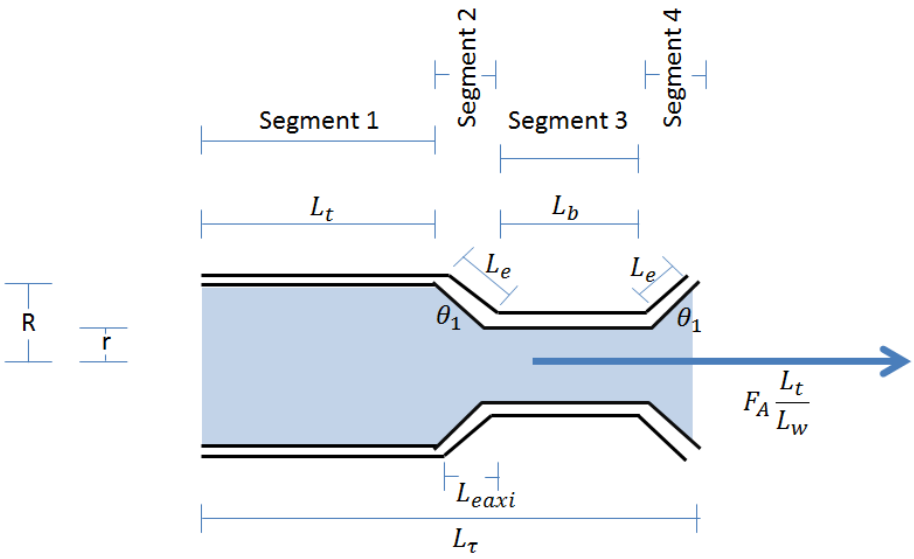

Figure 178. Simplified 3D Model, variables

Starting with segment 1 and 3, the portion of the forces exerted on them is opposed by the static forces of adhesion between the concrete and the reinforcement wire. The opposing force is defined as the surface area of the segment multiplied by the shear stress per unit surface area. For the cylindrical regions in segments 1 and 3 this is defined by the following equations. Figure 179 shows the force diagram for these regions.

$$F_1 = S_s L_t 2\pi R \quad (7)$$

$$F_3 = S_s L_b 2\pi r \quad (8)$$

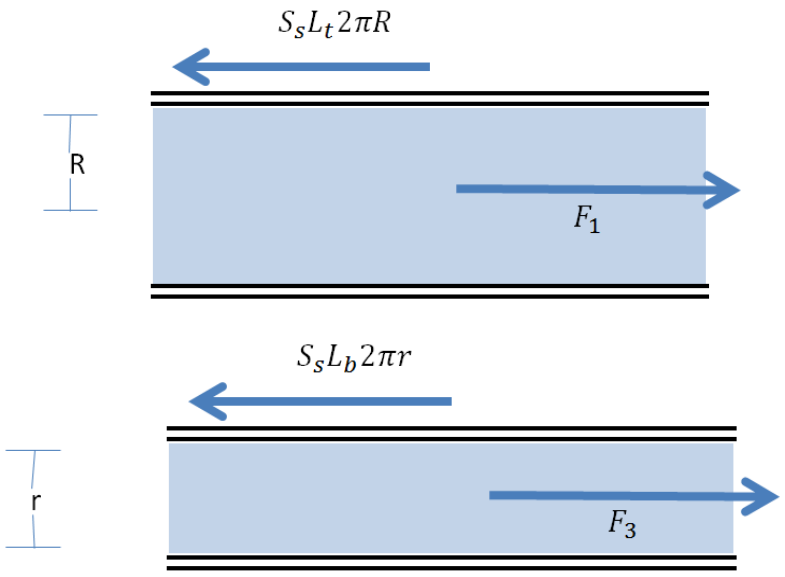

Figure 179. Simplified 3D Model, Segment 1 and 3

Figure 180 shows the force diagram for segment 2, the most significant segment in the simplified 3D model. The equations below show the derivation for the forces on segment 2. They consist of three parts frictional forces generated by the edge slope, forces generated by the edge slope parallel to the axis of the wire, and forces generated by the adhesive shear forces of concrete steel interface.

$$F_2 = F_{2saxi} + F_{2naxi} + F_{2n}\mu_s \cos(\theta_1) \quad (9)$$

$$F_{2saxi} = S_s L_{eaxi} \pi \frac{R-r}{2} \quad (10)$$

$$F_{2s} = \frac{F_{2saxi}}{\cos(\theta_1)} \quad (11)$$

$$F_{2n} = \tan(\theta_1) F_{2s} \quad (12)$$

$$F_{2naxi} = F_{2n} \cos(\theta_1) \quad (13)$$

$$F_{2naxi} = \tan(\theta_1) F_{2s} \cos(\theta_1) \quad (14)$$

$$F_{2naxi} = \tan(\theta_1) \frac{F_{2saxi}}{\cos(\theta_1)} \cos(\theta_1) \quad (15)$$

$$F_{2naxi} = \tan(\theta_1)\, S_s L_{eaxi} \pi \frac{R-r}{2} \quad (16)$$

$$F_2 = F_{2saxi} + F_{2naxi} + F_{2n}\mu_s \cos(\theta_1) \quad (17)$$

$$F_2 = S_s L_{eaxi} \pi \frac{R-r}{2} + F_{2n} \cos(\theta_1) + \tan(\theta_1) F_{2s} \mu_s \cos(\theta_1) \quad 18$$

$$F_2 = S_s L_{eaxi} \pi \frac{R-r}{2} + F_{2n} \cos(\theta_1) + \tan(\theta_1) \frac{F_{2saxi}}{\cos(\theta_1)} \mu_s \cos(\theta_1) \quad 19$$

$$F_2 = S_s L_{eaxi} \pi \frac{R-r}{2} + \tan(\theta_1) \frac{S_s L_{eaxi} \pi \frac{R-r}{2}}{\cos(\theta_1)} \cos(\theta_1) + \tan(\theta_1) \frac{S_s L_{eaxi} \pi \frac{R-r}{2}}{\cos(\theta_1)} \mu_s \cos(\theta_1) \quad 20$$

$$F_2 = S_s L_{eaxi} \pi \frac{R-r}{2} + \tan(\theta_1) S_s L_{eaxi} \pi \frac{R-r}{2} + \tan(\theta_1) \mu_s S_s L_{eaxi} \pi \frac{R-r}{2} \quad 21$$

$$F_2 = (1 + \tan(\theta_1) + \tan(\theta_1) \mu_s) S_s L_{eaxi} \pi \frac{R-r}{2} \quad 22$$

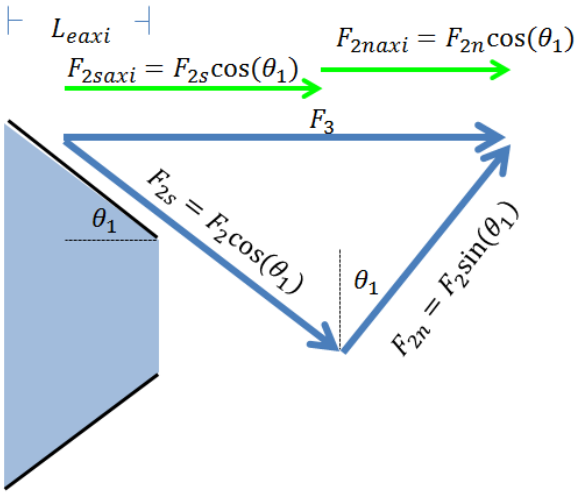

Figure 180. Simplified 3D Model, Segment 2

For segment 4 shown in Figure 181, the same assumptions made in the 2D model apply to this model. Since the backwards facing conical region is under tension loads, the forces generated by this surface interaction are considered negligible.

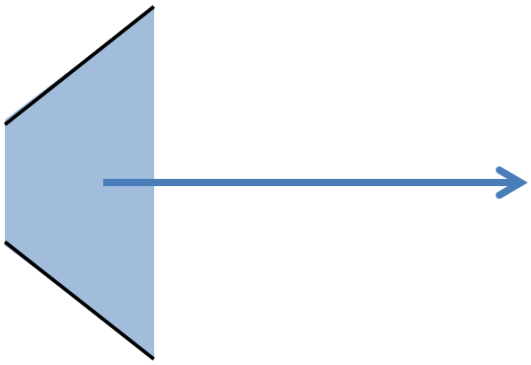

Figure 181. Simplified 3D Model, Segment 4

By combining the equations derived for segments 1 through 4. The sum of the forces generated by the forces $F_1, F_2, F_3,$ and F_4 must equal the forces applied to a period length of the reinforcement wire. The result is a single equation that relates the geometry of the reinforcement wire to the friction coefficient, adhesive shear stress, and the force applied during the pullout test.

$$F_A \frac{L_t}{L_w} = F_1 + F_2 + F_3 + F_4 \quad (23)$$

$$F_A \frac{L_t}{L_w} = S_s L_t 2\pi R + (1 + \tan(\theta_1) + \tan(\theta_1)\,\mu_s) S_s L_{eaxi} \pi \frac{R-r}{2} + S_s L_b 2\pi r + 0 \quad (24)$$

$$F_A \frac{L_t}{L_w} = S_s (L_t 2\pi R + (1 + \tan(\theta_1) + \tan(\theta_1)\,\mu_s) L_{eaxi} \pi \frac{R-r}{2} + L_b 2\pi r) \quad (25)$$

$$F_A \frac{L_t}{L_w} = S_s \pi \left[L_t 2R + (1 + \tan(\theta_1) + \tan(\theta_1)\,\mu_s) L_{eaxi} \frac{R-r}{2} + L_b 2r \right] \quad (26)$$

8.4.4 3D Model Design Detailed

For the detailed 3D model design a more intricate and realistic indent pattern was chosen while still keeping the equations geometrically simple. This 3D model has three indent patterns around the surface of the reinforcement wire. The indents in the model mimic the chevron style shape of the actual pre-stressing steel reinforcement wire. The only significant difference from this 3D model and the actual geometry of the reinforcement wire is that the indents are not tilted at an offset angle but are kept perpendicular to the axis of the reinforcement wire. This is done to keep the model derivation as simple as possible while capturing the critical geometrical feature

components. Figure 182 shows how the detailed 3D model relates to the actual geometry of the reinforcement wire. The indent basin is modeled as rectangular region. The indent edge walls are modeled as portions of an ellipses surface area. The remaining area that represents the outside surface of the reinforcement wire modeled as a cylindrical region.

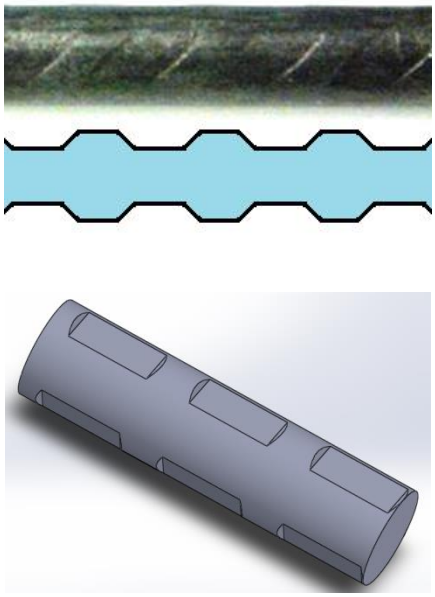

Figure 182. Detailed 3D Model

Following the same process that was used in the simplified model, the detailed model breaks the surface area into segments. Five segments were used in the detailed model. The equations below were derived to create the surface area equations necessary for the detailed model shown in Figure 182. The surface are components are the following: $A_e$indent edge surface area, $A_b$indent basin surface area, A_a surface area around indent edge, A_t surface area in-between indents, and A_s area alongside indented regions.

$$A_e = 2\int_0^{P_x}\left[\left(\frac{\beta}{\alpha}\sqrt{\alpha^2 - x^2}\right) - P_y\right] \quad 27$$

$$A_b = w_b L_b \quad 28$$

$$A_a = \int_0^h \left[2acos\left(\frac{R-d}{R}\right) - 2acos\left(1 - \frac{xd}{Rh}\right)\right] R\, dx \quad 29$$

$$A_t = 2acos\left(\frac{R-d}{R}\right) R(P - l_{indent}) \quad 30$$

$$A_s = \left(\frac{2}{3}\pi - 2\,acos\left(\frac{R-d}{R}\right)\right) RP \qquad 31$$

The five segments of the surface area are combined into one single equation. The equation below provides a means of relating the pullout force, f, to the adhesive shear stress , S, and to the coefficient of friction, μ.

$$f\frac{L_t}{L_w} = 3S[(1 + \tan(\theta) + \tan(\theta)\,\mu)A_e + 2A_a + A_b + A_t + A_s] \qquad 32$$

With this modeling technique, any geometry of reinforcement can be modeled. The model chosen was considered an accurate enough representation to the actual reinforcement wires considered in this study, while keeping the geometry of the model as simple as possible. The model is based on the assumption of a constant coefficient of friction and adhesive shear stress for all wires, these two parameters must be determined prior to being able to predict the pullout force of other reinforcement wires. This was done by using the data of two reinforcement wires at the extremes of geometrical properties. The two wires had the shallowest and largest indents and are referred to as wires WG and WF, respectively. The input parameters to the model are shown below. The input parameters were used to determine all the parameters $A_e, A_a, A_b, A_t,$ and A_s in equation 29. By using two different reinforcement wires we are able to establish a system of two equations with two unknowns (μ, S). By solving for these two unknowns we have an equation that we can use to predict the performance off all other reinforcement wires. In order to perform the measurements of the wires profile, a custom non-contact profilometry system is used.

$$\begin{aligned} d_1 &= .203\,mm & d_2 &= .90\,mm \\ \theta_1 &= .627\,rads & \theta_2 &= .468\,rads \\ l_{indent1} &= 3.16mm & l_{indent2} &= 2.61 \\ f_1 &= 33361.7N & f_2 &= 18237.7N \end{aligned}$$

8.5 Influence of Individual Parameters

For the simplified 3D model graphs were made analyzing how the modeled pull out force varies with varying a single input parameter. The other input variables were held constant at the median value of their range.

Figure 183 shows the relationship between the indent edge wall angle and the required pull out force. This parameter has a non-linear relationship as the amount of indent edge wall surface area varies with the $\sin(\theta)$.

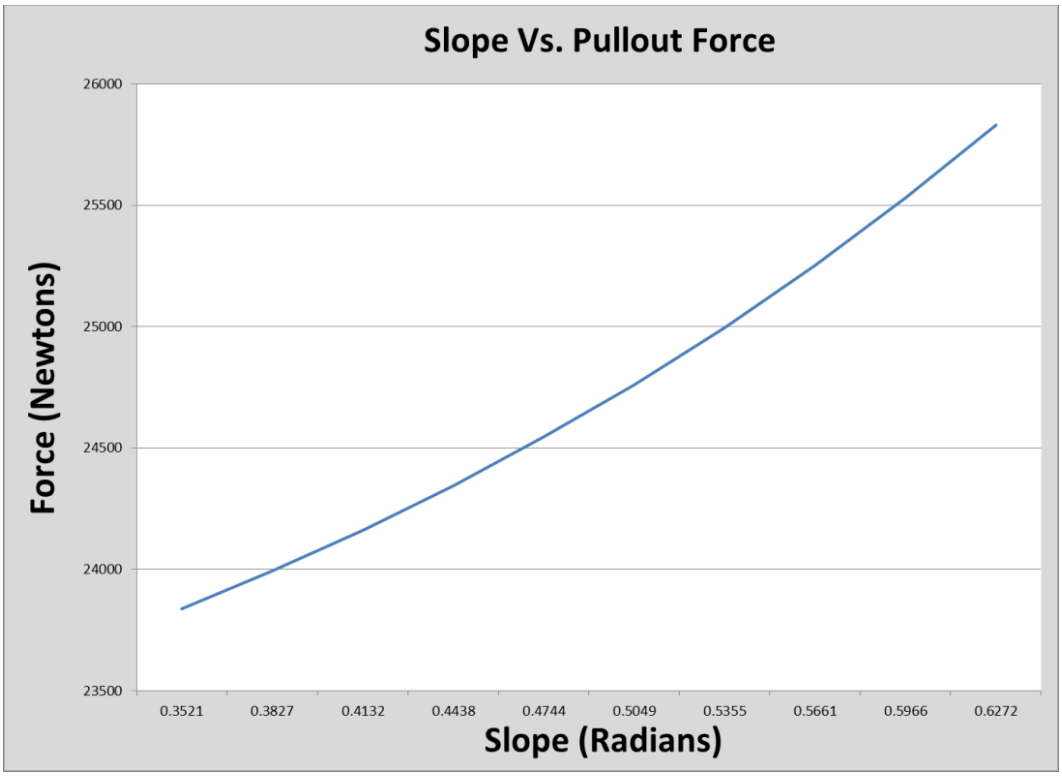

Figure 183. Graphing Slope Vs Pull Out Force

Figure 184 shows relationship between the indent width and the pull out force. As this model only considers frictional faces and not the shear strength of the concrete, increase the indent width only increases the distance between edge walls on the wire creating a lower overall axial surface area per unit of wire.

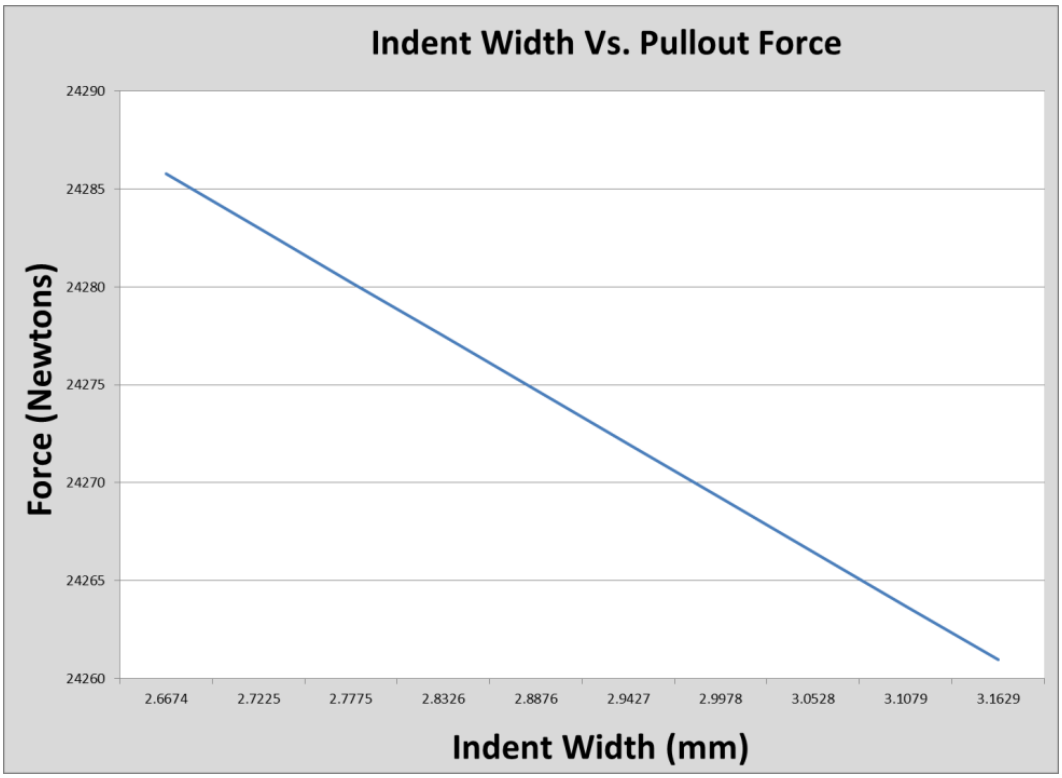

Figure 184. Graphing Indent Width Vs. Pull Out Force

Figure 185 shows the relationship between the indent depth and the pullout force. This has a near linear relationship. As the indent depth is increased the model predicts that the pull out force will also increase.

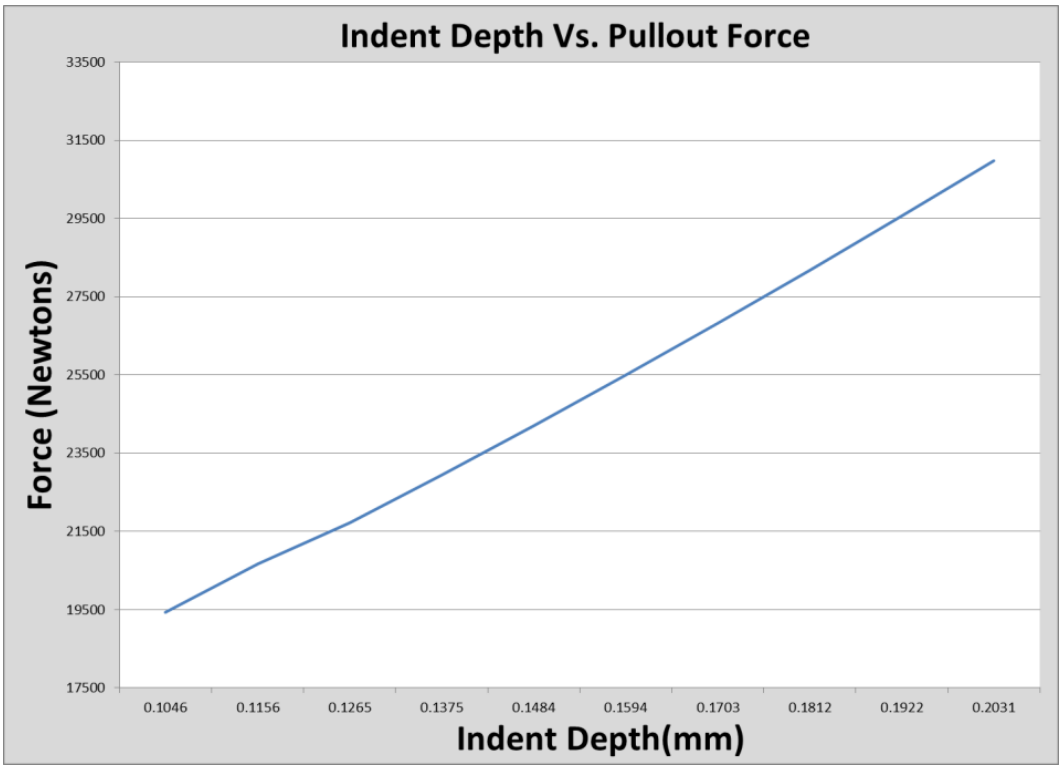

Figure 185. Graphing Indent Depth Vs. Pull Out Force

8.6 Data for Model

Samples were taken on 1 cm section of reinforcement wire for all 12 reinforcement wires available. This was done using a custom developed reinforcement wire profiling system to obtain sub-micron resolution measurements [1, 6]. However, these measurements could be performed in a variety of different ways. Measurements were taken to adhere to modern GD&T guidelines for the ASME Y14.5-2009 standard [10, 20, 26].

8.6.1 Pullout Tests

Figure 186 shows the pullout tests for the reinforcement wires used in this study. The wires are cast in a 4 inch diameter 6 inch tall cylinder. 6 pullout tests were performed for each reinforcement wire. The results are averaged together to represent one single pullout result for each of the force curves in the graph. The far right of the graph a stair-step pattern is seen, this occurs when the pull out experiment must be terminated. The profile of the curve generated from these pull out tests is not traditional for these experiments. Typically, there exists a linear relationship between force and end slip while the reinforcement undergoes elastic deformation. Then a non-linear relationship occurs once plastic deformation of the material begins. However, for these experiments there is no clearly defined elastic deformation occurring. This creates a challenge for determining the critical pull force for the experiment. Because of this several different methods were chosen to try and determine the critical pull out force [16, 30].

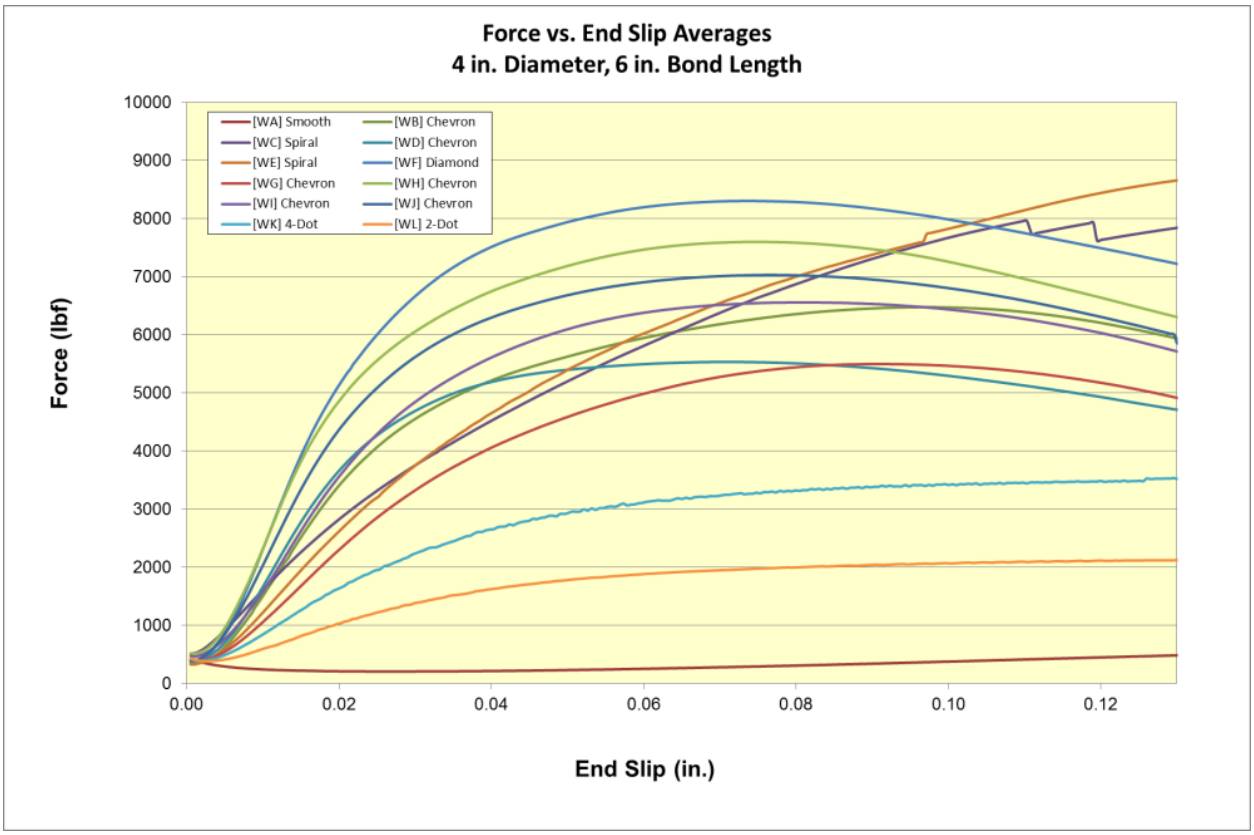

Figure 186. Pullout Test Averaged Results

8.7 Model results

The model was used to predict the pull out force in three different scenarios for the detailed 3D model and one scenario for the simplified 3D model. In order to determine the effectiveness of the models generated, the seven chevron style reinforcement wires were considered. This is done at their geometrical features are the easiest to relate to one another with the geometrical models created thus far. Two of the chevron reinforcements were used to determine the effective yielding shear stress and the remaining 5 reinforcement wires were used to predict the pull out force with the theoretical model. As there are 6 experiments per reinforcement wire this give a total of 30 pullout experiments to validate the theoretical model.

8.7.1 Simplified 3D Model

The simplified 3D model was compared to the maximum pullout out force of each experiment. Figure 187 shows the simplified models result. The graph illustrates the experimental results verses the models predicted value. We can see that there is some lack of fit between the predictions and experimental results. However, the average deviation of predicted to experimental results is about 10%, which is not unreasonable for engineering applications.

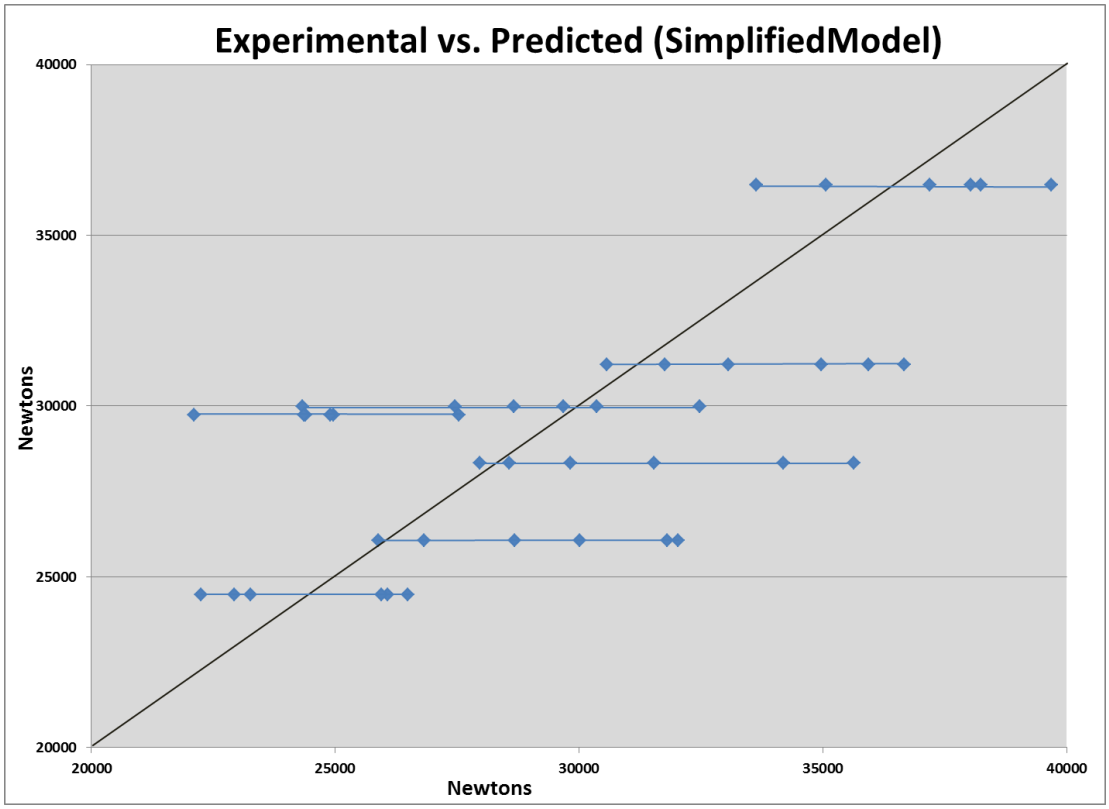

Figure 187. Simplified Model Results

8.7.2 Detailed 3D Model

The detailed 3D models experimental verses predicted results is shown in Figure 188 for the maximum pullout force. In this graph we see a nearly identical performance as the simplified 2D model. While some of the reinforcement wires are closer to the line of prediction equally experimental result, some of them also performed worse at predicting the wires performance. The deviation of the predicted and experimental values in this model is also 10%. There is no significant benefit between the detailed and simple 3D model designs.

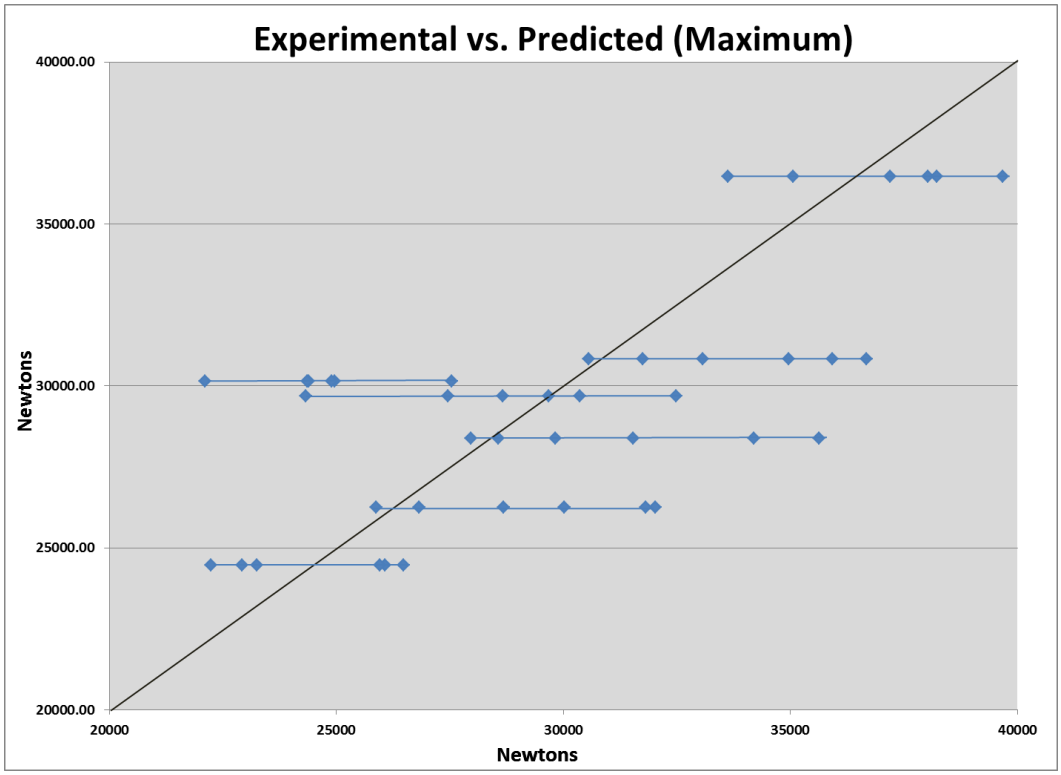

Figure 188. Detailed Model at Maximum Pullout Force

8.7.3 Models at fixed displacement

Figure 189 shows the result of using the force applied at .02" end slip as the value for critical pullout force (as opposed to using the maximum pullout force. Again, for these pullout experiments there is no clear indicator for when elastic deformation ends and plastic deformation begins. Additionally, the force curves generated varies greatly in curvature for the different reinforcements. The result of this is poorer than the using the maximum pullout force. The average deviation of actual pullout force to predicted values is 12.8%

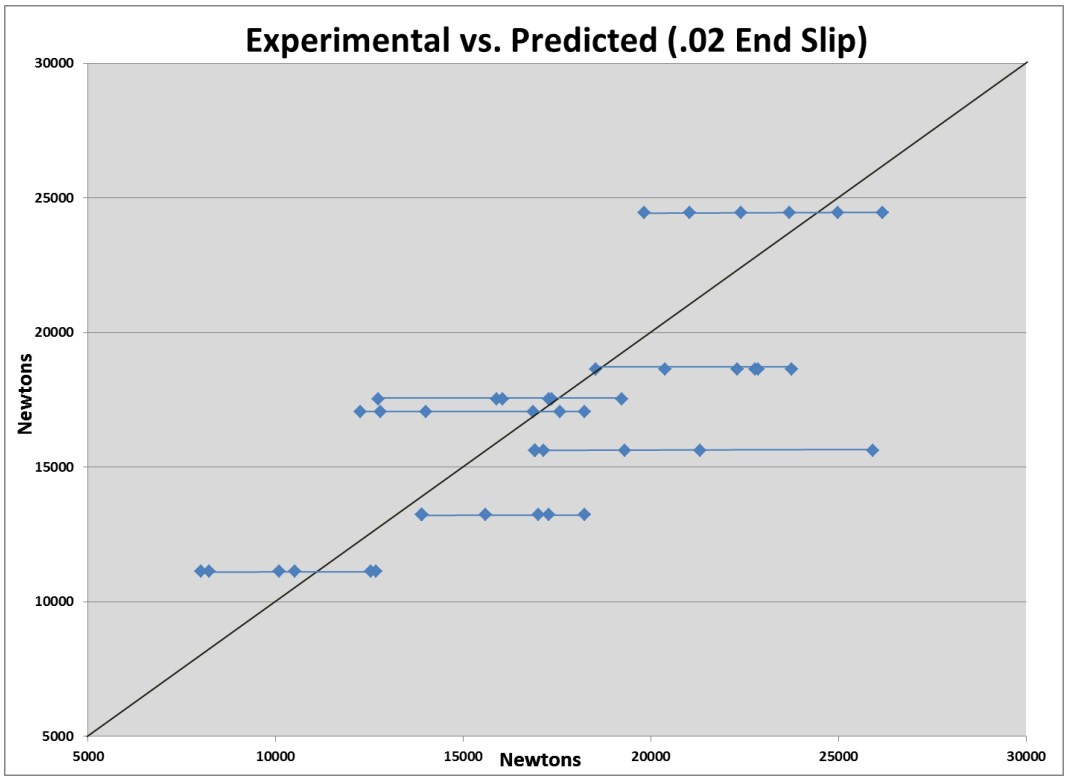

Figure 189. Detailed Model with Force at .02" End Slip

Figure 190 shows the second attempt at determining a better representation of the critical pull out force. This model uses the force from the pullout test at .04 end slip. Again this did not perform as well as using the maximum pullout force as the critical pullout force. The average deviation of predicted to experimental results is 11.5%.

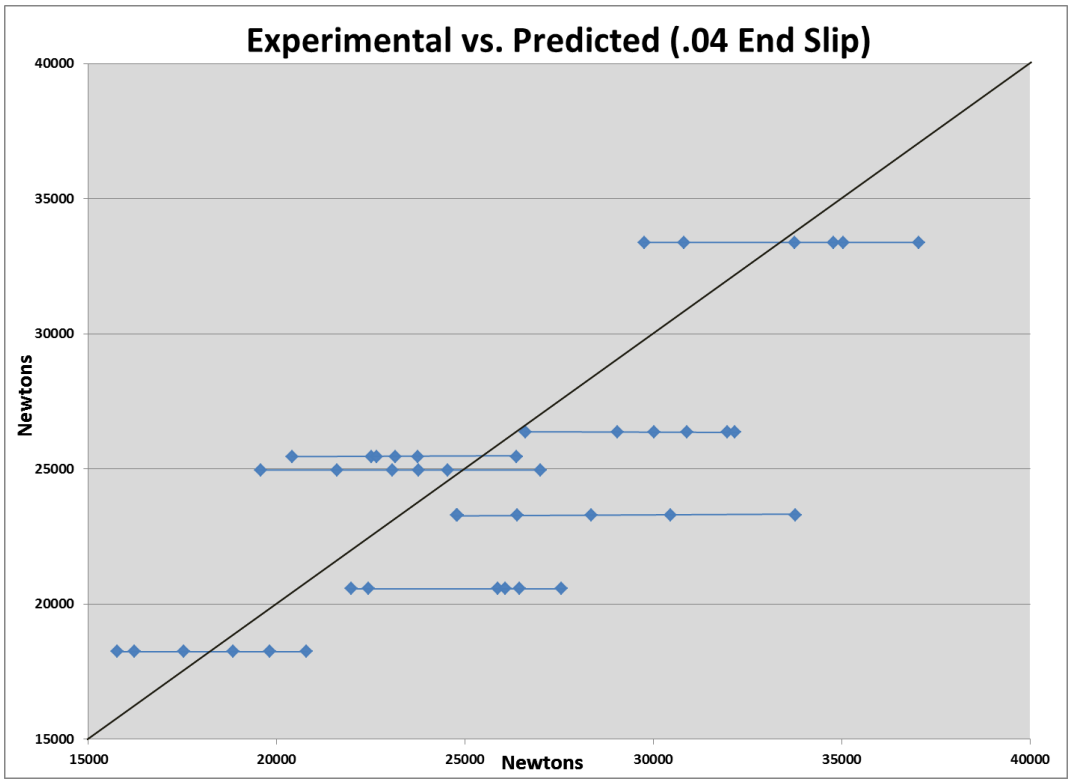

Figure 190. Detailed Model with Force at .04" End Slip

Both of the models at a fixed end slip performed worse than the models used at the maximum pull out value. In general all of the models perform reasonable well considering the assumptions that had to be made. There are two primary factors that separate the theoretical model from the experimental results. The first is that for the reinforcement wires all of them have a unique surface texture and finish which leads them to having different coefficients of friction. The model assumes that all reinforcement wires have the same coefficient of friction, while this is clearly not true for the experimental data that is available. The second is that the actual geometry of the reinforcement wire still deviates from the model design. As the model balances geometry complexity with actual wire geometry accuracy is lost in the model.

8.7.4 Optimized Model

Previous research shows that an inverse problem solving approach can result in significant improved model performance for strand bond stress-slip relationship in pre-stressed concrete [58]. The inverse problem solving approach presented used non-linear search techniques to back calculate the fundamental model coefficients so that the difference between the predicted value and empirical value is minimized.

The optimization model used is presented by the equation below. The sum of the square error between the empirical pull out force and the predicted pullout force is minimized. Where $F_{Ei}: i \in [1, N]$ is the empirical pullout force for sample i where this is a total of N samples. $F_{Ai}: i \in [1, N]$ is the predicted pullout force from a variant of the simplified model. With decision variables: Shear Stress, S_s; Static Friction Coefficient, μ_s; and constant, C. For each F_{Ai} there is a corresponding d_i for indent depth, θ_i for indent edge wall angle, $L_{b,i}$ for length of indent basin, and $L_{eaxi,i}$ for the length of the indent edge wall. The optimization of the model was done using non-linear search techniques similar to that described in chapter 3. The minimization determines local optima values for $S_s, \mu_s,$ and C.

$$Minimize \sum_{i=1}^{N} (F_{Ei} - F_{Ai})^2$$

$$F_{Ai} = S_s \left[(1 + \tan(\theta_i) + \mu_s \tan(\theta_i)) L_{eaxi,i} \left(\frac{d_i}{2} \right) + 2L_{b,i}(R - d_i) \right] + \mathrm{C}$$

The inverse problem solving technique was applied to the simplified model to predict the pullout force at a .02" end slip. Non-linear search algorithms were used to optimize the calculation of S_s and μ_s. The resulting coefficient values were found to be 77.5 and 2271, respectively. Figure 191 shows the graph of predicted vs actual values. In the graph the whiskers show the standard deviation of the pullout tests. The standard deviation whiskers overlap the zero error line with the exception of wire type WD which had a uniquely different behavior than the other wires during the pullout tests.

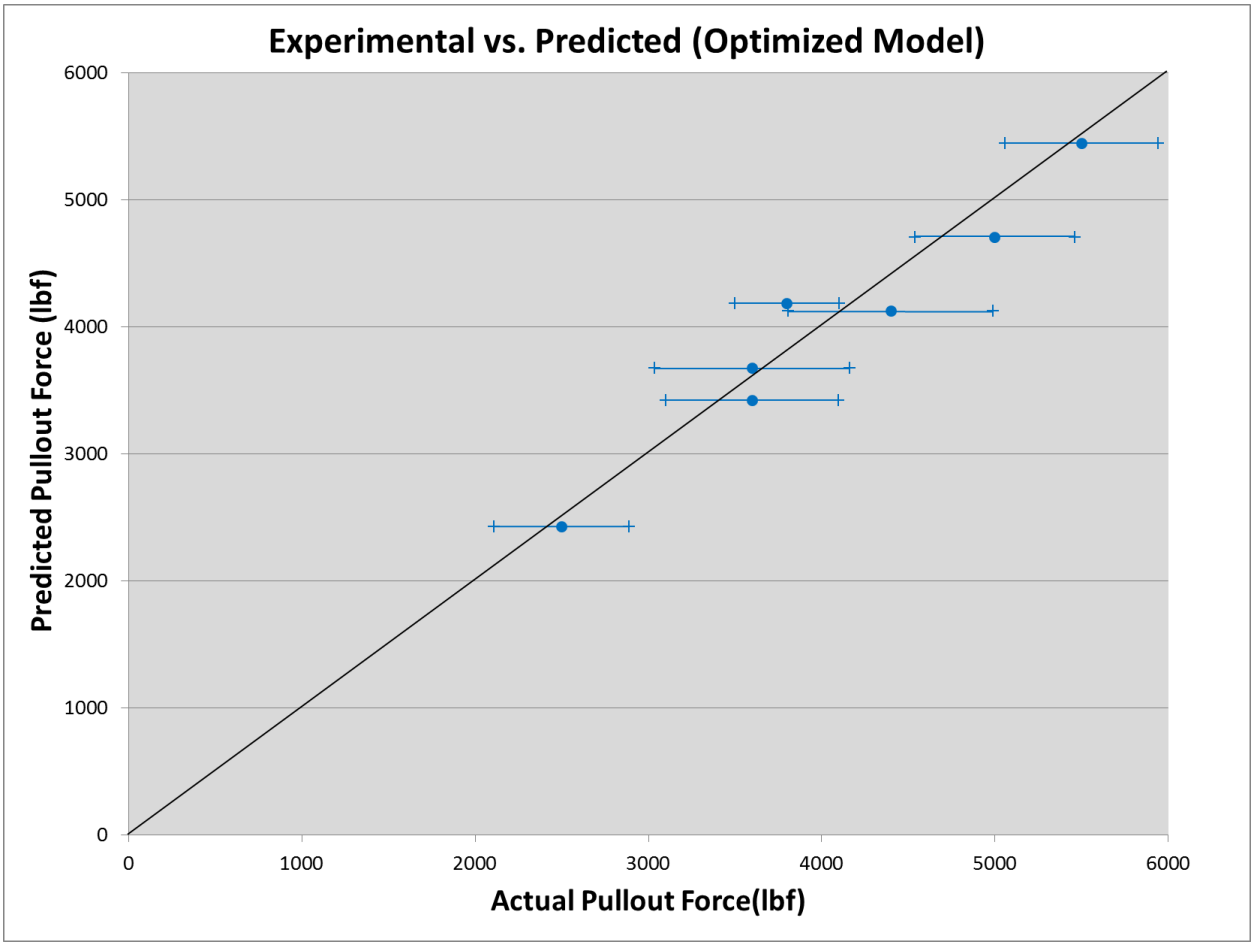

Figure 191. Optimized Model Results

Figure 192 shows the results of the optimized model including wire type WA. The model predicts that the smooth wire type WA will have no pullout force while the actual test showed that it had a couple hunder pound pull out force.

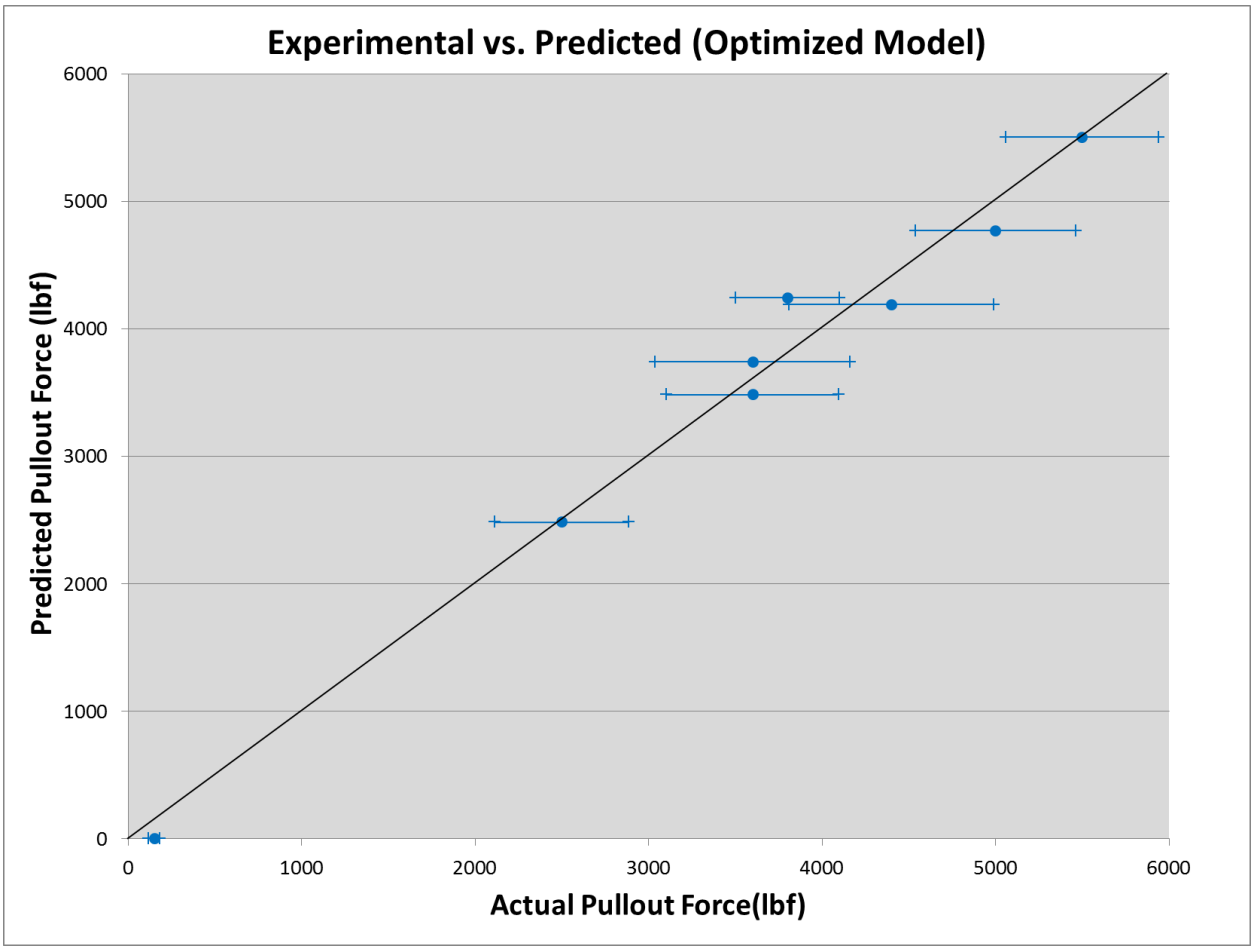

Figure 192. Optimized Model Results Including Smooth Wire

The optimized models perform well at predicting the pullout force of pre-stressed indented wires given basic wire geometry as input parameters. The ability to predict the bonding force given the wire geometry presents opportunities to modify indent design geometry to improve bonding characteristics and overall pre-stressed concrete quality.

Wire WD's pullout behavior is an outlier that offsets the models performance. The model presented is able to predict the pullout force to within an error of 400 lbs. The standard deviation

of the pullout test varies to up to as much as 591 lbs. The model performs well given the practical limitations and natural variability inherent in performing destructive concrete testing.

8.8 Comparison to Statistical Model

In addition to the development of the theoretical model, multivariable linear regressions were made to relate the pull out forces to various geometrical features of the reinforcement wire. The developed multi-variable linear regressions are considerably more accurate than the theoretical model. However, the regressions make no attempt at understanding the frictional coefficient or the effective yielding shear stress of the reinforcement wire.

The statistical models shown in the previous chapter have strong statistical significance. Of the statistical models listed the three and four parameter models are viewed as the best fitting per number of variables. The statistical models serve as better predictors of the reinforcement wire performance in the pull out test than the theoretical model. However, the theoretical model provides explanation to how the frictional coefficient and effective yielding shear stress impacts the pull out force of the wire.

8.9 Converting Pull Out Force to Transfer Length

Prior research done has shown that there is a strong correlation between the pull out force of reinforcement wire and the transfer length of the wire when used in concrete members. This information was used to create the following basic conversion from pullout force to transfer length. Assuming that there is linear relationship between pullout forces and transfer length. The maximum force difference contained within an inch of concrete is the maximum pullout force divided by the length of the concrete cylinder.

$$(Total\ Pretensioning\ Force)\frac{4\ inch}{Max\ Pullout\ Force} = Transfer\ Length$$

Figure 193 illustrates the concept. Assuming the concrete bears the load uniformly across its length, a force per unit length of concrete can be determined. Division of the Total Pretensioning Force by the force per unit length results in a crude estimate of transfer length.

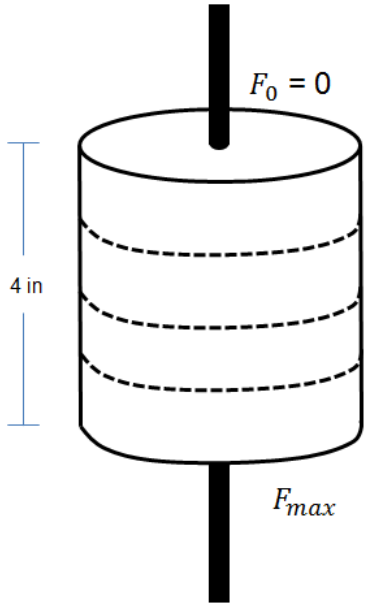

Figure 193. Converting Pullout Force to Transfer Length

8.10 Predicting Concrete Ties

This conversion technique was used to predict the transfer length given the wire geometry for actual measured concrete cross ties. The model has significant difference between a few predicted values, however, the trend of the model from one wire type to the next are very close [32]. Figure 194 shows the results of predicted transfer lengths along the box plots from actual empirical transfer length data.

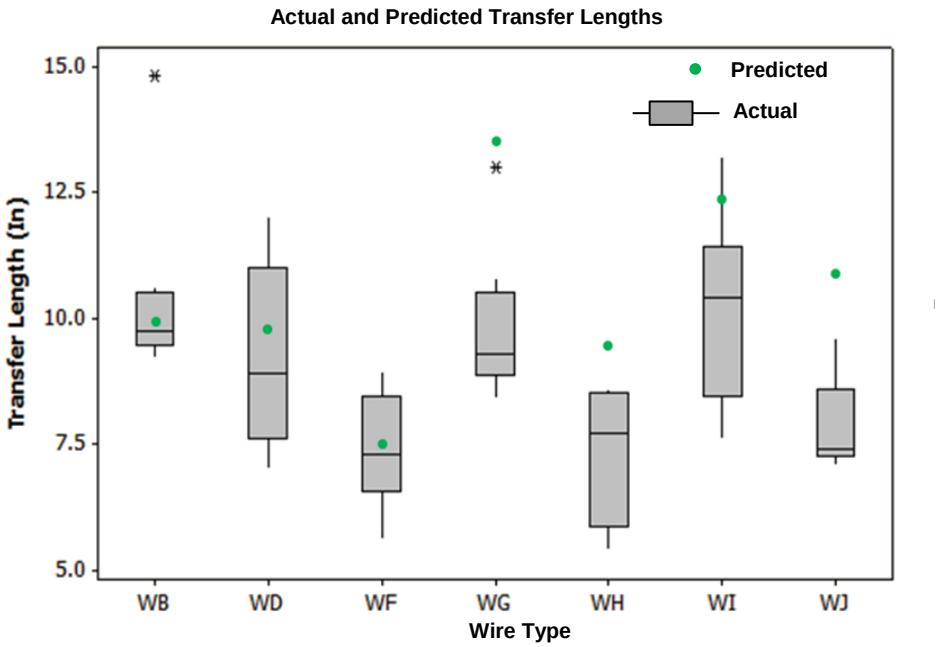

Figure 194. Predicting Concrete Ties

8.11 Conclusions

The developed theoretical model performs reasonably well at predicting the pull out force of the reinforcement wire, given the assumptions that were made. It is hypothesized the deviation of experimental results and theoretical results, is due to the differences in the reinforcement wires having different surface finishes as well as corrosion build up as well as differences between actual reinforcement wire geometry and the geometries used in the theoretical model. Given the limited number of different reinforcement wires available in the market, it is difficult to be able to test a variety of wire profiles that have the same surface finishing. Of the four different theoretical models developed, the simplified 3D model using the maximum pull out force is recommended. Another cause of error between may be related to the force curves generated during the pullout tests. The gradual transitions to the maximum pull out force make it difficult to identify when failure of the reinforcement begins and ends. There is no clear division between elastic deformation and plastic deformation during the pull out tests.

8.12 Recommendations for Future Work

The theoretical model may have applications in other areas besides pull out experiments. One of the key metrics for determining the quality of pre-stressing steel reinforcement wires is the transfer length. The transfer length designates how far it takes for the pre-stressing force to reach a maximum and stabilize inside the concrete reinforcement. It may be possible to reuse the modeling techniques described in this paper to create a modeling that predicts transfer length from the frictional coefficient, effective yielding shear stress, and the geometry of the wire.

One of the failure modes between concrete members and steel reinforcement wire is splitting fractures due to the radial forces generated by the wire. As the model generated used in this study quantizes the axial forces generated by the indent patterns it can also be used to predict the radial forces generated by the reinforcement wire. A further analysis on the radial loads exerted unto the concrete may explain these splitting fractures.

Chapter 9 — Validations

This chapter documents the validations of the instrumentations, measurements, and findings of this research. This section covers the testing of individual components as well as the indent profiling system as a whole.

9.1 Verifying Measurement Detail

The first test performed was to verify the quality of the scanned data received from the indent profiling system. Figure 195 shows the results from performing a scratch test with the first prototype. A small scratch was made on the surface of the pre-stressing steel reinforcement wire with a file. Then the wire was scanned and the 3D model in the upper section of Figure 195 was rendered. The system was able to capture the scratch in fine detail as can be seen by the two images.

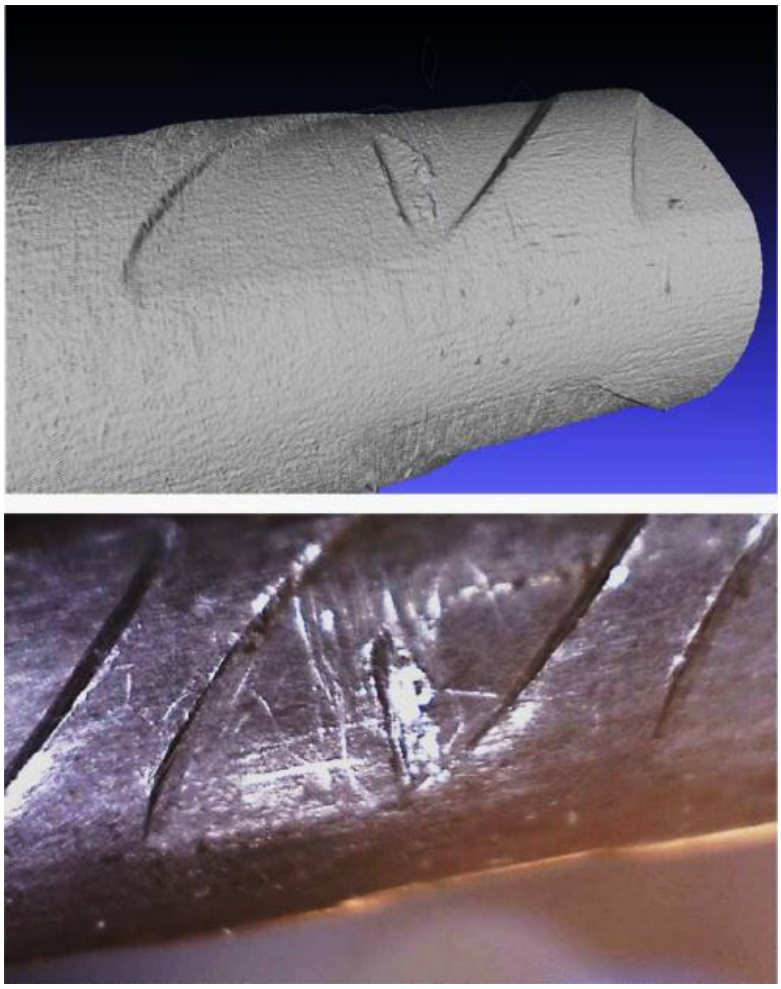

Figure 195. Scratch Test on Reinforcement Wire

9.2 Comparison between measurement methods

In order to verify the accuracy of the indent profiling system, three different measurement methods were tested. Figure 196 illustrates the three methods. The first, Manual, is manual measurement with a depth micrometer and linear stage as is currently being performed under the ASTM A881 standard. The second method labeled Graph is 2D plots of the data collected from the indent profiling system to measure the surface profile. The third method labeled Software, is a fully automated measurement process. After the indent is scanned, automated processing software is used to identify the indent regions and perform measurements. The image shown is of the output of this process.

Manual
Depth Micrometer
Per ASTM A881-2010

Graph
Manual analysis of 3D scan data

Software
Fully automated analysis
(1 button processing)

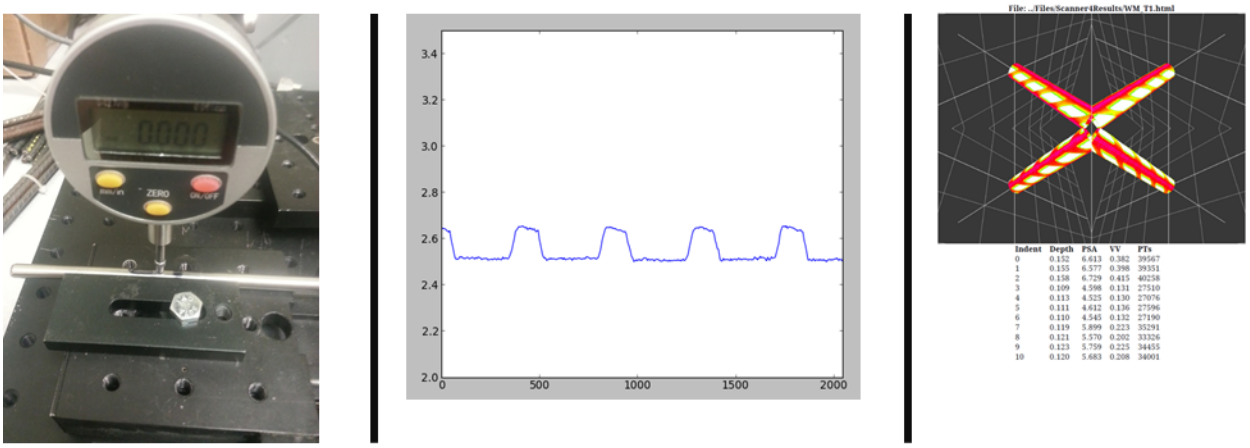

Figure 196. Three Methods of Measuring Indent Profiles

The results from the three measurement methods are shown in Figure 197. Eleven indents were tested. The three different measurement methods coincide well with each other and capture the variation of the indents on this single wire type. The differences within the measurements is within the range of the surface roughness and surface variation of the reinforcement wire.

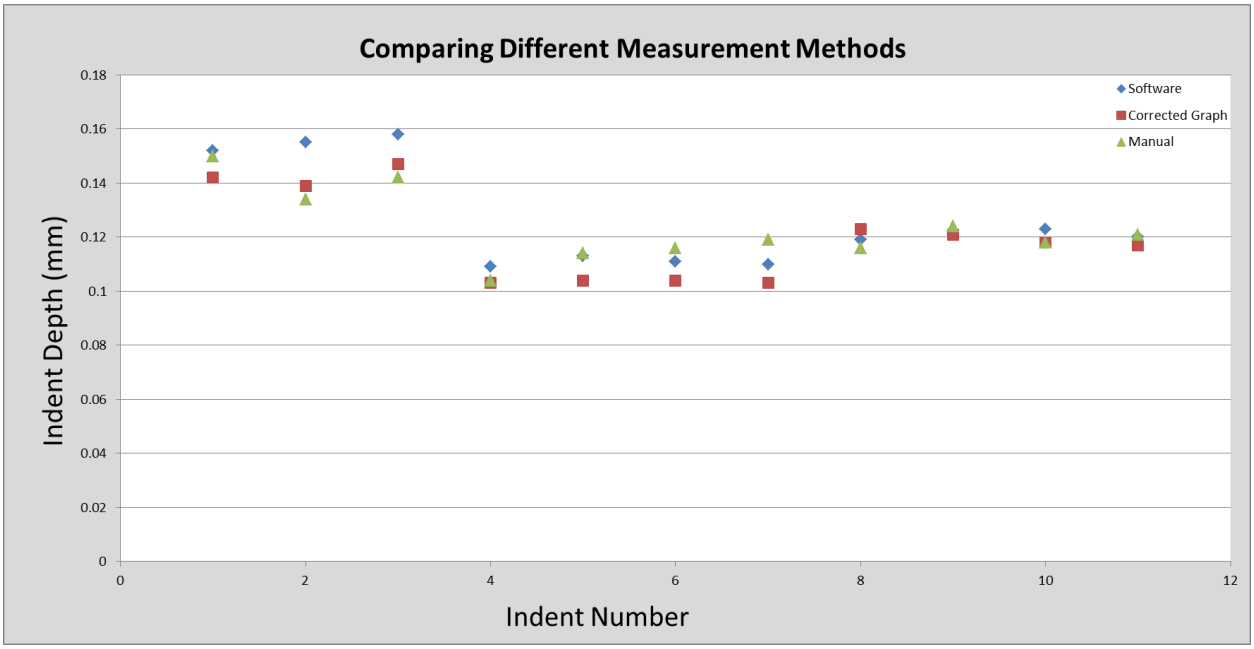

Figure 197. Results from Three Different Measurement Methods

Table 42 shows testing to confirm accurate measurement of the indent edge wall angle with the non-contact indent profiling system. 6 wires were machined during this research with a known indent edge wall angle and compared to the measurement results from the indent profiling system. The indent profiling system was able to measure the edge wall angle with an average error from the anticipated value of 3.1 degrees. The Worst case scenario was an error of 7.9 degrees, which could be a combination of measurement error and anticipated angle error.

Table 42. Verifying Indent Edge Wall Measurements

	Actual Angle	Anticipated Angle	Difference	
15 Shallow	10.9	10.7	0.2	Degrees
15 Deep	13.3	10.7	2.6	Degrees
30 Shallow	19.1	22.2	3.1	Degrees
30 Deep	21.3	22.2	0.9	Degrees
45 Shallow	27.3	35.2	7.9	Degrees
45 Deep	31.1	35.2	4.1	Degrees
			3.7	**Average**
			7.9	**Worst Case**

9.3 Understanding the Profile of an Indent

This section covers an explanation as to how indent profiles vary from one wire type to the next. Given that each wire type is unique and has a fundamentally different design than its competition, developing a measurement algorithm that is ubiquitous to all designs of pre-stressing reinforcement steel has some challenges.

Figure 198 shows the typical profile of for wire WF. The depth of the indents are small relative to the length of the indent.

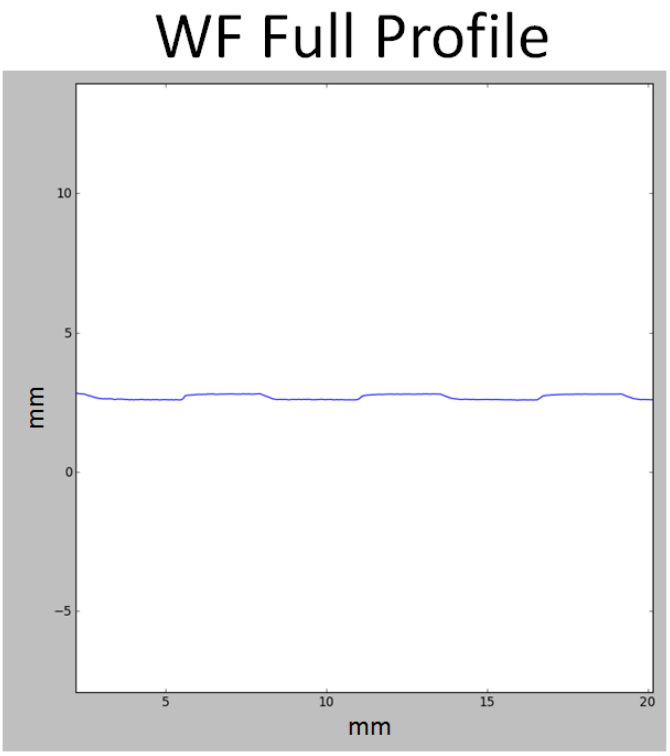

Figure 198. Profile of WF Section

Zooming in further in Figure 199 a single indent is shown. It is clear that the indent edge on the right is steeper than that of the left, however at this magnitude it is still difficult to make out the scale of the depth, we need to increase the magnitude on the y axis while keeping the x axis the same.

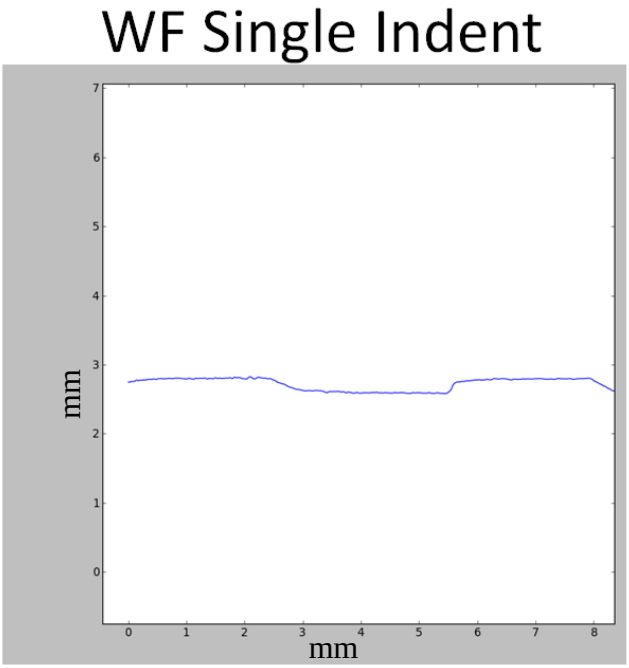

Figure 199. Profile of WF Single Indent

Figure 200 is of the same indent as Figure 199. The y axis has been scaled to show detail depth variation across the indents full width. It is clear from this figure that the criterion for the start and stop of the indent edge wall is subjective and multiple measurements may be taken from the same indent.

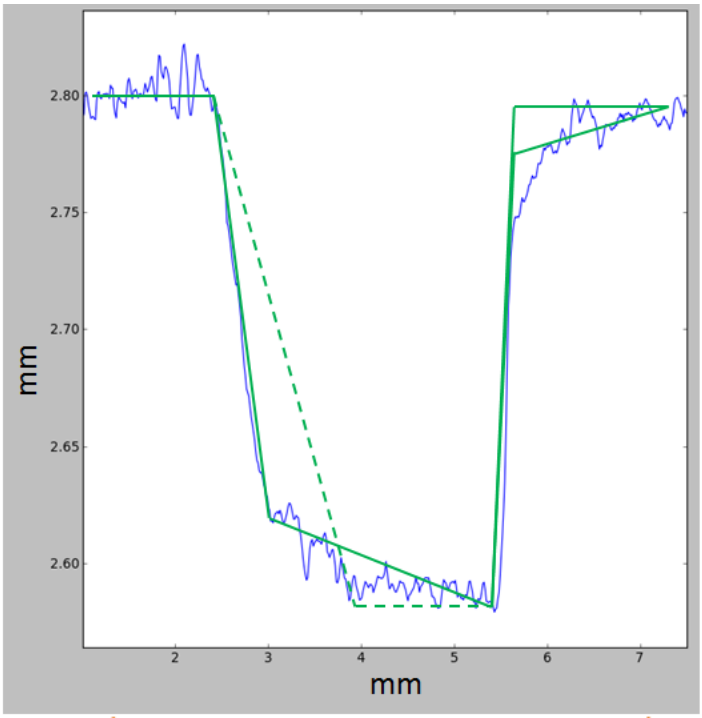

Figure 200. Multiple Ways to Measure the Same Profile (Uneven Scales)

If we choose to say that the portion with no slope is the indent basin and the remainder is the indent edge wall we would get the result shown in Figure 201. Keeping in mind that the scales are uneven from the y and x axis, the left edge wall has an angle of 10 degrees. The right edge wall has an angle of 60 degrees. If the indent edge wall angle was chosen based off the alternative method in Figure 200 the indents would have similar angles but we would only be measuring of portion of the indent edge wall and now there would be a measurable slope to the indent basin that is separate from the edge wall.

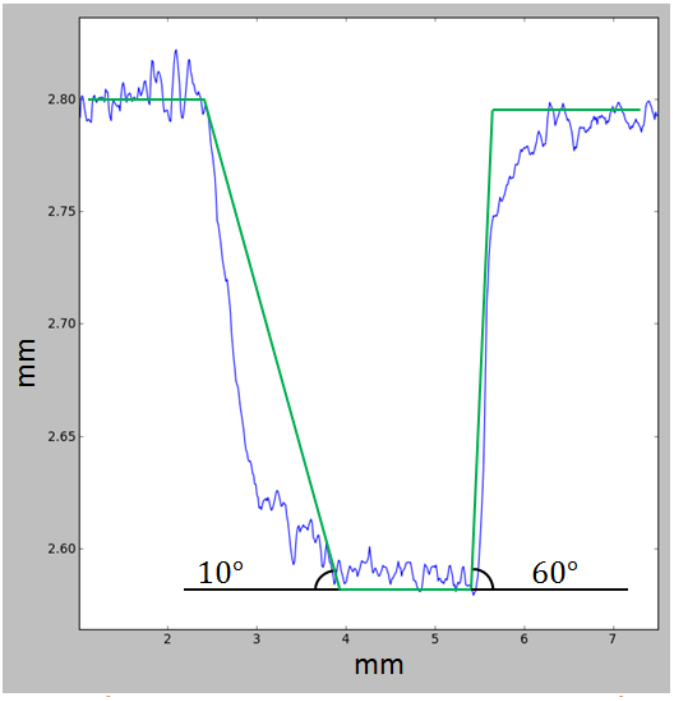

Figure 201. Largely Varying Angles on the Same Indent (Uneven Scales

Figure 202 shows another example situation. Wire WC has a rounded top portion outside the indent. There are multiple ways to determine what the top of the indent is, which results in multiple measurements of the indent edge wall angle.

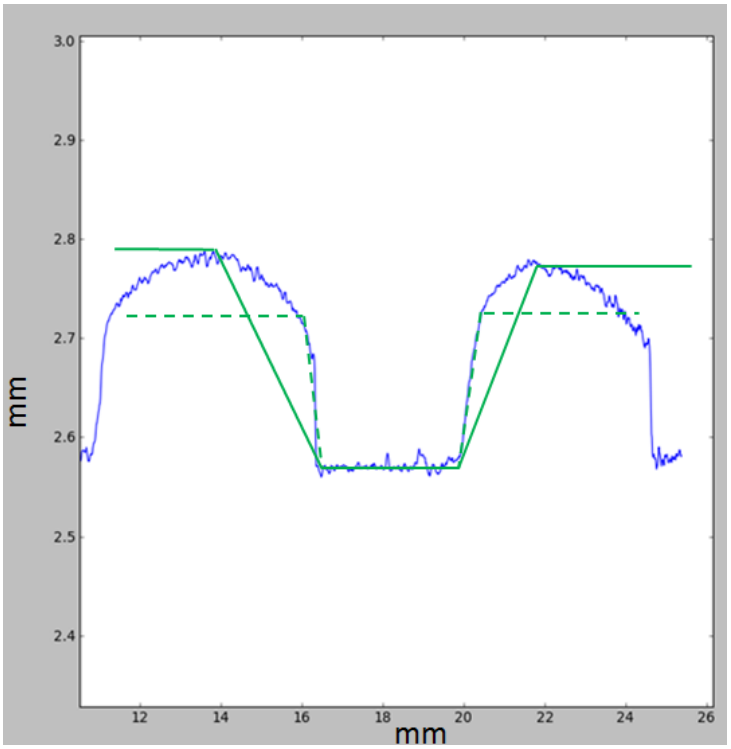

Figure 202. Determining the Beginning of an Indented Region on WC (Uneven Scales)

9.4 Measurement system repeatability and resolution

Tests were performed to confirm the measurement systems repeatability. The test in Figure 203 was performed by scanning the same surface 5 times in the same direction. The surface was an anodized aluminum plate. The surface profiles match almost exactly on top of each other, the noise in the linear traverse and measurement device is very small.

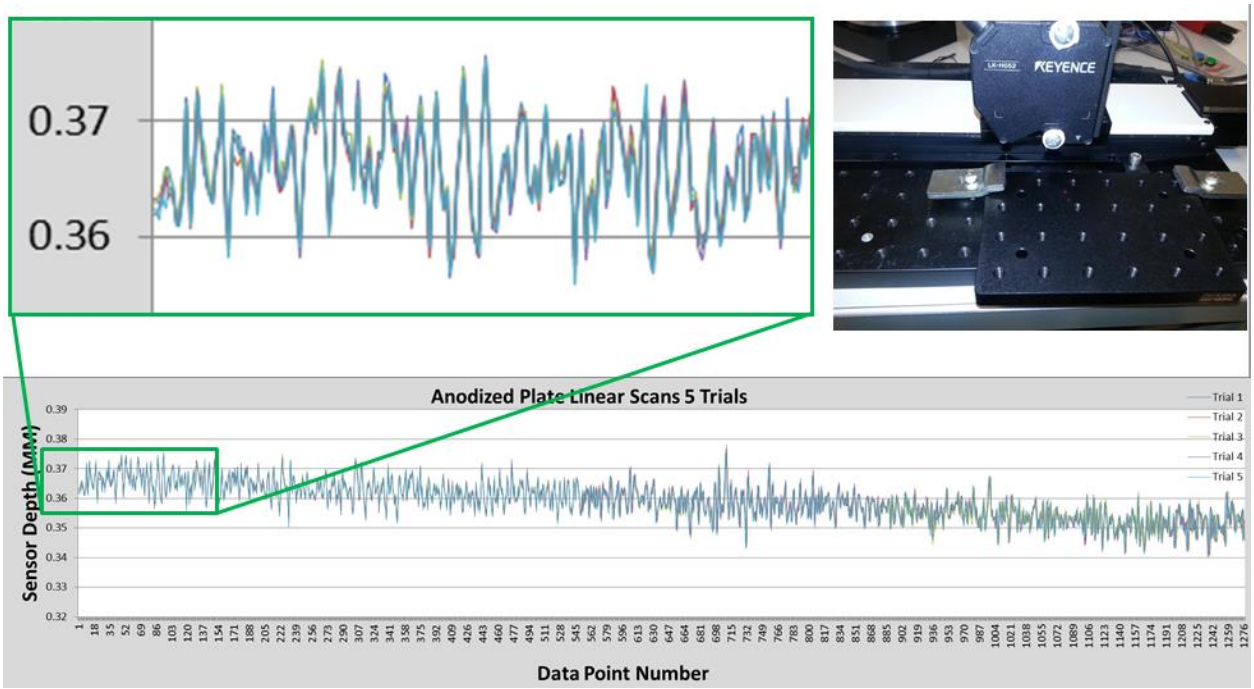

Figure 203. Testing Repeatability

Another test was performed in Figure 204 with 10 scan lines on an indent profile. Five scans lines were in the forward direction of the traverse, five scan lines were in the reverse direction of the traverse. Scan lines going in the same direction (like during the actual scanning of the wires) are nearly exactly the same. A mean shift can be seen by the scan lines in the reverse direction which is the backlash in the traverse system used.

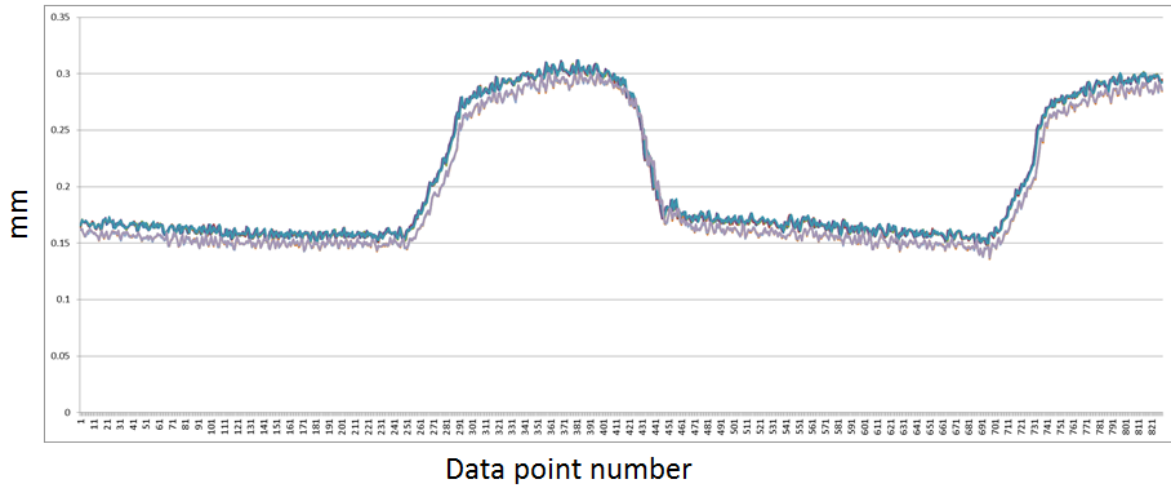

Figure 204. Testing Repeatability and Measuring Backlash

Chapter 10 — Conclusion

This research provides a detailed analysis into the influence of pre-stressing steel reinforcement surface profile on the quality and reliability of pre-stressed concrete railroad ties. This research addresses ongoing problems with the design and quality control of modern pre-stressed concrete railroad ties. The research identifies critical aspects of the geometrical design of pre-stressing reinforcement wire that directly relate to pre-stressed concrete railroad ties. Novel geometrical features have been established that have a strong correlation to the transfer length of pre-stressed concrete members. A method of measuring and performing quality control on the geometrical design is presented. The method relies on principles of datuming and measurement as defined by ASME Y14.5-2009 standard for Dimensioning and Tolerancing.

A novel 3D surface profilometry system has been developed that provides detailed surface profile information of pre-stressing steel with a resolution of one micron. Such a detailed surface profiling of concrete reinforcement steel has never been done before. This profilometry system provides both a means of engineering improved reinforcement wire designs and implementing more complete reinforcement wire quality control. Scanning systems developed with data processing rates and overall design characteristics suited for practical industrial application.

Novel 3D spatial analysis and geometrical feature measurement algorithms have been developed to provide automated and semi-automated analysis of high resolution surface profiles. The geometrical feature measurement algorithms have been proven within this study to perform better than the current ASTM-A881profile requirements and predicting the performance of pre-stressed concrete members made with the reinforcement steel. The algorithms adhere to the principles of datuming and measurement defined by ASME Y14.5-2009. Dimensional requirements defined with stable, functional, and usable datums provide a more robust means of measurement across different testing systems and different measurement operators.

Novel theoretical and empirical models have been developed that predict the transfer length given reinforcement wire geometry. Models have been developed with a coefficient of determination in excess of 95% and strong statistical significance. Empirical models are based

upon testing of 4 wire concrete prisms with known transfer lengths. Theoretical models rely on fundamental principles of friction coefficients and adhesive shear properties of concrete. Models have developed combining reinforcement wire geometry and release strength of the concrete member to create an all-inclusive model to predict transfer length given the conditions of the concrete member.

It is recommended that these research findings be used to develop optimized reinforcement wire geometry and to provide sustaining reinforcement wire quality control. Modifications should be made to ASTM-A881 within accordance to these findings so that the production and testing requirements of the pre-stressing steel reinforcement wire may be improved.

References

[1] Mark D. Haynes, Chih-Hang J. Wu, B. Terry Beck, Robert J. Peterman (2012). "Non-Contact Measurement of Wire Indent Profiles on Prestressing Reinforcement Steel." In Proceedings of the American Railway Engineering and Maintenance-of-way Association (AREMA) Conference. Sept 16-19, 2012 Chicago, IL

[2] Mark D. Haynes, Chih-Hang J. Wu, B. Terry Beck, Robert J. Peterman(2013). "3D non-contact profilometry for reinforcement steel quality control." In Proceedings of the Industrial and Systems Engineering Research Conference(ISERC). May 2013 San Juan, Puerto Rico.

[3] Mark D. Haynes, Chih-Hang J. Wu, B. Terry Beck, Robert J. Peterman(2013). "Automated Real-Time Search and Analysis Algorithms for a Non-Contact 3D Profiling System." In Proceedings of the SPIE, Volume 8791, id. 87911G 12 pp. Munich, Germany

[4] Mark D. Haynes, Chih-Hang J. Wu, B. Terry Beck, Robert J. Peterman (2013). "Prestressing Steel Reinforcement Wire Bond Index Number." In Proceedings of the Joint Rail Conference(JRC). April 2013 Knoxville, TN

[5] Mark D. Haynes, Chih-Hang J. Wu, B. Terry Beck, Robert J. Peterman(2014). "Prestressing Steel Reinforcement Wire Measurement Protocol". In Proceeding of the Joint Rail Conference(JRC). April 2014 Colorado Springs, CO

[6] Mark D. Haynes, Levi DeLissa, Chih-Hang John Wu, B. Terry Beck, and Robert J. Peterman. "Design of a Non-Contact Surface Profilometry System for Automated Geometrical Dimensioning and Tolerancing." In International Journal of Engineering Inventions, Volume 3, Issue 2PP:15-19. Sept 20, 2013

[7] Mark Haynes, Chih-Hang J. Wu, B. Terry Beck, Naga N.B. Bodapati, and Robert J. Peterman "An Investigation into Non-Linear Search Modifications for Minimizing Objective Function Computations," Proceedings of the 2014 Industrial & Systems Engineering Research Conference (ISERC), ISERC2014-I393 May 31-June 3 2014, Montréal, Canada

[8] Mark D. Haynes, Chih-Hang J. Wu, N. B. Bodapati, B. Terry Beck, and Robert J. Peterman "Modeling the Behavior of Pre-Stressed Concrete Railroad Ties", In Proceeding of the Joint Rail Conference(JRC). March 2015 San Jose, CA

[9] Weixin Zhao, B. Terry Beck, Robert J. Peterman, Robert Murphy, Chih-Hang John Wu, Grace Lee "A Direct Comparison of the Traditional Method and a New Approach in Determining 220 Transfer Lengths in Prestressed Concrete Railroad Ties" Proceedings of the 2013 Joint Rail Conference (JRC), JRC2-13-2469 April 15-18, 2013, Knoxville, TN, USA

[10] American Society of Mechanical Engineers, ASME Y14.5-2009. "Dimensioning and Tolerancing", February 2009.

[11] Joseph Holste, Mark Haynes, Robert Peterman, B. Terry Beck, Chih-Hang John Wu, "Application of Tensioned Pullout Tests to Investigate Bond and Splitting Characteristics" Pre-stressed Concrete Institute, National Bridge Conference, (PCI/NBC)Setpember 6-9, 2014

[12] ASTM International, 2010 "Standard Specification for Steel Wire, Indented, Low-Relaxation for Prestressed Concrete Railroad Ties", Designation: A881/A881M – 10

[13] Weixin Zhao, B. Terry Beck, Robert J. Peterman, CHih-Hang John Wu, Grace Lee, Naga Narendra B. Bodapati. "Determining Transfer Length in Pre-Tensioned Concrete Railroad Ties: Is a New Evaluation Method Needed" Proceedins of the ASME 2013 Rail

Transportation Division Fall Technical Conference (RTDF2013) October 15-17, 2013 Altoona, Pennsylvania, USA (RTDF2013-4727)

[14] Weixin Zhao, B. Terry Beck, Robert J. Peterman, Chih-Hang John Wu, "Development of a 5-Camera Transfer Length Measurement System for Real-Time Monitoring of Railroad Crosstie Production" Proceedings of the 2013 Joint Rail Conference (JRC2013) April 15-18, 2013, Knoxville, TN, USA

[15] Weixin Zhao, Kyle Larson, Robert J. Peterman, B. Terry Beck, Chih-Hang J. Wu. "Development of a Laser Speckle Imaging Device to Determine the Transfer Length in Pretensioned Concrete Members" PCI Journal, Winter 2012, pp135-143

[16] Matthew L. Arnold, Robert J. Peterman, Naga Narendra B. Bodapati, B. Terry Beck, Chih-Hang (John) Wu. "Development of a Standard Bond Test for Indented Prestressing Wires" Proceedings of the 2013 Joint Rail Conference (JRC2013). April 15-18, 2013, Knoxville, Tennessee, USA (JRC2013-2461)

[17] B. Terry Beck, Weixin Zhao, Robert J. Peterman, Chih-Hang John Wu, et al. "Effect of Surface-Strain Sampling Interval on the Reliability of Transfer Length Measurements" Pre-stressed Concrete Institute, National Bridge Conference, (PCI/NBC)Setpember 6-9, 2014

[18] Fuchang Gao, Lixing Han. "Implementing the Nelder-Mead simplex algorithm with adaptive parameters" Computation Optimization and Applications, January 2012, Volume 51, Issue 1, pp 259-277

[19] Stang, H., Li, Z., and Shah, S. (1990). "Pullout Problem: Stress versus Fracture Mechanical Approach." *J. Eng. Mech.*, 116(10), 2136–2150.

[20] Henzold, George, "Geometrical Dimensioning and Tolerancing for Design, Manufacturing and Inspection, Second Edition: A Handbook for Geometrical Product

Specification using ISO and ASME standards" copyright: 2006 Published by Elsevier Ltd.

[21] S.T. Huang, K. C. Fan, John H. Wu, "New Minimum Zone Method for Evaluating Straightness Errors". Precision Engineering Vol. 15, Issue 3, July 1993, Pages 158-165 Precision Engineering

[22] J.A. Nelder. "A simplex method for function minimization" The Computer Journal (1965) 7 (4):308-313

[23] Jeffrey C. Lagaria, "Convergence Properties of the Nelder-Mead Simplex Method in Low Dimensions" Society for Industrial and Applied Mathematics Journal on Optimization (1998) Vol. 9, No. 1, pp. 112-147

[24] Jiing-Yih J, Ing-Hong Chen, "Minimum Zone Evaluation of Circles and Cylinders. International" Journal of Machine Tools and Manufacture. Vol. 36, Issue 4, April 1996, pp 435-451

[25] Joseph R. Holste, Mark Haynes, Robert J. Peterman, B. Terry Beck, John C.-H. Wu, "Tensioned Pullout Test used to Investigate Wire Splitting Propensity in Concrete Railroad Ties," Proceedings of the 2014 Joint Rail Conference, JRC2014-3799 April 2-4, 2014, Colorado Spring, Colorado, USA.

[26] Krulikowski, Alex, "Fundamentals of Geometric Dimensioning and Tolerancing, Third Edition" copyright 2012 Published by Effective Training Inc.

[27] Lawrence, P. (1972). "Some theoretical considerations of fibre pull-out from an elastic matrix." Journal of Material Science, 7(1), 1-6

[28] Laws, V. (1982). "Micromechanical aspects of the fibre-cement bond." Composites, 13, Apr., 145-151.

[29] Margaret H. Wright, “Nelder, Mead, and the Other Simplex Method” Documenta Mathematica (2012) 271-276 Extra Volume ISMP

[30] Mathew Arnold, “Un-Tensioned Pullout Tests to Predict the Transfer Length of Different Prestressing Reinforcements Used in Concrete Railroad Ties” Master Thesis, May 2013, Kansas State University, Manhattan, Kansas, USA.

[31] Naga N.B. Bodapati, Robert J. Peterman, B. Terry Beck, Chih-Hang John Wu, “Effect of Concrete Properties on Transfer Lengths in Concrete Rail-Road Ties”. In Proceedings of the Joint Rail Concference(JRC). April 2014 Colorado Springs, CO

[32] Naga N.B. Bodapati, Robert J. Peterman, Weixin Zhao, B. Terry Beck, Chih-Hang John Wu, Joseph R. Holse, Matthew L. Arnold, Ryan Benteman, Robert Schweiger, “Transfer Length Measurements on Concrete Railroad Ties Fabricated with 15 Different Prestressing Reinforcements”. Prestressed Concrete Institute National Bridge Conference 2013 PCI/NBC

[33] Naga N.B. Bodapati, Weixin Zhao, Robert J. Peterman , John C.-H. Wu, B. Terry Beck, Mark Haynes and Joseph R. Holste, "Influence Of Indented Wire Geometry And Concrete Parameters On The Transfer Length In Prestressed Concrete Crossties " Proceedings of the 2013 Joint Rail Conference, JRC2013-2463 April 15-18, 2013, Knoxville, Tennessee, USA. doi: 10.1115/JRC2013-2463.

[34] C.-H. Wu, W. Zhao, T. Beck, R. Peterman, “Optical Sensor Developments for Measuring the Surface Stains in Prestressed Concrete Members” Strain: An International Journal for Experimental Mechanics. Strain (2011) 47, pp376-386

[35] Weixin Zhao, B. Terry Beck, Robert J. Peterman, Chih-Hang John Wu, Naga Narendra B. Bodapati, Grace Lee, “Reliable Transfer Length Assesment for Real-Time Monitoring

of Railroad Crosstie Production" Proceedings of the 2014 Joint Rail Conference (JRC2014) April 2-4, 2014, Colorado Springs, CO, USA (JRC2014-3830)

[36] Robert L. Murphy., "Determining the Transfer Length in Prestressed Concrete Railroad Ties Produced in the United States", Master Thesis, 2012, Kansas State University, Manhattan, Kansas, USA.

[37] Umesh Arasu, John Wu "Geometric Tolerance Verification Algorithms for Computer Vision Inspection." Kansas State University (1997)

[38] W. Yeih, R. Huang, J.J. Chang, C.C.Yang, "A Pullout Test for Determining Interface Properties between Rebar and Concrete." Journal of Advanced Cement Based Materials, March (1997)

[39] Walter Gander, Gene H. Golub, and Rolf Strebel, "Least Squares Fitting of Circles and Ellipses" BIT 34(1994), 558-578

[40] Weixin Zhao, B. Terry Beck, Robert J. Peterman, Robert L. Murphy, et al. "An Automated Transfer Length Measurement System for Use on Concrete Railroad Ties" Prestressed Concrete Institute National Bridge Conference (2012 PCI/NBC)

[41] Weixin Zhao, Robert L. Murphy, Robert J. Peterman, M.ASCE, B. Terry Beck, Chih-Hang John Wu, and Pelle N. Duong "Noncontact Inspection Method to Determine the Transfer Length in Pretensioned Concrete Railroad Ties". Journal of Engineering Mechanics 2013. 139:256-263.

[42] Di Angelo, Luca. "Automatic evaluation of form errors in high-density acquired surfaces". International Journal of Production Research 17 January 2010

[43] Radu Bogdan, Rusu. "Fast 3D Recognition and Pose Using the Viewpoint Feature Histogram." Intelligent Robots and Systems (IROS), 2010 IEEE/RSJ International Conference 18-22 October 2010

[44] Tian Chen. “Application of Optical Inspection and Metrology in Quality Control for Aircraft Components.” Computer Engineering and Technology (ICCET), 2010 2nd Internation Conference V5-294-298 16-18 April 2010

[45] Fahraz Ali, “Part Design and Evaluation through Reverse Engineering Approach”, Proceedings of the International Journal of Modern Engineering IAJC-IJME International Conference 2008

[46] Ming-June Tsai, “Development of a high-precision surface metrology system using structured light projection” , Measurement, Volume 38, Issue 3, October 2005, Pages 236-247, ISSN 0263-2241

[47] Susana Martinez, “Analysis of Laser Scanning and Strategies for Dimensional and Geometrical Control”, International Journal of Advanced Manufacturing Technology (2010) 45:621-629

[48] Hong-Tzong Yau, “An Automated Dimensional Inspection Environment for Manufactured Parts Using Coordinate Measuring Machines”, International Journal of Production Research 1992, Vol. 20, No 7, 1517-1536

[49] J. Gao, “An Automated GD&T Inspection System Based on Non-Contact 3D Digitization”, International Journal of Production Research, Vol. 44, No. 1, 1 January 2006, 117-134

[50] Antonia J. Spyridi, “Automatic Programming of Coordinate Measuring Machines”, International Conference of Robotics and Automation (ICRA) 1994: 1107-1112

[51] Roberto Raffaeli, “Context Dependent Automatic View Planning: The Inspection of Mechanical Components Computer-Aided Design and Applications”, 10(1), 2013, 111-127

[52] Y. Rong, “Locating Error Analysis and Tolerance Assignemnt for Computer Aided Fixture Design”, International Journal of Production Research 2001, Vol. 39, No. 15, 3529-3545 20

[53] Y14.5.1 Subcommittee, 1992, “Mathematization of Dimensioning and Tolerancing”, The American Society of Mechanical Engineers, N.Y., USA.

[54] Lowe, D.G., “Local Feature View Clustering for 3D Object Recognition, Computer Vision and Pattern Recognition”, 2001. CVPR 2001. Proceedings of the 2001 IEEE Computer Society Conference Volume 1 I-682-688

[55] Lowe, D.G., “Object Recognition from Local Scale-Invariant Features”, Computer Vision, 1999 Proceedings of the 7th IEEE International Conference 20 Sept 1999, pg 1150-1157

[56] Herbert Bay, Tinne Tuytelaars, Luc Van Gool, “SURF: Speeded Up Robust Features” Proceedings of the ninth European Conference on Computer Vision, May 2006

[57] ASTM International, 2014 “Standard Specification for Deformed and Plain Carbon-Steel Bars for Concrete Reinforcement”, Designation: A615/A615M – 14

[58] Deng, Yaohua. Morcuous, George. Ma, Zhongguo, 2015 “Strand bond stress-slip relationship for prestressed concrete members at prestress release”, Materials and Structures. 30 January 2015 DOI 10.1617/s11527-015-0546-1

[59] Dang, Canh. Murray, Cameron. Royce, Floyd. Hale, Micah. Vargas, J. R. Marti “Correlation of Strand Surface Quality to Transfer Length” Title No. 111-S106. ACI Structural Journal. V. 111, No. 5 September-October 2014.

[60] Dang, Canh “Measurement of Transfer and Development Lengths of 0.7 in. Strands on Pretensioned Concrete Elements” A Dissertation. University of Arkansas, May 2015.

[61] SAS Institute Inc. “SAS/STAT(R) 9.2 User’s Guide, Second Edition” 2009 Cary, NC, USA

Abbreviations and Acronyms

Abbreviation	Definition
2D	2 Dimensional
3D	3 Dimensional
ADC	Analog to Digital Conversion/Converter
Adj R-Square (R^2)	adjusted coefficient of determination
ANOVA	ANalysis of VAriance
ASME	American Society of Mechanical Engineers
ASTM	American Society for Testing and Materials
Avg	Average
AvgAngle	Average Indent Edge Wall Angle
AvgDepth	Average Indent Depth
AvgVal	Average value collected from non-contact sensor (mm)
AvgWidth	Average Indent Width
axialdist	Indent length as measured across the axis of the reinforcement wire (mm)
BFGS	Broydent-Fletcher-Goldfarb-Shanno algorithm
BIN	Bond Index Number
CMM	Coordinate Measuring Machines
CNC	Computer Numerical Control
CosSqAngle	Cosine of the Squared Edge Wall Angle
CPU	Central Processing Unit
Depth	Depth of the indented region (mm)
DevAngle	Standard Deviation of Indent Edge Wall Angle
DevDepth	Standard Deviation of Indent Depth
DevWidth	Standard Deviation of Indent Width
DF	Degrees of Freedom
EdgePSA	Indent edge projected surface area (mm^2)
EdgePSAtfsa	Indent edge slope determined by dividing EdgePSA by EdgeTFSA (unitless)
EdgeSlope	Slope of the indented edge (Deg./Rad.)

EdgeTFSA	Indent edge surface area as measured by the sum of the triangular facets (mm^2)
EL	Length of the ellipsoidal region from fitted ellipse of indent (mm)
EW	Width of the ellipsoidal region from fitted ellipse of indent (mm)
FR	Fletcher Reeves conjugate gradient method
GD&T	Geometric Dimensioning and Tolerancing
GPU	Graphical Processor Unit
IO	Input / Output
KSI	Release strength in kilo pounds per square inch
Lap1	Average value of the first order laplacian filter (mm)
Lap2	Average value of the second order laplacian filter (mm)
MCU	Microcontroller Unit
MSE	Mean Square Error
NM	Nelder Mead
NMParallel	Nelder Mead parallel processing algorithm
Ori	Orientation of the indented region (Deg./Rad.)
PC	Personal Computer
PLC	Programmable Logic Controller
PR	Polak Ribiere conjugate gradient method
PRParallel	Polak Ribiere parallel processing algorithm
PRUSS	Programmable Realtime Unit Sub-System
PSA	Projected surface area of the indent (mm^2)
PSAcm	Projected surface area of the indent per cm length of reinforcement (mm^2)
PSI	Release strength in pounds per square inch
Pr (p-value)	probability of observing a test statistic that is more extreme than observation
RAM	Random Access Memory
RotatDist	Indent width as measured across the axis of the reinforcement wire (mm)
R-Square (R^2)	coefficient of determination
s.t.	Subject To
SD	Steepest Descent search method
SPI	Serial Peripherial Interface
StDev, StdDev	Standard Deviation

TFSA	Indent surface area as measured by the sum of the triangular facets (mm^2)
TIR	Timer Interrupt Routine
TL	Transfer Length (general) (in)
USB	Universal Serial Bus
VV	Volumetric space of the indented region (mm^3)
VVcm	Volumetric space of the indented region per cm length of reinforcement (mm^3)
WA	Smooth prestressing steel wire used as a control sample
WB,WC,…,WM	Label for type of commercially available reinforcement wire
WN	Commercial reinforcement wire pulled from ties that failed at plant
ZL	Transfer Length (using Zhao Lee Method) (in)